TECHNISCHE UNIVERSITÄT MÜNCHEN

Lehrstuhl für Kommunikation und Navigation

Bias Estimation for Precise Point Positioning

Zhibo Wen

Vollständiger Abdruck der von der Fakultät für Elektrotechnik und Informationstechnik der Technischen Universität München zur Erlangung des akademischen Grades eines

Doktor-Ingenieurs

genehmigten Dissertation.

Vorsitzende: Prof. Dr.-Ing. Antonia Wachter-Zeh
Prüfer der Dissertation:
1. Prof. Dr. sc. nat. Christoph-Georg Günther
2. Prof. Dr.techn. Bernhard Hofmann-Wellenhof

Die Dissertation wurde am 21.06.2017 bei der Technischen Universität München eingereicht und durch die Fakultät für Elektrotechnik und Informationstechnik am 28.08.2017 angenommen.

Abstract

The Global Navigation Satellite System (GNSS) provides precise location and time information, where precision belongs one key value of satellite navigation. Millimeter- to centimeter-level accuracy enables various scientific and industrial applications, ranging from geodetic surveying, aeronautical navigation, precise farming, all the way to automated driving in future.

There are two main methods which achieve centimeter-level positioning accuracy, well-established double difference approaches and absolute approaches with a single-receiver, i.e. precise point positioning (PPP). PPP has become more and more attractive as it does not require the exchange of full set of measurements from a nearby station. However, there remains a challenge with PPP to reach the ultimate accuracy within a shortest period of time. The resolution of carrier phase ambiguities plays an essential role to shorten convergence time, which requires precise a priori corrections, including satellite phase and code biases.

This thesis shortly gives an overview of both methods, i.e. double difference and PPP, then presents multi-frequency PPP concepts and algorithms. In this work, new algorithms are proposed to estimate phase and code biases with regional and global networks of stations. Cascaded Kalman filters are introduced to separate the estimation of geometric and ionospheric terms in the second stage, while treating them as combined parameters in the first stage. A decorrelation method, the Bryson's method, is applied so that the measurements for the second-stage is no longer correlated over time. Moreover, a new algorithm is introduced to estimate the ionospheric delays and code biases using Kriging method, which shows outstanding performance compared to existing methods. Last but not least, the proposed algorithms in this work are validated with various real GNSS data.

Contents

Chapter 1

Introduction

Since GPS came into operation, positioning and navigation can be achieved with less effort [1, 2]. Nowadays, Global Navigation Satellite System (GNSS) includes GPS, GLONASS, Galileo and BeiDou systems [3]. In this thesis we will mainly focus on the most widely-used system GPS, since the positioning concepts of the other systems are similar. As long as a user has enough satellite coverage, he could determine his position at meter to centimeter level [4–6]. The positioning accuracy depends on many factors including, among others, available measurement types and frequencies, positioning algorithms, environmental constraints.

Two types of measurements, code and carrier phase, provide ranging information. Code measurements represent signal travel time from satellites to receivers multiplied with the speed of light. The travel time is determined by the offset between spreading codes of the satellite and of the local replica, obtained from finding peaks of the correlation function. The chip length is however in the order of 300 meters. Receivers with good design can achieve accuracy of code measurements only at meter level. Carrier phase measurements represent the phase of the carrier wave. The wavelength, e.g. 19 cm for GPS L1 frequency, is several orders of magnitude smaller than one chip length of the spreading code. Carrier phase measurements are able to provide a precision at the millimeter level. However, the number of integer cycles in the phase measurements is ambiguous and needs to be resolved. In order to achieve centimeter-level accuracy using GPS signals, carrier phase measurements have to be used jointly with the code measurements.

Zumberge et al. first introduced the concept of precise point positioning (PPP) in [7], where a single receiver determines its position with a high accuracy anywhere on the earth. This can be realized by applying precise corrections, including satellite orbit and clock corrections, earth modelling corrections, bias corrections, etc. PPP has one advantage that it does not need observations from a reference station, like in the case of differential positioning. Another advantage is its homogeneous positioning quality on a global scale.

Ambiguity resolution is a challenging task in PPP. A user needs to wait for a relatively long time, in the order of 15 minutes, to have the first ambiguity fixed. The phase biases, typically coming from unknown hardware delays, would jeopardise the ambiguity resolution. Traditional PPP approaches apply satellite wide-lane and narrow-lane phase bias calibrations to perform ambiguity resolution, as proposed by Laurichesse et al. in [8, 9], Ge et al. in [10] and Geng et al. in [11]. However, it is difficult to fix the ambiguities, as the narrow-lane wavelength is reduced to almost one half of the wavelength of L1.

This thesis proposes new algorithms for the estimation of uncombined phase and code biases with a network of reference stations. Günther, Henkel and Wen have proposed in [1, 12–14] a full-rank measurement model for the network estimation via a set of parameter

mappings. The precise bias information can be used to enable ambiguity fixing and reduce convergence time in precise point positioning. Besides, it is observed by Vergara et al. in [15] that different receiver types would lead to different bias estimates. The network for bias estimation is suggested to consist of same type of receivers.

Environmental constraints also belong to challenges for PPP. Code multipath remains one of the largest error sources which degrade the position solution. It is thus essential for precise positioning to mitigate the multipath. The most popular mitigation techniques are developed in the tracking loops, e.g. using narrow correlators by Van Dierendonck et al. in [16]. However, there could still be substantial remaining code multipath, which eventually degrades ambiguity resolution. In this work, two methods for mitigating code multipath are suggested, namely sidereal filtering for stationary receivers and multipath states augmentation in state vectors.

For PPP with single-frequency measurements, the user would need to correct the ionospheric delays as well as the ionospheric biases from external sources. The thin-shell model for the ionosphere allows the association between slant delay and vertical delay with a mapping function. A rank-deficiency still exists if the vertical delay and the ionospheric biases are jointly estimated, as there are as many slant delay measurements as states of vertical delays. Thus, the total electron content (TEC) of the ionosphere has to be properly modelled to overcome the rank-deficiency. In this work, the Kriging method, a well-established method in geostatistics, is used to model the ionosphere. A Kalman filter is applied for the joint estimation with a network of stations.

1.1 Thesis Outline

In the first chapter, a generalized model for the absolute code and phase measurements is presented. We then briefly introduce the two main methods achieving centimeter-level accuracy, namely double difference and precise point positioning.

Chapter 2 starts with introduction on error mitigation for PPP. Additionally, the correlation among tropospheric zenith delay, receiver clock offset and receiver height is studied analytically. Then a traditional PPP approach is presented, where ionosphere-free combinations are applied to code and phase measurements. Next, we propose a multi-frequency algorithm for PPP using a Kalman filter with absolute and uncombined measurements. The integer ambiguities are kept as real-valued parameters. Additional improvements are made to the PPP algorithm by imposing extra constraint on zenith delays and by introducing a subset of code multipath into the state vector. Besides, the algorithm is augmented to solve a multi-GNSS system, e.g. a combined GPS and Galileo system.

The assumption that the link biases can be split to satellite- and receiver biases, enables the estimation of the biases in Chapter 3 with a network of stations. Necessary methods are still to be applied to remove the rank-deficiency in the system. Cascaded Kalman filters are suggested to estimate the phase and code biases in two steps, where the geometric states are not further separated in the first-stage. The Bryson and Henrikson's method is applied to decouple the colored measurement noise for the second-stage filter. Additionally, sidereal filtering helps to mitigate repeatable multipath patterns and as a consequence it improves the stability of the bias estimates significantly.

Chapter 4 focuses on the ionospheric bias estimation. Several current ionospheric mod-

els are introduced, such as the planar fitting [17], the Neustrelitz model [18], and the bicubic splines interpolation [19, 20]. In this chapter, a new algorithm is proposed to jointly estimate vertical ionospheric delays and ionospheric biases with Kriging method. The Kriging estimator is unbiased and optimized in the sense of minimizing the estimation error. A Kalman filter is employed to estimate the states, after the rank-deficiency is removed by introducing an iterative selection procedure to map the vertical delays. In the end, real data from a network of 24 IGS stations are collected to validate the algorithm.

As the current broadcast orbit is only accurate at meter level, chapter 5 presents the concept of providing a standard receiver with precise broadcast-like satellite ephemeris. Precise orbits published by IGS are given in Cartesian coordinates, while internet connection is also required to obtain them. Curve fit methods are suggested to convert the precise orbits to standard ephemeris in this chapter.

Last but not least, chapter 6 concludes the thesis. In this thesis, not only algorithms are proposed for precise point positioning and for the estimation of phase and code biases, but also practices are performed with real measurement data for all proposed algorithms.

1.2 Generalized Measurement Model

Assuming the link biases could be split into receiver and satellite components, i.e. $\beta^k_{m,r} = \beta_{m,r} + \beta^k_m$ and $b^k_{m,r} = b_{m,r} + b^k_m$, a generalized model for the code and carrier phase measurements ρ and $\lambda\varphi$ for receiver r, satellite k on frequency f_m is presented by

$$\begin{aligned}
\rho^k_{m,r}(t) = &\left(\vec{\boldsymbol{e}}_r^{\,k}(t)\right)^{\mathrm{T}} \cdot \left(\vec{\boldsymbol{r}}_r(t) + \Delta\vec{\boldsymbol{r}}_{r,\mathrm{et}}(t) - \vec{\boldsymbol{r}}^{\,k}(t')\right) + c\delta_r(t) - c\delta^k(t') + m^k_{\mathrm{T},r}(t)T_{\mathrm{z},r}(t) + \\
&\frac{f_1^2}{f_m^2} I^k_{1,r}(t) + b_{m,r} + b^k_m + \eta^k_{m,r}(t), \\
\lambda_m\varphi^k_{m,r}(t) = &\left(\vec{\boldsymbol{e}}_r^{\,k}(t)\right)^{\mathrm{T}} \cdot \left(\vec{\boldsymbol{r}}_r(t) + \Delta\vec{\boldsymbol{r}}_{r,\mathrm{et}}(t) - \vec{\boldsymbol{r}}^{\,k}(t')\right) + c\delta_r(t) - c\delta^k(t') + m^k_{\mathrm{T},r}(t)T_{\mathrm{z},r}(t) - \\
&\frac{f_1^2}{f_m^2} I^k_{1,r}(t) + \lambda_m(N^k_{m,r} + \beta_{m,r} + \beta^k_m) + \lambda_m\varphi^k_{\mathrm{pw},r}(t) + \lambda_m\varphi_{\mathrm{pcv},m,r}(t) + \\
&\lambda_m\varphi^k_{\mathrm{pcv},m}(t) + \varepsilon^k_{m,r}(t),
\end{aligned} \tag{1.1}$$

where the parameters are explained as

t	time of signal reception
t'	time of signal transmission
$\vec{\boldsymbol{e}}_r^{\,k}$	unit vector from satellite to receiver,
$\vec{\boldsymbol{r}}_r$	position vector of receiver phase center,
$\Delta\vec{\boldsymbol{r}}_{r,\mathrm{et}}$	site displacement due to earth tides
$\vec{\boldsymbol{r}}^{\,k}$	position vector of satellite phase center,
$c\delta_r$	receiver clock offset,
$c\delta^k$	satellite clock offset,
$m^k_{\mathrm{T},r}$	tropospheric mapping function from zenith to slant direction,
$T_{\mathrm{z},r}$	tropospheric zenith delay,
$I^k_{1,r}$	slant ionospheric delay on frequency f_1,

$b_{m,r}$	receiver code bias,
b_m^k	satellite code bias,
λ_m	wavelength of m-th carrier,
$N_{m,r}^k$	carrier phase integer ambiguity,
$\beta_{m,r}$	receiver phase bias,
β_m^k	satellite phase bias,
φ_{pw}^k	phase wind-up,
$\varphi_{\mathrm{pcv},m,r}$	receiver antenna phase center variation,
$\varphi_{\mathrm{pcv},m}^k$	satellite antenna phase center variation,
$\eta_{m,r}^k$:	code noise including multipath,
$\varepsilon_{m,r}^k$:	phase noise including multipath.

For simplicity the epoch index t is omitted later, unless state transitions are discussed.

1.3 Double Difference

Double difference (DD) performs both between-receiver and between-satellite differences for a user u and a reference station r, i.e.

$$\begin{aligned}\rho_{m,ur}^{k\ell} &= (\rho_{m,u}^k - \rho_{m,u}^\ell) - (\rho_{m,r}^k - \rho_{m,r}^\ell),\\ \lambda_m\varphi_{m,ur}^{k\ell} &= (\lambda_m\varphi_{m,u}^k - \lambda_m\varphi_{m,u}^\ell) - (\lambda_m\varphi_{m,r}^k - \lambda_m\varphi_{m,r}^\ell),\end{aligned} \tag{1.2}$$

with the satellite index ℓ representing the reference satellite. Double difference eliminates common errors such as the receiver and satellite clock offsets, the code and phase biases, as well as most of the atmospheric delays. Under favorite circumstances, this provides millimeter to centimeter positioning accuracy [21]. One major disadvantage of double difference is the need of a nearby reference station providing a full set of observations.

From Eq. (1.2), the DD phase and code measurement model is obtained as

$$\begin{aligned}\rho_{m,ur}^{k\ell} + \vec{\boldsymbol{e}}_{ur}^{\,k,\mathrm{T}}\vec{\boldsymbol{r}}^{\,k} - \vec{\boldsymbol{e}}_{ur}^{\,\ell,\mathrm{T}}\vec{\boldsymbol{r}}^{\,\ell} + \vec{\boldsymbol{e}}_r^{\,k\ell,\mathrm{T}}\vec{\boldsymbol{r}}_r &= \vec{\boldsymbol{e}}_u^{\,k\ell,\mathrm{T}}\vec{\boldsymbol{r}}_u + \frac{f_1^2}{f_m^2}I_{1,ur}^{k\ell} + T_{ur}^{k\ell} + \eta_{m,ur}^{k\ell},\\ \lambda_m\varphi_{m,ur}^{k\ell} + \vec{\boldsymbol{e}}_{ur}^{\,k,\mathrm{T}}\vec{\boldsymbol{r}}^{\,k} - \vec{\boldsymbol{e}}_{ur}^{\,\ell,\mathrm{T}}\vec{\boldsymbol{r}}^{\,\ell} + \vec{\boldsymbol{e}}_r^{\,k\ell,\mathrm{T}}\vec{\boldsymbol{r}}_r &= \vec{\boldsymbol{e}}_u^{\,k\ell,\mathrm{T}}\vec{\boldsymbol{r}}_u - \frac{f_1^2}{f_m^2}I_{1,ur}^{k\ell} + T_{ur}^{k\ell} + \lambda_m N_{m,ur}^{k\ell} + \varepsilon_{m,ur}^{k\ell}.\end{aligned} \tag{1.3}$$

The equations are only valid, if the measurements at the receiver and at the reference station are perfectly synchronized. Otherwise, there are two orbit positions at two different time instants. These equations will later be complemented with additional terms, such as the earth tides, the phase wind-up, the antenna phase center offsets and variations. They are neglected in Eq. (1.3) for simplicity. It is noted that, since the user and the reference station have different receiver clocks, the satellite positions refer to different signal time of transmission. Thus, the receiver clock offsets have to be first estimated individually for each receiver, e.g. via standard iterative Newton's method.

In order to use the more precise phase measurements, the integer ambiguities need either to be eliminated in carrier smoothing, or to be estimated together with the position of the user. For short baselines (less than 50km) with co-altitude receivers, the atmospheric

delays are most likely cancelled out, leaving only the baseline vector and the ambiguities as unknowns [21]. In other cases the double difference ionospheric delays shall be included in the state vector, while the tropospheric delays can be corrected from models.

1.4 Precise Point Positioning

Precise point positioning (PPP) is able to provide position solutions at centimeter level for a single receiver. PPP relies on precise satellite orbits and clock offsets, which can be determined from a global distributed network. The International GNSS Service (IGS) is a widely used data source for these precise corrections, including orbits and clocks with accuracies up to 2.5 cm, estimated from over three hundred stations by several analysis centers [22]. The corresponding accuracy and latency for different products are listed in Tab. 1.1.

Source	Type	Accuracy	Latency	Sample interval
Broadcast	Orbit	1 m	Real-time	2 hours
	Clock	5 ns RMS[1] 2.5 ns DEV		
IGS Ultra Rapid (predicted half)	Orbit	5 cm	Real-time	15 min
	Clock	3 ns RMS 1.5 ns DEV		
IGS Final	Orbit	2.5 cm	12-18 days	15 min
	Clock	75 ps RMS 20 ps DEV		30 sec

Table 1.1: Summary of selected GPS satellite orbit and clock products [23].

To retrieve the orbit at an arbitrary time instant, IGS orbit products can be interpolated with high-order polynomial fitting (typically 11th-13th order, in this work 12-th) [24]. Since clock behaviour is difficult to be predicted, only up to 3rd-order polynomial fitting is suggested for satellite clock interpolation [25].

Furthermore, PPP algorithms needs corrections of various satellite-, receiver- or propagation-related effects, such as the satellite and receiver phase center offset and variations, the phase wind-up effect, the tide-induced site displacements, etc. These effects are mitigated by either proper modelling or prior calibration and are presented in the next chapter.

[1]RMS stands for root mean square. DEV stands for standard deviation.

Chapter 2

Algorithms for Precise Point Positioning

Precise point positioning (PPP) aims at achieving centimeter-level accuracy with a single receiver. This chapter focuses on all relevant corrections for PPP as well as PPP algorithms. Section 2.1 explains various effects which are to be considered. The effects could solely depend on the satellite, such as the satellite orbit and clock offset, the satellite phase center offset and variation, or on the receiver, including the travel-time correction, the receiver clock offset, the site displacements, or on the link such as the ionospheric and tropospheric delays, the phase wind-up, etc. In Section 2.2, a traditional PPP method is described, where dual-frequency receivers form ionosphere-free combinations to eliminate ionospheric delays. Without additional bias information, the position accuracy normally takes more than 15 minutes to reach centimeter-level, due to large convergence time of ambiguity estimates [5]. Section 2.3 introduces a new PPP algorithm for uncombined measurements. The positioning accuracy and stability are further improved by introducing proper tropospheric zenith delay constraints and code multipath states. Additionally, the absolute PPP model is augmented with multi-GNSS measurements. All algorithms are applied to real GNSS data to analyze the positioning performance.

2.1 Error Mitigation for PPP

This section describes necessary effects to be considered in PPP and their mitigation methods. The effects are presented in three categories, including satellite-related, receiver-related and link-related effects.

2.1.1 Satellite-related Effects

The effects are grouped as satellite-related, because they are either induced by satellites itself, such as satellite orbits and clock offsets, satellite phase center offsets and variations, satellite phase and code biases, or corrected specifically for individual satellites, such as time of signal transmission, time group delay. The satellite phase and code biases are often caused by unknown hardware delays and are observed to be stable over a few hours. Except for the biases, the other effects are listed as follows and are described in the next sub-sections.

- Time of transmission and travel-time correction
- Satellite orbits and clock offsets
- Satellite phase center offsets and variations
- Differential P1-P2 code biases

Time of transmission and travel-time correction

It is well-known that the time of transmission of the signal at the satellite needs to be determined very accurately, as the satellite flies at a speed of roughly 4 km/s in the Earth-Centered Earth-Fixed (ECEF) frame. While a receiver combines signals from multiple satellites at the same time to solve for its position, the time of transmission for each signal is calculated individually for each satellite.

The approach is illustrated in Fig. 2.1, where the duration between the time of reception t' using receiver clock and the time of transmission t^k referenced to system time shall be computed. It consists of two parts: first the propagation time from the satellite to the receiver, and second the satellite clock offset with respect to the system time. By definition the first part is obtained by dividing the pseudorange measurement with the speed of light.

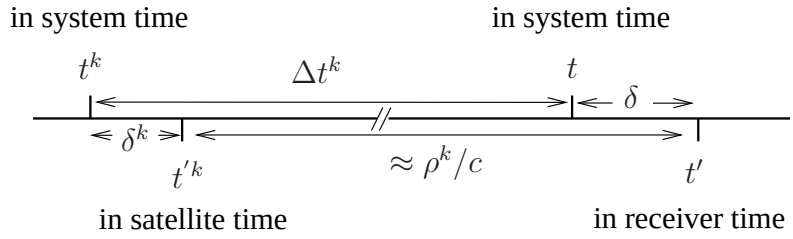

Figure 2.1: A signal transmitted at t'^k with respect to the satellite clock arrives at the receiver at its own time t'. The time of transmission and arrival with respect to the system time are given by t^k and t respectively, and thus the satellite and receiver clock offsets are denoted by δ^k and δ.

The time of transmission is then approximated by

$$t^k \approx t' - \left(\frac{\rho^k}{c} + \delta^k \right), \tag{2.1}$$

where the approximation comes from neglecting the pseudorange noise, and δ^k itself is a function of the time of signal transmission. A recursive approach is applied to determine t^k where 2 steps are often enough to reach the convergence, i,e.

$$\begin{aligned} \text{Step 1}: \quad & t_0^k \approx t' - \frac{\rho^k}{c}, \\ & \delta_0^k = \delta^k(t_0^k), \\ \text{Step 2}: \quad & t_1^k \approx t' - \left(\frac{\rho^k}{c} + \delta_0^k \right), \\ & \delta_1^k = \delta^k(t_1^k). \end{aligned} \tag{2.2}$$

After the satellite positions are calculated at the time of transmissions, they need to be transformed at the time of reception t in system time. The orbit representation in ECEF coordinate frame needs consideration of the earth rotation during the signal travel time. Thus the travel-time $\Delta t^k = t - t^k$ is needed, which shall not be confused with the interval

corrected in Eq. (2.1). The travel-time Δt^k is calculated by

$$\begin{aligned}\Delta t^k &\approx \frac{\rho^k}{c} - \delta + \delta^k \\ &\approx \frac{\|\vec{\boldsymbol{r}} - \vec{\boldsymbol{r}}^{\,k}\|}{c} + \frac{I^k + T^k}{c},\end{aligned} \tag{2.3}$$

which neglects the code biases and noise. The position of the satellite at system time t is then given by

$$\vec{\boldsymbol{r}}^{\,k}(t) = \boldsymbol{R}_z\left(\dot{\Omega}_\mathrm{e}\Delta t^k\right)\cdot\vec{\boldsymbol{r}}^{\,k}(t^k) \tag{2.4}$$

with $\boldsymbol{R}_z$ denoting the rotation matrix along z axis (the rotation axis pointing towards the north), and $\dot{\Omega}_\mathrm{e}$ being the angular velocity of the earth.

In the practice, the atmospheric delays in Eq. (2.3) can be neglected without actual loss of accuracy. Take an example: assume an extreme case of the atmospheric delays being 50 m, the satellite position being $\vec{\boldsymbol{r}}^{\,k} = 10^7\cdot[0.4,\ -1.8,\ 1.9]^\mathrm{T}$ at t^k, the receiver position being $\vec{\boldsymbol{r}} = 10^6\cdot[4.2,\ 0.8,\ 4.8]^\mathrm{T}$ and apply $\dot{\Omega}_\mathrm{e} = 7.2921151467\cdot10^{-5}$ rad/c [26]. The error $\vec{\boldsymbol{\epsilon}}_{\vec{\boldsymbol{r}}^k}$ on the satellite positions due to neglecting atmospheric delays in travel-time correction can be computed by

$$\vec{\boldsymbol{\epsilon}}_{\vec{\boldsymbol{r}}^k} = \left(\boldsymbol{R}_z\left(\dot{\Omega}_\mathrm{e}\frac{\|\vec{\boldsymbol{r}} - \vec{\boldsymbol{r}}^{\,k}\|}{c}\right) - \boldsymbol{R}_z\left(\dot{\Omega}_\mathrm{e}\frac{\|\vec{\boldsymbol{r}} - \vec{\boldsymbol{r}}^{\,k}\| + 50}{c}\right)\right)\cdot\vec{\boldsymbol{r}}^{\,k} = \begin{bmatrix}0.2\\0.05\\0\end{bmatrix}\ \mathrm{mm}, \tag{2.5}$$

which is far under the measurement noise and is thus negligible.

Satellite orbits and clock offsets

Precise satellite orbits and clock offsets are required to be corrected for PPP. The IGS publishes final he orbit and clock products with centimeter-level accuracies [22]. In this section, we focus on the comparison between the broadcast and the IGS final products, to indicate the importance of the corrections.

Cautions should be taken when comparing the orbits of IGS and broadcast ephemerides. The IGS orbits are determined and published relative to the satellites' center of mass, while the broadcast ephemerides refer to the satellites' antenna phase center. The GPS control segment uses internally a different set of phase center offset values from the IGS (see Appendix. A), which are accessible at "NGA GPS Ephemeris/Station/Antenna Offset" in [27]. The difference between the two orbits at the satellite center of mass is given by

$$\boldsymbol{\epsilon}_{\vec{\boldsymbol{r}}^{\,k}} = \boldsymbol{R}_{\mathrm{ECEF}\to\mathrm{RAC}}\cdot\left((\vec{\boldsymbol{r}}^{\,k}_{\mathrm{PC,NGA}} - \boldsymbol{R}_{\mathrm{Body}\to\mathrm{ECEF}}\cdot\Delta\vec{\boldsymbol{r}}^{\,k}_{\mathrm{PCO,NGA}}) - \vec{\boldsymbol{r}}^{\,k}_{\mathrm{CM,IGS}}\right), \tag{2.6}$$

with the error vector $\boldsymbol{\epsilon}_{\vec{\boldsymbol{r}}^{\,k}} = [\epsilon_{r^k_\mathrm{Rd}},\ \epsilon_{r^k_\mathrm{Al}},\ \epsilon_{r^k_\mathrm{Cr}}]^\mathrm{T}$ expressed in satellite radial, along- and cross-track (RAC) coordinate frame, and the indices NGA and IGS to distinguish the two different sources. The indices PC, PCO, CM represent phase center, phase center offset, and center of mass, respectively.

The origin of the RAC coordinate frame locates at the satellite's center of mass. The radial axis points away from the center of the earth. The along-track axis points to the

direction of satellite velocity, and the cross-track axis completes the right-hand system. The transformation matrix from ECEF to RAC frame is given by

$$\boldsymbol{R}^k_{\mathrm{ECEF}\to\mathrm{RAC}} = \left[\vec{\boldsymbol{e}}^{\,k}_{\mathrm{R}},\ \vec{\boldsymbol{e}}^{\,k}_{\mathrm{A}},\ \vec{\boldsymbol{e}}^{\,k}_{\mathrm{C}}\right]^{\mathrm{T}}, \tag{2.7}$$

where the three unit vectors are obtained by

$$\vec{\boldsymbol{e}}^{\,k}_{\mathrm{R}} = -\frac{\vec{\boldsymbol{r}}^{\,k}}{\|\vec{\boldsymbol{r}}^{\,k}\|}, \quad \vec{\boldsymbol{e}}^{\,k}_{\mathrm{A}} = \frac{\dot{\vec{\boldsymbol{r}}}^{\,k}}{\|\dot{\vec{\boldsymbol{r}}}^{\,k}\|}, \quad \vec{\boldsymbol{e}}^{\,k}_{\mathrm{C}} = \frac{\vec{\boldsymbol{e}}^{\,k}_{\mathrm{A}} \times \vec{\boldsymbol{e}}^{\,k}_{\mathrm{R}}}{\|\vec{\boldsymbol{e}}^{\,k}_{\mathrm{A}} \times \vec{\boldsymbol{e}}^{\,k}_{\mathrm{R}}\|}, \tag{2.8}$$

with $\times$ being the cross product.

The satellite body coordinate frame is constructed as

- The origin is located at the center of mass.
- The z'-axis points to the center of the earth.
- The y'-axis is the rotation axis of the solar panel, thus corresponds to the cross product of the z-axis and the vector from the satellite to the sun $\vec{\boldsymbol{r}}_{\mathrm{sun}} - \vec{\boldsymbol{r}}^{\,k}_{\mathrm{CM}}$.
- The x'-axis completes the right-hand system.

The transformation matrix $\boldsymbol{R}^k_{\mathrm{Body}\to\mathrm{ECEF}}$ is therefore given by

$$\boldsymbol{R}^k_{\mathrm{Body}\to\mathrm{ECEF}} = \left[\vec{\boldsymbol{u}}^{\,k}_{x'},\ \vec{\boldsymbol{u}}^{\,k}_{y'},\ \vec{\boldsymbol{u}}^{\,k}_{z'}\right], \tag{2.9}$$

with the unit vectors being

$$\begin{aligned}
\vec{\boldsymbol{u}}^{\,k}_{x'} &= \frac{\vec{\boldsymbol{u}}^{\,k}_{y'} \times \vec{\boldsymbol{u}}^{\,k}_{z'}}{\|\vec{\boldsymbol{u}}^{\,k}_{y'} \times \vec{\boldsymbol{u}}^{\,k}_{z'}\|} \\
\vec{\boldsymbol{u}}^{\,k}_{y'} &= \frac{\vec{\boldsymbol{u}}^{\,k}_{z'} \times (\vec{\boldsymbol{r}}_{\mathrm{sun}} - \vec{\boldsymbol{r}}^{\,k}_{\mathrm{CM}})}{\|\vec{\boldsymbol{u}}^{\,k}_{z'} \times (\vec{\boldsymbol{r}}_{\mathrm{sun}} - \vec{\boldsymbol{r}}^{\,k}_{\mathrm{CM}})\|} \\
\vec{\boldsymbol{u}}^{\,k}_{z'} &= -\frac{\vec{\boldsymbol{r}}^{\,k}_{\mathrm{CM}}}{\|\vec{\boldsymbol{r}}^{\,k}_{\mathrm{CM}}\|}.
\end{aligned} \tag{2.10}$$

Fig. 2.2 shows the comparison for all PRNs grouped by satellite Block types in GPS week 1761. The mean $\bar{m}_i$ and the standard deviation $\bar{\sigma}_i$ for Block type i are computed as

$$\begin{aligned}
\bar{m}_i &= \frac{1}{n_i}\sum_{k=1}^{n_i}\frac{1}{T}\sum_{t=1}^{T}\epsilon^k, \\
\bar{\sigma}_i &= \sqrt{\frac{1}{n_i}\sum_{k=1}^{n_i}\frac{1}{T}\sum_{t=1}^{T}(\epsilon^k)^2},
\end{aligned} \tag{2.11}$$

where ϵ^k represents one of $\epsilon_{r^k_{\mathrm{Rd}}}$, $\epsilon_{r^k_{\mathrm{Al}}}$, $\epsilon_{r^k_{\mathrm{Cr}}}$, or $\epsilon_{c\delta^k}$, T denotes the total number of epochs, and n_i denotes the number of satellites included in the same Block type.

The radial errors are depicted in Fig. 2.2(a), where the oldest type Block IIA exhibits the largest error with the standard deviation being 23 cm. The broadcast orbits of the modernized types have roughly 2-times smaller radial errors of about 10 cm, while the most

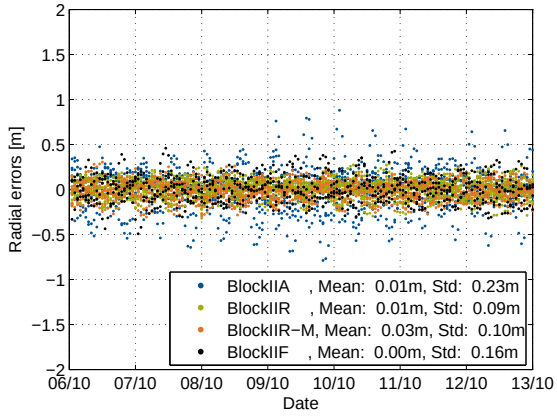

(a) Radial errors. The oldest type Block IIA shows the largest error, while the radial errors of the other satellites are around 10 to 15 cm.

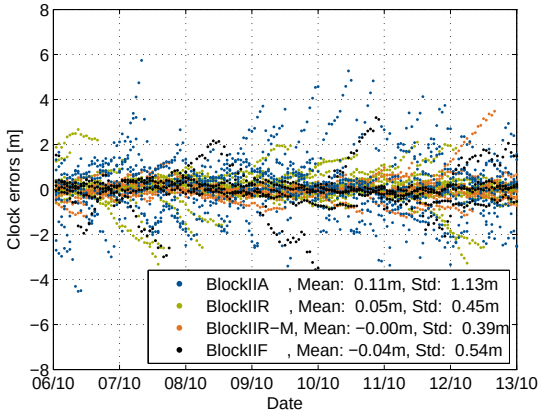

(b) Clock errors. The standard deviations are significantly reduced from Block IIA to IIR-M. The probable reason for the large clock drifts lies in the difficulty in modelling the clock.

Figure 2.2: Broadcast orbit and clock errors for GPS week 1761, where the IGS final orbit and clock products are used as references. The sampling rate is set to 1 hour.

recent type Block IIF has a slightly larger radial error. Similar analysis can be conducted for along- and cross-errors, where cross-track errors are in the range of 50 to 60 centimeters and the along-track is the most difficult component to estimate with standard deviation of 80 to 90 centimeters.

Fig. 2.2(b) shows the broadcast clock errors, which have similar trends in terms of standard deviations among the four satellite groups with Fig. 2.2(a). It is noted that a common shift has been applied to all PRNs aligning the two clock products, which just results in different estimates for receiver clock offsets for the positioning of the user. Large variations up to 6 m can also be observed in Fig. 2.2(b), which is probably due to the difficulty in modelling and predicting the clock behaviour, unlike the well-modelled satellite orbit with high order polynomial fitting. The broadcast clock tends to drift away until the next update on the clock estimate is arrived. It is also seen that the modernization of the satellite type reduces the trend, while one unexpected large variation in Block IIF comes from PRN 24 (with cesium clock).

To study the satellite broadcast ephemerides error combining the orbit and clock, the measure of Signal-in-Space (SIS) Range Error (RE) ϵ^k_{RE} is introduced in [28] as

$$\epsilon^k_{\mathrm{RE}} = \sqrt{\left(\epsilon_{r^k_{\mathrm{Rd}}} - \epsilon_{c\delta^k}\right)^2 + \frac{1}{49}\left(\left(\epsilon_{r^k_{\mathrm{Al}}}\right)^2 + \left(\epsilon_{r^k_{\mathrm{Cr}}}\right)^2\right)}. \tag{2.12}$$

The Root Mean Square (rms) of the SIS Range Error has been plotted for the year 2013, while the RMS for different satellite groups are distinguished. A clear trend of improved broadcast products is observed along the modernization of the satellites. Among all satellites, the broadcast ephemerides error lies around 0.8 m. The newest generation Block IIF satellites have the smallest RMS error of roughly 0.35 m.

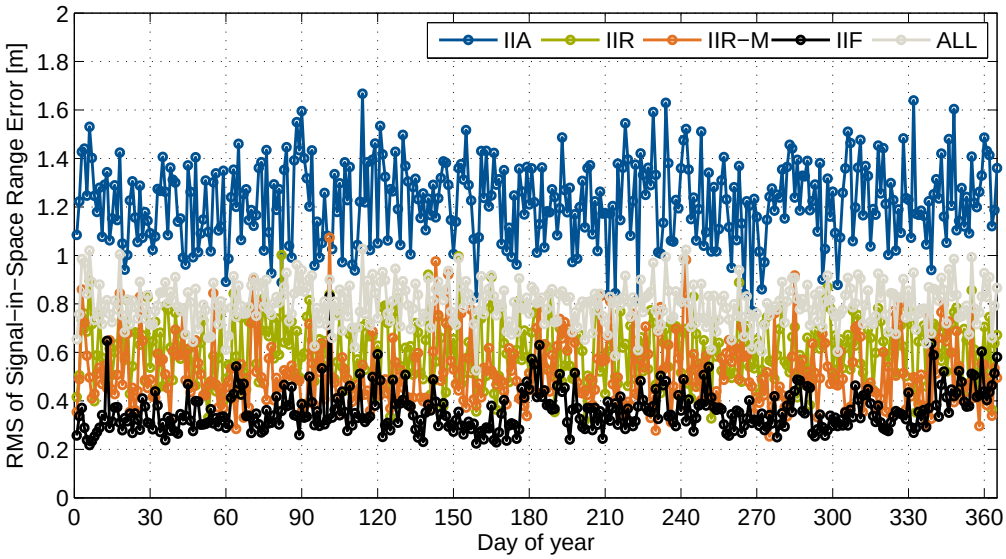

Figure 2.3: The Root Mean Square error of the SIS RE over the year 2013. An improvement of the ephemerides error can be observed along the modernization of the satellite types, i.e. from around 1.2 m for Block IIA satellites to less than 0.4 m for Block IIF satellites.

Phase center offsets and variations

It is important to know the exact positions of the antenna phase centers, which indicate the beginning and the end of a measurement. The phase center position is characterized by two parts, the phase center offset (PCO) and the phase center variation (PCV). For the satellite, the PCO denotes the vector from the satellite center of mass (CM) to the mean phase center, expressed in the satellite body frame. The PCV describes the phase shift from the mean phase center to the instantaneous phase center projected on the propagation link.

A simple drawing for the satellite PCO and PCV is made in Fig. 2.4, which represents a special case of the PCO vector in nadir direction. The line-of-sight direction is characterized by a nadir angle ϕ and an azimuth angle α. The vector $\vec{\boldsymbol{r}}^{\,k}_{\mathrm{PCO}}$ denotes the satellite PCO. An offset $(\Delta r_x,\, \Delta r_y,\, \Delta r_z)$ locates the instantaneous phase center from the mean phase center.

The PCO and PCV are fully correlated by definition, which can be analyzed more intuitively in vertical and horizontal decompositions. A satellite antenna offset Δr_z in the nadir direction could be translated into a cosine-dependent phase center variation $\Delta\varphi_{\mathrm{PCV,z}}$ in the line-of-sight direction, namely the nadir-dependent PCV noted by Schmid and Rothacher in [29] as

$$\Delta\varphi_{\mathrm{PCV,z}}(\phi) = \Delta r_z \cos\phi. \tag{2.13}$$

Moreover, the satellite clock offset is correlated with the nadir-dependent PCV, since a clock offset can be seen as a common shift in the nadir-dependent PCVs for all satellites. Thus, a constraint is imposed over the sum of all PCVs [29] such that

$$\sum_{\phi=0^\circ}^{14^\circ} \Delta\varphi_{\mathrm{PCV,z}}(\phi) = 0, \tag{2.14}$$

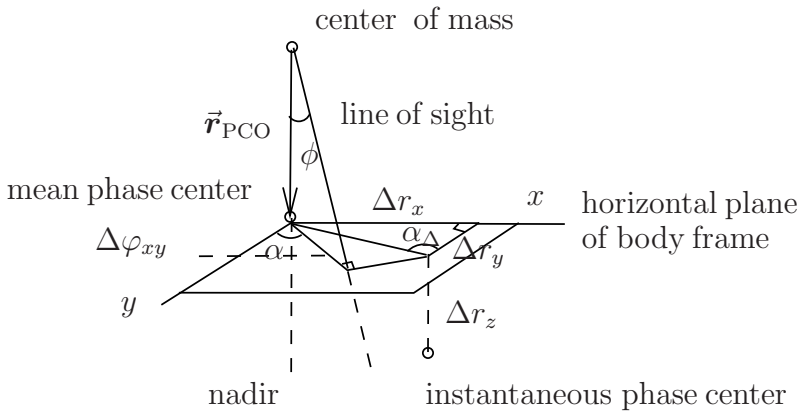

Figure 2.4: Illustration of satellite antenna PCO and PCV. The corrections of offset and variation are fully correlated, where a vertical phase center offset results in a nadir-dependent PCV and a horizontal offset translates into an azimuth-dependent PCV.

where the PCVs are considered at discrete integer nadir angles. Fig. 2.5 shows the nadir-dependent PCVs under different satellite Block types. The sum of the variations over all nadir angles for each curve is constrained to be zero.

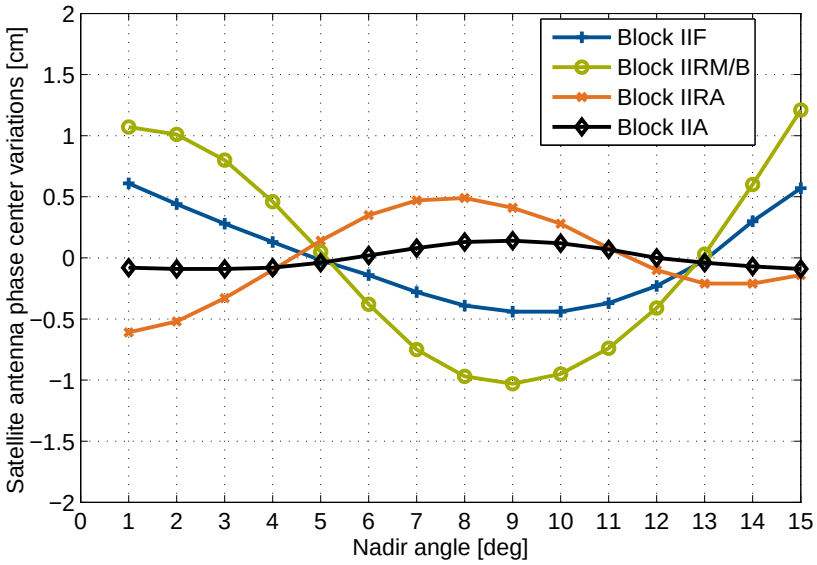

Figure 2.5: The nadir-dependent satellite antenna PCVs for different Block-types.

On the other hand, a horizontal offset of the phase center $(\Delta r_x, \Delta r_y)$ can be interpreted as azimuth-dependent PCV [30]. As shown in Fig. 2.4, the phase center shift $\Delta\varphi_{xy}$ in the azimuth direction is calculated as

$$\Delta\varphi_{xy} = \sqrt{\Delta r_x^2 + \Delta r_y^2} \cdot \cos\left(\alpha_\Delta - \alpha\right), \quad \text{with } \alpha_\Delta = \arg(\Delta r_y + i\Delta r_x), \tag{2.15}$$

with $\arg(\cdot)$ representing the argument operator. The product of $\Delta\varphi_{xy}$ with the sine of the

nadir angle yields the horizontal-dependent PCV $\Delta\varphi_{\mathrm{PCV,h}}(\alpha,\phi)$, i.e.

$$\Delta\varphi_{\mathrm{PCV,h}}(\alpha,\phi) = \sqrt{\Delta r_x^2 + \Delta r_y^2} \cdot \cos\left(\alpha_\Delta - \alpha\right) \cdot \sin\phi \tag{2.16}$$

There exists not only correlation between satellite antenna PCO and PCV, but also between satellite and receiver phase center corrections. The four fully correlated groups cannot be estimated simultaneously, i.e. the determination for one group needs the others be fixed. The receiver PCO and PCV can be obtained from precise absolute robotic calibration to millimeter-level accuracy [31].

Schmid and Rothacher, Schmid et al. proposed the estimation of the satellite antenna PCO and PCV proposed in [29,32]. The phase center offsets are first fixed to a pre-assumed set. From a global network of more than 100 IGS stations, double difference code and phase measurements are used to estimate the orbital elements, tropospheric delays, earth rotation parameters, as well as the phase center variations. The nadir-dependent PCVs are modelled with piecewise linear functions, while the azimuth-dependent variations are modelled with spherical harmonic functions [33]. The estimated PCVs are raw PCVs, which are to be split in the next step into a correction to the pre-fixed PCO and a PCV. The additional constraint in Eq. (2.14) helps to distinguish the z-offset from the nadir-dependent PCVs, while the azimuthal PCVs are fitted to a cosine function for a fixed nadir angle ϕ_0 to get the horizontal offset error, i.e.

$$f(\alpha,\phi_0) = A \cdot \cos(\alpha_\Delta - \alpha). \tag{2.17}$$

Using Eq. (2.16), the horizontal offsets Δr_x and Δr_y can be easily derived.

The satellite PCO is applied when using the IGS orbit products, which are referred to the center of mass. The $\vec{\boldsymbol{r}}^{\,k}_{\mathrm{PCO}}$ vector is normally given in the satellite body coordinate frame, thus, a transformation to the ECEF frame is needed as

$$\vec{\boldsymbol{r}}^{\,k} = \vec{\boldsymbol{r}}^{\,k}_{\mathrm{CM}} + \boldsymbol{R}^k_{\mathrm{Body}\to\mathrm{ECEF}} \cdot \vec{\boldsymbol{r}}^{\,k}_{\mathrm{PCO}}, \tag{2.18}$$

with the index CM representing the center of mass. The transformation matrix is obtained in Eq. (2.9).

Differential P1-P2 code biases

The inter-frequency P1-P2 bias accounts for the difference in the group delays between L1 and L2 frequencies, which is an important correction term for single-frequency users. As described in the GPS Interface Control Document (ICD) in [26], a single-frequency user should correct the satellite clock offset by the satellite differential group delay T^k_{GD}. The reason for this is the coefficient a_{f0} of the clock correction in the navigation message was estimated based on the ionosphere-free combination. The IGS also provides the inter-frequency differential P1-P2 bias products. The DCB P1-P2 biases are provided in the form of $b_{\mathrm{P1P2}} = b_{\mathrm{P1}} - b_{\mathrm{P2}}$. There are both receiver-dependent biases $b_{\mathrm{P1P2},r}$, as well as satellite-dependent ones b^k_{P1P2}. We mainly focus on the latter ones. There exists a linear relationship between the group delay T^k_{GD} and the P1-P2 biases b_{P1P2}.

The model for the code measurements using broadcast clock corrections $c\delta^k_{\mathrm{BRD}}$ can be expressed with

$$\begin{aligned}
\rho^k_{\mathrm{P1},r} &= \left\|\vec{\boldsymbol{r}}_r - \vec{\boldsymbol{r}}^{\,k}\right\| + c\delta_r - \left(c\delta^k + \Delta t^k_{\mathrm{rel}} - T^k_{\mathrm{GD}}\right) + I^k_{\mathrm{P1},r} + T^k_{\mathrm{P1},r} + b_{\mathrm{P1},r} + \eta^k_{\mathrm{P1},r} \\
\rho^k_{\mathrm{P2},r} &= \left\|\vec{\boldsymbol{r}}_r - \vec{\boldsymbol{r}}^{\,k}\right\| + c\delta_r - \left(c\delta^k + \Delta t^k_{\mathrm{rel}} - \frac{f_1^2}{f_2^2}T^k_{\mathrm{GD}}\right) + I^k_{\mathrm{P2},r} + T^k_{\mathrm{P2},r} + b_{\mathrm{P2},r} + \eta^k_{\mathrm{P2},r},
\end{aligned} \tag{2.19}$$

with $\Delta t^k_{\mathrm{rel}}$ being the relativistic correction to the satellite clock offset.

The IGS model for the pseudorange measurements on the other hand, is given by

$$\begin{aligned}
\rho^k_{\mathrm{P1},r} &= \left\|\vec{\boldsymbol{r}}_r - \vec{\boldsymbol{r}}^{\,k}\right\| + c\delta_r - \left(c\delta^k + \Delta t^k_{\mathrm{rel}}\right) + I^k_{\mathrm{P1},r} + T^k_{\mathrm{P1},r} + b_{\mathrm{P1},r} + b^k_{\mathrm{P1}} + \eta^k_{\mathrm{P1},r} \\
\rho^k_{\mathrm{P2},r} &= \left\|\vec{\boldsymbol{r}}_r - \vec{\boldsymbol{r}}^{\,k}\right\| + c\delta_r - \left(c\delta^k + \Delta t^k_{\mathrm{rel}}\right) + I^k_{\mathrm{P2},r} + T^k_{\mathrm{P2},r} + b_{\mathrm{P2},r} + b^k_{\mathrm{P2}} + \eta^k_{\mathrm{P2},r}.
\end{aligned} \tag{2.20}$$

The P1-P2 biases b^k_{P1P2} can be obtained by subtracting $\rho^k_{\mathrm{P2},r}$ from $\rho^k_{\mathrm{P1},r}$ in Eq. (2.20), while the same can be done in Eq. (2.19). By comparison, the linear relationship between the two products is given by

$$b^k_{\mathrm{P1P2}} = b^k_{\mathrm{P1}} - b^k_{\mathrm{P2}} = (1 - \frac{f_1^2}{f_2^2})T^k_{\mathrm{GD}}. \tag{2.21}$$

Since the differential P1-P2 biases are observed stable over weeks, both the navigation message and the IGS provide one bias estimate pro satellite each month. A comparison is made between the two bias products for January 2011. The DCB P1-P2 biases are divided by the coefficient given by Eq. (2.21) to compare with the time group delays. The difference $T^k_{\mathrm{GD}} - 1/(1 - f_1^2/f_2^2) \cdot b^k_{\mathrm{P1P2}}$ is shown in Fig. 2.6. The bias values agree within ± 20 cm. The deviation values are consistent with the accuracies of both products, i.e. the accuracy of time group delay is about 45 cm (one sigma) [26] and best accuracy of IGS ionospheric estimation is about 30 cm [22]. A common shift is applied to all IGS satellite bias estimates. The shift can be absorbed in the receiver code bias.

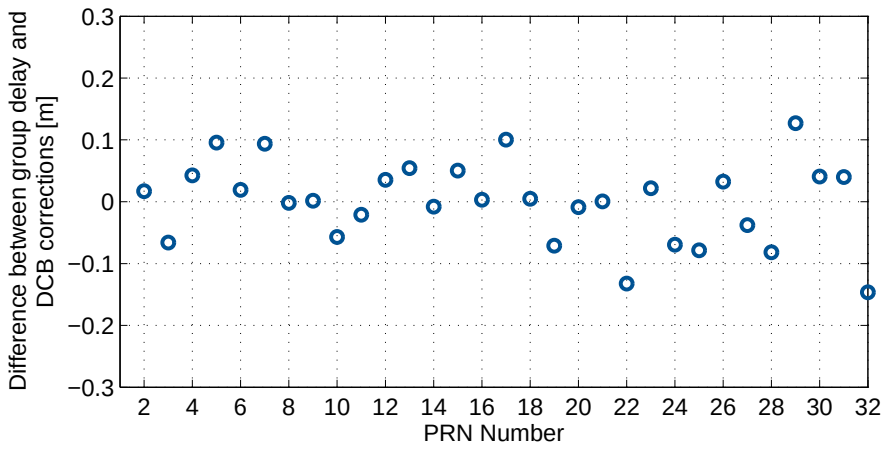

Figure 2.6: The difference between the time group delays and the differential code biases for January 2011. The two products agree within ± 20 cm.

Moreover, it is by IGS convention that the geometry-preserving ionosphere-free combination does not need to correct for any satellite inter-frequency biases [34]. Therefore, the IGS precise satellite clock correction contains a specific combination of biases $f_1^2/(f_1^2 - f_2^2) \cdot b_{\mathrm{P1}}^k - f_2^2/(f_1^2 - f_2^2) \cdot b_{\mathrm{P2}}^k$.

2.1.2 Receiver-related Effects

The effects are meant to be receiver-related either due to receiver characteristics, such as receiver clock offsets, differential P1-C1 code biases, receiver phase center offsets and variations, receiver phase and code biases, measurement noise, or due to the location and environment of the receiver, such as site displacements and multipath.

The receiver clock offset represents the inaccuracy of the local clock compared to system time and must be estimated. The receiver phase and code biases result from unknown hardware delays and can be calibrated before application. The multipath and noise are treated as random error in most applications, which is assumed to follow Gaussian distribution. Except for the above effects, the other items are listed as follows and are presented in the next sub-sections.

- Differential P1-C1 code biases
- Receiver phase center offsets and variations
- Site displacements: solid earth tides, ocean tidal loading, polar motion

Differential P1-C1 code biases

The P1-C1 bias represents the differential code bias between P-code and C/A code on L1 frequency. There exist different tracking techniques for a network with mixed receiver types. Satellite-dependent biases are found between cross-correlation type receivers and modern receivers reporting P1 and P2 observations. Hence, the P1-C1 differential code bias $b_{\mathrm{P1-C1}}$ is introduced by Ray in [35], so that a consistent set of code measurements can be used, e.g. the P1 and P2 set. There are mainly three kinds of measurement sets considered in [34], i.e.

1. For cross-correlation type receiver which reports C/A code (C1) and X2, a synthetic P2 code generated from C1 and the cross-correlation of encrypted P2-P1 code, the consistent measurement set $(\rho_{\mathrm{P1}}, \rho_{\mathrm{P2}})$ is obtained from

$$\rho_{\mathrm{P1}} \triangleq \rho_{\mathrm{C1}} + b_{\mathrm{P1-C1}}, \quad \text{and} \quad \rho_{\mathrm{P2}} \triangleq \rho_{\mathrm{X2}} + b_{\mathrm{P1-C1}}. \tag{2.22}$$

2. For a receiver reporting only C1 and P2 measurements, the C1 measurement is corrected by

$$\rho_{\mathrm{P1}} \triangleq \rho_{\mathrm{C1}} + b_{\mathrm{P1-C1}}. \tag{2.23}$$

3. For a receiver reporting P1 and P2 already as a consistent set, no correction is necessary.

Receiver phase center offsets and variations

Receiver PCO and PCV can be calibrated and applied as a priori corrections. The receiver PCO denotes the vector from the antenna reference point (ARP) to the mean phase center

(PC) in East-North-Up (ENU) frame. The phase center in ECEF frame is obtained by multiplying a transformation matrix $\boldsymbol{R}_{\text{ENU}\to\text{ECEF}}$ with the PCO vector $\vec{\boldsymbol{r}}_{\text{PCO},r}$, i.e.

$$\vec{\boldsymbol{r}}_{\text{PC},r} = \vec{\boldsymbol{r}}_{\text{ARP},r} + \boldsymbol{R}_{\text{ENU}\to\text{ECEF}} \cdot \vec{\boldsymbol{r}}_{\text{PCO},r}. \tag{2.24}$$

The transformation matrix $\boldsymbol{R}_{\text{ENU}\to\text{ECEF}}$ is given by

$$\boldsymbol{R}_{\text{ENU}\to\text{ECEF}} = \begin{bmatrix} -\sin\lambda & -\cos\lambda\sin\phi & \cos\lambda\cos\phi \\ \cos\lambda & -\sin\lambda\sin\phi & \sin\lambda\cos\phi \\ 0 & \cos\phi & \sin\phi \end{bmatrix}, \tag{2.25}$$

with λ, ϕ being the longitude and latitude of the receiver.

The receiver phase center variation consists of elevation- and azimuth-dependent PCV corrections. Given the elevation and azimuth angles, the PCV can be obtained by a bi-linear interpolation and corrected directly from the measurements.

Solid earth tides

The solid earth tides are caused by the gravitational forces from the moon and the sun acting onto the crust of the earth. The resulting displacements are described using spherical harmonics of degree n and order m characterized by the Love number h_{nm} and the Shida number l_{nm} in IERS Conventions [36]. The degree $n = 2$ tides are the dominant ones, while the other degrees have millimeter-level or less effect [37] and are thus negligible for navigation purposes. The steps for calculating the displacement corrections are suggested in [36], and the displacement vector is given by

$$\Delta\vec{\boldsymbol{r}}_{\text{et}} = \sum_{j=2}^{3} \frac{GM_j R_{\text{e}}^4}{GM_{\text{e}} R_j^3} \left(h(\varphi) \left(\frac{3(\vec{\boldsymbol{e}}_{R_j}^{\,\text{T}} \vec{\boldsymbol{e}}_r)^2}{2} - \vec{\boldsymbol{e}}_r \right) + 3l(\varphi)(\vec{\boldsymbol{e}}_{R_j}^{\,\text{T}} \vec{\boldsymbol{e}}_r) \left(\vec{\boldsymbol{e}}_{R_j} - (\vec{\boldsymbol{e}}_{R_j}^{\,\text{T}} \vec{\boldsymbol{e}}_r)\vec{\boldsymbol{e}}_r \right) \right), \tag{2.26}$$

where the effect from the moon is represented by $j = 2$, from the sun by $j = 3$, GM_{e} and GM_j are the gravitational parameters for the earth and the moon or the sun, R_{e} and R_j denote the corresponding radii, $\vec{\boldsymbol{e}}_r$ and $\vec{\boldsymbol{e}}_{R_j}$ represent the unit vectors from the station and the moon or the sun to the earth center, and $h(\varphi)$ and $l(\varphi)$ denote the effective degree 2 Love and Shida numbers depending on the station latitude.

Fig. 2.7 shows the modelled site displacements for 2 stations, respectively mid-latitude and equatorial. A strong latitude dependency is observed especially for the height coordinate, where Malindi has over 45 cm vertical variations over one day and Munich has around 30 cm vertical variations.

Ocean tidal loading

Like the solid earth tides, the gravitational forces from the moon and the sun also generate tides on the ocean. The ocean tides result in a mass redistribution of the water, which causes the deformation on the crust as the earth is not rigid. This deformation from the load of the ocean tides is called ocean tidal loading.

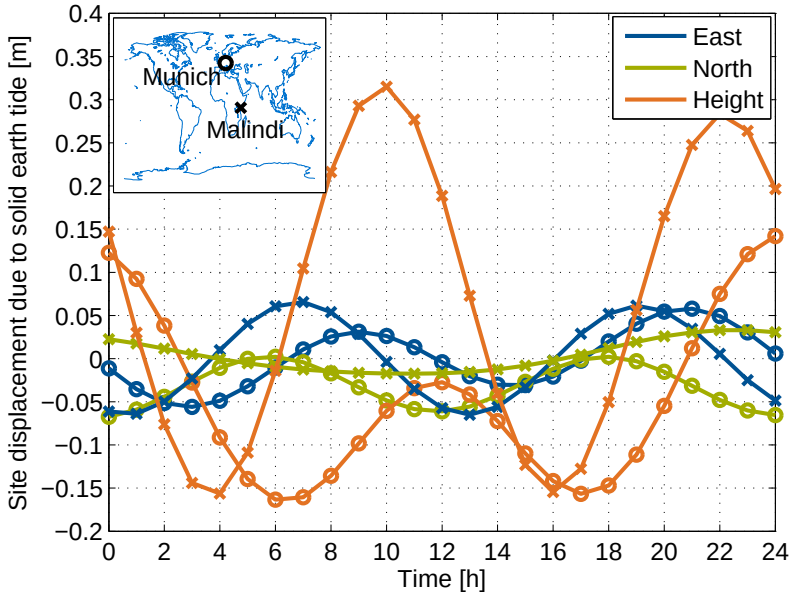

Figure 2.7: The latitude dependency of the calculated site displacements due to solid earth tides on Oct. 6, 2013. Stations in Munich and Malindi are located at mid-latitude, and equatorial areas. The horizontal displacements are similar having up to 10 cm variations, while the vertical displacements display a strong dependency on latitude.

A simplified model for the displacement due to ocean loading is given in [22, 36] as follows, which is enough for a precision of 1-3 mm, i.e.

$$\Delta r_{\mathrm{ol},i} = \sum_{j=1}^{N} a_{j,i} \cos(\omega_j t + \chi_j - \phi_{j,i}), \tag{2.27}$$

where the index $i = 1, 2, 3$ represents the vertical, south, and west directions respectively, and N denotes the number of tidal constituents. The parameters ω_j and χ_j specify the angular velocity and the initial astronomical argument of the j-th tide, respectively. Their values are listed in Table 2.1 for 11 main tidal constituents.

The location dependent amplitudes and phases, namely $a_{j,i}$ and $\phi_{j,i}$, are obtained by convolution integrals of tidal heights and mass loading Green's functions. The more detailed expressions are found in Appendix B. There exist numerous global tide models, which do not differ on the cm precision level [38]. The amplitudes and phases are tabulated for most reference stations [22].

Fig. 2.8 and 2.9 depict the modelled maximal site displacements in vertical and horizontal directions in the region of Europe. Results show that the vertical displacement at the near ocean sites could reach up to 10 cm, while the maximal horizontal displacement is roughly 3 cm.

Polar motion

The earth rotation axis has so far been assumed fixed, but is actually shifting relative to a point fixed in the earth. The centrifugal force produced by the rotation changes accordingly,

Tidal constituent		ω_j [rad/h]	χ_j [rad]
Semidiurnal	M_2	0.506	$2h - 2s$
	S_2	0.524	0
	N_2	0.497	$2h - 3s + q$
	K_2	0.525	$2h$
Diurnal	K_1	0.263	$h + \pi/2$
	O_1	0.243	$h - 2s - \pi/2$
	P_1	0.261	$-h - \pi/2$
	Q_1	0.234	$h - 3s + q - \pi/2$
Long-period	M_f	0.019	$2s$
	M_m	0.0095	$s - q$
	S_{sa}	0.0014	$2h$

Table 2.1: Angular velocities and astronomical arguments of 11 main tidal constituents [39]. The variables h, s and q in this table denote the mean longitudes of the sun, the moon and the lunar perigee at the beginning of a day respectively.

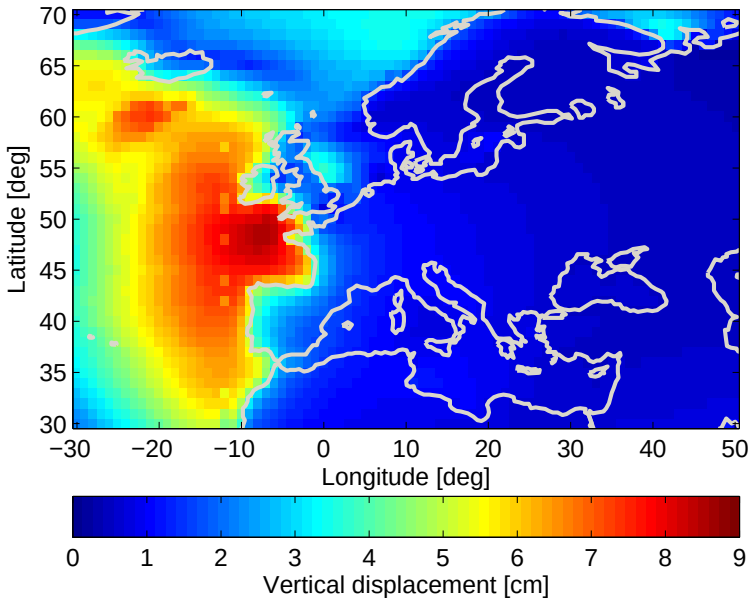

Figure 2.8: Maximal vertical site displacement due to ocean tidal loading in Europe.

which causes the pole tide. The pole tide could reach up to 2.5 cm in vertical and 0.7 cm in horizontal direction. However, unlike the solid earth tides, the pole tide experiences a much lower frequency, i.e. at periods of 14 months (the Chandler wobble effect) and one year [37].

The model to calculate the site displacements (positive in north, east, and up directions,

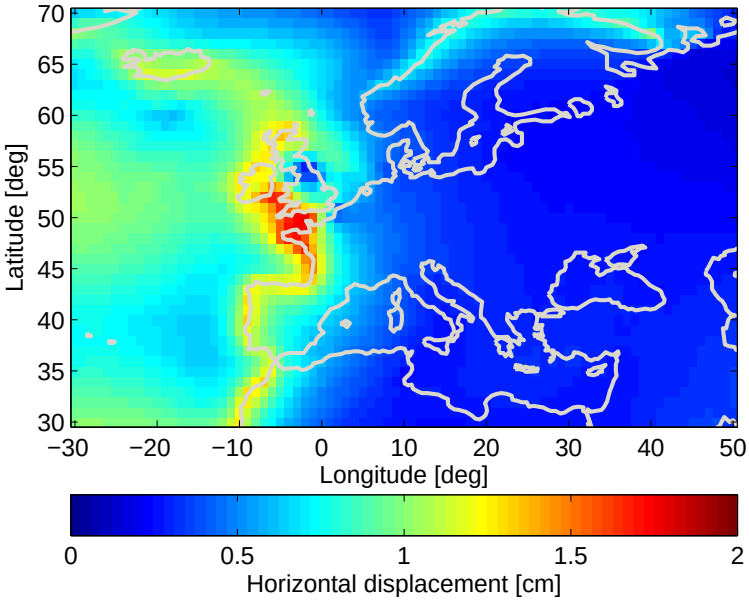

Figure 2.9: Maximal horizontal site displacement due to ocean tidal loading in Europe.

in unit of mm) due to pole tide is suggested in [36] as

$$\begin{aligned}\Delta r_{\mathrm{u}} &= -33\sin(2\phi)(m_1\cos\lambda + m_2\sin\lambda),\\ \Delta r_{\mathrm{e}} &= \quad 9\sin(\phi)(m_1\sin\lambda - m_2\cos\lambda),\\ \Delta r_{\mathrm{n}} &= -9\cos(2\phi)(m_1\cos\lambda + m_2\sin\lambda),\end{aligned} \tag{2.28}$$

where $m_1 = x_p - \bar{x}_p$ and $m_2 = -(y_p - \bar{y}_p)$ denote the offsets (in arcseconds) from the mean pole $(\bar{x}_p, \bar{y}_p)$ to the instantaneous pole (x_p, y_p) in x- and y-axis. A detailed derivation is found in Appendix C.

Fig. 2.10 shows the modelled vertical displacements over 14 years at Wettzell and Addis Ababa, respectively. The polar motion is obtained from IGS Earth Rotation Parameters products[1]. The mid-latitude site Wettzell experiences a much larger vertical variation over the years than the equatorial site Addis Ababa, which can be justified from Eq. (2.28) that the coefficient with $\sin(2\phi)$ tends to its maximum as latitude approaches 45°. The 14-month period can also be observed from the height variations.

2.1.3 Link-related Effects

Link-related effects refer to the effects on the propagation link, e.g. atmospheric delays, or effects having both satellite and receiver dependencies, such as integer ambiguities and phase wind-up. The listed items below are described in the next sub-sections.

- Ionospheric delays
- Tropospheric delays
- Phase wind-up
- Integer ambiguities

[1]Online access: ftp://cddis.gsfc.nasa.gov/gps/products/

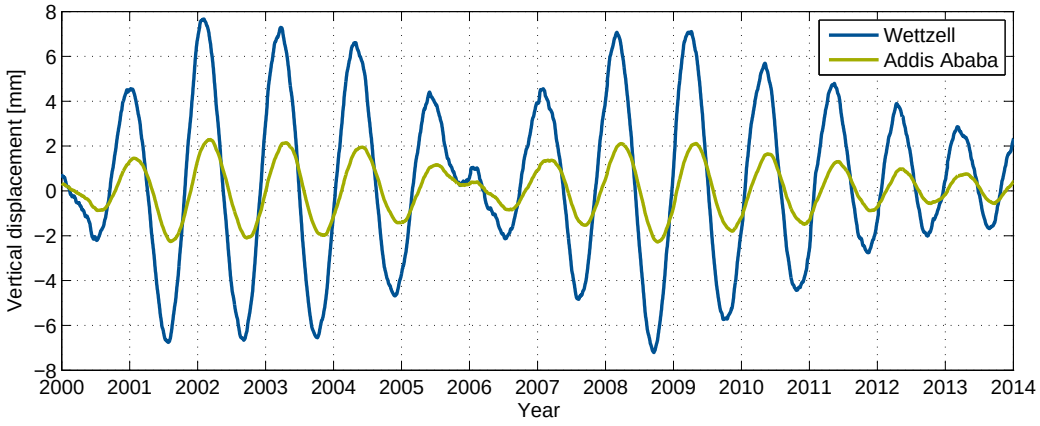

Figure 2.10: Modelled vertical displacements due to pole tide at Wettzell and Addis Ababa from 2000 to 2013.

Ionospheric delays

The ionosphere contains ionized particles, which induce excess delays and phase advance to electro-magnetic waves. The ionospheric delay is proportional to the total electron density (TEC), which is mostly concentrated between 250 and 400 km. For most precise applications, it is sufficient to consider the first-order ionospheric delay. The higher order terms are only considered for applications at millimeter-level [36].

The ionosphere is typically assumed to be concentrated on a single layer, this allows the transition from slant ionospheric delays to the corresponding vertical delays with elevation-dependent mapping functions. There are numerous models on the vertical ionospheric delays. A widely used one, the Klobuchar model, is however not accurate enough, correcting only about 50% of the ionospheric delay [40]. Another blind model, the NeQuick model, provides a better modelling for the ionosphere [41]. It describes a three-dimensional and time dependent ionospheric electron density model, and is used in the standard Galileo single-frequency receivers.

A grid based ionospheric model can also be applied, where the area of the ionospheric layer is filled with pre-defined grid points. The vertical delays at these grid points are estimated with a network of stations, and are broadcast to users as correction data. As an example, the final ionospheric Total Electron Content (TEC) from IGS offers an accuracy of 2 to 8 TECU (TEC Units) [22]. One TECU equals 10^{16} electrons/m^2, which implies 16.3 cm at GPS L1 frequency.

A dual-frequency receiver can take advantage of the dispersive property of the ionospheric delay. The ionospheric delay can be either eliminated by applying ionosphere-free combination, or estimated in the state vector. More details on ionospheric delays and mitigation methods are described in the Chapter 4.

Tropospheric delays

The total tropospheric delay is usually separated into a hydrostatic and a wet delay, where the hydrostatic part can be more precisely determined. Each component in slant direction

is further modelled by a product of the delay in zenith direction T_z and a mapping function m_T as

$$T_r^k = m_{\mathrm{T,h},r}^k T_{\mathrm{z,h},r} + m_{\mathrm{T,w},r}^k T_{\mathrm{z,w},r}, \tag{2.29}$$

where the indices h and w represent hydrostatic and wet parts respectively.

By integral over the hydrostatic refractivity, the hydrostatic zenith delay is expressed in closed form as a function of the total pressure at the surface, the receiver's latitude and height. The refraction constants in the integral were determined by Saastamoinen in [42], and by Davis et al. in [43] with slightly better precision. The hydrostatic zenith delay can be obtained with millimeter accuracy under hydrostatic equilibrium [44]. As for the zenith wet delay, it is affected by the distribution of water vapor, which is very difficult to be modelled based only on the surface measurements. Thus, the wet delay is often estimated as an additional parameter in the precise point positioning.

Marini in [45] first developed the tropospheric mapping function in continued fraction form, which serves the base for various modern mapping functions. Among these, Niell used the truncated three-term fraction and determined the coefficients a, b, and c in

$$m_\mathrm{T} = \cfrac{1 + \cfrac{a}{1 + \cfrac{b}{1+c}}}{\sin E + \cfrac{a}{\sin E + \cfrac{b}{\sin E + c}}}, \tag{2.30}$$

where E denotes the elevation angle. The coefficients depend on the latitude of the receiver and the day of the year, and can be obtained in a look-up table in [46]. The Niell mapping function is applied in the PPP algorithm developed in this work. The hydrostatic zenith delay is corrected from the Saastamoinen model, while the surface measurements are obtained from the Global Pressure and Temperature (GPT) model introduced by Böhm et al. in [47].

It is worth pointing out that, the difficulty in precisely determining the tropospheric zenith delay in PPP comes from the high correlation with the receiver height, as well as with the receiver clock offset. Using the linear measurement model in Eq. (1.1), we take the partial derivative of the code measurement with respect to the tropospheric zenith delay T_z and obtain

$$\frac{\partial \rho^k}{\partial T_\mathrm{z}} = m_\mathrm{T} \simeq \frac{1}{\sin E^k}. \tag{2.31}$$

The approximation is justified by evaluating the denominator of Eq. (2.30). For an elevation cut-off angle of 10°, we obtain

$$\begin{aligned} &\sin E \geq \sin(10^\circ) = 0.17 \gg c, \\ &\sin^2 E \geq \sin^2(10^\circ) = 0.03 \gg a, b, \end{aligned} \tag{2.32}$$

where c is typically in the order of 10^{-2}, a and b are in the order of 10^{-3} to 10^{-4}.

Similarly, the partial derivatives for the receiver clock offset $c\delta$ and receiver height r_h

are calculated by

$$\begin{aligned}\frac{\partial \rho^k}{\partial c\delta} &= 1,\\ \frac{\partial \rho^k}{\partial r_h} &= \vec{\boldsymbol{e}}^{\,k,\mathrm{T}}\vec{\boldsymbol{e}}_u = \cos\left(\pi - \theta^k\right) = -\sin E^k,\end{aligned} \tag{2.33}$$

where $\vec{\boldsymbol{e}}^{\,k}$ is the unit vector from the satellite to the receiver in ECEF frame, and $\vec{\boldsymbol{e}}_u$ represents the unit vector in the up direction of ENU frame expressed in ECEF frame, which is given in [3] by

$$\vec{\boldsymbol{e}}_u = \begin{bmatrix} \cos\lambda\cos\phi \\ \sin\lambda\cos\phi \\ \sin\phi \end{bmatrix}, \tag{2.34}$$

with ϕ and λ being the receiver latitude and longitude. The dot-product of the unit vectors in Eq. (2.33) yields the cosine of the angle in-between, i.e. the supplementary angle of the zenith angle θ^k.

If all satellites are in the zenith, it would be impossible to separate the tropospheric zenith delay, the receiver clock offset and the height from each other, as the dependencies on the elevation angle are removed from Eq. (2.31) and (2.33). Therefore satellites from lower elevations help the separation as the differences in the coefficients grow larger. On the other hand, the tropospheric mapping function becomes less accurate at lower elevations, while multipath effect also increases for signals coming from nearer the horizon.

We perform an analysis to study the correlation. To simplify the system, let us assume the other parameters including the horizontal coordinates, the ionospheric delay, the integer ambiguities are all known, leaving the receiver height, the receiver clock offset, and the tropospheric zenith delay as unknowns. As these terms are non-frequency dependent and appear the same for code and phase measurements, so we assume only one type of measurement on one frequency is studied. Having K visible satellites with elevations $\boldsymbol{E} = \left[E^1, \ldots, E^K\right]^{\mathrm{T}}$, the design matrix $\boldsymbol{H}$ is given by

$$\boldsymbol{H} = \left[\frac{1}{\sin \boldsymbol{E}},\ \boldsymbol{1},\ -\sin \boldsymbol{E}\right]. \tag{2.35}$$

Assume every measurement has the same noise variance of σ^2, the covariance matrix is derived as

$$\left(\boldsymbol{H}^{\mathrm{T}}\boldsymbol{\Sigma}^{-1}\boldsymbol{H}\right)^{-1} = \frac{\sigma^2}{\det\left(\boldsymbol{H}^{\mathrm{T}}\boldsymbol{H}\right)}\cdot$$

$$\begin{bmatrix} K\sum\limits_{i=1}^{K}(s^i)^2 - (\sum\limits_{i=1}^{K} s^i)^2 & K\sum\limits_{i=1}^{K} s^i - \sum\limits_{i=1}^{K}(s^i)^2\sum\limits_{i=1}^{K}\frac{1}{s^i} & K^2 - \sum\limits_{i=1}^{K} s^i\sum\limits_{i=1}^{K}\frac{1}{s^i} \\ K\sum\limits_{i=1}^{K} s^i - \sum\limits_{i=1}^{K}(s^i)^2\sum\limits_{i=1}^{K}\frac{1}{s^i} & \sum\limits_{i=1}^{K}(s^i)^2\sum\limits_{i=1}^{K}\frac{1}{(s^i)^2} - K^2 & \sum\limits_{i=1}^{K} s^i\sum\limits_{i=1}^{K}\frac{1}{(s^i)^2} - \sum\limits_{i=1}^{K}\frac{K}{s^i} \\ K^2 - \sum\limits_{i=1}^{K} s^i\sum\limits_{i=1}^{K}\frac{1}{s^i} & \sum\limits_{i=1}^{K} s^i\sum\limits_{i=1}^{K}\frac{1}{(s^i)^2} - \sum\limits_{i=1}^{K}\frac{K}{s^i} & \sum\limits_{i=1}^{K}\frac{K}{(s^i)^2} - \left(\sum\limits_{i=1}^{K}\frac{1}{s^i}\right)^2 \end{bmatrix}, \tag{2.36}$$

where s^i stands for $\sin E^i$ to save space. The determinant $\det(\cdot)$ drops out in the calculation of the correlation coefficients γ between the tropospheric zenith delay and the other two terms.

The correlation coefficients $\gamma_{T_z,\,c\delta}$ and $\gamma_{T_z,\,r_h}$ are calculated by

$$\gamma_{T_z,\,c\delta} = \frac{\sum_{i=1}^{K} K s^i - \sum_{i=1}^{K}(s^i)^2 \sum_{i=1}^{K} \frac{1}{s^i}}{\sqrt{\sum_{i=1}^{K} K(s^i)^2 - (\sum_{i=1}^{K} s^i)^2} \cdot \sqrt{\sum_{i=1}^{K}(s^i)^2 \sum_{i=1}^{K} \frac{1}{(s^i)^2} - K^2}},$$

$$\gamma_{T_z,\,r_h} = \frac{K^2 - \sum_{i=1}^{K} s^i \sum_{i=1}^{K} \frac{1}{s^i}}{\sqrt{\sum_{i=1}^{K} K(s^i)^2 - (\sum_{i=1}^{K} s^i)^2} \cdot \sqrt{\sum_{i=1}^{K} \frac{K}{(s^i)^2} - \left(\sum_{i=1}^{K} \frac{1}{s^i}\right)^2}}. \tag{2.37}$$

Finding a lower bound for Eq. (2.37) would be difficult, because the distribution of the elevation angle could be arbitrary. Thus, we present here a numerical approach, where the elevations of the satellites are assumed uniformly distributed from the cut-off angle $E_{\min}$ up to the zenith.

Tab. 2.2 lists the correlation coefficients for different numbers of visible satellites and elevation cut-off angles. The correlation increases with increased cut-off angle. This is due to the reduce of the number of satellites having lower elevations. For the same reason, an increased number of satellites reduces the correlation, i.e. the correlation coefficients go towards zero. The strong correlations between the parameters prevent from precise determination of the receiver clock offset, the receiver height and the tropospheric zenith delay. The receiver clock offset would be partially decorrelated if there would exist signals from satellites below the horizon. The tropospheric zenith delay could be imposed by some constraints as it does not change rapidly over short time period. A similar study on the correlation coefficients was conducted by Rothacher and Beutler in [48].

K	$E_{\min}$	$\gamma_{T_z,\,c\delta}$	$\gamma_{T_z,\,r_h}$	K	$E_{\min}$	$\gamma_{T_z,\,c\delta}$	$\gamma_{T_z,\,r_h}$
6	10°	-0.952	-0.903	9	10°	-0.945	-0.888
	15°	-0.973	-0.937		15°	-0.971	-0.931
	20°	-0.984	-0.958		20°	-0.984	-0.956
7	10°	-0.948	-0.895	10	10°	-0.945	-0.887
	15°	-0.972	-0.933		15°	-0.971	-0.931
	20°	-0.984	-0.957		20°	-0.984	-0.956
8	10°	-0.946	-0.891	11	10°	-0.945	-0.886
	15°	-0.971	-0.932		15°	-0.971	-0.931
	20°	-0.984	-0.956		20°	-0.984	-0.956

Table 2.2: Correlation coefficients between tropospheric zenith delay and receiver clock offset, receiver height. The elevation angles are assumed uniformly distributed from the cut-off angle $E_{\min}$ up to the zenith.

Phase wind-up

The GPS satellites transmit signals carried by right hand circularly polarized (RHCP) waves (seen from the satellite towards the earth), and thus, the orientation of the satellite

and receiver antennas directly affects the carrier phase measurements. This increased or decreased carrier phase due to the change of the relative orientations is called the phase wind-up.

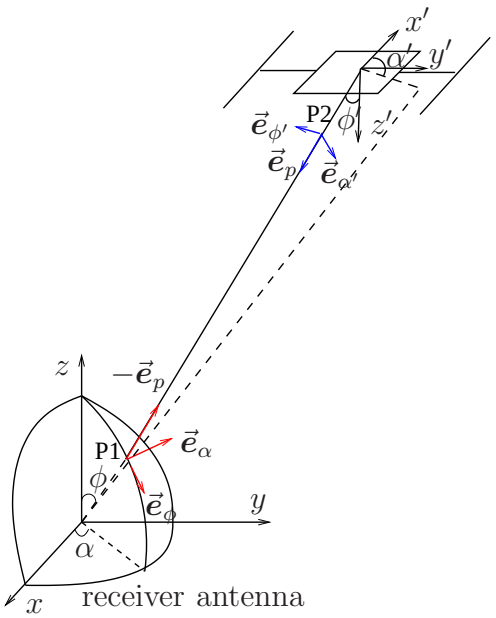

Figure 2.11: The orientation of the receiver and satellite antennas, i.e. xy and $x'y'$ represent the antenna planes, while z and z' point to the boresight and nadir directions. P1 and P2 denote the instantaneous phase centers.

Wu et al. have derived the analytical expressions for the phase wind-up effect in [49]. As shown in Fig. 2.11, a signal is propagating in the direction $\vec{e}_p$. The angles ϕ and α denote the zenith and azimuth angles at the receiver antenna coordinate frame (x, y, z), while ϕ' and α' are the corresponding ones at the satellite local frame (x', y', z'). Let $\vec{e}_\alpha$ and $\vec{e}_\phi$ denote the spherical unit vectors for the receiver, and $\vec{e}_{\alpha'}$, $\vec{e}_{\phi'}$ for the satellite.

One can split the calculation for the phase wind-up into three parts. The first two parts are the calculation of α' and α. They are obtained from the phase difference between the orientation of the antenna at the phase center and the attitude of the antenna, for the satellite and the receiver separately. As a third part, the difference between the two antenna orientations is calculated. The overall phase wind-up φ_{pw} in unit of cycles is obtained as

$$\varphi_{\text{pw}} = \frac{1}{2\pi}\left(\alpha' + \alpha + \text{sgn}\left(\vec{e}_p^{\,\text{T}}(\vec{e}_{\phi'} \times \vec{e}_\phi)\right)\arccos\left(\vec{e}_{\phi'}^{\,\text{T}}\vec{e}_\phi\right)\right), \tag{2.38}$$

with $\text{sgn}(\cdot)$ being the sign function. Eq. (2.38) indicates that, a rotation of the receiver or satellite antenna around the boresight or nadir axis, or the orbiting of the satellite around the earth, would all cause changes in phase measurements.

An experiment is carried out to observe the phase wind-up effect. The receiver antenna is rotated along the z-axis multiple times, which causes change in α and thus in the phase measurements. The larger effects such as the range, the clock offset must be eliminated, so that the phase wind-up having typical values of a few centimeters are observable. The geometry- and ionosphere-free combination was not applied, because the code measurements would be involved and the change due to phase wind-up would be difficult to observe

under the large code noise. We chose therefore the geometry-free, ionosphere-preserving phase combination, while the ionospheric delay is left with the phase wind-up.

In the first step, the geometry-free, ionosphere-preserving (IP) phase combination $\lambda_{\mathrm{IP}}\varphi^k_{\mathrm{IP},r}$ is formed as

$$\begin{aligned}\lambda_{\mathrm{IP}}\varphi^k_{\mathrm{IP},r} &= \sum_{m=1}^{2}\alpha_{\mathrm{IP},m}\lambda_m\varphi^k_{m,r}\\ &= I^k_{1,r} + \sum_{m=1}^{2}\alpha_{\mathrm{IP},m}\lambda_m(N^k_{m,r}+\beta_{m,r}+\beta^k_m) + \sum_{m=1}^{2}\alpha_{\mathrm{IP},m}\lambda_m\varphi^k_{\mathrm{pw},r} + \sum_{m=1}^{2}\alpha_{\mathrm{IP},m}\varepsilon^k_{m,r},\end{aligned} \tag{2.39}$$

with the coefficients $\alpha_{\mathrm{IP},1} = f_2^2/(f_1^2-f_2^2)$, $\alpha_{\mathrm{IP},2} = -f_2^2/(f_1^2-f_2^2)$.

Then by time-differencing with respect to the beginning epoch t_0, the second term in Eq (2.39) which includes the time-invariant ambiguities and phase biases drops out. The change on the slant ionospheric delays along with the phase wind-up remains

$$\begin{aligned}\lambda_{\mathrm{IP}}(\varphi^k_{\mathrm{IP},r}(t)-\varphi^k_{\mathrm{IP},r}(t_0)) = I^k_{1,r}(t) - I^k_{1,r}(t_0) + \sum_{m=1}^{2}\alpha_{\mathrm{IP},m}\lambda_m\left(\varphi^k_{\mathrm{pw},r}(t)-\varphi^k_{\mathrm{pw},r}(t_0)\right) +\\ + \sum_{m=1}^{2}\alpha_{\mathrm{IP},m}(\varepsilon^k_{m,r}(t)-\varepsilon^k_{m,r}(t_0)).\end{aligned} \tag{2.40}$$

One way of mitigating the ionospheric delay is to set up another nearby receiver to perform between-receiver single-difference, which also increases the noise and makes the phase wind-up more difficult to observe. The other way is to perform the experiment during a quiet ionosphere, which is presented in this work.

The data was collected at around 21:30 local time on April 15th 2013, using a JAVAD-Triumph receiver with internal antenna. Fig. 2.12 shows two clockwise rotations each with 90°, viewed from the positive end of the boresight axis of the receiver towards the origin, were first performed with 5-minute interval, as seen in Fig. 2.12(a). Each clockwise rotation gives an addition of $\pi/2$ in the azimuth angle α, resulting in an absolute phase lag of $\varphi_{\mathrm{pw}} = 1/4$ cycle according to Eq. (2.38). This corresponds to about $1/4\cdot(\alpha_{\mathrm{IP},1}\lambda_1+\alpha_{\mathrm{IP},2}\lambda_2) = -2.1$ cm change in the phase combination in Eq. (2.40), which is verified in Fig. 2.12(a), as seen in the amplified curve for PRN 25.

Fig. 2.12(b) showed two counter-clockwise rotations each with 90° and 180° in 2-minute interval, which cause phase lags of 2.1 cm and 4.2 cm in the combination respectively for all visible satellites.

Integer Ambiguities

Integer ambiguities represent the ambiguous numbers of full cycles in the carrier phase measurements. In order to take advantage of the phase measurements and reach centimeter-accuracy, the ambiguities need to be resolved as integers.

There are numerous integer ambiguity fixing strategies, such as integer least-squares, integer bootstrapping, best integer equivariant estimator [50–52]. We shortly describe the integer least-squares (ILS) estimator with its fast implementation i.e. the least-squares ambiguity decorrelation adjustment (LAMBDA) method proposed by Teunissen [50, 53].

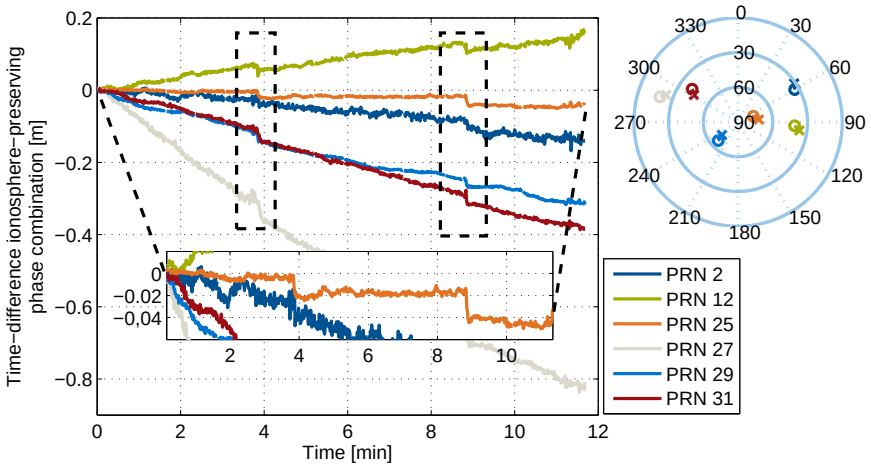

(a) Two clockwise rotations of the receiver antenna with 90° caused phase changes at all visible satellites. The phase jumps due to the rotation of the antenna are clearly seen in the amplified curve of PRN 25.

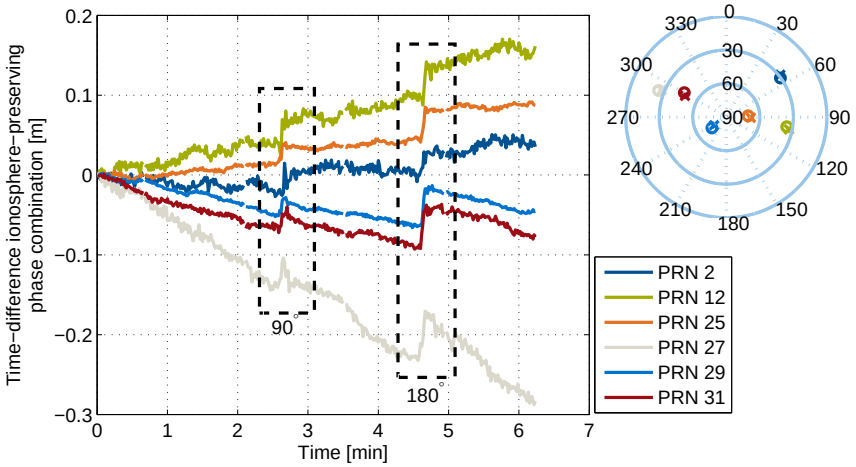

(b) The common phase jumps are due to two counter-clockwise rotations with 90° and 180°.

Figure 2.12: The phase change over time due to the ionosphere and the wind-up effect. The different slopes show the difference in ionospheric delays with elevation-dependent mapping functions, while the jumps indicated in the dashed boxes are caused by the phase wind-up. The skyplots of the satellites are shown on the right, where a circle represents the starting epoch and a cross represents the ending epoch.

This is one of the most widely used estimators. The solution consists of three steps. First a float solution is obtained ignoring the integer property of the ambiguities. Then the float ambiguities are fixed to integers by an integer least-squares estimator. Finally, other real-valued parameters are adjusted by the residuals of the fixed ambiguities. Recently, Günther and Henkel have improved in [54] the LAMBDA method with reduced complexity, by an advanced LDL^{T}-decomposition of the ambiguity covariance matrix and a functional determination of the integer decorrelation transformation matrix.

Let $\boldsymbol{y}$ denote the measurement vector containing all pseudorange and carrier phase measurements. A general linear observation equation can be formed as

$$\boldsymbol{y} = \boldsymbol{H}\boldsymbol{\xi} + \boldsymbol{A}\boldsymbol{N} + \boldsymbol{\eta}, \tag{2.41}$$

where all real-valued parameters are included in the m-dimensional vector $\boldsymbol{\xi}$, and integer ambiguities are collected in the n-dimensional vector $\boldsymbol{N}$. Their coefficient matrices are represented by $\boldsymbol{H}$ and $\boldsymbol{A}$ respectively. The measurement noise is assumed to be normal distributed, i.e. $\boldsymbol{\eta} \sim \mathcal{N}(\boldsymbol{0}, \boldsymbol{\Sigma})$.

Eq. (2.41) can be solved optimally by minimizing the error norm under weighting matrix $\boldsymbol{\Sigma}^{-1}$.

$$\begin{bmatrix} \hat{\boldsymbol{\xi}} \\ \hat{\boldsymbol{N}} \end{bmatrix} = \underset{\boldsymbol{\xi}\in\mathbb{R}^m, \boldsymbol{N}\in\mathbb{Z}^n}{\operatorname{argmin}} \|\boldsymbol{y} - \boldsymbol{H}\boldsymbol{\xi} - \boldsymbol{A}\boldsymbol{N}\|^2_{\boldsymbol{\Sigma}^{-1}}, \tag{2.42}$$

The minimization is a constrained least-squares problem, where an additional integer constraint $\boldsymbol{N} \in \mathbb{Z}^n$ is imposed on the ambiguity vector.

The solution to the integer least-squares estimation in (2.42) can be described in a three-step procedure. First, the float solution for all parameters is determined by the standard weighted least-squares as

$$\begin{bmatrix} \hat{\boldsymbol{\xi}} \\ \hat{\boldsymbol{N}} \end{bmatrix} = \left(\begin{bmatrix} \boldsymbol{H}^{\mathrm{T}} \\ \boldsymbol{A}^{\mathrm{T}} \end{bmatrix} \boldsymbol{\Sigma}^{-1} [\boldsymbol{H} \;\; \boldsymbol{A}] \right)^{-1} \begin{bmatrix} \boldsymbol{H}^{\mathrm{T}} \\ \boldsymbol{A}^{\mathrm{T}} \end{bmatrix} \boldsymbol{\Sigma}^{-1} \boldsymbol{y}, \tag{2.43}$$

with the variances for $\hat{\boldsymbol{\xi}}$ and $\hat{\boldsymbol{N}}$ as $\boldsymbol{\Sigma}_{\hat{\boldsymbol{\xi}}}$ and $\boldsymbol{\Sigma}_{\hat{\boldsymbol{N}}}$, and the covariance matrix being $\boldsymbol{\Sigma}_{\hat{\boldsymbol{\xi}}\hat{\boldsymbol{N}}}$.

Second, the float ambiguity estimate and its covariance matrix are used to compute the integer solution $\check{\boldsymbol{N}}$. The following minimization is solved:

$$\check{\boldsymbol{N}} = \underset{\boldsymbol{N}\in\mathbb{Z}^n}{\operatorname{argmin}} \|\hat{\boldsymbol{N}} - \boldsymbol{N}\|^2_{\boldsymbol{\Sigma}^{-1}_{\hat{N}}}. \tag{2.44}$$

A search is involved in finding the integer ambiguity estimates. As the ambiguities are always correlated, it is inefficient to perform a tree-search over the whole integer space. A $\boldsymbol{Z}$-transformation can be performed to reduce the search complexity through

$$\hat{\boldsymbol{N}}' = \boldsymbol{Z}\hat{\boldsymbol{N}}, \;\; \boldsymbol{\Sigma}_{\hat{\boldsymbol{N}}'} = \boldsymbol{Z}\boldsymbol{\Sigma}_{\hat{\boldsymbol{N}}}\boldsymbol{Z}^{\mathrm{T}}. \tag{2.45}$$

The transformation matrix $\boldsymbol{Z}$ and the back-transformations shall both be integer preserving, i.e. the transformed ambiguity vector $\hat{\boldsymbol{N}}'$ should be still in integer space. The details for constructing the matrix is described by Jonge et al. in [53]. It is noted that the transformed search space has the same number of integer candidates as the original space, thus the decorrelation has no influence on the result.

In the third step, the real-valued parameter is updated to the fixed solution, by correcting the residuals from the integer ambiguity estimates, i.e.

$$\check{\boldsymbol{\xi}} = \hat{\boldsymbol{\xi}} - \boldsymbol{\Sigma}_{\hat{\boldsymbol{\xi}}\hat{\boldsymbol{N}}}\boldsymbol{\Sigma}^{-1}_{\hat{\boldsymbol{N}}}(\hat{\boldsymbol{N}} - \check{\boldsymbol{N}}). \tag{2.46}$$

And the covariance matrix is calculated by

$$\boldsymbol{\Sigma}_{\check{\boldsymbol{\xi}}} = \boldsymbol{\Sigma}_{\hat{\boldsymbol{\xi}}} - \boldsymbol{\Sigma}_{\hat{\boldsymbol{\xi}}\hat{\boldsymbol{N}}}\boldsymbol{\Sigma}^{-1}_{\hat{\boldsymbol{N}}}\boldsymbol{\Sigma}_{\hat{\boldsymbol{N}}\hat{\boldsymbol{\xi}}}. \tag{2.47}$$

2.1.4 Summary

In summary, Tab. 2.3 lists an overview of satellite-related, receiver-related and link-related effects in PPP with mitigation methods and error contributions.

Satellite orbits and clock offsets are provided by the GPS broadcast ephemerides and the IGS. The broadcast ephemerides offer real-time orbit and clock corrections with meter-level accuracy, while the most accurate orbit and clock come from the IGS final orbit with around 2 cm error, but are only available for post-processing [22].

The satellite antenna phase center offset is split into a horizontal and vertical PCO. The horizontal PCO has an error of about 1 cm [55]. The horizontal PCO is sometimes highly correlated with the orbital elements, and could reach up to 30 cm rarely depending on the attitude of the satellite. This happens when the along-track direction almost coincides with the satellite x- or y-axis (the angle close to 0° or 180°) [32]. On the other hand, the vertical PCO has the magnitude of $2 - 3$ m with an accuracy of around 7 to 15 cm. The error is due to the correlation with the station heights [31, 56]. According to Zhu et al. in [57], the change on station height Δr follows roughly the relationship $\Delta r \simeq -0.05\Delta z$, where Δz denotes the change in the vertical PCO. This indicates that, an error of 15 cm in Δz corresponds to 7.5 mm on station height. Besides, the satellite phase center variations can be determined to an accuracy of 1 mm [29].

The receiver antenna PCO and PCV can be well determined to 2 mm by various calibration methods according to Schmid in [31]. Both the satellite and the receiver PCO and PCV values are published in the IGS ANTEX (Antenna Exchange Format) product[1].

The receiver needs also to account for the tidal effects, including the solid earth tides, the ocean tidal loading, the polar tides, etc.. The solid earth tides contribute the largest to the tidal effects, having up to 50 cm vertical and up to 10 cm horizontal variations. The model suggested by the IERS (International Earth Rotation and Reference Systems Service), can correct the effect to millimeter-level accuracy [36]. The ocean tidal loading is non-negligible at coastal areas, where the vertical displacement could reach up to 10 cm. The state-of-the-art ocean tide models agree on the level of 1 mm [58]. The polar tide could have a maximum vertical displacement of 2.5 cm, with an accuracy of 1 mm [36].

The first-order ionospheric delay ranges from a few meters to tens of meters, and can be eliminated or estimated by using dual-frequency measurements. The second-order ionospheric delay may reach up to 2 cm [59], and should be considered for high accuracy applications. The tropospheric slant delay is projected to the zenith direction by a mapping function. The hydrostatic zenith delay is around 2 m, while the wet component is much smaller at around 20 cm. The errors for the ionospheric delay and tropospheric zenith delay are given by 1 cm and 5 mm, which are obtained from state covariance from the estimation. Besides, the phase wind-up effect depends on the orientation of the transmitting and receiver antennas, and could get to as large as one wavelength. The model developed by Wu et al. in [49] provides millimeter-level accuracy.

Moreover, the phase and code biases have not been addressed in the table. Without the correction for the phase biases, the ambiguity term shall be estimated as float parameter in absolute positioning. The correction can be obtained from estimation with a network of receivers. The code biases could be treated separately according to frequency dependency,

[1] Online access: ftp://igscb.jpl.nasa.gov/igscb/station/general/igs08.atx

i.e. as geometric- and ionospheric parts. The code geometric biases can be combined with the satellite and receiver clock offsets, while the ionospheric parts are absorbed in the slant ionospheric delay. The latter code bias is only of concern for single-frequency receiver.

Effect		Mitigation method	Accuracy
Satellite-related	Orbit	IGS final orbit	2 cm
	Clock offset	IGS final clock offset	2.5 cm
	Phase center offset	IGS ANTEX correction	15 cm
	Phase center variation	IGS ANTEX correction	1 mm
Receiver-related	Position	State estimate	1 cm
	Clock offset	State estimate	1 cm
	Phase center offset	Calibration	2 mm
	Phase center variation	Calibration	2 mm
	Solid earth tide	Model correction	1 mm
	Ocean tidal loading	Model correction	1 mm
	Polar tides	Model correction	1 mm
Link-related	Tropo. zenith hydrostatic delay	Model correction	1 mm
	Tropo. zenith wet delay	State estimate	5 mm
	Ionospheric first-order slant delay	State estimate	1 cm
	Phase wind-up	Model correction	1 mm
	Integer ambiguity	State estimate	1 cm

Table 2.3: Summary of the considered effects in PPP, along with mitigation methods and error contributions.

2.2 Traditional PPP Approach with Ionosphere-Free Combinations

A traditional approach for precise point positioning with a dual-frequency receiver is to form ionosphere-free combination for code and carrier phase measurements. The first-order ionospheric delay is thereby eliminated, however the measurement noise and the multipath are meanwhile amplified about three times. Besides, the ionospheric combination is quite costly in terms of redundancy, as four sets of measurements are reduced to two sets.

Step 1: Wide-lane combination

The algorithm consists of two steps. First, the Melbourne-Wübbena combination [60, 61] with the code and phase measurements eliminates both the non-dispersive geometry term and the dispersive first-order ionospheric delay, i.e.

$$\begin{aligned}\lambda_{\mathrm{WL}}\varphi^k_{\mathrm{WL},r} &= \left(\frac{f_1}{f_1-f_2}\lambda_1\varphi^k_{1,r} - \frac{f_2}{f_1-f_2}\lambda_2\varphi^k_{2,r}\right) - \left(\frac{f_1}{f_1+f_2}\rho^k_{1,r} + \frac{f_2}{f_1+f_2}\rho^k_{2,r}\right)\\ &= \lambda_{\mathrm{WL}}N^k_{\mathrm{WL},r} + b_{\mathrm{WL},r} + b^k_{\mathrm{WL}} + \varepsilon^k_{\mathrm{WL},r},\end{aligned} \tag{2.48}$$

with the index 'WL' being the abbreviation for wide-lane. The wavelength is increased from 19.0 cm on L1 and 24.4 cm on L2 to $\lambda_{\mathrm{WL}} = c/(f_1 - f_2) = 86.2$ cm. Besides the

large wavelength, another advantage of the combination is the preservation of the integer property, i.e. the wide-lane ambiguity is given by

$$N^k_{\mathrm{WL},r} = N^k_{1,r} - N^k_{2,r}. \tag{2.49}$$

The wide-lane biases are obtained by

$$\begin{aligned} b_{\mathrm{WL},r} &= \frac{c}{f_1 - f_2}\left(\beta_{1,r} - \beta_{2,r}\right) - \frac{1}{f_1 + f_2}\left(f_1 b_{1,r} + f_2 b_{2,r}\right) \\ b^k_{\mathrm{WL}} &= \frac{c}{f_1 - f_2}\left(\beta^k_1 - \beta^k_2\right) - \frac{1}{f_1 + f_2}\left(f_1 b^k_1 + f_2 b^k_2\right), \end{aligned} \tag{2.50}$$

which can be determined by fixing the wide-lane ambiguities. For each satellite-receiver link, the Melbourne-Wübbena combination can be averaged over time to reduce the noise and multipath. The integer part of the average is fixed as wide-lane ambiguity $\check{N}^k_{\mathrm{WL},r}$, while the fractional part leads to the receiver and satellite biases, i.e.

$$\begin{aligned} \check{N}^k_{\mathrm{WL},r} &= \left[\frac{\mathrm{E}_t\{\lambda_{\mathrm{WL}}\varphi^k_{\mathrm{WL},r}\}}{\lambda_{\mathrm{WL}}}\right] \\ \hat{b}_{\mathrm{WL},r} + \hat{b}^k_{\mathrm{WL}} &= \mathrm{E}_t\{\lambda_{\mathrm{WL}}\varphi^k_{\mathrm{WL},r}\} - \lambda_{\mathrm{WL}}\check{N}^k_{\mathrm{WL},r}, \end{aligned} \tag{2.51}$$

with $[\cdot]$ denoting the rounding operator. Having the combination from one link, the receiver bias is not separable from the satellite bias. However they can be estimated separately by using a network of receivers, up to a common reference.

The wide-lane biases are observed to be very stable over long time, e.g. by Ge et al. in [10]. Fig. 2.13 depicts the wide-lane biases observed from an IGS station in Kiruna (kiru) between 20:00 and 02:00(+1) in January 2011. The plot shows a high stability of all biases over one month, with the most stable one varying only 3 cm and the worst about 10 cm, which are all much smaller than the wide-lane wavelength 86.2 cm. This allows the biases to be used as a priori corrections for wide-lane ambiguity fixing. After subtracting the biases from the Melbourne-Wübbena combination on Jan 1, 2011, the residuals are shown in Fig. 2.14. The average for each satellite curve is calculated, where all averages are close to integer values which are fixed as wide-lane ambiguities.

After the wide-lane ambiguities $N^k_{\mathrm{WL},r}$ have been fixed reliably, they are assumed constant and are used as corrections from now on.

Step 2: Narrow-lane combination

Second, the geometry-preserving ionosphere-free combination is applied on the phase and code measurements respectively, which is known as the narrow-lane combination. Thus, the measurement model, with index 'IF' for ionosphere-free, is written as

$$\begin{aligned} \rho^k_{\mathrm{IF},r} &= \frac{f_1^2}{f_1^2 - f_2^2}\cdot\rho^k_{1,r} - \frac{f_2^2}{f_1^2 - f_2^2}\cdot\rho^k_{2,r} \\ &= (\vec{\boldsymbol{e}}^{\,k}_r)^{\mathrm{T}}(\vec{\boldsymbol{r}}_r - \vec{\boldsymbol{r}}^{\,k}) + c(\delta_r - \delta^k) + m^k_{\mathrm{T},r}T_{\mathrm{z},r} + b_{g,r} + b^k_g + \eta^k_{\mathrm{IF},r}, \\ \lambda_{\mathrm{IF}}\varphi^k_{\mathrm{IF},r} &= \frac{f_1^2}{f_1^2 - f_2^2}\cdot\lambda_1\varphi^k_{1,r} - \frac{f_2^2}{f_1^2 - f_2^2}\cdot\lambda_2\varphi^k_{2,r} \\ &= (\vec{\boldsymbol{e}}^{\,k}_r)^{\mathrm{T}}(\vec{\boldsymbol{r}}_r - \vec{\boldsymbol{r}}^{\,k}) + c(\delta_r - \delta^k) + m^k_{\mathrm{T},r}T_{\mathrm{z},r} + \lambda_{\mathrm{IF}}(N^k_{\mathrm{IF},r} + \beta_{\mathrm{IF},r} + \beta^k_{\mathrm{IF}}) + \varepsilon^k_{\mathrm{IF},r}, \end{aligned} \tag{2.52}$$

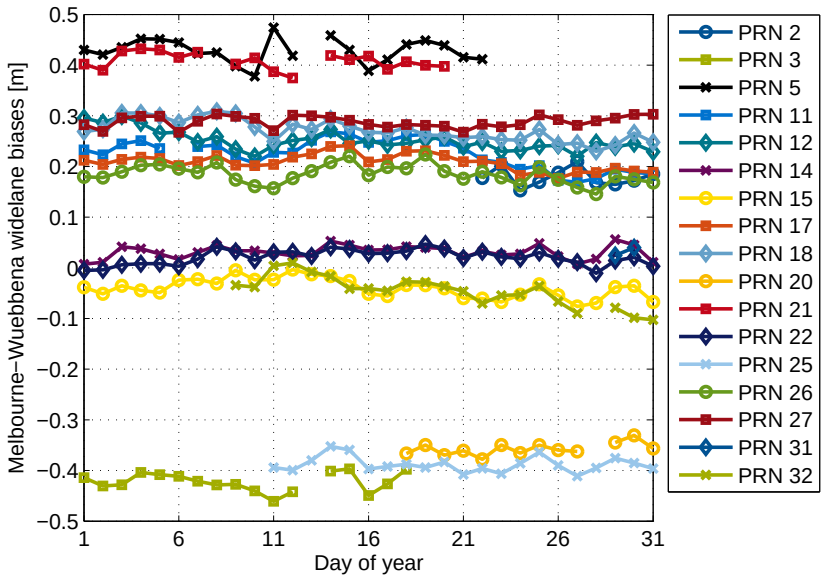

Figure 2.13: The Melbourne Wübbena wide-lane bias estimates from an IGS station kiru during 20:00 and 02:00(+1) in January 2011. A high stability can be observed on all plotted PRNs, while the bias on PRN 21 exhibits the smallest variation with 3 cm over one month.

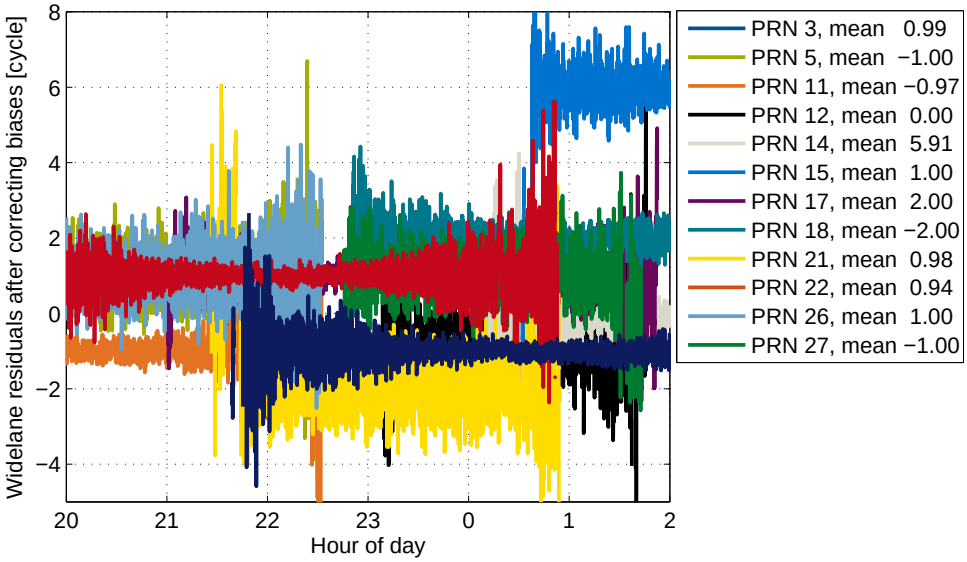

Figure 2.14: The Melbourne-Wübbena combination after correcting the wide-lane biases. It is clearly seen that all residual curves are centered closely at integer values, which indicate the wide-lane ambiguity estimates.

where $b_{g,r}$, b_g^k are the geometric code biases due to the preservation of the geometry, $\beta_{\mathrm{IF},r}$, β_{IF}^k are the narrow-lane phase biases, and the narrow-lane ambiguity $N_{\mathrm{IF},r}^k$ is no longer an integer. However, applying Eq. (2.49) $N_{\mathrm{IF},r}^k$ can be expressed as a combination of the integer ambiguity $N_{1,r}^k$ on L1 and the wide-lane ambiguity $N_{\mathrm{WL},r}^k$. The narrow-lane ambiguities

and phase biases are expressed by

$$\begin{aligned}\lambda_{\mathrm{IF}} N^k_{\mathrm{IF},r} &= \frac{cf_1}{f_1^2 - f_2^2} \cdot N^k_{1,r} - \frac{cf_2}{f_1^2 - f_2^2} \cdot \left(N^k_{1,r} - N^k_{\mathrm{WL},r}\right) \\ &= \underbrace{\frac{c}{f_1 + f_2}}_{\lambda_{\mathrm{IF}}} \cdot \underbrace{\left(N^k_{1,r} + \frac{f_2}{f_1 - f_2} N^k_{\mathrm{WL},r}\right)}_{N^k_{\mathrm{IF},r}}, \\ \beta_{\mathrm{IF},r} &= \frac{f_1\beta_{1,r} + f_2\beta_{2,r}}{f_1 - f_2}, \quad \beta^k_{\mathrm{IF}} = \frac{f_1\beta^k_1 + f_2\beta^k_2}{f_1 - f_2}. \end{aligned} \tag{2.53}$$

In the case of GPS, the narrow-lane wavelength is only as small as 10.6 cm, which makes it difficult and less reliable to perform integer ambiguity fixing for $N^k_{1,r}$.

User mode

The geometric code biases $b_{g,r}$ and b^k_g can be mapped into the receiver and satellite clock offsets in Eq. (2.52), and compensates them in the phase equation.

$$\begin{aligned}\rho^k_{\mathrm{IF},r} &= (\vec{\boldsymbol{e}}_r^{\,k})^{\mathrm{T}}(\vec{\boldsymbol{r}}_r - \vec{\boldsymbol{r}}^{\,k}) + c(\tilde{\delta}_r - \tilde{\delta}^k) + m^k_{\mathrm{T},r} T_{\mathrm{z},r} + \eta^k_{\mathrm{IF},r} \\ \lambda_{\mathrm{IF}}\varphi^k_{\mathrm{IF},r} - \frac{cf_2}{f_1^2 - f_2^2}\check{N}^k_{\mathrm{WL},r} &= (\vec{\boldsymbol{e}}_r^{\,k})^{\mathrm{T}}(\vec{\boldsymbol{r}}_r - \vec{\boldsymbol{r}}^{k}) + c(\tilde{\delta}_r - \tilde{\delta}^k) + m^k_{\mathrm{T},r} T_{\mathrm{z},r} + \lambda_{\mathrm{IF}}(N^k_{1,r} + \beta_{\mathrm{IF},r} + \beta^k_{\mathrm{IF}}) \\ &\quad - b_{g,r} - b^k_g + \varepsilon^k_{\mathrm{IF},r}, \end{aligned} \tag{2.54}$$

with

$$c\tilde{\delta}_r = c\delta_r + b_{g,r}, \quad c\tilde{\delta}^k = c\delta^k - b^k_g. \tag{2.55}$$

We combine the phase biases and the compensated code biases with the ambiguity into one real-valued parameter, i.e.

$$\tilde{N}^k_{\mathrm{IF},r} \triangleq N^k_{1,r} + \beta_{\mathrm{IF},r} + \beta^k_{\mathrm{IF}} - \frac{1}{\lambda_{\mathrm{IF}}}(b_{g,r} + b^k_g), \quad \tilde{N}^k_{\mathrm{IF},r} \in \mathbb{R} \tag{2.56}$$

The observation model of Eq. (2.54) matches the one suggested by IGS in [22], which allows us to directly apply the IGS precise satellite orbit and clock offsets. We now bring the satellite orbit and clock corrections to the left-hand side of Eq. (2.54), and denote the corrected measurements as $\Delta\rho^k_{\mathrm{IF},r}$ and $\lambda_{\mathrm{IF}}\Delta\varphi^k_{\mathrm{IF},r}$. The model is simplified to

$$\begin{aligned}\Delta\rho^k_{\mathrm{IF},r} &= (\vec{\boldsymbol{e}}^{\,k})^{\mathrm{T}}\vec{\boldsymbol{r}}_r + c\tilde{\delta}_r + m^k_{\mathrm{T},r} T_{\mathrm{z},r} + \eta^k_{\mathrm{IF},r}, \\ \lambda_{\mathrm{IF}}\Delta\varphi^k_{\mathrm{IF},r} &= (\vec{\boldsymbol{e}}_r^{\,k})^{\mathrm{T}}\vec{\boldsymbol{r}}_r + c\tilde{\delta}_r + m^k_{\mathrm{T},r} T_{\mathrm{z},r} + \lambda_{\mathrm{IF}}\tilde{N}^k_{\mathrm{IF},r} + \varepsilon^k_{\mathrm{IF},r}, \end{aligned} \tag{2.57}$$

A Kalman filter can be introduced to estimate the receiver position, the receiver clock offset, the tropospheric zenith delay and the real-valued ambiguity/bias term. The state vector is thus given by

$$\boldsymbol{x} = \left[\vec{\boldsymbol{r}}_r^{\,\mathrm{T}},\ c\delta_r,\ T_{\mathrm{z},r},\ \tilde{\boldsymbol{N}}^{\mathrm{T}}_{\mathrm{IF},r}\right]^{\mathrm{T}}, \tag{2.58}$$

where $\tilde{\boldsymbol{N}}_{\mathrm{IF},r}$ denotes the vector stacking ambiguities from all available satellites.

The algorithm has been applied to real GPS data obtained from IGS station kiru from 20:00 to 02:00(+1) GPS Time on Jan 1, 2011. Each state is assumed to follow a random walk process. The standard deviations of the process noise are assumed to be: 1 mm for the receiver position, 1 m for the receiver clock offset, 1 mm for the tropospheric zenith delay, and 1 millicycle for the real-valued combined ambiguity/bias term. The measurement noise is assumed white Gaussian distributed with the standard deviation following an exponential function of elevation angle.

Fig. 2.15 depicts the positioning errors in east-, north- and up-directions. The centimeter accuracy is first reached shortly before 30th minute, while the ambiguities are kept as float estimates. There exists a large variation on the up error, which is mainly due to the correlation of the receiver height and the tropospheric zenith delay. This will be addressed later in this work.

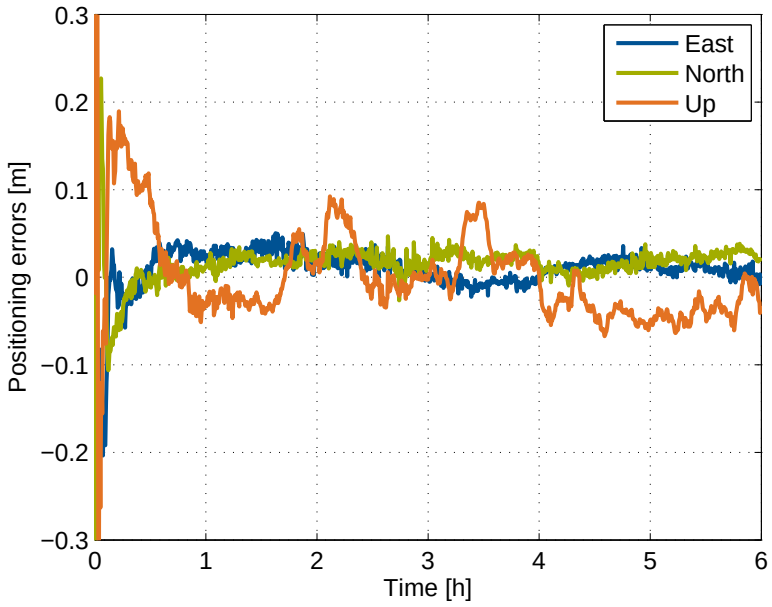

Figure 2.15: The positioning errors in east-, north- and up-directions at station kiru. After convergence, the east and north errors remain below 3 cm, while the up error is smaller than 10 cm.

Network mode

In order to resolve the L1 ambiguities $N_{1,r}^k$ in Eq. (2.56), the precise knowledge of the phase biases and the geometric code biases shall be known. Laurichesse et al. have presented an integer-PPP method in [8, 9]. A slightly different representation from Eq. (2.54) is introduced, where different clock offsets have been assigned for carrier phase $c\delta_{\varphi,r}$, $c\delta_{\varphi}^k$ and code $c\delta_{\rho,r}$, $c\delta_{\rho}^k$. The model is essentially the same, as the phase biases are absorbed into the phase clock offsets, i.e.

$$\rho_{\mathrm{IF},r}^k = (\vec{\boldsymbol{e}}_r^{\,k})^{\mathrm{T}}(\vec{\boldsymbol{r}}_r - \vec{\boldsymbol{r}}^{\,k}) + c(\delta_{\rho,r} - \delta_{\rho}^k) + m_{\mathrm{T},r}^k T_{\mathrm{z},r} + \eta_{\mathrm{IF},r}^k, \tag{2.59}$$

$$\lambda_{\mathrm{IF}}\varphi^k_{\mathrm{IF},r} - \frac{cf_2}{f_1^2 - f_2^2}\check{N}^k_{\mathrm{WL},r} = (\vec{\boldsymbol{e}}_r^{\,k})^{\mathrm{T}}(\vec{\boldsymbol{r}}_r - \vec{\boldsymbol{r}}^{\,k}) + c(\delta_{\varphi,r} - \delta^k_{\varphi}) + m^k_{\mathrm{T},r}T_{\mathrm{z},r} + \lambda_{\mathrm{IF}}N^k_{1,r} + \varepsilon^k_{\mathrm{IF},r}, \tag{2.60}$$

with

$$\begin{aligned} c\delta_{\rho,r} &= c\delta_r + b_{g,r}, \quad c\delta^k_{\rho} = c\delta^k - b^k_g, \\ c\delta_{\varphi,r} &= c\delta_r + \lambda_{\mathrm{IF}}\beta_{\mathrm{IF},r}, \quad c\delta^k_{\varphi} = c\delta^k - \lambda_{\mathrm{IF}}\beta^k_{\mathrm{IF}}. \end{aligned} \tag{2.61}$$

The code and phase clocks are estimated with a network of stations in the first step, with the ambiguities being fixed to integers. Then the fixed clock products containing the biases can be provided to a single user for its narrow-lane ambiguity resolution.

The network mode proceeds as follows. After correcting the satellite orbits from the raw measurements, an extended Kalman filter can be introduced to estimate the orbit corrections, the satellite and station phase clock offsets, the code/phase clock biases, the tropospheric zenith delays, and the narrow-lane ambiguities. The ambiguities are fixed when the standard deviation is small enough, afterwards the fixed ambiguities are added as new measurements with noise being 0. The state vector thus reads

$$\boldsymbol{x} = \left[\Delta\vec{\boldsymbol{r}}^{\mathrm{T}},\, c\boldsymbol{\delta}^{\mathrm{T}}_{\varphi},\, c\boldsymbol{\delta}^{\varphi,\mathrm{T}},\, (c\boldsymbol{\delta}_{\rho} - c\boldsymbol{\delta}_{\varphi})^{\mathrm{T}},\, (c\boldsymbol{\delta}^{\rho} - c\boldsymbol{\delta}^{\varphi})^{\mathrm{T}},\, \boldsymbol{T}^{\mathrm{T}}_{\mathrm{z}},\, \boldsymbol{N}^{\mathrm{T}}_1\right]^{\mathrm{T}}, \tag{2.62}$$

where $\Delta\vec{\boldsymbol{r}}$ denotes the vector for satellite orbit corrections, $c\boldsymbol{\delta}_{\rho}$ and $c\boldsymbol{\delta}_{\varphi}$ denote the vectors stacking all receiver clock offsets, and $c\boldsymbol{\delta}^{\rho}$ and $c\boldsymbol{\delta}^{\varphi}$ denote the vectors stacking all satellite clock offsets for code and phase respectively. The states are assumed to follow random walk processes, and the standard deviation for each process noise is listed in Tab. 2.4 [9].

Phase satellite clock	∞	purely stochastic
Phase station clock	∞	purely stochastic
Code/phase satellite clock bias	1 mm	
Code/phase station clock bias	1 cm	
Tropospheric zenith delay	1 mm	
Satellite orbit corrections (along-track, cross-track)	4 mm, 2 mm	radial correction set to 0
Phase ambiguities	0	initial variance set to 100 m^2

Table 2.4: Process noise model for narrow-lane fixing in network processing. (Source: Laurichesse et al. [9])

The user would operate his PPP algorithm in a similar way. The wide-lane combination is first formed in order to fix the wide-lane ambiguities. Next, the ionosphere-free combinations are taken to estimate the position along with the narrow-lane ambiguities. With the help of the fixed wide-lane ambiguities from the first step and the fixed code and phase clock solution from the network processing, the ambiguities on L1 are able to be fixed to integers.

The same network algorithm has been performed in the IGS analysis center (AC) CNES/CLS (Centre National d'Etudes Spatiales/Collecte Localisation Satellites) and contributed to orbit solutions for IGS [62], whereas the precise satellite orbit product benefits from the

narrow-lane bias estimation and ambiguity fixing. Some other IGS ACs do not estimate the phase biases, instead they fix the ionosphere-free double difference (DD) ambiguities baseline-by-baseline. Traditionally, the fixing takes place sequentially according to the variances [63], e.g. from NOAA/NGS (National Oceanic and Atmospheric Administration/National Geodetic Survey) analysis center [64]. Ge et al. further improved the fixing criteria by sorting the DD ambiguities under the wide-lane and narrow-lane fixing probabilities, which check both the statistical variance and the real estimate [65]. This algorithm has been adopted by IGS analysis centers GFZ (GeoForschungsZentrum), and ESOC (European Space Operation Center) [66, 67].

2.3 Multi-frequency PPP Algorithm

Most PPP approaches are based on ionosphere-free combinations. In this section, a generic multi-frequency PPP approach is proposed with uncombined measurements. The ionospheric delays are no longer removed by combinations but estimated in the system. This has the advantage of reduced code noise. Meanwhile, the ambiguities also remain uncombined, which have larger wavelength than the narrow-lane ambiguities.

A flow diagram is shown in Fig. 2.16, which starts with the absolute code ρ_m^k and phase measurements $\lambda_m \varphi_m^k$ as input. We present an example with two GPS frequencies. The algorithm can be easily extended to multi-frequencies. The measurement model is given by

$$\begin{aligned}
&\rho_m^k + (\vec{\boldsymbol{e}}^{\,k})^{\mathrm{T}} \vec{\boldsymbol{r}}^{\,k} + c\delta^k - (\vec{\boldsymbol{e}}^{\,k})^{\mathrm{T}} \Delta \vec{\boldsymbol{r}}_{\mathrm{et}} = (\vec{\boldsymbol{e}}^{\,k})^{\mathrm{T}} \vec{\boldsymbol{r}} + c\delta + m_{\mathrm{T}}^k T_{\mathrm{z}} + \frac{f_1^2}{f_m^2} I_1^k + \eta_m^k, \\
&\lambda_m \varphi_m^k + (\vec{\boldsymbol{e}}^{\,k})^{\mathrm{T}} \vec{\boldsymbol{r}}^{\,k} + c\delta^k - \lambda_m \varphi_{\mathrm{pw}}^k - \varphi_{\mathrm{pcv},m}^k - (\vec{\boldsymbol{e}}^{\,k})^{\mathrm{T}} \Delta \vec{\boldsymbol{r}}_{\mathrm{et}} - \varphi_{\mathrm{pcv},m} = (\vec{\boldsymbol{e}}^{\,k})^{\mathrm{T}} \vec{\boldsymbol{r}} + c\delta + m_{\mathrm{T}}^k T_{\mathrm{z}} - \\
&\qquad\qquad - \frac{f_1^2}{f_m^2} I_1^k + \lambda_m \tilde{N}_m^k + \varepsilon_m^k, \quad (2.63)
\end{aligned}$$

where $\vec{\boldsymbol{e}}^{\,k}$ denotes the unit vector from the satellite to the receiver. The ambiguity term $\tilde{N}$ combines the integer ambiguities with the phase biases, namely $\tilde{N}_m^k \triangleq N_m^k + \beta_m + \beta_m^k$. The reason for the combination is that, the phase biases cannot be estimated separately from the integer ambiguities with a single station due to rank deficiency. The measurement vector $\boldsymbol{z}$ reads

$$\boldsymbol{z} = \left[\lambda_1 \boldsymbol{\varphi}_1^{\mathrm{T}},\ \lambda_2 \boldsymbol{\varphi}_2^{\mathrm{T}},\ \boldsymbol{\rho}_1^{\mathrm{T}},\ \boldsymbol{\rho}_2^{\mathrm{T}}\right]^{\mathrm{T}}, \tag{2.64}$$

with each vector stacking one measurement type with all visible satellites.

First, we screen the observations for outliers and cycle slips in the pre-processing. Possible outliers in the geometric and ionospheric terms are checked through time-differenced geometry-preserving (GP) ionosphere-free (IF) combination and geometry-free (GF) ionosphere-preserving (IP) combination of the code and phase measurements, respectively. If the temporal change of the combinations goes beyond the normal change of orbit or ionospheric delay, it is detected as an outlier. An exception is that if the sudden change in the GP IF combination appears the same for all satellites, it is recognized as a receiver clock behaviour rather than an outlier.

Melbourne-Wübbena (MW) combination is formed as a third check. The Melbourne-Wübbena combination, described in Eq. (2.48), eliminates both the geometric and the

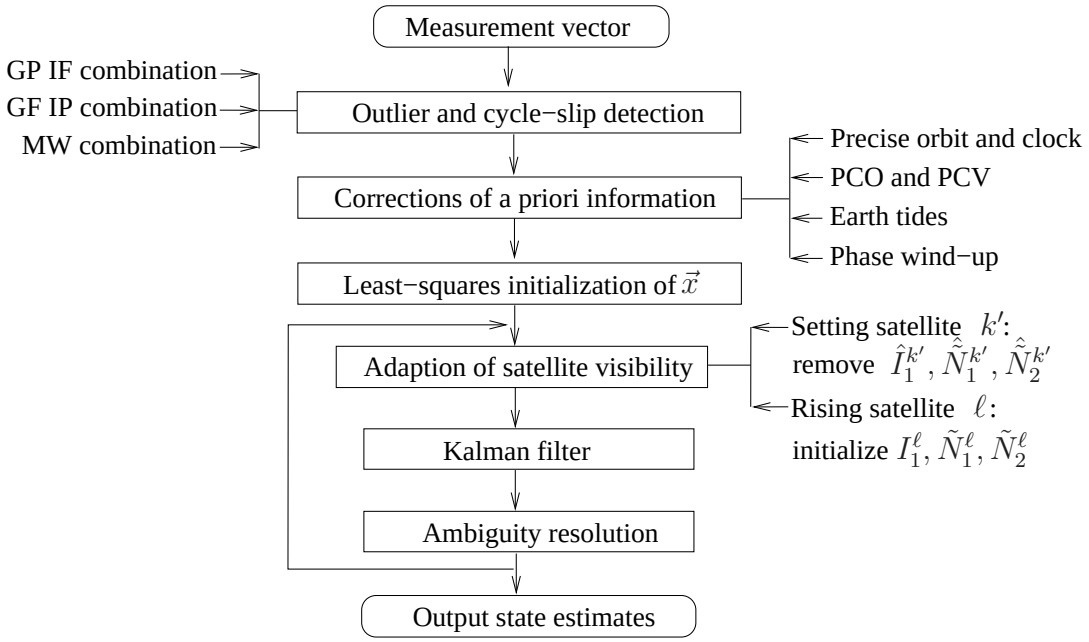

Figure 2.16: A generalized flow diagram for the PPP algorithm with absolute measurements. Precise corrections are applied onto the cleaned measurements, before a Kalman filter is employed to take advantage of state transitions. Without the knowledge on phase biases, the absolute ambiguity estimates are fixed to real-valued parameters.

ionospheric terms, which leaves only a combination of ambiguities and biases and combined noise. Since the ambiguities and biases are constant over time, the combination is expected to be white Gaussian noise centered at the constant value. The standard deviation of the noise of the MW combination is about 0.7 times that of code noise on L1, assuming same noise statistics for L1 and L2. Moreover, the wavelength of the wide-lane ambiguity is about 86 cm, thus a spike or a shift could be observed in the combination in the case of an outlier or a cycle-slip.

To increase the reliability of the detection, continuous observations from one satellite are screened together as one arc. For each arc we study two elements, namely the rms and the slope of the first-order fitting of the arc. A similar technique is suggested by the Bernese software in [33], where only rms is studied. An outlier or a cycle-slip is detected if the rms and the slope appear larger than given thresholds. The location can be found out by halving the arc recursively. It is noted that because of the combination, only the difference between the cycle slips on two frequencies can be detected. However it is very unlikely to happen that the ambiguities N_1 and N_2 have the same cycle slips at the same time. If an outlier or a cycle-slip is detected, the measurements on that epoch will be removed.

The next step is the correction of a priori knowledge, i.e. the satellite orbits and clocks, as well as various well-modelled effects including earth tides, phase wind-up, phase center variations, etc. The corrected measurements are denoted by $\Delta\rho_m^k$ and $\lambda_m\Delta\varphi_m^k$, i.e.

$$\begin{aligned}\Delta\rho_m^k &= \rho_m^k + (\vec{\boldsymbol{e}}^{\,k})^{\mathrm{T}}\vec{\boldsymbol{r}}^{\,k} + c\delta^k - (\vec{\boldsymbol{e}}^{\,k})^{\mathrm{T}}\Delta\vec{\boldsymbol{r}}_{\mathrm{et}},\\ \lambda_m\Delta\varphi_m^k &= \lambda_m\varphi_m^k + (\vec{\boldsymbol{e}}^{\,k})^{\mathrm{T}}\vec{\boldsymbol{r}}^{\,k} + c\delta^k - \lambda_m\varphi_{\mathrm{pw}}^k - \varphi_{\mathrm{pcv},m}^k - (\vec{\boldsymbol{e}}^{\,k})^{\mathrm{T}}\Delta\vec{\boldsymbol{r}}_{\mathrm{et}} - \varphi_{\mathrm{pcv},m}.\end{aligned} \tag{2.65}$$

A Kalman filter is introduced to estimate the states, which consist of the receiver position, the receiver clock offset, the tropospheric zenith delay, the slant ionospheric delays, and the absolute ambiguities. The state vector reads

$$\boldsymbol{x} = \left[\vec{\boldsymbol{r}}^{\mathrm{T}},\ c\delta,\ T_{\mathrm{z}},\ \boldsymbol{I}_1^{\mathrm{T}},\ \tilde{\boldsymbol{N}}_1^{\mathrm{T}},\ \tilde{\boldsymbol{N}}_2^{\mathrm{T}}\right]^{\mathrm{T}}. \tag{2.66}$$

The Kalman filter takes advantage of the dynamic process and recursively estimates the states [68]. The filter is generally described by a measurement model for $\boldsymbol{z}$ and a state space model for $\boldsymbol{x}$, as

$$\begin{aligned} \boldsymbol{z}_n &= \boldsymbol{H}_n\boldsymbol{x}_n + \boldsymbol{v}_n \\ \boldsymbol{x}_n &= \boldsymbol{\Phi}_{n-1}\boldsymbol{x}_{n-1} + \boldsymbol{w}_{n-1}, \end{aligned} \tag{2.67}$$

with n indicating the epoch, $\boldsymbol{H}$ and $\boldsymbol{\Phi}$ denoting the design matrix and the state transition matrix, $\boldsymbol{v}$ and $\boldsymbol{w}$ being the measurement and process noise.

At each epoch, the Kalman filter performs a prediction and an update step. The state estimates are updated with the measurement residuals from the prediction step scaled by a Kalman gain $\boldsymbol{K}$. The Kalman gain is obtained by minimizing the expectation of the squared error norm of the state vector. The state covariance matrix $\boldsymbol{P}$ addresses the precision of the estimates.

$$\left.\begin{aligned} \hat{\boldsymbol{x}}_n^- &= \boldsymbol{\Phi}_{n-1}\hat{\boldsymbol{x}}_{n-1}^+ \\ \boldsymbol{P}_n^- &= \boldsymbol{\Phi}_{n-1}\boldsymbol{P}_{n-1}^+\boldsymbol{\Phi}_{n-1}^{\mathrm{T}} + \boldsymbol{\Sigma}_{\mathrm{Q},\,n-1} \end{aligned}\right\} \text{Prediction}$$

$$\left.\begin{aligned} \boldsymbol{K}_n &= \boldsymbol{P}_n^-\boldsymbol{H}_n^{\mathrm{T}}(\boldsymbol{H}_n\boldsymbol{P}_n^-\boldsymbol{H}_n^{\mathrm{T}} + \boldsymbol{\Sigma}_{\mathrm{R},\,n})^{-1} \\ \hat{\boldsymbol{x}}_n^+ &= \hat{\boldsymbol{x}}_n^- + \boldsymbol{K}_n(\boldsymbol{z}_n - \boldsymbol{H}_n\hat{\boldsymbol{x}}_n^-) \\ \boldsymbol{P}_n^+ &= (\boldsymbol{I} - \boldsymbol{K}_n\boldsymbol{H}_n)\boldsymbol{P}_n^-, \end{aligned}\right\} \text{Update} \tag{2.68}$$

where $\boldsymbol{\Sigma}_{\mathrm{R}}$ and $\boldsymbol{\Sigma}_{\mathrm{Q}}$ represent the measurement and process noise covariance matrices, and the upper indices "-" and "+" denote a priori and a posteriori estimation respectively.

The dynamics of rising and setting satellites have to be considered in the Kalman filter. In the case of satellite setting, it is straightforward to remove the corresponding entries from the states and covariances, while in rising cases new states are introduced. The new states are initialized with least-squares using existed state estimates as corrections. Taking an example of a rising satellite ℓ, three new variables are to be initialized, i.e. the slant ionospheric delay and the ambiguities $\boldsymbol{x}^\ell = \left[I_1^\ell, \tilde{N}_1^\ell, \tilde{N}_2^\ell\right]^{\mathrm{T}}$. The receiver position, the receiver clock offset, and the tropospheric zenith delay are obtained from the filter estimates, and corrected from the new measurements. The correction vector is thus given by $\hat{\boldsymbol{x}}_{\mathrm{c}}^- = \left[\hat{\vec{\boldsymbol{r}}}^{\mathrm{T}},\ c\hat{\delta},\ \hat{T}_{\mathrm{z}}\right]^{\mathrm{T}}$. Let the design matrices for the unknown and the correction vector be $\boldsymbol{H}_{\boldsymbol{x}^\ell}$ and $\boldsymbol{H}_{\hat{\boldsymbol{x}}_{\mathrm{c}}}^\ell$ respectively, the measurement model for the new satellite is written as

$$\boldsymbol{z}^\ell - \boldsymbol{H}_{\hat{\boldsymbol{x}}_{\mathrm{c}}}^\ell\hat{\boldsymbol{x}}_{\mathrm{c}}^- = \boldsymbol{H}_{\boldsymbol{x}^\ell}\boldsymbol{x}^\ell + \boldsymbol{\eta}_{z^\ell}. \tag{2.69}$$

The noise $\boldsymbol{\eta}_{z^\ell}$ is Gaussian distributed with covariance matrix $\tilde{\boldsymbol{\Sigma}}_{\mathrm{R}}^\ell$, i.e. $\boldsymbol{\eta}_{z^\ell} \sim \mathcal{N}(\boldsymbol{0}, \tilde{\boldsymbol{\Sigma}}_{\mathrm{R}}^\ell)$. The measurement covariance matrix is transformed due to the correction from the original $\boldsymbol{\Sigma}_{\mathrm{R}}^\ell$ into

$$\tilde{\boldsymbol{\Sigma}}_{\mathrm{R}}^\ell = \boldsymbol{\Sigma}_{\mathrm{R}}^\ell + \boldsymbol{H}_{\hat{\boldsymbol{x}}_{\mathrm{c}}}^{\ell,\,\mathrm{T}}\boldsymbol{P}_{\hat{\boldsymbol{x}}_{\mathrm{c}}}^-\boldsymbol{H}_{\hat{\boldsymbol{x}}_{\mathrm{c}}}^\ell, \tag{2.70}$$

with $\boldsymbol{P}^{-}_{\hat{\boldsymbol{x}}_\mathrm{c}}$ denoting the a priori state covariance matrix for the correction vector.

The least-squares estimate $\hat{\boldsymbol{x}}^{\ell}$ and the covariance matrices are calculated as

$$\begin{aligned}
\hat{\boldsymbol{x}}^{\ell} &= \left(\boldsymbol{H}^{\mathrm{T}}_{\boldsymbol{x}^{\ell}}\left(\tilde{\boldsymbol{\Sigma}}^{\ell}_{\mathrm{R}}\right)^{-1}\boldsymbol{H}_{\boldsymbol{x}^{\ell}}\right)^{-1}\boldsymbol{H}^{\mathrm{T}}_{\boldsymbol{x}^{\ell}}\left(\tilde{\boldsymbol{\Sigma}}^{\ell}_{\mathrm{R}}\right)^{-1}(\boldsymbol{z}^{\ell}-\boldsymbol{H}^{\ell}_{\hat{\boldsymbol{x}}_\mathrm{c}}\hat{\boldsymbol{x}}^{-}_{\mathrm{c}}),\\
\boldsymbol{P}^{-}_{\hat{\boldsymbol{x}}^{\ell}} &= \left(\boldsymbol{H}^{\mathrm{T}}_{\boldsymbol{x}^{\ell}}\left(\tilde{\boldsymbol{\Sigma}}^{\ell}_{\mathrm{R}}\right)^{-1}\boldsymbol{H}_{\boldsymbol{x}^{\ell}}\right)^{-1},\\
\boldsymbol{P}^{-}_{\hat{\boldsymbol{x}}^{\ell}\hat{\boldsymbol{x}}_\mathrm{c}} &= -\boldsymbol{P}^{-}_{\hat{\boldsymbol{x}}^{\ell}}\boldsymbol{H}^{\mathrm{T}}_{\boldsymbol{x}^{\ell}}\left(\tilde{\boldsymbol{\Sigma}}^{\ell}_{\mathrm{R}}\right)^{-1}\boldsymbol{H}^{\ell}_{\hat{\boldsymbol{x}}_\mathrm{c}}\boldsymbol{P}^{-}_{\hat{\boldsymbol{x}}_\mathrm{c}},
\end{aligned} \tag{2.71}$$

where $\boldsymbol{P}^{-}_{\hat{\boldsymbol{x}}^{\ell}\hat{\boldsymbol{x}}_\mathrm{c}}$ represents the covariance matrix between the new states and the existed state estimates. This is needed for the initialization of the a priori covariance matrix in the Kalman filter.

For the settings of the Kalman filter, the states are assumed to follow random walk processes, while the measurement noise is assumed to follow zero-mean white Gaussian distribution, with standard deviation being an exponential function of the elevation angle. The float ambiguity estimates are then input to the fixing block, where the temporal variation of the float estimates is observed over a time window. If the temporal variation is below a certain threshold, the ambiguity is fixed to the float value and eliminated from the state vector.

As it is presented in the previous section, the high correlation between the tropospheric delay and the receiver height prevents from a precise solution. Code multipath is another important factor affecting the positioning accuracy. The next two sections will focus on the improvement for the PPP algorithm by adding constraint on the tropospheric zenith delay, and by introducing new states of code multipath.

2.3.1 Estimation of Tropospheric Delays with Interval

The high correlation between the tropospheric zenith delay and the receiver clock offset, the receiver height comes from the design matrix, i.e. the inversion of $\boldsymbol{H}^{\mathrm{T}}{\boldsymbol{\Sigma}_{\boldsymbol{R}}}^{-1}\boldsymbol{H}$. The inversion is performed every epoch, which makes the three terms difficult to be estimated precisely, as errors in the state estimates could shift among each others. Given that the tropospheric zenith delay rarely changes over short time, an additional constraint can be imposed. The zenith delay is assumed to be constant over a short interval, after it has been estimated epoch-wise to reach convergence. The state space model for the zenith delay is thus described as

$$\hat{T}_{\mathrm{z},n} = \begin{cases} \hat{T}_{\mathrm{z},n-1} + w_{n-1} & 1 < n < n_0 \\ \hat{T}_{\mathrm{z},n-d} + w_{n-d} & n > n_0, \text{ and } n \bmod d = 0 \\ \hat{T}_{\mathrm{z},\lfloor n/d \rfloor \cdot d} & \text{else,} \end{cases} \tag{2.72}$$

where n_0 denotes the duration in the beginning, d represents the length of the interval without estimating the zenith delay, and the process noise w_n is assumed normal distributed as $w_n \sim \mathcal{N}(0, \sigma^2_{T_\mathrm{z}})$ with variance $\sigma^2_{T_\mathrm{z}}$.

Now two different state vectors are involved in the estimation, let $\boldsymbol{x}$ be the one including the zenith delay as stated in Eq. (2.66), and let $\tilde{\boldsymbol{x}}$ denote the state vector without it, i.e.

$$\tilde{\boldsymbol{x}} = \left[\vec{\boldsymbol{r}}^{\mathrm{T}},\, c\delta,\, \boldsymbol{I}^{\mathrm{T}}_1,\, \tilde{\boldsymbol{N}}^{\mathrm{T}}_1,\, \tilde{\boldsymbol{N}}^{\mathrm{T}}_2\right]^{\mathrm{T}}. \tag{2.73}$$

Within the interval, the state update equation of the Kalman filter are given by

$$\hat{\tilde{\boldsymbol{x}}}_n^+ = \hat{\tilde{\boldsymbol{x}}}_n^- + \boldsymbol{K}_n(\boldsymbol{z}_n - \boldsymbol{H}_{T_\mathrm{z},n}\hat{T}^+_{\mathrm{z},\lfloor n/d \rfloor \cdot d} - \boldsymbol{H}_{\tilde{\boldsymbol{x}},n}\hat{\tilde{\boldsymbol{x}}}_n^-), \tag{2.74}$$

where $\boldsymbol{H}_{T_\mathrm{z}}$ and $\boldsymbol{H}_{\tilde{\boldsymbol{x}}}$ denote the design matrix for the zenith delay and for other states respectively, $\boldsymbol{K}$ is the Kalman gain, and $\boldsymbol{v}$ denotes the measurement noise.

When the zenith delay is again included in the state vector, it is initialized with the last estimate according to Eq. (2.72), while the variance can be initialized with the last variance. There exists covariance between the introduced zenith delay and the other state estimates in $\hat{\tilde{\boldsymbol{x}}}$, because the previous zenith delay estimate has been used as a correction. Assume at epoch n and $n-d$ the zenith delay is estimated in the state vector, we derive the a priori covariance $\boldsymbol{P}^-_{\hat{\tilde{\boldsymbol{x}}}_n,\hat{T}^+_{\mathrm{z},n-d}}$ by applying Eq. (2.74) as

$$\begin{aligned}
&\boldsymbol{P}^-_{\hat{\tilde{\boldsymbol{x}}}_n,\hat{T}^+_{\mathrm{z},n-d}} = \boldsymbol{P}^+_{\hat{\tilde{\boldsymbol{x}}}_{n-1},\hat{T}_{\mathrm{z},n-d}} = \mathrm{E}\left\{\left(\hat{\tilde{\boldsymbol{x}}}^+_{n-1} - \tilde{\boldsymbol{x}}_{n-1}\right)\left(\hat{T}^+_{\mathrm{z},n-d} - T_{\mathrm{z},n-d}\right)\right\} \\
&= \mathrm{E}\left\{\left(\hat{\tilde{\boldsymbol{x}}}^-_{n-1} + \boldsymbol{K}_{n-1}\left(\boldsymbol{H}_{\tilde{\boldsymbol{x}},n-1}\tilde{\boldsymbol{x}}_{n-1} + \boldsymbol{H}_{T_\mathrm{z},n-1}T_{\mathrm{z},n-d} + \boldsymbol{v}_{n-1} - \boldsymbol{H}_{T_\mathrm{z},n-1}\hat{T}^+_{\mathrm{z},n-d} - \right.\right.\right. \\
&\qquad \left.\left.\left. -\boldsymbol{H}_{\tilde{\boldsymbol{x}},n-1}\hat{\tilde{\boldsymbol{x}}}^-_{n-1}\right) - \tilde{\boldsymbol{x}}_{n-1}\right) \cdot \left(\hat{T}^+_{\mathrm{z},n-d} - T_{\mathrm{z},n-d}\right)\right\} \\
&= \mathrm{E}\left\{\left((\boldsymbol{I} - \boldsymbol{K}_{n-1}\boldsymbol{H}_{\tilde{\boldsymbol{x}},n-1})\left(\hat{\tilde{\boldsymbol{x}}}^-_{n-1} - \tilde{\boldsymbol{x}}_{n-1}\right) - \boldsymbol{K}_{n-1}\boldsymbol{H}_{T_\mathrm{z},n-1}\left(\hat{T}^+_{\mathrm{z},n-d} - T_{\mathrm{z},n-d}\right) + \right.\right. \\
&\qquad \left.\left. +\boldsymbol{K}_{n-1}\boldsymbol{v}_{n-1}\right) \cdot \left(\hat{T}^+_{\mathrm{z},n-d} - T_{\mathrm{z},n-d}\right)\right\} \\
&= (\boldsymbol{I} - \boldsymbol{K}_{n-1}\boldsymbol{H}_{\tilde{\boldsymbol{x}},n-1})\,\boldsymbol{P}^-_{\hat{\tilde{\boldsymbol{x}}}_{n-1},\hat{T}^+_{\mathrm{z},n-d}} - \boldsymbol{K}_{n-1}\boldsymbol{H}_{T_\mathrm{z},n-1}\boldsymbol{P}^+_{\hat{T}^+_{\mathrm{z},n-d}}.
\end{aligned} \tag{2.75}$$

This gives a recursive solution for the initial covariance between the introduced zenith delay and other states, i.e.

$$\begin{aligned}
\boldsymbol{P}^-_{\hat{\tilde{\boldsymbol{x}}}_n,\hat{T}^+_{\mathrm{z},n-d}} = &\prod_{j=1}^{d-1}(\boldsymbol{I} - \boldsymbol{K}_{n-j}\boldsymbol{H}_{\tilde{\boldsymbol{x}},n-j})\boldsymbol{P}^+_{\hat{\tilde{\boldsymbol{x}}}_{n-d},\hat{T}^+_{\mathrm{z},n-d}} - \sum_{i=1}^{d-1}\left(\prod_{j=1}^{i-1}(\boldsymbol{I} - \boldsymbol{K}_{n-j}\boldsymbol{H}_{\tilde{\boldsymbol{x}},n-j})\right) \cdot \\
&\boldsymbol{K}_{n-i}\boldsymbol{H}_{T_\mathrm{z},n-i}\boldsymbol{P}^+_{\hat{T}^+_{\mathrm{z},n-d}}
\end{aligned} \tag{2.76}$$

Fig. 2.17 shows the benefit of applying the constraint on the tropospheric zenith delay, where Fig. 2.17(a) and Fig. 2.17(b) represent the case for epoch-wise estimation and spaced estimation of the variable respectively. Some of the large variations on the receiver height errors are reduced by 2 times in the right figure. The interval for correcting a priori zenith delay is set to 300 epochs (seconds), while the beginning 1000 epochs are kept epoch-wise for convergence. The zenith delay errors are dropped below 1 cm and most of the height errors are reduced to ±10 cm.

2.3.2 Estimation of Code Multipath

Code multipath is one of the major error sources which degrade the position solution. In the previous models, code multipath is included in the code noise, which is assumed to be white Gaussian distributed. However, code multipath could reach several meters and is

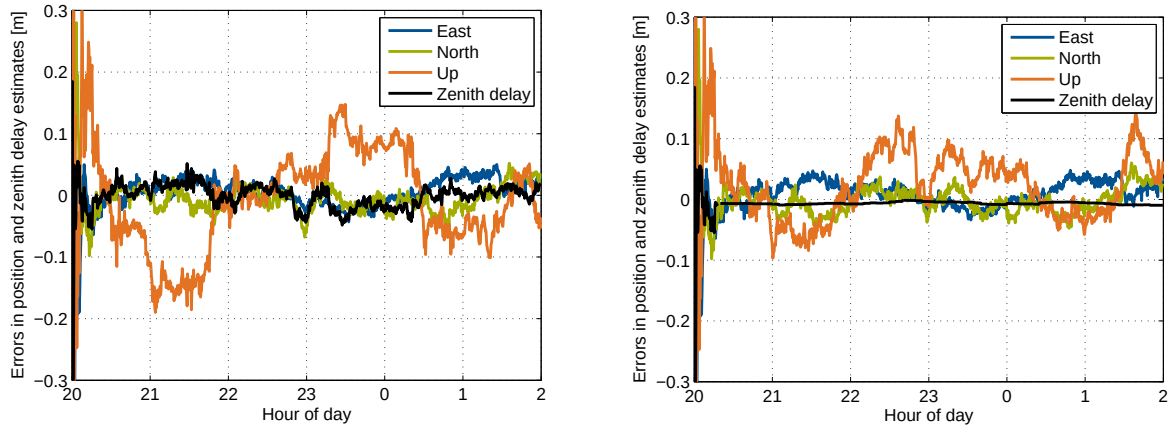

(a) Epoch-wise estimation of the tropospheric zenith delay.

(b) The tropospheric zenith delay is estimated with an interval of 300 seconds.

Figure 2.17: Benefit of adding constraint on the tropospheric zenith delay in PPP, where the position for an IGS station kiru is determined.

not necessarily zero-mean. We can further split the code noise η^k from Eq. (2.63) into the code multipath p and the white code noise $\tilde{\eta}$ as

$$\eta^k = p^k + \tilde{\eta}^k. \tag{2.77}$$

The model for the code measurements is modified from Eq. (2.63) and Eq. (2.65), while the unchanged phase measurement model is also listed for completeness, i.e.

$$\begin{aligned} \Delta\rho_m^k &= (\vec{\boldsymbol{e}}^{\,k})^{\mathrm{T}}\vec{\boldsymbol{r}} + c\delta + m_{\mathrm{T}}^k T_{\mathrm{z}} + \frac{f_1^2}{f_m^2} I_1^k + p_m^k + \tilde{\eta}_m^k, \\ \lambda_m \Delta\varphi_m^k &= (\vec{\boldsymbol{e}}^{\,k})^{\mathrm{T}}\vec{\boldsymbol{r}} + c\delta + m_{\mathrm{T}}^k T_{\mathrm{z}} - \frac{f_1^2}{f_m^2} I_1^k + \lambda_m \tilde{N}_m^k + \varepsilon_m^k. \end{aligned} \tag{2.78}$$

However, it is not possible to estimate all variables, because the system of equations is under-determined. Having K visible satellites, there are $5K + 5$ unknowns but only $4K$ measurements. In order to exploit the invariance property of the integer ambiguities, we suggest to combine several consecutive time instants [69]. Let n_0 denote the number of time instants considered jointly, the measurement vector is expressed by

$$\begin{aligned} \boldsymbol{z}_n = \big[&\Delta\boldsymbol{\rho}_{1,n}^{\mathrm{T}},\ \Delta\boldsymbol{\rho}_{2,n}^{\mathrm{T}},\ \lambda_1\Delta\boldsymbol{\varphi}_{1,n}^{\mathrm{T}},\ \lambda_2\Delta\boldsymbol{\varphi}_{2,n}^{\mathrm{T}},\ \Delta\boldsymbol{\rho}_{1,n+1}^{\mathrm{T}},\ \Delta\boldsymbol{\rho}_{2,n+1}^{\mathrm{T}},\ \lambda_1\Delta\boldsymbol{\varphi}_{1,n+1}^{\mathrm{T}},\ \lambda_2\Delta\boldsymbol{\varphi}_{2,n+1}^{\mathrm{T}}, \ldots, \\ &\Delta\boldsymbol{\rho}_{1,n+n_0-1}^{\mathrm{T}},\ \Delta\boldsymbol{\rho}_{2,n+n_0-1}^{\mathrm{T}},\ \lambda_1\Delta\boldsymbol{\varphi}_{1,n+n_0-1}^{\mathrm{T}},\ \lambda_2\Delta\boldsymbol{\varphi}_{2,n+n_0-1}^{\mathrm{T}}\big]^{\mathrm{T}}, \end{aligned} \tag{2.79}$$

where each measurement type includes all visible satellites, and n denotes the first time index in this epoch.

The system is yet still rank-deficient to estimate all code multipath, because there exists correlation among the receiver clock offset, the ionospheric delay, the code multipath, and the integer ambiguities. A same change in the code multipath p_m^k and the ambiguities multiplied with the wavelengths $\lambda_m \tilde{N}_m^k$ for all satellites, can be fully compensated by an opposite change in the receiver clock offset $c\delta$. Similarly, a change of $f_1^2/f_m^2 \cdot p_m^k$ and

an opposite change of $cf_1^2/f_m \cdot \tilde{N}_m^k$, can be equivalently seen as the same change in the ionospheric delays. Therefore, only a subset of code multipath can be estimated, while the other code multipath cannot be separated from the code noise.

The state vector is thus obtained as

$$\begin{aligned}\boldsymbol{x}_n = \Big[&\vec{\boldsymbol{r}}_n^{\,\mathrm{T}},\, \vec{\boldsymbol{r}}_{n+1}^{\,\mathrm{T}}, \ldots,\, \vec{\boldsymbol{r}}_{n+n_0-1}^{\,\mathrm{T}},\, c\delta_n, \ldots,\, c\delta_{n+n_0-1},\, T_{\mathrm{z},n},\, \boldsymbol{I}_{1,n}^{\mathrm{T}}, \ldots,\, \boldsymbol{I}_{1,n+n_0-1}^{\mathrm{T}},\, \tilde{\boldsymbol{N}}_{1,n}^{\mathrm{T}},\, \tilde{\boldsymbol{N}}_{2,n}^{\mathrm{T}},\\ &\boldsymbol{p}_{1,n}^{\mathrm{T}},\, \boldsymbol{p}_{2,n}^{\mathrm{T}}, \ldots,\, \boldsymbol{p}_{1,n+n_0-1}^{\mathrm{T}},\, \boldsymbol{p}_{2,n+n_0-1}^{\mathrm{T}}\Big]^{\mathrm{T}},\end{aligned} \tag{2.80}$$

where $\boldsymbol{p}$ denotes the estimated subset of the code multipath, including a number of K_p satellites. Besides the time-invariant ambiguities, the tropospheric zenith delay is assumed invariant in one epoch. The number of states now becomes $4n_0 + 1 + n_0K + 2K + 2n_0K_p$, while there exists $4n_0K$ number of measurements.

Increasing n_0 allows more multipath states to be estimated, which enhances the modelling for the measurements. On the other hand, the condition of the design matrix becomes worse with more multipath states included. Therefore a compromise has to be made on the number of the multipath estimates. Considering the multipath is significantly less from satellites having larger elevation angles, we only estimate multipath from low elevation satellites.

The design matrix $\boldsymbol{H}$ for the Kalman filter is expressed in the form of sub-matrices representing each component in the state vector, where a static receiver is assumed, i.e.

$$\boldsymbol{H} = [\, \boldsymbol{H}_e,\, \boldsymbol{H}_{c\delta},\, \boldsymbol{H}_{T_{\mathrm{z}}},\, \boldsymbol{H}_I,\, \boldsymbol{H}_N,\, \boldsymbol{H}_p \,] \tag{2.81}$$

with the sub-matrices described by

$$\begin{aligned}
\boldsymbol{H}_e &= \begin{bmatrix} \mathbf{I}_4 \otimes \boldsymbol{H}_{e,n} \\ \vdots \\ \mathbf{I}_4 \otimes \boldsymbol{H}_{e,n+n_0-1} \end{bmatrix}, \quad \boldsymbol{H}_{e,n_i} = \begin{bmatrix} \left(\vec{\boldsymbol{e}}_{n_i}^{\,1}\right)^{\mathrm{T}} \\ \vdots \\ \left(\vec{\boldsymbol{e}}_{n_i}^{\,K}\right)^{\mathrm{T}} \end{bmatrix},\\
\boldsymbol{H}_{c\delta} &= \mathbf{1}_{\,n_0} \otimes \mathbf{I}_{4K},\\
\boldsymbol{H}_{T_{\mathrm{z}}} &= \begin{bmatrix} \mathbf{I}_4 \otimes \boldsymbol{m}_{T_{\mathrm{z}},n} \\ \vdots \\ \mathbf{I}_4 \otimes \boldsymbol{m}_{T_{\mathrm{z}},n+n_0-1} \end{bmatrix}, \quad \boldsymbol{m}_{T_{\mathrm{z}},n_i} = \begin{bmatrix} m_{T_{\mathrm{z}},n_i}^1 \\ \vdots \\ m_{T_{\mathrm{z}},n_i}^K \end{bmatrix},\\
\boldsymbol{H}_I &= \mathbf{1}_{\,n_0} \otimes \left[\begin{bmatrix} 1 \\ q_{12}^2 \\ -1 \\ -q_{12}^2 \end{bmatrix} \otimes \mathbf{1}_K \right],\\
\boldsymbol{H}_{\tilde{N}} &= \mathbf{I}_{n_0} \otimes \begin{bmatrix} \mathbf{0}_{\,2K\times 1} \\ \begin{bmatrix} \lambda_1 & 0 \\ 0 & \lambda_2 \end{bmatrix} \otimes \mathbf{1}_{\,K} \end{bmatrix},\\
\boldsymbol{H}_p &= \mathbf{1}_{\,n_0} \otimes \begin{bmatrix} \mathbf{1}_{\,2} \otimes \boldsymbol{A}_{K\times K_p} \\ \mathbf{0}_{\,2K\times 2K_p} \end{bmatrix},
\end{aligned} \tag{2.82}$$

where q_{12} denotes the frequency ratio f_1/f_2, $\mathbf{I}$ denotes an all-1s vector, and $\mathbf{1}$ denotes an identity matrix. The matrix $\boldsymbol{A}$ represents a basic design matrix mapping the multipath

subset to the code measurement on one frequency at one time instant. The element $\boldsymbol{A}_{ij}$ (i-th row, j-th column) has the value

$$\boldsymbol{A}_{ij} = \begin{cases} 1 & \text{if } j = a_i \text{ and } \boldsymbol{s}_p(i) = 1 \\ 0 & \text{else.} \end{cases}, \quad \text{with } i \in \{1, \ldots, K\},\ j \in \{1, \ldots, K_p\}. \tag{2.83}$$

Let vector $\boldsymbol{s}_p$ denote a selection vector having length K, where a "1" represents the inclusion of the corresponding visible satellite in the subset. The vector $\boldsymbol{a}$ then denotes the cumulative sum of the selection vector, i.e. $a_i = \sum_{j=1}^{i} \boldsymbol{s}_p(j),\ i \in \{1, \ldots, K\}$.

The code multipath states p_n^k at epoch n are modelled to follow a random walk process, i.e.

$$p_n^k = p_{n-1}^k + w_{p,n-1}^k, \tag{2.84}$$

with the process noise being w_p^k. The standard deviation for w_p^k is set to 50 cm in this work.

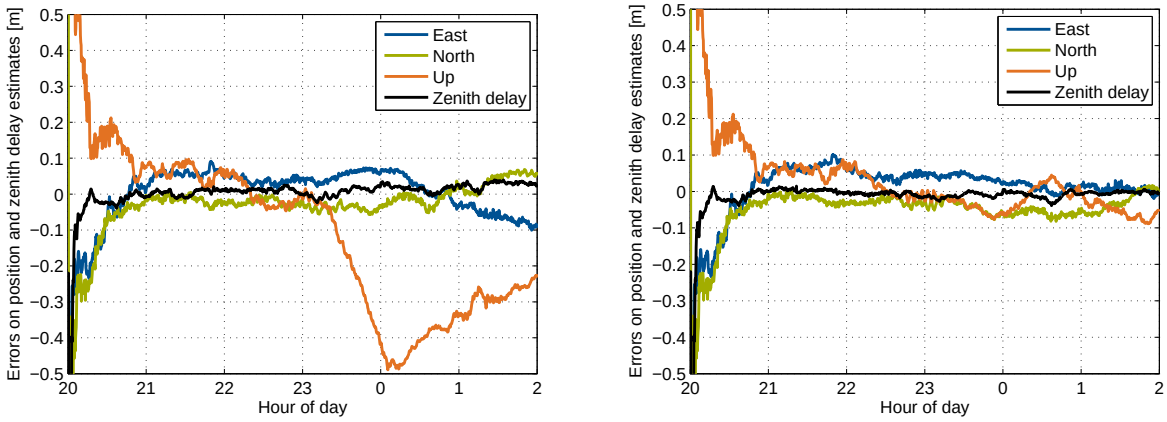

(a) PPP with standard settings, where code multipath is modelled together with the code noise.

(b) A subset of code multipath is jointly estimated for the PRNs with elevation angles below 30°.

Figure 2.18: Benefit of estimating a subset of code multipath for IGS station *vill*.

The algorithm is applied on real GPS data from IGS station *vill*, with each epoch containing measurements from three seconds. The code multipath is estimated for satellites with an elevation angle below 30°. Fig. 2.18 shows the comparison of the position solutions, where the only difference lies in the estimation of code multipath. The left figure Fig. 2.18(a) performs the PPP algorithm presented in Section 2.3, where a large variation occurred on the height estimate after 3 hours. The right figure 2.18(b) shows the position errors after the multipath states are introduced, where the large variation vanishes and all coordinates as well as the tropospheric zenith delay converged to under 10 cm.

Furthermore, in order to validate the estimates on the multipath, we apply some combinations on the raw data to obtain reference code multipath (including measurement noise). The first combination y_1^k eliminates the geometric term by subtracting the phase from the code measurements as

$$\begin{aligned} y_1^k &= \rho_1^k - \lambda_1 \varphi_1^k \\ &= 2I_1^k + b_1 + b_1^k - \lambda_1 (N_1^k + \beta_1 + \beta_1^k) + \eta_1^k - \varepsilon_1^k. \end{aligned} \tag{2.85}$$

Second, the geometry-free ionosphere-preserving phase combination yields the ionospheric delay shifted by a combination of ambiguities and biases, i.e.

$$\begin{aligned} I_\varphi^k &= \frac{f_2^2}{f_1^2 - f_2^2}\lambda_1\varphi_1^k - \frac{f_2^2}{f_1^2 - f_2^2}\lambda_2\varphi_2^k \\ &= I_1^k + \lambda_{\mathrm{IP}}\tilde{N}_{\mathrm{IP}}^k + \varepsilon_{\mathrm{IP}}^k, \end{aligned} \tag{2.86}$$

where the wavelength λ_{IP} and the combination $\tilde{N}_{\mathrm{IP}}^k$ are not the major foci and thus are not expanded in details.

Replacing the ionospheric delay in Eq. (2.85) by Eq. (2.86) yields

$$\begin{aligned} \tilde{p}_1^k &= y_1^k - 2I_\varphi^k \\ &= \underbrace{b_1 + b_1^k - \lambda_1(N_1^k + \beta_1 + \beta_1^k) - 2\lambda_{\mathrm{IP}}\tilde{N}_{\mathrm{IP}}^k}_{\text{constant over short time}} + \eta_1^k - \varepsilon_1^k - 2\varepsilon_{\mathrm{IP}}^k, \end{aligned} \tag{2.87}$$

where $\tilde{p}_1^k$ denotes the reference multipath on the first frequency shifted by a constant combination. The first part in Eq. (2.87) is constant over time, while the code noise dominates in the noise part and the phase noise is negligible. This gives us an opportunity to observe the code multipath, although the amplitude of the combination is a superposition of multipath and noise.

Fig. 2.19 shows the validation of the multipath estimates, where the reference is depicted in blue lines that are shifted by a constant value to be on top of the multipath estimates. The elevation angles are shown in orange referring to the right axes, and it is clear the multipath increases dramatically towards the elevation mask of 10°. It is observed that the multipath estimates match well with the oscillating multipath pattern in the reference code noise. The amplitude of some multipath is much larger than 2−3 m at low elevations, which goes far beyond the usually assumed standard deviation of the code noise. Furthermore, the large multipath on PRN 12 in Fig. 2.19(c) along with PRN 5 in Fig. 2.19(a) after the third hour results in the large variation on the up-direction starting after 23:00 in Fig. 2.18(a).

2.3.3 Model Extension for Multi-GNSS

Precise point positioning would benefit from more observations, if additional GNSS system such as Galileo, BeiDou, GLONASS is augmented. In this section, a PPP algorithm with combined GPS and Galileo system is presented.

Galileo open service signal characteristics are listed in Table 2.5. The E1 signal has the same center frequency with the GPS L1 signal, but the BOC(1,1)[1] modulation prevents the interference by splitting the main lobe of the spectrum off the center frequency. Among various advantages, the E5 broadband signal has a large bandwidth of about 50MHz [70], which makes the code noise significantly smaller than that of GPS. The E5a and E5b signals together share the E5 band, where low-cost receivers can use a single band. Two QPSK(10) signals are generated coherently and transmitted on the E5a and E5b bands, while the E5 signal have alternate BOC (AltBOC) modulation. The AltBOC modulation multiplies the base-band signal by a complex rectangular subcarrier, and instead of splitting it shifts the signal spectrum to higher or lower frequencies [71].

[1] BOC(m, n) denotes the Binary Offset Carrier modulation with a subcarrier frequency m and a code rate n

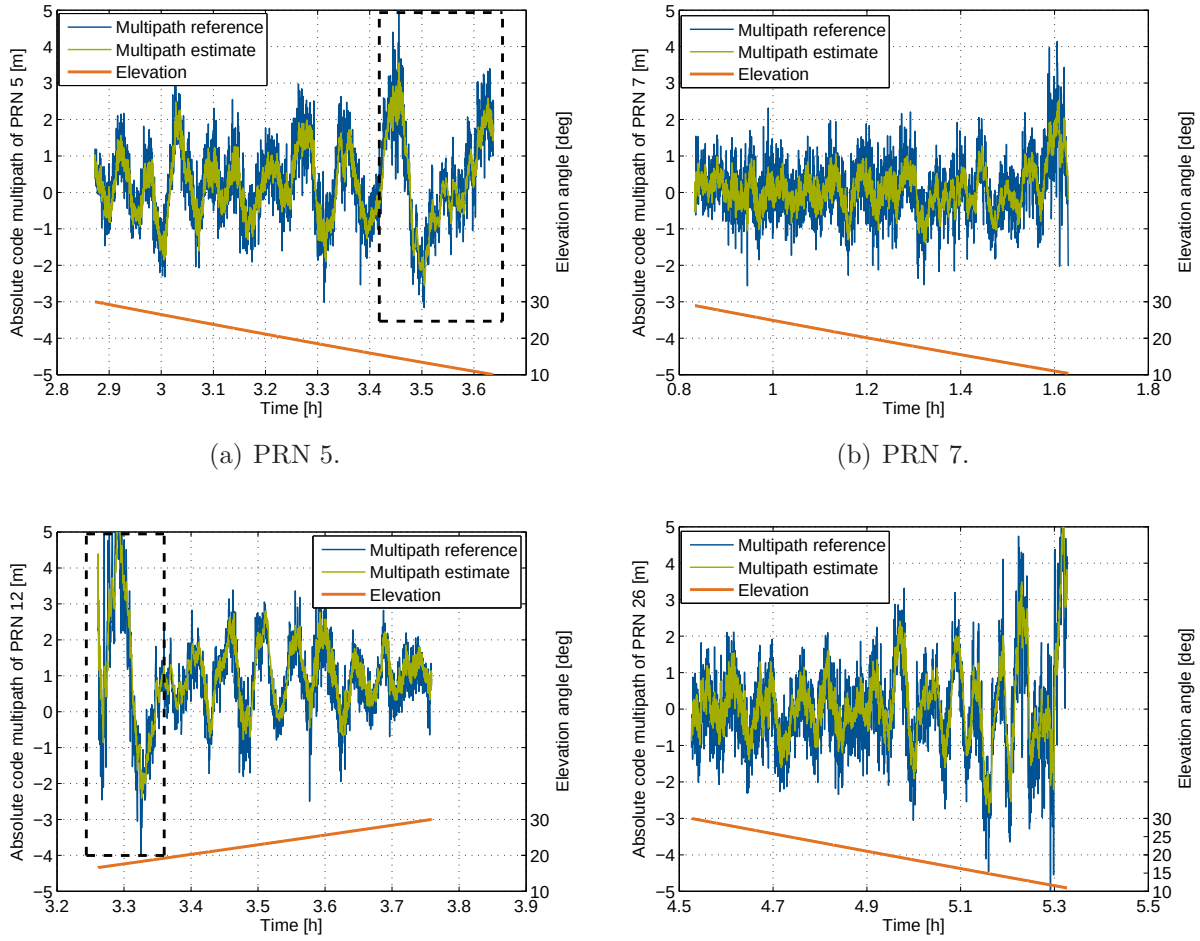

(a) PRN 5.

(b) PRN 7.

(c) PRN 12.

(d) PRN 26.

Figure 2.19: Comparison between the multipath estimates and the reference. The code multipath and the elevation angle are plotted at the left and the right side respectively. The large variation of PRN 12 over 5 m has most likely caused the deviation of the position solution in Fig. 2.18(a).

Signal	Carrier frequency (MHz)	Receiver reference bandwidth (MHz)	Modulation
E1	$154 \cdot 10.23$	$24 \cdot 1.023$	BOC(1,1)
E5a	$115 \cdot 10.23$	$25 \cdot 1.023$	QPSK(10)
E5b	$118 \cdot 10.23$	$25 \cdot 1.023$	QPSK(10)
E5	$116.5 \cdot 10.23$	$50 \cdot 1.023$	AltBOC(15,10)

Table 2.5: Overview of Galileo open service signals [70, 71].

An inter-system bias must be considered when both navigation systems are employed. For this purpose, we assign different receiver clock offsets for GPS and Galileo measurements respectively. The measurement model for the code and phase measurements from

GPS and Galileo on two frequencies is expressed by

$$\begin{bmatrix} \lambda_{\mathrm{L1}}\Delta\boldsymbol{\varphi}_{\mathrm{L1}} \\ \lambda_{\mathrm{L2}}\Delta\boldsymbol{\varphi}_{\mathrm{L2}} \\ \lambda_{\mathrm{E1}}\Delta\boldsymbol{\varphi}_{\mathrm{E1}} \\ \lambda_{\mathrm{E5}}\Delta\boldsymbol{\varphi}_{\mathrm{E5}} \\ \Delta\boldsymbol{\rho}_{\mathrm{L1}} \\ \Delta\boldsymbol{\rho}_{\mathrm{L2}} \\ \Delta\boldsymbol{\rho}_{\mathrm{E1}} \\ \Delta\boldsymbol{\rho}_{\mathrm{E5}} \end{bmatrix} = [\boldsymbol{H}_e,\ \boldsymbol{H}_{c\delta},\ \boldsymbol{H}_{T_{\mathrm{z}}},\ \boldsymbol{H}_I,\ \boldsymbol{H}_{\tilde{N}}] \cdot \begin{bmatrix} \vec{\boldsymbol{r}} \\ c\delta_{\mathrm{G}} \\ c\delta_{\mathrm{E}} \\ T_{\mathrm{z}} \\ \boldsymbol{I}_{\mathrm{L1}} \\ \boldsymbol{I}_{\mathrm{E1}} \\ \tilde{\boldsymbol{N}}_{\mathrm{L1}} \\ \tilde{\boldsymbol{N}}_{\mathrm{L2}} \\ \tilde{\boldsymbol{N}}_{\mathrm{E1}} \\ \tilde{\boldsymbol{N}}_{\mathrm{E5}} \end{bmatrix} + \begin{bmatrix} \boldsymbol{\varepsilon}_{\mathrm{L1}} \\ \boldsymbol{\varepsilon}_{\mathrm{L2}} \\ \boldsymbol{\varepsilon}_{\mathrm{E1}} \\ \boldsymbol{\varepsilon}_{\mathrm{E5}} \\ \boldsymbol{\eta}_{\mathrm{L1}} \\ \boldsymbol{\eta}_{\mathrm{L2}} \\ \boldsymbol{\eta}_{\mathrm{E1}} \\ \boldsymbol{\eta}_{\mathrm{E5}} \end{bmatrix}, \tag{2.88}$$

with index G and E denoting the GPS and Galileo systems respectively. The ambiguity vector $\tilde{\boldsymbol{N}}$ contains also the phase biases, and thus is estimated as a real-valued parameter vector. The last term denotes the vector for the measurement noise, which is modelled as white Gaussian noise with standard deviations depending on the elevations.

The design matrices are given by

$$\begin{aligned}
&\boldsymbol{H}_e = \mathbf{I}_2 \otimes \begin{bmatrix} \mathbf{I}_2 \otimes \boldsymbol{H}_{e,\mathrm{G}} \\ \mathbf{I}_2 \otimes \boldsymbol{H}_{e,\mathrm{E}} \end{bmatrix},\ \boldsymbol{H}_{e,\mathrm{G}} = \begin{bmatrix} (\vec{\boldsymbol{e}}_{\mathrm{G}}^{\,1})^{\mathrm{T}} \\ \vdots \\ (\vec{\boldsymbol{e}}_{\mathrm{G}}^{\,K_{\mathrm{G}}})^{\mathrm{T}} \end{bmatrix},\ \boldsymbol{H}_{e,\mathrm{E}} = \begin{bmatrix} (\vec{\boldsymbol{e}}_{\mathrm{E}}^{\,1})^{\mathrm{T}} \\ \vdots \\ (\vec{\boldsymbol{e}}_{\mathrm{E}}^{\,K_{\mathrm{E}}})^{\mathrm{T}} \end{bmatrix}, \\
&\boldsymbol{H}_{c\delta} = \mathbf{I}_2 \otimes \begin{bmatrix} \mathbf{I}_{2K_{\mathrm{G}}} & \mathbf{0}_{2K_{\mathrm{G}}\times 1} \\ \mathbf{0}_{2K_{\mathrm{E}}\times 1} & \mathbf{I}_{2K_{\mathrm{E}}} \end{bmatrix}, \\
&\boldsymbol{H}_{T_{\mathrm{z}}} = \mathbf{I}_2 \otimes \begin{bmatrix} \mathbf{I}_2 \otimes \boldsymbol{m}_{\mathrm{T,G}} \\ \mathbf{I}_2 \otimes \boldsymbol{m}_{\mathrm{T,E}} \end{bmatrix},\ \boldsymbol{m}_{\mathrm{T,G}} = \begin{bmatrix} m_{\mathrm{T,G}}^{1} \\ \vdots \\ m_{\mathrm{T,G}}^{K_{\mathrm{G}}} \end{bmatrix},\ \boldsymbol{m}_{\mathrm{T,E}} = \begin{bmatrix} m_{\mathrm{T,E}}^{1} \\ \vdots \\ m_{\mathrm{T,E}}^{K_{\mathrm{E}}} \end{bmatrix}, \\
&\boldsymbol{H}_{\boldsymbol{I}} = \begin{bmatrix} -1 \\ 1 \end{bmatrix} \otimes \begin{bmatrix} \left[1, \frac{f_{\mathrm{L1}}^2}{f_{\mathrm{L2}}^2}\right]^{\mathrm{T}} \otimes \mathbf{1}_{K_{\mathrm{G}}} & \mathbf{0}_{2K_{\mathrm{G}}\times K_{\mathrm{E}}} \\ \mathbf{0}_{2K_{\mathrm{E}}\times K_{\mathrm{G}}} & \left[1, \frac{f_{\mathrm{E1}}^2}{f_{\mathrm{E5}}^2}\right]^{\mathrm{T}} \otimes \mathbf{1}_{K_{\mathrm{E}}} \end{bmatrix}, \\
&\boldsymbol{H}_{\tilde{\boldsymbol{N}}} = \begin{bmatrix} 1 \\ 0 \end{bmatrix} \otimes \begin{bmatrix} \begin{bmatrix} \lambda_{\mathrm{L1}} & 0 \\ 0 & \lambda_{\mathrm{L2}} \end{bmatrix} \otimes \mathbf{1}_{K_{\mathrm{G}}} & \mathbf{0}_{2K_{\mathrm{G}}\times 2K_{\mathrm{E}}} \\ \mathbf{0}_{2K_{\mathrm{E}}\times 2K_{\mathrm{G}}} & \begin{bmatrix} \lambda_{\mathrm{E1}} & 0 \\ 0 & \lambda_{\mathrm{E5}} \end{bmatrix} \otimes \mathbf{1}_{K_{\mathrm{E}}} \end{bmatrix},
\end{aligned} \tag{2.89}$$

where K_{G} and K_{E} denote the number of visible GPS and Galileo satellites respectively, $\mathbf{I}$ denotes an all-1s vector, and $\mathbf{1}$ denotes an identity matrix. The vectors $\boldsymbol{m}_{\mathrm{T,G}}$ and $\boldsymbol{m}_{\mathrm{T,E}}$ stack the tropospheric mapping functions for the GPS and Galileo satellites.

Similarly as GPS, the precise Galileo satellite orbit shall be corrected. The reference point of the orbit is provided to the center of mass. Therefore the phase center offsets for the Galileo satellites are required to obtain the positions of phase centers. It is noted by the IGS Multi-GNSS Experiment (MGEX) in [72] that, a set of conventional PCO values of $[0.2\,\mathrm{m}, 0, 0.6\,\mathrm{m}]$ in satellite local coordinate frame is adopted for all Galileo satellites due to a lack of publicly available information.

	$\sigma_{\rho,\mathrm{G}}$	$\sigma_{\rho,\mathrm{E}}$	$\sigma_{\varphi,\mathrm{G}}$	$\sigma_{\varphi,\mathrm{E}}$
$E = 15°$	1.2 m	0.3 m	0.05 m	0.01 m
$E = 75°$	0.4 m	0.1 m	0.01 m	0.002 m

Table 2.6: Measurement noise assumptions for the GPS L1/L2 and Galileo E1/E5a signals.

Real GPS L1/L2, and Galileo E1/E5a measurements have been collected from a geodetic station *dlf1* for continuous 24 hours on August 3rd, 2013. The data epoch interval is 30 seconds. The assumptions for the standard deviations of the measurement noise are presented in Table 2.6, where the values for the Galileo measurements refer to some experimental data from Mishukova in [73]. The states are assumed to follow random-walk processes in the Kalman filter, with the following standard deviations assumed for the process noise: 1 cm for the receiver position, 1 m for the receiver clocks, 5 mm for the tropospheric zenith delay, 0.2 m for the slant ionospheric delay, and 1 millicycle for the ambiguities.

Fig. 2.20(a) shows the satellite visibility from each system, where a maximum of 13 GPS satellites are visible and all available Galileo satellites at the moment can be observed. The different receiver clock offset estimates are depicted in Fig. 2.20(b). The estimates show similar trends however the offset is not linear but varies under 20 cm.

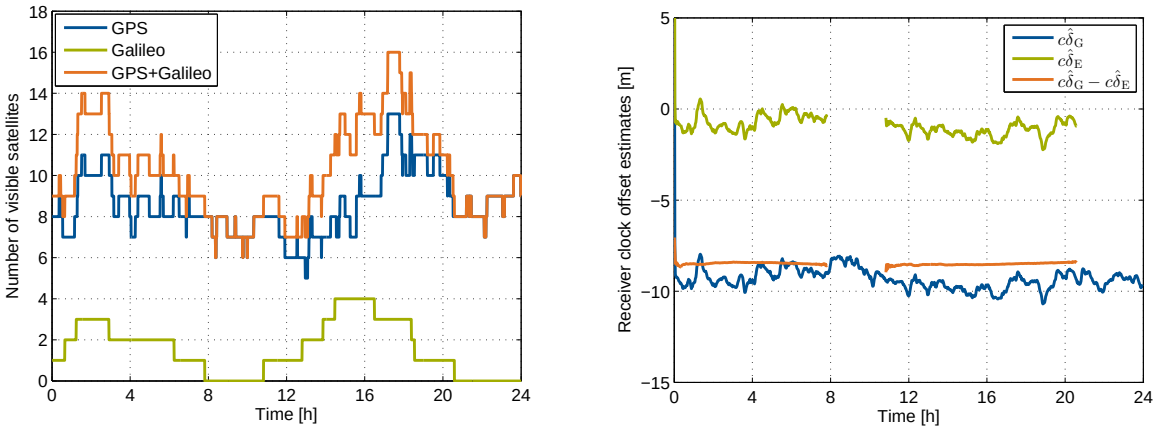

(a) Number of visible satellites with an elevation mask being 10°.

(b) Different clock estimates are assigned for both systems, which show similar but not identical variations with difference under 20 cm.

Figure 2.20: Satellite visibility and receiver clock offset estimates over 24 hours.

Benefit of the combined system on the positioning errors is shown in Fig. 2.21, The process noise in the Kalman filter has been kept the same for both scenarios, while the only difference comes from the inclusion of Galileo measurements. All three directions have reached slightly better accuracies with smaller variations on the east and up component. One reason for the limited improvement could be due to the available Galileo satellites are minority compared to GPS. Nevertheless, the errors on the east and up components are reduced by 5 to 10 cm, when the total number of satellites reaches 16 at around hour 17 to 18.

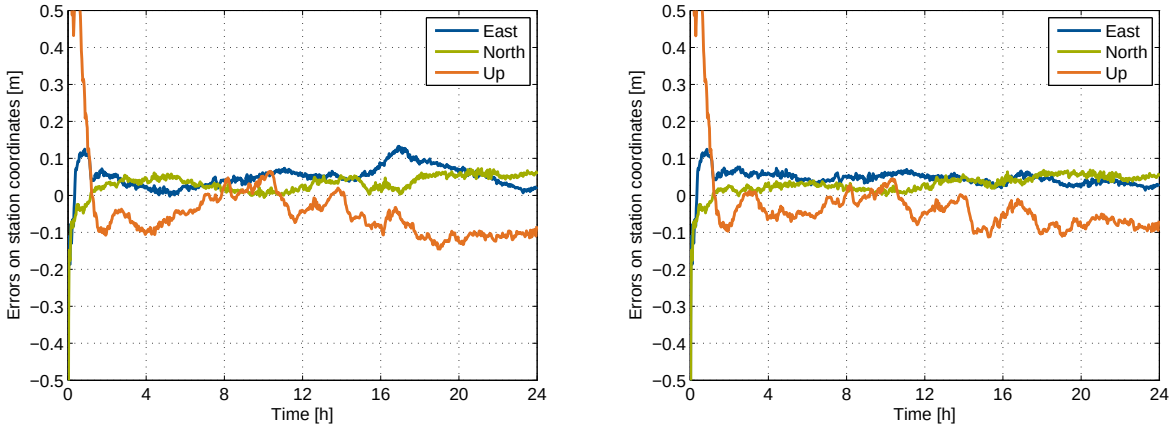

(a) PPP with GPS-only.

(b) PPP with GPS and Galileo.

Figure 2.21: Comparison of positioning errors using PPP with GPS-only and with GPS and Galileo. A slightly better performance is observed in the east and up directions after 15:00, where the number of Galileo satellites reached maximum.

2.4 Conclusions

First, major error sources in precise point positioning that are above centimeter-level were presented in section 2.1. A summary table with descriptions can be found in section 2.1.4. Next, a widely used PPP approach applying ionosphere-free combinations was introduced. A new PPP algorithm using uncombined measurements was then proposed in this chapter. This algorithm is easily applicable for multi-frequency measurements. The positioning accuracy can be improved by using the property that the troposphere changes slowly over time. This is specifically implemented by reducing the update rate of the tropospheric state to $1/5\,\mathrm{min}^{-1}$. A further improvement is to include a subset of code multipath in the state vector. Results with real GPS measurements have shown the code multipath estimates followed precisely the multipath pattern from their references (from combination of raw measurements). Thus, large deviations of position estimates were removed.

Until now, the phase ambiguities are estimated as float ones, which means the integer property of the ambiguities is not exploited. Estimating the ambiguities requires a precise knowledge of the biases. As a consequence, we will focus on the bias estimation which will enable the separation of the integer ambiguities and the float biases.

Chapter 3

Estimation of Phase and Code Biases Using Cascaded Kalman Filters

Precise positioning with centimeter-level accuracy requires integer ambiguity resolution. In order to fix the ambiguities into integers using absolute measurements, the phase biases are required to be known precisely. Errors in the phase biases would project into errors in the ambiguity estimates, which affects directly the position solution.

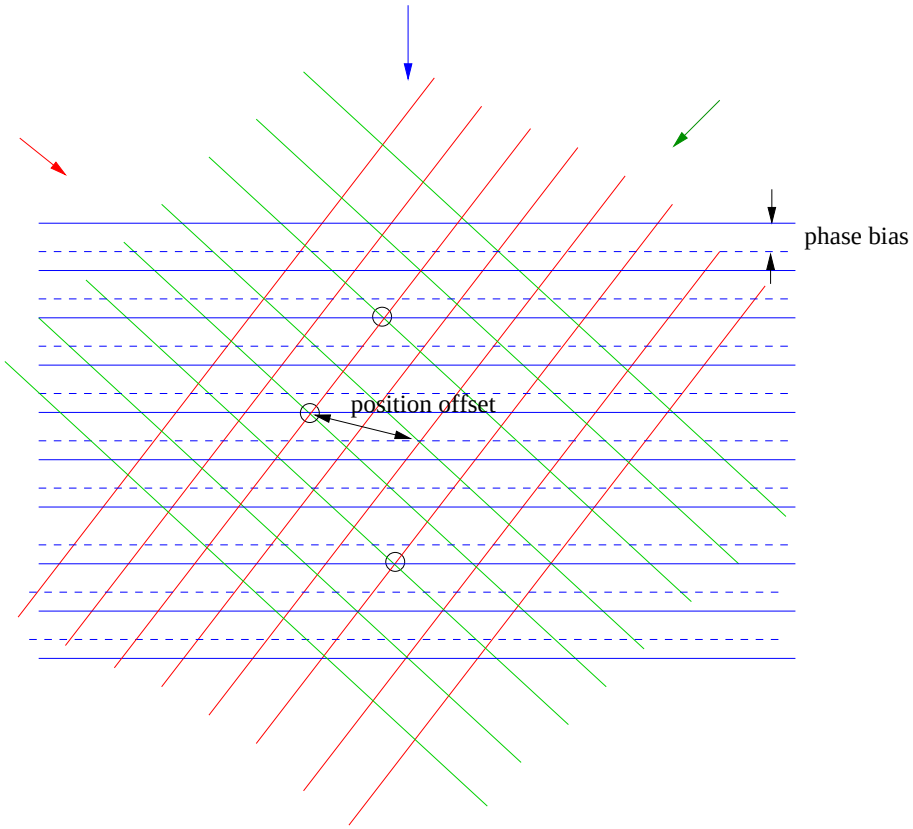

Figure 3.1: A simplified positioning scenario with three signals, whose intersections indicate best position estimates [74]. Carrier phase offsets results in different ambiguity resolutions, and subsequently in different position estimates.

A simplified example is shown in Fig. 3.1. Three satellite signals are received from different directions, where the wavefronts of the carrier phase signals are depicted with solid lines. Possible position estimates are indicated in circles, which are obtained by

finding intersections of the wavefronts. Now assume the signal in blue has a phase offset, i.e. the new wavefronts are displayed with dashed lines. The intersection of the two signals and the phase bias shifted signal gives the position estimate in the center of the figure. The phase bias offset is now transformed to an offset of the position estimate, resulting from different resolutions of the ambiguities from the signals. It is intuitively seen from this example that, precise phase bias information is essential for precise positioning using absolute measurements. Besides, code biases are also to be known to precise model code measurements, to ultimately help ambiguity resolution.

The phase and code biases are commonly assumed to be separated into satellite and receiver phase and code biases [1]. This separation reduces the link-dependency of the biases to satellite- and receiver-dependencies (the number of bias parameters drop from the multiplication of number of receivers and satellites to the sum of them). Furthermore, not all satellite biases are observable. There remains one degree of freedom, where a reference bias shall be chosen. This reference can be a satellite bias, or a receiver bias, or a combination of biases.

Gabor and Nerem [75] and Ge et al. [10] have proposed a method to estimate L1 and L2 satellite-satellite single difference (SD) phase biases. The wide-lane and narrow-lane combinations were applied. This approach has the disadvantage that the obtained bias estimates are only applicable to narrow-lane ionosphere-free linear combination with a wavelength of at most 10.7 cm.

This chapter proposes the estimation of phase and code biases in two-stage Kalman filters. A set of mathematical transformations is performed to achieve a full-rank measurement system. This chapter presents a sidereal filtering technique, which strongly suppresses code multipath. Bryson's method is introduced to decorrelate the measurements for the second-stage Kalman filter. Finally, real GPS data is applied to analyze the algorithm.

Cascaded Kalman filters are introduced, in order to shorten convergence time and help the ambiguity fixing. In the first stage the phase biases and the ambiguities are estimated, while the float ambiguity estimates are fixed sequentially based on the actual deviation to the integer values. In the second stage, the geometric state estimates from the first stage are used as measurements, which need to be decoupled due to the correlation over time.

3.1 Measurement Model and Parameter Mappings

The geometric term g_r^k is defined as

$$g_r^k = \left\| (\vec{\boldsymbol{r}}_r + \Delta\vec{\boldsymbol{r}}_{r,\mathrm{et}}) - \vec{\boldsymbol{r}}^{\,k} \right\| + c\delta_r - c\delta^k + m_{\mathrm{T},r}^k T_{\mathrm{z},r}. \tag{3.1}$$

It includes the non-frequency dependent variables, i.e. the geometric range, the receiver and satellite clock offsets, and the tropospheric delay. Introducing the geometric term into Eq. (1.1), the model for the code and phase measurements on two frequencies is given by

$$\begin{aligned}
\rho_{1,r}^k &= g_r^k + \quad I_{1,r}^k + b_{1,r} + b_1^k + \eta_{1,r}^k, \\
\rho_{2,r}^k &= g_r^k + \frac{f_1^2}{f_2^2} I_{1,r}^k + b_{2,r} + b_2^k + \eta_{2,r}^k, \\
\lambda_1 \varphi_{1,r}^k &= g_r^k - \quad I_{1,r}^k + \lambda_1 (N_{1,r}^k + \beta_{1,r} + \beta_1^k) + \varepsilon_{1,r}^k
\end{aligned}$$

$$\lambda_2 \varphi_{2,r}^k = g_r^k - \frac{f_1^2}{f_2^2} I_{1,r}^k + \lambda_2 (N_{2,r}^k + \beta_{2,r} + \beta_2^k) + \varepsilon_{2,r}^k, \tag{3.2}$$

where multipath errors are included in the code and phase noise. It is not feasible to estimate all biases in Eq. (3.2), as the system of equations is under-determined. Thus, a set of parameter mappings is proposed to remove the rank-deficiency.

In the first step, the code biases are split into geometric and ionospheric components, denoted by the indices g and I, i.e.

$$b_{m,r} = b_{\mathrm{g},r} + q_{1m}^2 b_{\mathrm{I},r}, \quad b_m^k = b_{\mathrm{g}}^k + q_{1m}^2 b_{\mathrm{I}}^k, \tag{3.3}$$

with $r \in \{1, \ldots, R\}$, $k \in \{1, \ldots, K\}$, $q_{1m} = f_1 / f_m$ being the frequency ratio, R and K being the total number of receivers and satellites. The geometric code biases are absorbed in the receiver and satellite clock offsets, while the ionospheric code biases are mapped into slant ionospheric delays.

$$\begin{aligned} c\tilde{\delta}_r &= c\delta_r + b_{\mathrm{g},r}, \quad c\tilde{\delta}^k = c\delta^k - b_{\mathrm{g}}^k, \\ \tilde{I}_{1,r}^k &= I_{1,r}^k + b_{\mathrm{I},r} + b_{\mathrm{I}}^k. \end{aligned} \tag{3.4}$$

A new geometric term is formed by bringing in the new definitions $c\tilde{\delta}_r$ and $c\tilde{\delta}^k$, i.e.

$$\tilde{g}_r^k = g_r^k + b_{\mathrm{g},r} + b_{\mathrm{g}}^k. \tag{3.5}$$

Since the new geometric and ionospheric terms appear in the phase measurements as well, the phase equation now becomes

$$\lambda_m \varphi_{m,r}^k = \tilde{g}_r^k - \frac{f_1^2}{f_m^2} \tilde{I}_{1,r}^k - b_{\mathrm{g},r} - b_{\mathrm{g}}^k + \frac{f_1^2}{f_m^2} (b_{\mathrm{I},r} + b_{\mathrm{I}}^k) + \lambda_m (N_{m,r}^k + \beta_{m,r} + \beta_m^k) + \varepsilon_{m,r}^k. \tag{3.6}$$

The phase measurements can be compensated by defining

$$\lambda_m \tilde{\beta}_{m,r} = \lambda_m \beta_{m,r} - b_{\mathrm{g},r} + q_{1m}^2 b_{\mathrm{I},r}, \quad \lambda_m \tilde{\beta}_m^k = \lambda_m \beta_m^k - b_{\mathrm{g}}^k + q_{1m}^2 b_{\mathrm{I}}^k. \tag{3.7}$$

In the second step, the rank-deficiency is removed from the pairs of receiver and satellite biases/clock offsets. There are different possibilities to solve this, e.g. IGS constraints that the sum of the satellite biases/clock offsets equals to zero [22]. In this work, one of the satellite biases/clock offsets is mapped to the receiver parts and subtracted from other satellite biases/clock offsets, i.e.

$$\begin{aligned} \tilde{\tilde{\beta}}_{m,r} &= \tilde{\beta}_{m,r} + \tilde{\beta}_m^\ell, \quad \tilde{\tilde{\beta}}_m^k = \tilde{\beta}_m^k - \tilde{\beta}_m^\ell, \\ c\tilde{\tilde{\delta}}_r &= c\tilde{\delta}_r + c\tilde{\delta}^\ell, \quad c\tilde{\tilde{\delta}}^k = c\tilde{\delta}^k - c\tilde{\delta}^\ell, \end{aligned} \tag{3.8}$$

with $k \in \{1, \ldots, K\}$, $k \neq \ell$, and satellite ℓ being the reference satellite.

Last but not least, the remaining rank-deficiency lies between the phase biases and the ambiguities. We denote the receiver and satellite phase biases and the ambiguities in vector forms, as $\tilde{\tilde{\boldsymbol{\beta}}}_{\mathrm{R}}$, $\tilde{\tilde{\boldsymbol{\beta}}}^{\mathrm{K}}$ and $\boldsymbol{N}$ after the second-step mapping. For simplicity, we take an

example of a network of R stations with K common satellites in view. The vectors before the third-step mapping are constructed as

$$\begin{aligned}
\tilde{\tilde{\boldsymbol{\beta}}}_{\mathrm{R}} &= \left[\tilde{\tilde{\beta}}_{1,1}, \ldots, \tilde{\tilde{\beta}}_{1,R},\ \tilde{\tilde{\beta}}_{2,1}, \ldots, \tilde{\tilde{\beta}}_{2,R}\right]^{\mathrm{T}} \\
\tilde{\tilde{\boldsymbol{\beta}}}^{\mathrm{K}} &= \left[\tilde{\tilde{\beta}}_1^1, \ldots, \tilde{\tilde{\beta}}_1^{\ell-1},\ \tilde{\tilde{\beta}}_1^{\ell+1}, \ldots, \tilde{\tilde{\beta}}_1^K, \tilde{\tilde{\beta}}_2^1, \ldots, \tilde{\tilde{\beta}}_2^{\ell-1},\ \tilde{\tilde{\beta}}_2^{\ell+1}, \ldots, \tilde{\tilde{\beta}}_2^K\right]^{\mathrm{T}} \\
\boldsymbol{N} &= \left[N_{1,1}^1, \ldots,\ N_{1,1}^K, \ldots,\ N_{1,R}^K,\ N_{2,1}^1, \ldots,\ N_{2,R}^K\right]^{\mathrm{T}}.
\end{aligned} \tag{3.9}$$

To have a better understanding, we only focus on the sub-system involving the phase biases and ambiguities, the phase measurement equation is thus simplified as

$$\lambda\boldsymbol{\varphi} = \ldots + \boldsymbol{H}_{\tilde{\tilde{\boldsymbol{\beta}}}_R}\tilde{\tilde{\boldsymbol{\beta}}}_{\mathrm{R}} + \boldsymbol{H}_{\tilde{\tilde{\boldsymbol{\beta}}}^K}\tilde{\tilde{\boldsymbol{\beta}}}^{\mathrm{K}} + \boldsymbol{H}_{\boldsymbol{N}}\boldsymbol{N} + \ldots, \tag{3.10}$$

where $\boldsymbol{H}_{\tilde{\tilde{\boldsymbol{\beta}}}_R}$, $\boldsymbol{H}_{\tilde{\tilde{\boldsymbol{\beta}}}^K}$ and $\boldsymbol{H}_{\boldsymbol{N}}$ are the coefficient matrices for phase biases and ambiguities. The measurement vector $\lambda\boldsymbol{\varphi}$ is expressed by

$$\lambda\boldsymbol{\varphi} = \left[\lambda_1\varphi_{1,1}^1, \ldots, \lambda_1\varphi_{1,1}^K, \ldots, \lambda_1\varphi_{1,R}^K, \ldots, \lambda_2\varphi_{2,R}^K\right]^{\mathrm{T}}. \tag{3.11}$$

The coefficient matrices are correspondingly obtained as

$$\begin{aligned}
\boldsymbol{H}_{\tilde{\tilde{\boldsymbol{\beta}}}_{\mathrm{R}}} &= \begin{bmatrix} \lambda_1 & 0 \\ 0 & \lambda_2 \end{bmatrix} \otimes \left[\mathbf{1}_R \otimes \mathbf{I}_K\right], \\
\boldsymbol{H}_{\tilde{\tilde{\boldsymbol{\beta}}}^{\mathrm{K}}} &= \begin{bmatrix} \lambda_1 & 0 \\ 0 & \lambda_2 \end{bmatrix} \otimes \left[\mathbf{I}_R \otimes \begin{bmatrix} \mathbf{1}_{(\ell-1)} & \mathbf{0}_{(\ell-1)\times(K-\ell)} \\ \mathbf{0}_{1\times(\ell-1)} & \mathbf{0}_{1\times(K-\ell)} \\ \mathbf{0}_{(K-l)\times(\ell-1)} & \mathbf{1}_{(K-\ell)} \end{bmatrix}\right], \\
\boldsymbol{H}_{\boldsymbol{N}} &= \begin{bmatrix} \lambda_1 & 0 \\ 0 & \lambda_2 \end{bmatrix} \otimes \mathbf{1}_s,
\end{aligned} \tag{3.12}$$

where $s = RK$ denotes the number of phase measurements on one frequency, $\mathbf{I}$ denotes an all-1s vector, and $\mathbf{1}$ denotes an identity matrix. The matrix $[\boldsymbol{H}_{\tilde{\tilde{\boldsymbol{\beta}}}_{\mathrm{R}}},\ \boldsymbol{H}_{\tilde{\tilde{\boldsymbol{\beta}}}^{\mathrm{K}}},\ \boldsymbol{H}_{\boldsymbol{N}}]$ is rank-deficient, because the matrix $\boldsymbol{H}_{\boldsymbol{N}}$ has already full rank. In order to obtain a full-rank system, a subset of at least $2R + 2(K-1)$ ambiguities needs to be mapped into the phase biases and other ambiguities. The selection of the subset and the mapping is realized through Gaussian Elimination, as described in [13] in details. The basic idea is to use elementary row operations to modify the design matrix into a reduced row-echelon form. The reduced row-echelon form reveals which ambiguities are linear dependent on others, and thus implies the mapping.

A numerical example is given below for an intuitive understanding with a reduced dimension of the network.

A numerical example

In order to visualize the third-step mapping, let us assume a minimal network with $R = 2$ receivers and $K = 2$ common satellites. The number of phase measurements s on each frequency and the number of phase biases s_b are given by

$$\begin{aligned}
s &= RK = 4, \\
s_b &= 2R + 2(K-1) = 6.
\end{aligned} \tag{3.13}$$

According to Eq. (3.9), the vectors $\tilde{\tilde{\boldsymbol{\beta}}}_{\mathrm{R}}$, $\tilde{\tilde{\boldsymbol{\beta}}}^{\mathrm{K}}$ and $\boldsymbol{N}$ are given by

$$\begin{aligned}
\tilde{\tilde{\boldsymbol{\beta}}}_{\mathrm{R}} &= \left[\tilde{\tilde{\beta}}_{1,1},\ \tilde{\tilde{\beta}}_{1,2},\ \tilde{\tilde{\beta}}_{2,1},\ \tilde{\tilde{\beta}}_{2,2}\right]^{\mathrm{T}}, \\
\tilde{\tilde{\boldsymbol{\beta}}}^{\mathrm{K}} &= \left[\tilde{\tilde{\beta}}^{2}_{1},\ \tilde{\tilde{\beta}}^{2}_{2}\right]^{\mathrm{T}}, \\
\boldsymbol{N} &= \left[N^{1}_{1,1},\ N^{2}_{1,1},\ N^{1}_{1,2},\ N^{2}_{1,2},\ N^{1}_{2,1},\ N^{2}_{2,1},\ N^{1}_{2,2},\ N^{2}_{2,2}\right]^{\mathrm{T}},
\end{aligned} \tag{3.14}$$

where the first satellite bias was mapped away. Gaussian Elimination is now applied on the design matrix $[\boldsymbol{H}_{\tilde{\tilde{\boldsymbol{\beta}}}_{\mathrm{R}}},\ \boldsymbol{H}_{\tilde{\tilde{\boldsymbol{\beta}}}^{\mathrm{K}}},\ \boldsymbol{H}_{\boldsymbol{N}}]$, to obtain a reduced row-echelon form. A permutation is performed in the last step, which splits the full-rank part and the dependent part $\boldsymbol{G}$. The linear coefficients in $\boldsymbol{G}$ can be used for re-constructing the mapped ambiguities later.

$$\boldsymbol{A}_1 = \left[\begin{array}{cccc|cc|cccccccc}
\lambda_1 & 0 & 0 & 0 & 0 & 0 & \lambda_1 & 0 & 0 & 0 & 0 & 0 & 0 & 0 \\
\lambda_1 & 0 & 0 & 0 & \lambda_1 & 0 & 0 & \lambda_1 & 0 & 0 & 0 & 0 & 0 & 0 \\
0 & \lambda_1 & 0 & 0 & 0 & 0 & 0 & 0 & \lambda_1 & 0 & 0 & 0 & 0 & 0 \\
0 & \lambda_1 & 0 & 0 & \lambda_1 & 0 & 0 & 0 & 0 & \lambda_1 & 0 & 0 & 0 & 0 \\
0 & 0 & \lambda_2 & 0 & 0 & 0 & 0 & 0 & 0 & 0 & \lambda_2 & 0 & 0 & 0 \\
0 & 0 & \lambda_2 & 0 & 0 & \lambda_2 & 0 & 0 & 0 & 0 & 0 & \lambda_2 & 0 & 0 \\
0 & 0 & 0 & \lambda_2 & 0 & 0 & 0 & 0 & 0 & 0 & 0 & 0 & \lambda_2 & 0 \\
0 & 0 & 0 & \lambda_2 & 0 & \lambda_2 & 0 & 0 & 0 & 0 & 0 & 0 & 0 & \lambda_2
\end{array}\right] \xrightarrow{\text{Gaussian Elimination}}$$

$$\boldsymbol{A}_2 = \left[\begin{array}{cccc|cc|cccccccc}
1^* & 0 & 0 & 0 & 0 & 0 & 0 & 1 & 1 & -1 & 0 & 0 & 0 & 0 \\
0 & 1^* & 0 & 0 & 0 & 0 & 0 & 0 & 1 & 0 & 0 & 0 & 0 & 0 \\
0 & 0 & 1^* & 0 & 0 & 0 & 0 & 0 & 0 & 0 & 0 & 1 & 1 & -1 \\
0 & 0 & 0 & 1^* & 0 & 0 & 0 & 0 & 0 & 0 & 0 & 0 & 1 & 0 \\
0 & 0 & 0 & 0 & 1^* & 0 & 0 & 0 & -1 & 1 & 0 & 0 & 0 & 0 \\
0 & 0 & 0 & 0 & 0 & 1^* & 0 & 0 & 0 & 0 & 0 & 0 & -1 & 1 \\
0 & 0 & 0 & 0 & 0 & 0 & 1^* & -1 & -1 & 1 & 0 & 0 & 0 & 0 \\
0 & 0 & 0 & 0 & 0 & 0 & 0 & 0 & 0 & 0 & 1^* & -1 & -1 & 1
\end{array}\right] \xrightarrow{\text{Permutation}}$$

$$\boldsymbol{A}_3 = \left[\begin{array}{cccc|cc|cccccccc}
1^* & 0 & 0 & 0 & 0 & 0 & 0 & 0 & 1 & 1 & -1 & 0 & 0 & 0 \\
0 & 1^* & 0 & 0 & 0 & 0 & 0 & 0 & 0 & 1 & 0 & 0 & 0 & 0 \\
0 & 0 & 1^* & 0 & 0 & 0 & 0 & 0 & 0 & 0 & 0 & 1 & 1 & -1 \\
0 & 0 & 0 & 1^* & 0 & 0 & 0 & 0 & 0 & 0 & 0 & 0 & 1 & 0 \\
0 & 0 & 0 & 0 & 1^* & 0 & 0 & 0 & 0 & -1 & 1 & 0 & 0 & 0 \\
0 & 0 & 0 & 0 & 0 & 1^* & 0 & 0 & 0 & 0 & 0 & 0 & -1 & 1 \\
0 & 0 & 0 & 0 & 0 & 0 & 1^* & 0 & -1 & -1 & 1 & 0 & 0 & 0 \\
0 & 0 & 0 & 0 & 0 & 0 & 0 & 1^* & 0 & 0 & 0 & -1 & -1 & 1
\end{array}\right]. \tag{3.15}$$

The pivot 1s from Gaussian Elimination are marked with asterisks. The matrix $\boldsymbol{A}_2$ suggests that the ambiguities $N^1_{1,1}$ and $N^1_{2,1}$ form a full-rank system with the phase biases, while the other ambiguities have to be mapped into the full-rank set of states. The new states are thus obtained as

$$\begin{aligned}
\tilde{\tilde{\beta}}_{1,1} &= \tilde{\tilde{\beta}}_{1,1} + N^2_{1,1} + N^1_{1,2} - N^2_{1,2}, \quad & \tilde{\tilde{\beta}}_{1,2} &= \tilde{\tilde{\beta}}_{1,2} + N^1_{1,2}, \\
\tilde{\tilde{\beta}}_{2,1} &= \tilde{\tilde{\beta}}_{2,1} + N^2_{2,1} + N^1_{2,2} - N^2_{2,2}, \quad & \tilde{\tilde{\beta}}_{2,2} &= \tilde{\tilde{\beta}}_{2,2} + N^1_{1,2},
\end{aligned}$$

$$\begin{aligned}
\tilde{\tilde{\beta}}_1^2 &= \tilde{\beta}_1^2 \; - N_{1,2}^1 + N_{1,2}^2, & \tilde{\tilde{\beta}}_2^2 &= \tilde{\beta}_2^2 \; - N_{2,2}^1 + N_{2,2}^2 \\
\tilde{N}_{1,1}^1 &= N_{1,1}^1 - N_{1,1}^2 - N_{1,2}^1 + N_{1,2}^2, & \tilde{N}_{2,1}^1 &= N_{2,1}^1 - N_{2,1}^2 - N_{2,2}^1 + N_{2,2}^2.
\end{aligned} \tag{3.16}$$

To generalize the Gaussian Elimination and the permutation, the reduced row-echelon form $\boldsymbol{A}_3$ is expressed by

$$\boldsymbol{A}_3 = \begin{bmatrix} \mathbf{1}_{\,s_b} & \mathbf{0}_{\,s_b\times(2s-s_b)} & \boldsymbol{G}_{\,(2s)\times s_b} \\ \mathbf{0}_{\,(2s-s_b)\times s_b} & \mathbf{1}_{\,(2s-s_b)} & \end{bmatrix} = \boldsymbol{A}_2\boldsymbol{P}, \tag{3.17}$$

with $s_b = 2R + 2(K-1)$ being the number of the phase biases. The upper left identity matrix represents the phase biases. The ambiguities are re-ordered by the permutation matrix $\boldsymbol{P}$ so that the full-rank ones come first as the middle part, while the coefficient matrix $\boldsymbol{G}$ appears last. The matrix $\boldsymbol{P}$ has the form of

$$\boldsymbol{P} = \begin{bmatrix} \mathbf{1}_{\,s_b} & \mathbf{0}_{s_b\times(2s)} \\ \mathbf{0}_{(2s)\times s_b} & \boldsymbol{P}_N \end{bmatrix}, \tag{3.18}$$

where the phase biases always have full-rank, and $\boldsymbol{P}_N$ denotes the sub-permutation matrix for the ambiguities. In the case above, $\boldsymbol{P}_N$ is given by

$$\boldsymbol{P}_N = \begin{bmatrix} 1 & 0 & 0 & 0 & 0 & 0 & 0 & 0 \\ 0 & 0 & 1 & 0 & 0 & 0 & 0 & 0 \\ 0 & 0 & 0 & 1 & 0 & 0 & 0 & 0 \\ 0 & 0 & 0 & 0 & 1 & 0 & 0 & 0 \\ 0 & 1 & 0 & 0 & 0 & 0 & 0 & 0 \\ 0 & 0 & 0 & 0 & 0 & 1 & 0 & 0 \\ 0 & 0 & 0 & 0 & 0 & 0 & 1 & 0 \\ 0 & 0 & 0 & 0 & 0 & 0 & 0 & 1 \end{bmatrix}. \tag{3.19}$$

In general, the full-rank ambiguity vector $\boldsymbol{N}_{\text{full}}$ and the linear dependent part $\boldsymbol{N}_{\text{sub}}$ are obtained from

$$\begin{aligned}
\boldsymbol{N}_{\text{full}} &= \left[\mathbf{1}_{\,(2s-s_b)},\;\; \mathbf{0}_{\,(2s-s_b)\times s_b}\right] \cdot \boldsymbol{P}_N^{\mathrm{T}} \cdot \boldsymbol{N}, \\
\boldsymbol{N}_{\text{sub}} &= \left[\mathbf{0}_{\,s_b\times(2s-s_b)},\;\; \mathbf{1}_{\,s_b}\right] \cdot \boldsymbol{P}_N^{\mathrm{T}} \cdot \boldsymbol{N},
\end{aligned} \tag{3.20}$$

where the selection matrices in front of the matrix $\boldsymbol{P}_N^{\mathrm{T}}$ pick out the corresponding parts from the permutated ambiguity vector. The coefficient matrix $\boldsymbol{H}_{\tilde{\boldsymbol{N}}}$ for the full-rank ambiguity part $\boldsymbol{N}_{\text{full}}$ is correspondingly given by

$$\boldsymbol{H}_{\tilde{\boldsymbol{N}}} = \boldsymbol{H}_{\boldsymbol{N}} \cdot \boldsymbol{P}_N \cdot \left[\mathbf{1}_{\,(2s-s_b)},\;\; \mathbf{0}_{\,(2s-s_b)\times s_b}\right]^{\mathrm{T}}. \tag{3.21}$$

The new phase bias and ambiguity vectors, $\tilde{\tilde{\boldsymbol{\beta}}}_{\mathrm{R}}$, $\tilde{\tilde{\boldsymbol{\beta}}}^{\mathrm{K}}$ and $\tilde{\boldsymbol{N}}$, are obtained from

$$\begin{bmatrix} \tilde{\tilde{\boldsymbol{\beta}}}_{\mathrm{R}} \\ \tilde{\tilde{\boldsymbol{\beta}}}^{\mathrm{K}} \\ \tilde{\boldsymbol{N}} \end{bmatrix} = \begin{bmatrix} \tilde{\tilde{\boldsymbol{\beta}}}_{\mathrm{R}} \\ \tilde{\tilde{\boldsymbol{\beta}}}^{\mathrm{K}} \\ \boldsymbol{N}_{\text{full}} \end{bmatrix} + \boldsymbol{G} \cdot \boldsymbol{N}_{\text{sub}}. \tag{3.22}$$

Full-rank system model

After all steps of mappings, the full-rank system model for code and carrier phase measurements on two frequencies is given by

$$\begin{aligned}
\rho_{1,r}^k &= \tilde{g}_r^k + \quad \tilde{I}_{1,r}^k + \eta_{1,r}^k, \\
\rho_{2,r}^k &= \tilde{g}_r^k + \frac{f_1^2}{f_2^2}\tilde{I}_{1,r}^k + \eta_{2,r}^k, \\
\lambda_1\varphi_{1,r}^k &= \tilde{g}_r^k - \quad \tilde{I}_{1,r}^k + \lambda_1(\tilde{N}_{1,r}^k + \tilde{\tilde{\beta}}_{1,r} + \tilde{\tilde{\beta}}_1^k) + \varepsilon_{1,r}^k, \\
\lambda_2\varphi_{2,r}^k &= \tilde{g}_r^k - \frac{f_1^2}{f_2^2}\tilde{I}_{1,r}^k + \lambda_2(\tilde{N}_{2,r}^k + \tilde{\tilde{\beta}}_{2,r} + \tilde{\tilde{\beta}}_2^k) + \varepsilon_{2,r}^k.
\end{aligned} \tag{3.23}$$

Furthermore, if there exist measurements on a third frequency, the code biases on the additional frequency can be determined explicitly to one common reference, while the phase biases still absorb a subset of ambiguities by Gaussian Elimination, i.e.

$$\begin{aligned}
\rho_{3,r}^k &= \tilde{g}_r^k + \frac{f_1^2}{f_3^2}\tilde{I}_{1,r}^k + \tilde{b}_{3,r} + \tilde{b}_3^k + \eta_{3,r}^k, \\
\lambda_3\varphi_{3,r}^k &= \tilde{g}_r^k - \frac{f_1^2}{f_3^2}\tilde{I}_{1,r}^k + \lambda_3(\tilde{N}_{3,r}^k + \tilde{\tilde{\beta}}_{3,r} + \tilde{\tilde{\beta}}_3^k) + \varepsilon_{3,r}^k.
\end{aligned} \tag{3.24}$$

3.2 Estimation of Phase Biases

In this section, a first-stage Kalman filter is introduced to solve the full-rank model after the parameter mappings. The output of this stage include the geometric- and ionospheric estimates, the phase bias estimates and the ambiguity estimates. The algorithm is tested with real GPS data from regional and global reference networks.

3.2.1 The First-stage Kalman Filter

The geometric state $\tilde{g}_r^k$ is non-linear as it contains the true range between the satellite and the receiver. As a certain knowledge on the satellite orbits and clock offsets is known prior to the estimation, e.g. from the broadcast navigation message, the state space model for the geometric state can be simplified and better described. We thus correct beforehand the station coordinates $\vec{\boldsymbol{r}}_r$, the satellite orbits $\hat{\vec{\boldsymbol{r}}}^{\,k}$ and clock offsets $c\hat{\delta}^k$ from the geometric state and obtain

$$\Delta\tilde{g}_r^k = \tilde{g}_r^k - \left\| \vec{\boldsymbol{r}}_r - \hat{\vec{\boldsymbol{r}}}^{\,k} \right\| + c\hat{\delta}^k, \tag{3.25}$$

which is assumed to follow a second-order linear state space model as

$$\Delta\tilde{g}_r^k(t_n) = \Delta\tilde{g}_r^k(t_{n-1}) + \Delta t \cdot \Delta\dot{\tilde{g}}_r^k(t_{n-1}) + \frac{1}{2}\Delta t^2 \cdot \Delta\ddot{\tilde{g}}_r^k(t_{n-1}) + w_{\Delta\tilde{g}_r^k}(t_{n-1}), \tag{3.26}$$

where Δt denotes the epoch interval, and $w_{\Delta\tilde{g}_r^k}$ denotes the process noise.

We assume a simplified scenario to explain the setup of the Kalman filter, where a network of R stations observes K common satellites. The code and the phase measurements

subtract not only the range and the satellite clock offset, but also the phase center offsets and variations, the solid earth tides, and the phase wind-up effects before the estimation. The measurement vector $\boldsymbol{z}$ for the system of equations (3.23) thus reads

$$\boldsymbol{z} = \left[\rho_{1,1}^{1}, \ldots, \rho_{1,1}^{K}, \ldots, \rho_{1,R}^{K}, \ldots, \rho_{2,R}^{K}, \lambda_1\varphi_{1,1}^{1}, \ldots, \lambda_1\varphi_{1,R}^{K}, \ldots, \lambda_2\varphi_{2,R}^{K}\right]^{\mathrm{T}}. \tag{3.27}$$

The measurement noise $\boldsymbol{v}$ is assumed to be zero-mean Gaussian distributed and uncorrelated between different propagation links. The standard deviation is assumed to follow an exponential function of the elevation angle.

The state vector includes the modified geometric term and its first- and second-order derivatives, the ionospheric delay and its rate, the phase biases and the ambiguities, i.e.

$$\begin{aligned}\boldsymbol{x} = \Big(&\Delta\tilde{g}_1^1, \ldots, \Delta\tilde{g}_1^K, \ldots, \Delta\tilde{g}_R^K, \Delta\dot{\tilde{g}}_1^1, \ldots, \Delta\dot{\tilde{g}}_R^K, \Delta\ddot{\tilde{g}}_1^1, \ldots, \Delta\ddot{\tilde{g}}_R^K, \tilde{I}_1^1, \ldots, \tilde{I}_R^K, \dot{\tilde{I}}_1^1, \ldots, \dot{\tilde{I}}_R^K, \\ &\dddot{\tilde{\beta}}_1, \ldots, \dddot{\tilde{\beta}}_R, \dddot{\tilde{\beta}}^1, \ldots, \dddot{\tilde{\beta}}^{\ell-1}, \dddot{\tilde{\beta}}^{\ell+1}, \ldots \dddot{\tilde{\beta}}^K, \tilde{\boldsymbol{N}}^{\mathrm{T}}\Big)^{\mathrm{T}}.\end{aligned} \tag{3.28}$$

The $\boldsymbol{H}$ matrix can be easily obtained from Eq. (3.12), (3.21) and (3.23), while the state transition matrix $\boldsymbol{\Phi}$ is written as

$$\boldsymbol{\Phi} = \begin{bmatrix} \mathbf{1}_s & \Delta t \cdot \mathbf{1}_s & \frac{1}{2}\Delta t^2 \cdot \mathbf{1}_s & \mathbf{0} & \mathbf{0} & \mathbf{0} \\ \mathbf{0} & \mathbf{1}_s & \Delta t \cdot \mathbf{1}_s & \mathbf{0} & \mathbf{0} & \mathbf{0} \\ \mathbf{0} & \mathbf{0} & \mathbf{1}_s & \mathbf{0} & \mathbf{0} & \mathbf{0} \\ \mathbf{0} & \mathbf{0} & \mathbf{0} & \mathbf{1}_s & \Delta t \cdot \mathbf{1}_s & \mathbf{0} \\ \mathbf{0} & \mathbf{0} & \mathbf{0} & \mathbf{0} & \mathbf{1}_s & \mathbf{0} \\ \mathbf{0} & \mathbf{0} & \mathbf{0} & \mathbf{0} & \mathbf{0} & \mathbf{1}_{2s} \end{bmatrix}. \tag{3.29}$$

The process noise covariance matrix $\boldsymbol{\Sigma}_{\mathrm{Q}}$ for the process noise is given by

$$\boldsymbol{\Sigma}_{\mathrm{Q}} = \begin{bmatrix} \boldsymbol{\Sigma}_{\mathrm{Q},\Delta\tilde{g}\Delta\dot{\tilde{g}}\Delta\ddot{\tilde{g}}} & \mathbf{0} & \mathbf{0} & \mathbf{0} & \mathbf{0} \\ \mathbf{0} & \boldsymbol{\Sigma}_{\mathrm{Q},\tilde{I}\dot{\tilde{I}}} & \mathbf{0} & \mathbf{0} & \mathbf{0} \\ \mathbf{0} & \mathbf{0} & \sigma_{\dddot{\beta}_r}^2\mathbf{1} & \mathbf{0} & \mathbf{0} \\ \mathbf{0} & \mathbf{0} & \mathbf{0} & \sigma_{\dddot{\beta}^k}^2\mathbf{1} & \mathbf{0} \\ \mathbf{0} & \mathbf{0} & \mathbf{0} & \mathbf{0} & \sigma_N^2\mathbf{1} \end{bmatrix}, \tag{3.30}$$

where the standard deviations for the receiver and satellite phase biases as well as the ambiguities are denoted by $\sigma_{\dddot{\beta}_r}$, $\sigma_{\dddot{\beta}^k}$, and σ_N. The covariance sub-matrices for the geometry and the ionospheric parts are respectively calculated as

$$\Sigma_{\mathrm{Q},\Delta\tilde{g}\Delta\dot{\tilde{g}}\Delta\ddot{\tilde{g}}} = \sigma_{\Delta\ddot{\tilde{g}}}^2 \cdot \begin{bmatrix} \frac{1}{20}\Delta t^4 & \frac{1}{8}\Delta t^3 & \frac{1}{6}\Delta t^2 \\ \frac{1}{8}\Delta t^3 & \frac{1}{3}\Delta t^2 & \frac{1}{2}\Delta t \\ \frac{1}{6}\Delta t^2 & \frac{1}{2}\Delta t & 1 \end{bmatrix}, \quad \Sigma_{\mathrm{Q},\tilde{I}\dot{\tilde{I}}} = \sigma_{\dot{\tilde{I}}}^2 \cdot \begin{bmatrix} \frac{1}{3}\Delta t^2 & \frac{1}{2}\Delta t \\ \frac{1}{2}\Delta t & 1 \end{bmatrix}, \tag{3.31}$$

with $\sigma_{\Delta\ddot{\tilde{g}}}$ and $\sigma_{\dot{\tilde{I}}}$ being the standard deviations for the range-acceleration and the rate of ionospheric delay respectively. The detailed derivation is found in [13].

The initialization for the Kalman filter is performed by a least-squares estimation combining three epochs, in order to retrieve the first- and second-order of the geometric state estimates. The a priori state covariance matrix $\boldsymbol{P}^{-}$ is also calculated from the least-squares covariance matrix.

The integer property of the ambiguities needs to be exploited, as the bias estimation benefits from ambiguity fixings [13]. The Kalman filter often provides an optimistic a posteriori state covariance, which is only influenced by the model in Eq. (2.67) rather than real measurement. In fact, multipath could cause strong variation in the phase bias and ambiguity estimates. In this work, the float ambiguities are fixed in a sequential manner, where the fixing criterion takes into account both the standard deviation and the actual convergence of the ambiguity estimates [14]. A float ambiguity is fixed into integer, if the standard deviation is small enough and in the mean time the deviation from the float estimate to the integer number is below a threshold $\epsilon_{\tilde{N}}$ during a time window T, i.e.

$$\sum_{i=n-T+1}^{n} f\left(\hat{\tilde{N}}_{m,r}^{k,+}(t_i)\right) \geq T \cdot p, \tag{3.32}$$

where p denotes a probability ($0 < p \leq 1$) allowing a certain outlier in the time window. The function f accumulates if the actual deviation at one epoch fulfills the criterion, i.e.

$$f\left(\hat{\tilde{N}}_{m,r}^{k,+}(t_i)\right) = \begin{cases} 1 & \text{if } \left|\hat{\tilde{N}}_{m,r}^{k,+}(t_i) - \left[\hat{N}_{m,r}^{k,+}(t_i)\right]\right| < \epsilon_{\tilde{N}} \\ 0 & \text{else.} \end{cases} \tag{3.33}$$

It is noted that the function f also fulfill another constraint that the rounded values $\left[\hat{N}_{m,r}^{k,+}(t_i)\right]$ in the time window must always refer to the same integer value.

The convergence of one ambiguity estimate is shown in Fig. 3.2, which gives a motivation for the fixing criterion. The ambiguity estimate is selected from a bias estimation from a regional network using real GPS data, which is presented in the following sections. The length of the time-window T, the probability p and the threshold for the actual deviation $\epsilon_{\tilde{N}}$ are chosen to be 600 epochs, 0.95, and 0.08 cycles respectively. The ambiguity is reliably fixed to the integer candidate -22, although it varies around -20 in the beginning of the convergence.

Finally, it is noted that the tildes on top of the state estimates have been introduced to explain the steps of parameter mappings, thus they are neglected for simplicity in the rest of this chapter.

3.2.2 Adaption of Satellite Visibility

Since the bias estimation needs a network of receivers over a period of several hours, the state vector of the Kalman filter changes according to the dynamics of the satellite visibility. An upcoming or a vanishing measurement from the satellite-receiver link would affect the states including geometry, ionospheric delay, phase biases and ambiguities. Different scenarios are discussed as follows for a link from satellite k to receiver r.

Assume the link comes up and is to be added to the system. The new states Δg_r^k, $\Delta \dot{g}_r^k$, $\Delta \ddot{g}_r^k$, I_r^k, and $\dot{I}_r^k$ are augmented into the state vector, while the corresponding new measurements $\lambda_m \varphi_{m,r}^k$ and $\rho_{m,r}^k$ are included in the measurement vector. The initialization for the new states is performed via least-squares combining three measurement epochs. Furthermore,

- if the receiver phase bias $\beta_{m,r}$ and the satellite phase bias β_m^k are already estimated in the state vector, then the new ambiguities $N_{m,r}^k$ could also be initialized using least-squares;

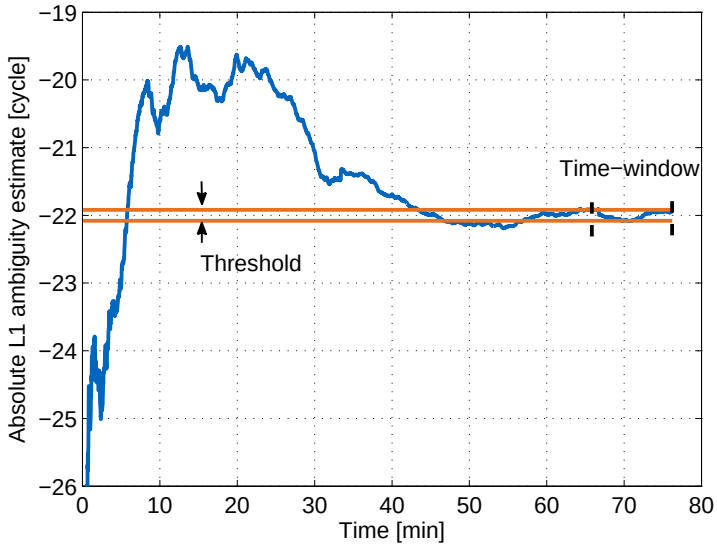

Figure 3.2: The convergence behavior of one ambiguity estimate on L1. The ambiguity is fixed to -22, as it remains stable under the threshold of 0.08 cycles (orange horizontal lines) for 10 minutes.

- if either the receiver phase bias $\beta_{m,r}$ or the satellite phase bias β_m^k needs to be initialized, i.e. the receiver r or the satellite k has not been included in the network, then the ambiguities on the new link have to be combined with the new phase bias estimate. The bias state $\beta_{m,r} + N_{m,r}^k$, or $\beta_m^k + N_{m,r}^k$ needs to be initialized in addition to the geometry and ionospheric states;
- if neither the receiver phase bias $\beta_{m,r}$ nor the satellite phase bias β_m^k is present in the state vector, which means the receiver and the satellite are both new to the system. This indicates the receiver r sees one satellite ℓ, while the satellite ℓ is only seen by the receiver r. Then the increased measurements are not enough to determine the biases nor the ambiguities. This link will be discarded until more measurements come for the receiver r or the satellite k.

Correspondingly, we now analyze the case when the link disappears. The states Δg_r^k, $\Delta \dot{g}_r^k$, $\Delta \ddot{g}_r^k$, I_r^k, and $\dot{I}_r^k$ are removed from the state vector, as well as $\lambda_m \varphi_{m,r}^k$ and $\rho_{m,r}^k$ from the measurement vector. If the ambiguities $N_{m,r}^k$ from the link are present in the state vector, they are removed together with the geometry and ionospheric states. However, if the ambiguities $N_{m,r}^k$ were combined in phase biases or other ambiguities in the stage of parameter mapping, or the ambiguities were already fixed and removed from the system, the following cases are studied.

- Both the receiver r and the satellite k are still seen by other satellites and receivers, which means the phase biases $\beta_{m,r}$ and β_m^k are kept in the state vector. Additional ambiguities must be mapped away due to the decreasing number of measurements, in order to keep a full-rank system. Therefore, an additional Gaussian Elimination is performed to determine which ambiguities to be mapped away, as well as the mapping coefficients to the other phase biases and ambiguities.

- The receiver r or the satellite k is no more seen by other satellites or receivers, which means the phase bias $\beta_{m,r}$ or β_m^k is to be removed. As a consequence, the rank-deficiency is resolved and no additional ambiguities need to be mapped.

As the bias estimates are subject to one satellite phase bias, the change of the reference satellite shall also be tracked along the estimation. Assume the reference satellite changes from k_1 at epoch t_{n-1} to k_2 at epoch t_n. The reference satellite is chosen such that it is seen by most of the stations and is kept until it is not visible from all stations, therefore the new reference satellite k_2 must have been visible also at the previous epoch t_{n-1}. The state transition for the phase bias $\hat{\beta}_m^k$ $(k \neq k_1,\ k_2)$ is given by

$$\begin{aligned} \hat{\beta}_m^{k,-}(t_n) &= \hat{\beta}_m^{k,+}(t_{n-1}) - \hat{\beta}_m^{k_2,+}(t_{n-1}), \\ \hat{\beta}_{m,r}^{-}(t_n) &= \hat{\beta}_{m,r}^{+}(t_{n-1}) + \hat{\beta}_m^{k_2,+}(t_{n-1}). \end{aligned} \tag{3.34}$$

3.2.3 Sidereal Filtering

The multipath errors have been so far included in the measurement noise. It is not feasible to estimate all multipath delays in real-time, as multipath affects each receiver-satellite link on each frequency differently. However, in the case of GPS for a stationary receiver the multipath repeats, i.e. after one sidereal day 23h 56min 4.2s, which is twice the orbital period of GPS satellites. This allows a separation of the multipath from all other error terms, and the multipath can be well observed from the repeatability of the residuals [76].

Dual-frequency GPS measurements have been collected from a few SAPOS (Satellitenpositionierungsdienst der deutschen Landesvermessung) stations in Bavaria, Germany, between May 30 and June 5 (day 150 to 156), 2011 [77]. The data span is from 8:00 to 9:40 for June 5, and is shifted by 3min 55.8s for each day backwards to align the sidereal time. A Kalman filter is set up for each station, estimating the geometry term, the slant ionospheric delay, the phase biases and the float ambiguities. The code residuals include the assumed white Gaussian measurement noise as well as the multipath.

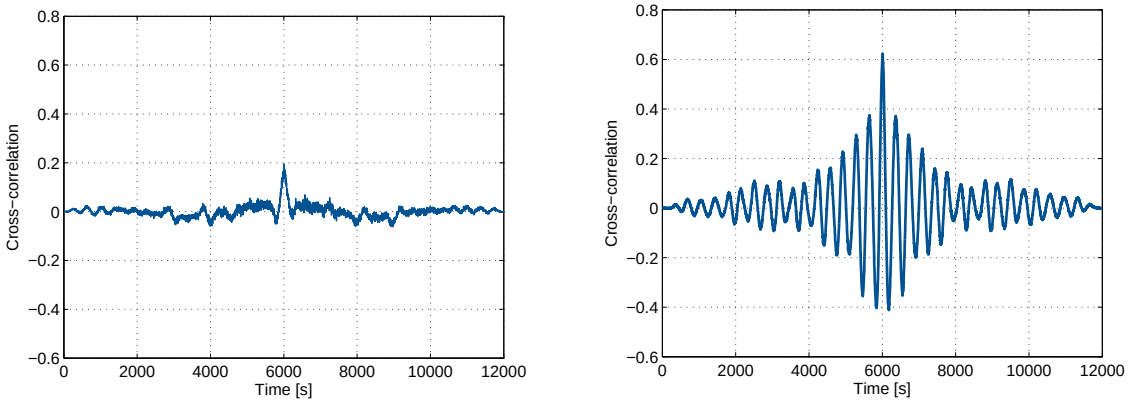

(a) Low correlation at station Rosenheim.

(b) High correlation at station Günzburg.

Figure 3.3: Temporal cross-correlation of the code residuals of PRN 5 at two SAPOS stations.

Fig. 3.3 shows the temporal cross-correlation of the code residuals of PRN 5 at two stations in Rosenheim and Günzburg between the first two days. The residuals in Fig. 3.3(a) have a relatively low cross-correlation of 0.2 when aligned, otherwise are approximately uncorrelated. The cross-correlation from station Günzburg gives a sinc-like result, with the peak being 0.8 when the two sequences are aligned according to sidereal time. Moreover, the side lobes have a constant spacing of about 6 minutes which indicates the time duration of the oscillating multipath pattern.

The code residuals of PRN 5 at station Günzburg are plotted as a function of elevation angle for 7 consecutive days in Fig. 3.4(a), from day 150 to 156 from the bottom to the top. There exists an impressive repeatability of the residuals under same geometry among days, especially at low elevations under 40°. The short-term large variations in the code residuals exhibit a strong multipath pattern.

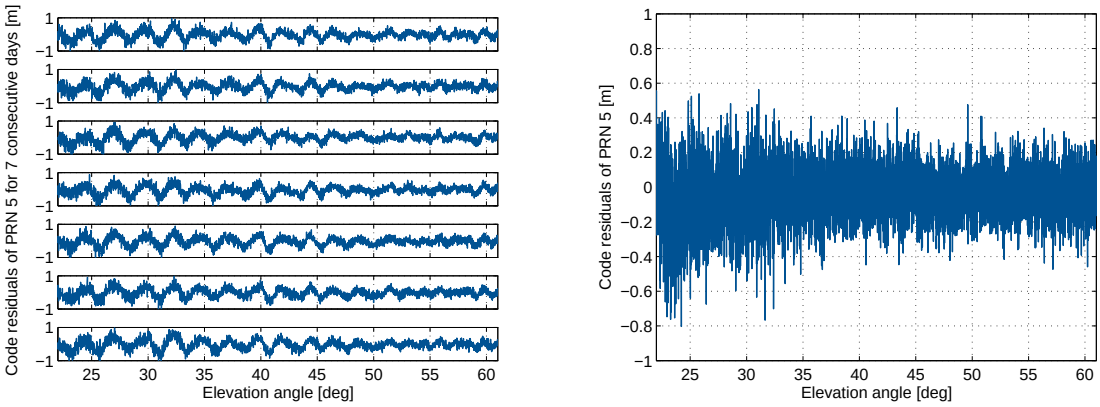

(a) A high repeatability is observed over one week, which can be explained by the repeating multipath errors under same satellite geometry.

(b) Code residuals after multipath correction on day 157. The correction results in a white Gaussian noise.

Figure 3.4: Impact of sidereal filtering on code residuals from PRN 5 at SAPOS station Günzburg.

We take advantage of the repeatable pattern of multipath, and subtract it as a priori information. First, the multipath pattern is extracted by averaging the code residuals over the consecutive 7 days. The mean curve for PRN 5 at station Günzburg is shown in Fig. 3.5. The strong code multipath up to 0.6 m is observed under 32° elevation. Then, the multipath is used as correction in the measurements on another day 157. The benefit of the correction is depicted in Fig. 3.4(b), where the code residuals show a white Gaussian noise with larger variance at lower elevations.

Spectral analysis can also bring information on the code residuals. A periodogram provides a way to estimate the power spectral density. Given a sequence x_n, the Discrete Fourier Transform (DFT) X_k is defined as

$$X_k = \sum_{n=0}^{N-1} x_n e^{-i2\pi kn/N}, \quad k \in \mathbb{Z}, \tag{3.35}$$

with N being the sequence length. The periodogram $\hat{S}(X_k)$ is then calculated as the

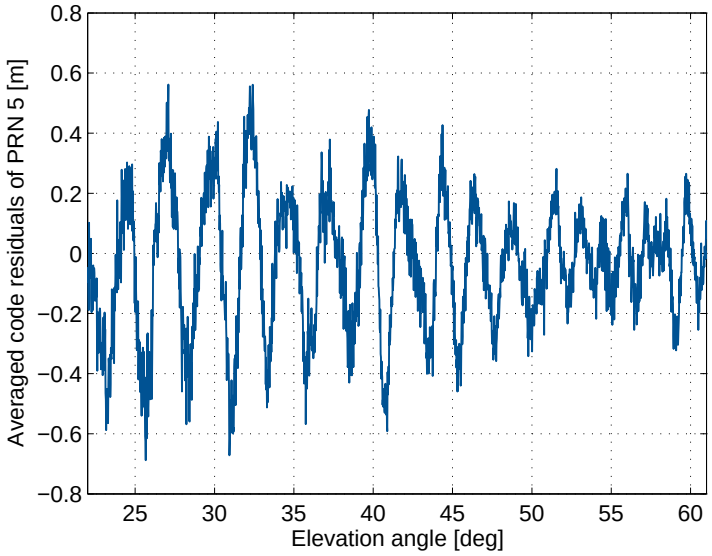

Figure 3.5: Sidereal filtered code residuals at station Günzburg over one week. The sidereal filtering substantially reduces the noise, which allows an accurate modelling of the multipath pattern.

squared norm of the DFT, i.e.

$$\hat{S}(X_k) = \frac{1}{N}|X_k|^2. \tag{3.36}$$

Fig. 3.6(a) depicts the comparison of the periodograms of the code residuals without and with the multipath correction. The peaks point out the frequencies of the multipath pattern. The largest peak of the blue curve locates at the frequency 0.0028Hz, which corresponds to a period of 357 seconds. This again confirms the oscillating period in Fig. 3.3(b) and Fig. 3.4(a). The peaks get completely discarded after applying the multipath correction, shown in the orange curve. The periodogram with correction approaches the one of white noise, which has by definition a constant power spectral density.

Histograms are drawn for the code residuals without and with multipath correction in Fig. 3.6(b). In both cases they are unbiased and well approximate a bell-shape of a Gaussian distribution, while the orange curve with correction concentrates more in the center, i.e. having much smaller variance than without correction.

ID	0256	0258	0259	0261	0265	0269	0272	0273	0274	0276
$\phi\,[^\circ N]$	48.14	48.53	48.37	48.57	48.43	47.60	47.87	48.04	48.45	48.84
$\lambda\,[^\circ E]$	11.59	11.51	10.89	13.44	12.93	10.42	12.11	10.49	10.28	10.50

Table 3.1: The coordinates of the 10 reference stations in the SAPOS network.

The correction of multipath also helps enhance the stability of the phase bias estimate, which helps the fixing of ambiguities. We apply the multipath correction in the network estimation for the phase biases using 10 SAPOS stations. The stations included are listed in Tab. 3.1. The data spans 6000 seconds from 8:23:36 to 10:03:35 on day 150, i.e. the same period determining the multipath correction. To simplify the rising and setting cases, 6

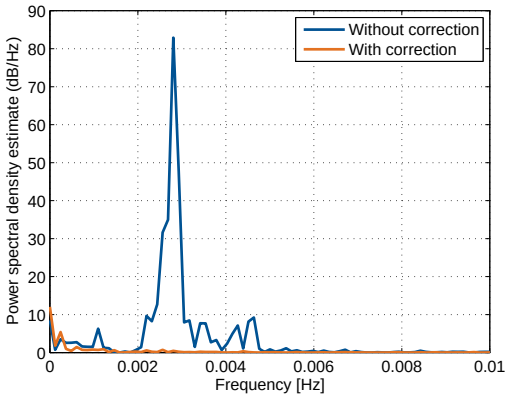

(a) Periodogram brings spectral information on the code residuals. After applying multipath corrections the main peaks disappear and the periodogram approaches a constant spectral density.

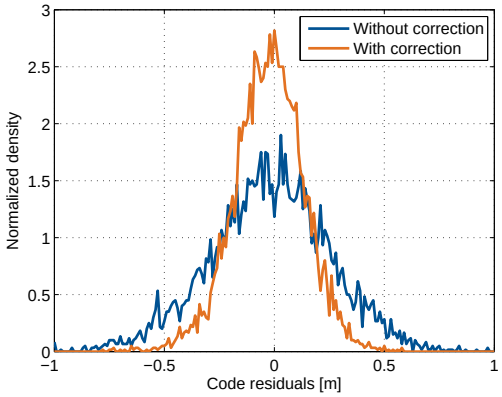

(b) Histogram of the code residuals. The multipath correction results in a Gaussian distribution with significantly reduced variance.

Figure 3.6: Benefit of applying multipath corrections obtained from sidereal filtering.

common satellites seen by all stations are considered because of continuous visibility: PRN $2, 5, 7, 8, 10, 13$, with PRN 2 being the reference satellite. Fig. 3.7 depicts the satellite phase bias estimates on L1, which shows the benefit of applying the multipath correction. It is obviously seen that the short-term variations on the phase bias estimates disappear comparing Fig. 3.7(a) and Fig. 3.7(b). Besides, each vertical line represents one ambiguity fixing. In Fig. 3.7(a) only 2 out of 90 ambiguity estimates are fixed before correction, while the number increases to 40 with multipath correction. Moreover, the first fixing also takes place much earlier in Fig. 3.7(b). The phase bias estimates achieve an accuracy of 1 cm (one sigma).

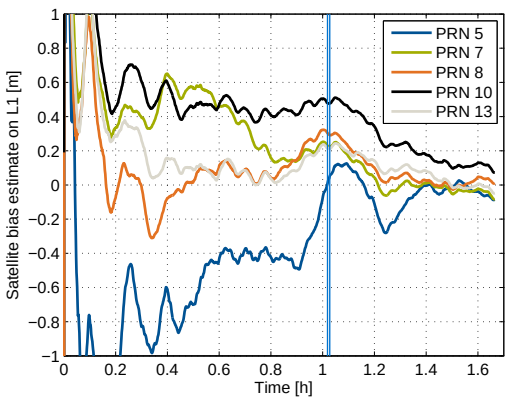

(a) Without multipath correction.

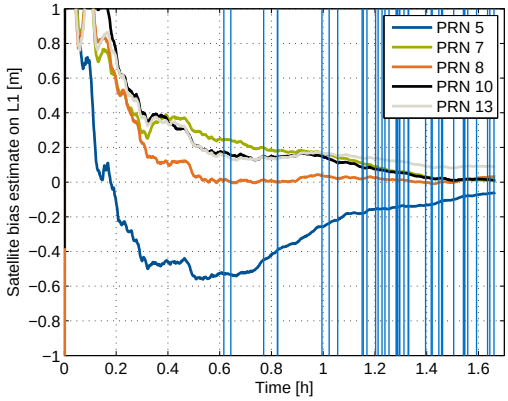

(b) With multipath correction.

Figure 3.7: Satellite phase bias estimates on L1 without and with multipath correction. The multipath error propagates into the bias estimates which show large variations over time and prevent a fast ambiguity fixing. The first fixing happens much earlier at 38th minute, while the number of ambiguity fixings increases from 2 to 40.

3.2.4 Real Data Analysis

In this section, more real GPS data is collected to perform the estimation algorithm of satellite and receiver phase biases. Two reference networks are taken, one is a regional SAPOS network in Germany, while the other is a global reference station network from IGS.

Regional SAPOS Network

The bias estimation algorithm has been applied with a network of 13 SAPOS reference stations in Bavaria, Germany, with the map shown in Fig. 3.8(a). All stations are operating the same type of receivers, i.e. Trimble NetR5, so that no additional bias would be introduced due to different receiver processing techniques. Dual-frequency phase and code measurements were collected for a continuous 24 hours on March 14th, 2011. It is further noted that, without additional effort the estimation algorithm can be applied also with a global network [78].

The coordinates of the reference stations are given in ETRS89 (European Terrestrial Reference System 1989) reference frame. A Helmert transformation is needed to convert them into ITRF08 reference frame, because the station coordinates are used in the same frame with the satellite coordinates. It includes three transformations, a scaling, and three rotations, i.e.

$$\vec{\boldsymbol{r}}_{\mathrm{ITRF08}} = \begin{bmatrix} \Delta x \\ \Delta y \\ \Delta z \end{bmatrix} + (1+\mu) \cdot \begin{bmatrix} 1 & \omega_z & -\omega_y \\ -\omega_z & 1 & \omega_x \\ \omega_y & -\omega_x & 1 \end{bmatrix} \cdot \vec{\boldsymbol{r}}_{\mathrm{ETRS89}}, \tag{3.37}$$

where μ denotes a scale factor and is unitless. Tab. 3.2 lists the transformation parameters at year epoch 2000.0, obtained from [79], as well as the rates to acquire the parameters at any epoch.[1]

Translation	Δx	0.0118 m	Rate of translation	$\Delta\dot{x}$	−0.1 mm/y
	Δy	−0.1432 m		$\Delta\dot{y}$	−0.1 mm/y
	Δz	0.1117 m		$\Delta\dot{z}$	1.8 mm/y
Rotation angle	ω_x	3.291 mas	Rate of rotation angle	$\dot{\omega}_x$	0.081 mas/y
	ω_y	6.190 mas		$\dot{\omega}_y$	0.490 mas/y
	ω_z	−11.012 mas		$\dot{\omega}_z$	−0.792 mas/y
Scaling	μ	$-1.224 \cdot 10^{-8}$	Rate of scaling	$\dot{\mu}$	$-8 \cdot 10^{-11}$ /y

Table 3.2: Transformation parameters and their yearly variation from reference frame ETRS89 to ITRF08 at epoch 2000.0.

After correcting satellite orbits and clock offsets, we scan and eliminate cycle-slips using triple-difference in the pre-processing. The stations are paired to perform double difference, leaving the double difference geometry terms, the double difference ionospheric delays and

[1] The conversion from milliarcsecond to radians is given by $1\,\mathrm{rad} = 10^{-3}/3600 \cdot \pi/180\,\mathrm{mas}$.

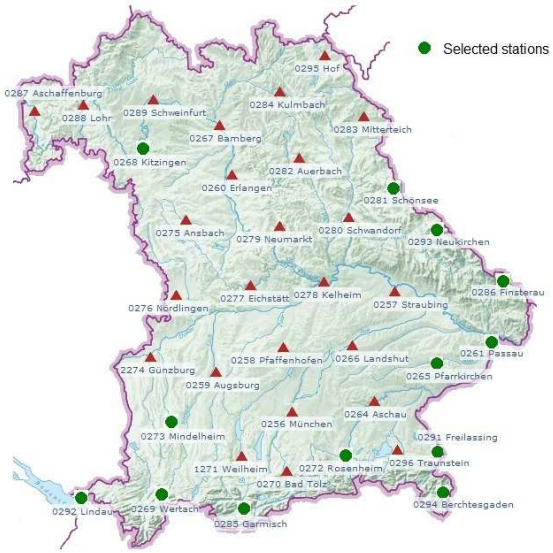

(a) The estimation network includes 13 SAPOS reference stations (green dots), which operate with the same type of receiver.

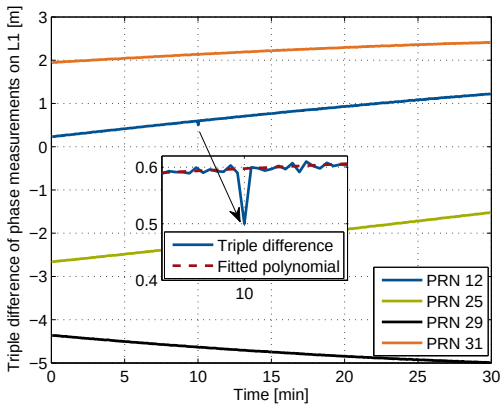

(b) Cycle-slip detection with triple-difference. PRN 12 with an artificial one half of a cycle slip is detected at station pair 0261 and 0265.

Figure 3.8: The estimation network and the pre-processing technique.

ambiguities. The between-epoch differencing is further expressed as

$$\lambda_m(\Delta\varphi^{k\ell}_{m,ij}(t_n) - \Delta\varphi^{k\ell}_{m,ij}(t_{n-1})) = \Delta g^{k\ell}_{ij}(t_n) - \Delta g^{k\ell}_{ij}(t_{n-1}) - \frac{f_1^2}{f_m^2}\left(I^{k\ell}_{1,ij}(t_n) - I^{k\ell}_{1,ij}(t_{n-1})\right) + \\ + \lambda_m(N^{k\ell}_{m,ij}(t_n) - N^{k\ell}_{m,ij}(t_{n-1})) + \varepsilon^{k\ell}_{m,ij}(t_n) - \varepsilon^{k\ell}_{m,ij}(t_{n-1}), \quad (3.38)$$

which would remove the ambiguities in case of no cycle-slip. The change of the other terms normally does not exceed a few centimeters, as long as the sampling interval is less than 1 minute. Exceptional situations include e.g. ionospheric disturbance, extremely long baseline etc. [80]. In this work, the receivers are operating in 1Hz, having most of the baseline lengths in the medium range of 100km, therefore a spike in the triple-difference would indicate a cycle-slip. An example is depicted in Fig. 3.8(b), where an artificial one half of a cycle slip is added on PRN 12 and detected through polynomial fitting of triple-difference result.

A Kalman filter is set up to estimate the geometry terms, the slant ionospheric delays, as well as the phase biases and the ambiguities. The second-order geometry and the first-order ionospheric delays are assumed to follow random walk processes with standard deviations $\sigma_{\Delta\ddot{g}} = 1\,\mathrm{m/s^2}$ and $\sigma_{\dot{I}} = 1\,\mathrm{cm/s}$, while the same assumption applies to the phase biases and the ambiguities with standard deviations $\sigma_{\beta_r} = 1\,\mathrm{mm}$, $\sigma_{\beta^k} = 0.1\,\mathrm{mm}$, and $\sigma_N = 10^{-3}\,\mathrm{cycle}$. The variances for the other states are obtained by

$$\sigma^2_{\Delta g} = \frac{1}{20}\Delta t^4 \cdot \sigma^2_{\Delta\ddot{g}} = 0.05\,\mathrm{m}^2,$$
$$\sigma^2_{\Delta\dot{g}} = \frac{1}{3}\Delta t^2 \cdot \sigma^2_{\Delta\ddot{g}} = 0.33\,\mathrm{m}^2/\mathrm{s}^2,$$
$$\sigma^2_{I} = \frac{1}{3}\Delta t^2 \cdot \sigma^2_{\dot{I}} = 0.33\,\mathrm{cm}^2. \quad (3.39)$$

The measurement noise is assumed to be white Gaussian distributed, with the standard deviation following an exponential function depending on the elevation angle E [deg], i.e.

$$\begin{aligned}\sigma_\rho(E) &= 2.24 \cdot e^{-E/37.28},\\ \sigma_\phi(E) &= 0.13 \cdot e^{-E/15.34}.\end{aligned} \tag{3.40}$$

Evaluating the functions at 15° and 75° yields the standard deviations for code and phase measurements in Tab. 3.3. The sample values are determined based on the code and phase ionospheric-preserving observations, where an assumption is made that the code and phase noise on the one frequency equals the noise on the other frequency.

	$E = 15°$	$E = 75°$
σ_ρ	1.5 m	0.3 m
σ_ϕ	0.05 m	0.001 m

Table 3.3: Assumptions for the standard deviations of code and phase measurements.

As additional parameter mappings may take place when visibility changes, the states are re-adjusted every time. Therefore, the satellite visibility is kept the same in blocks of time, e.g. 2000 epochs, allowing the states to converge better.

The real-valued ambiguity estimates are fixed to integers in a sequential manner. The fixing decision is based on both the state variance and the actual deviation from the integer values. The threshold for the standard deviation is set to 0.3 cycles, while the ambiguity estimate shall remain within the threshold of ±0.08 cycles for 90% of the time over the last 10 minutes.

The fractional part of the satellite phase bias estimates $\hat{\beta}^k_{m,\mathrm{frac}}$ on L1 and L2 is at interest, while the integer part is anyway not separable from the integer ambiguities. The fractional part is calculated as

$$\hat{\beta}^k_{m,\mathrm{frac}} = \hat{\beta}^k_m - \lambda_m \cdot \left\lfloor \frac{\hat{\beta}^k_m(t^k_{\mathrm{end}})}{\lambda_m} \right\rceil, \tag{3.41}$$

with t^k_{end} denoting the last available epoch for satellite k.

Fig. 3.9 shows the phase bias estimates from PRN 10, 14, 16, 26, 27, and 32 on L1 and L2, where the curves on two frequencies display strong correlations for each PRN. Because of the large number of states and the mapped ambiguities on top, the phase biases first needed time to converge and to apply ambiguity fixings. The estimates after the convergence show remarkable stabilities, with the most stable one having about 2 cm variation over 2 hours. Moreover, the repeatability is also observed on PRN 14 and 16. One could re-initialize the satellite phase bias with the previous converged value. Fig. 3.9 shows, even if they are not initialized with a priori information, they still converge to the previous value.

IGS Global Reference Network

The proposed algorithm does not have constraints on network size for estimating phase biases. Previous results showed a regional network of SAPOS stations in Bavaria, Germany.

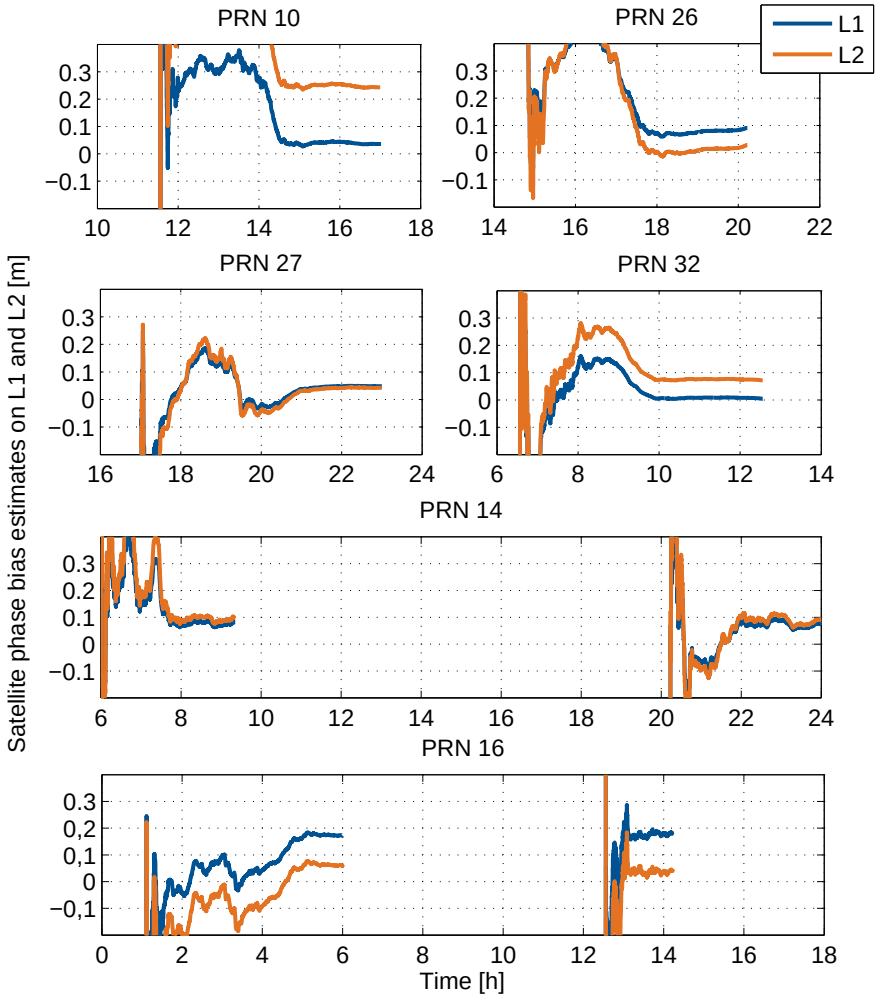

Figure 3.9: The satellite phase bias estimates for PRN 10, 14, 16, 26, 27, and 32 on L1 and L2. After fixing the ambiguities, the phase biases have converged with remarkable stabilities, i.e. the most stable one varying only about 2 cm over 2 hours. As PRN 14 and 16 are introduced again into the system, the phase biases converged to the same values.

This section will apply some real data from a global IGS network to the algorithm. The outcome of the 1st-stage Kalman filter will be used as measurements in the 2nd-stage estimation. The larger scale of network, with four times the number of stations in the regional network, will provide a better geometry for modelling satellite movement.

Fig. 3.10 depicts a global network of 40 IGS stations with the same type of receivers (Trimble NetR9 receivers). The raw GPS measurements are collected on Jan 1st, 2015, with an update rate of 30 seconds. There are a number of stations distributed on the oceans to have good geometry for global estimation, yet unfortunately not many stations are located in America, central Europe and Asia. It can be expected that if more stations were augmented in these areas, the accuracy of bias estimation would be increased.

The state vector includes ranges, range rates, slant ionospheric delays, phase biases and ambiguities. The range rate is assumed to follow a random-walk process, where the

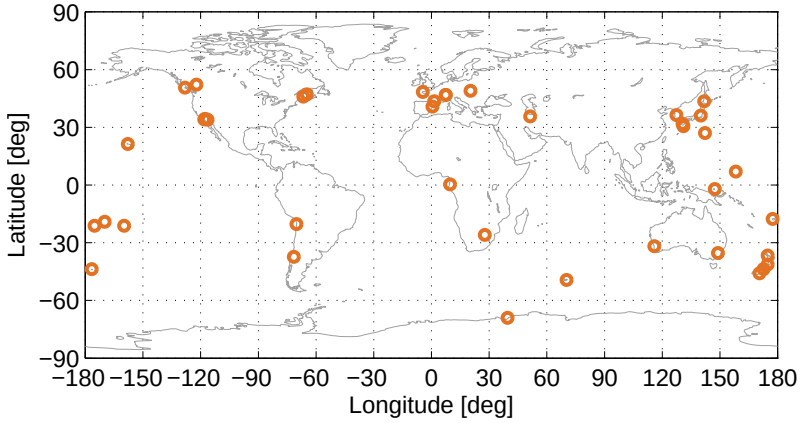

Figure 3.10: A global network of 40 IGS reference stations, having the same type of Trimble NetR9 receivers.

variance of the process noise $\sigma^2_{\Delta\dot{g}}$ is set to be 0.01 m^2/s^2. The standard deviations of the process noise for the slant ionospheric delays and biases are 0.1 m and 0.1 mm, respectively. The ambiguities are modelled to be constant over time and are fixed in a sequential manner. If the actual deviation to the same rounded integer is smaller than 0.1 cycle for 90% time in a 10-minute time window, the ambiguity is fixed to the integer value.

The measurement noise is assumed to follow zero-mean Gaussian distributions. The standard deviations are assumed to be two exponential functions for code and phase measurements, which are given by

$$\begin{aligned} \sigma_\rho(E) &= 0.95 \cdot e^{-E/86.56}, \\ \sigma_\phi(E) &= 0.13 \cdot e^{-E/15.34}, \end{aligned} \tag{3.42}$$

with E being the elevation angle in degrees. This corresponds to standard deviations of 0.8 m and 0.3 m for code, 5 cm and 1 mm for phase, at 15° and 75° elevations respectively. The sample values are determined based on the code and phase ionospheric-preserving observations, where an assumption is made that the code and phase noise on the one frequency equals the noise on the other frequency.

Fig. 3.11 shows the L1 phase bias estimates of selected satellites. These satellites are seen by more than 9 stations in average, while the bias estimates have converged to very stable values, i.e. having variations of 2-4 cm over almost 10 hours.

The satellite phase bias estimates are listed in Tab. 3.4. PRN 1 was selected as the reference satellite, thus no estimate exists for satellite biases from PRN 1. The standard deviations amount to around 0.13 cycle, which corresponds to an accuracy of 2.5 cm on L1 and of 3.2 cm on L2. PRN 8 was introduced into the system at hour 11, while averagely only 4 stations had PRN 8 in view. Thus the phase bias accuracy of PRN 8 was not as low as the other satellites.

The range estimates and their covariance matrix are stored for determining geometric code biases in the second-stage Kalman filter. In the next section, we will break the geometric term down into satellite orbits, clock offsets, biases and tropospheric delays. Compared to a regional network, the global network has a wider distribution of reference

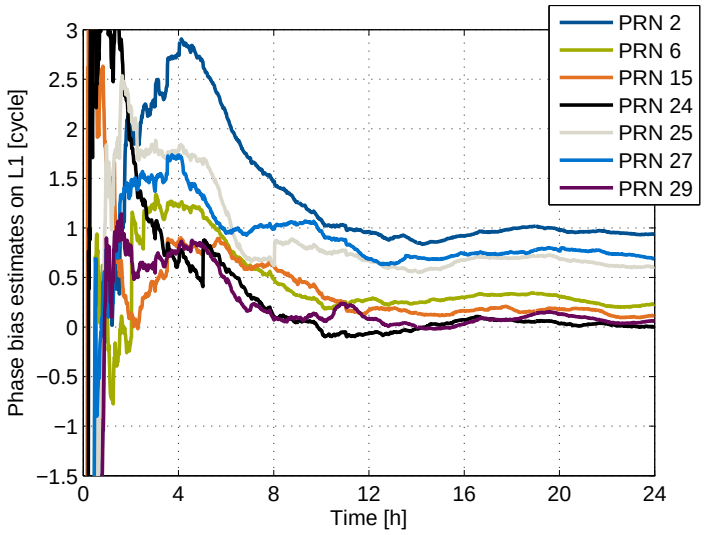

Figure 3.11: The phase bias estimates of a subset of satellites over 24 hours.

stations, which is beneficial for satellite orbit determination and code bias estimation.

3.3 Estimation of Geometric Code Biases

The geometric state obtained as $\Delta\hat{\tilde{g}}_r^k$, includes the orbital errors, the receiver clock offsets, the tropospheric zenith delays and the satellite geometric code biases. As the geometric measurements come from the state estimates from the Kalman filter for phase bias estimation, they are correlated over time. The measurements need to be first decoupled.

Consider a general linear model for the measurement vector $\boldsymbol{z}_n$ at epoch n as

$$\begin{aligned} \boldsymbol{z}_n &= \boldsymbol{H}_n \boldsymbol{x}_n + \boldsymbol{v}_n \\ \boldsymbol{v}_n &= \boldsymbol{\Gamma}_{n-1} \boldsymbol{v}_{n-1} + \boldsymbol{\zeta}_{n-1}, \end{aligned} \tag{3.43}$$

where $\boldsymbol{x}_n$ denotes the state vector, $\boldsymbol{v}_n$ denotes the colored noise vector, $\boldsymbol{H}_n$ denotes the design matrix, $\boldsymbol{\Gamma}_{n-1}$ describes the temporal relation for the noise $\boldsymbol{v}_n$, and $\boldsymbol{\zeta}_n$ is white Gaussian noise. The state space model for $\boldsymbol{x}_n$ is given by

$$\boldsymbol{x}_n = \boldsymbol{\Phi}_{n-1} \boldsymbol{x}_{n-1} + \boldsymbol{w}_{n-1}, \tag{3.44}$$

with the state transition matrix being $\boldsymbol{\Phi}_n$. The process noise $\boldsymbol{w}_n$ and $\boldsymbol{\zeta}_n$ are Gaussian distributed with zero means, and there exists no correlation between the two noise. The statistics are given by

$$\begin{aligned} &\mathrm{E}\{\boldsymbol{w}_n\} = \boldsymbol{0},\ \mathrm{E}\{\boldsymbol{w}_n \boldsymbol{w}_m^{\mathrm{T}}\} = \boldsymbol{Q}_n \delta_{nm}, \\ &\mathrm{E}\{\boldsymbol{\zeta}_n\} = \boldsymbol{0},\ \ \mathrm{E}\{\boldsymbol{\zeta}_n \boldsymbol{\zeta}_m^{\mathrm{T}}\} = \boldsymbol{R}_n \delta_{nm},\ \ \mathrm{E}\{\boldsymbol{w}_n \boldsymbol{\zeta}_m^{\mathrm{T}}\} = \boldsymbol{0}, \end{aligned} \tag{3.45}$$

where δ_{nm} represents the Kronecker delta function, and $\boldsymbol{Q}_n$ and $\boldsymbol{R}_n$ denote the covariance matrices for $\boldsymbol{w}_n$ and $\boldsymbol{\zeta}_n$ respectively.

PRN k	$\hat{\tilde{\beta}}_1^k$ [cycle]	$\sigma_{\hat{\tilde{\beta}}_1^k}$ [cycle]	$\hat{\tilde{\beta}}_2^k$ [cycle]	$\sigma_{\hat{\tilde{\beta}}_2^k}$ [cycle]
1	-	-	-	-
2	0.936	0.131	0.439	0.13
3	0.88	0.133	0.859	0.132
4	0.551	0.138	0.915	0.137
5	0.674	0.13	0.379	0.129
6	0.229	0.129	0.453	0.128
7	0.307	0.132	0.626	0.131
8	0.467	0.222	0.953	0.22
9	0.464	0.132	0.208	0.131
10	0.428	0.131	0.603	0.13
11	0.372	0.133	0.388	0.132
12	0.644	0.131	0.189	0.13
13	0.005	0.132	0.142	0.131
14	0.379	0.133	0.159	0.132
15	0.114	0.131	0.355	0.13
16	0.778	0.133	0.872	0.131
17	0.128	0.13	0.122	0.129
18	0.007	0.13	0.481	0.128
19	0.609	0.132	0.794	0.13
20	0.464	0.136	0.018	0.135
21	0.863	0.129	0.49	0.128
22	0.697	0.13	0.021	0.128
23	0.004	0.13	0.283	0.129
24	0.006	0.129	0.825	0.128
25	0.607	0.131	0.752	0.129
26	0.61	0.134	0.622	0.133
27	0.69	0.128	0.701	0.127
28	0.141	0.13	0.929	0.129
29	0.061	0.131	0.744	0.13
30	0.68	0.128	0.709	0.127
31	0.15	0.131	0.258	0.13
32	0.325	0.129	0.595	0.128

Table 3.4: A snapshot of the satellite phase bias estimates on L1 and L2 and the standard deviations at the last epoch.

An approach to perform the estimation with the traditional Kalman filter is to augment the state vector with the colored measurement noise $\boldsymbol{v}_n$ [68]. Thus, the augmented state vector $\tilde{\boldsymbol{x}}_n$, the state transition matrix $\tilde{\boldsymbol{\Phi}}_n$, the design matrix $\tilde{\boldsymbol{H}}_n$ and the process noise covariance matrix $\tilde{\boldsymbol{Q}}_n$ are described as

$$\tilde{\boldsymbol{x}}_n = \begin{bmatrix} \boldsymbol{x}_n \\ \boldsymbol{v}_n \end{bmatrix}, \quad \tilde{\boldsymbol{\Phi}}_n = \begin{bmatrix} \boldsymbol{\Phi}_n & \boldsymbol{0} \\ \boldsymbol{0} & \boldsymbol{\Gamma}_n \end{bmatrix}, \quad \tilde{\boldsymbol{H}}_n = [\boldsymbol{H}_n, \ \boldsymbol{1}], \quad \text{and} \quad \tilde{\boldsymbol{Q}}_n = \begin{bmatrix} \boldsymbol{Q}_n & \boldsymbol{0} \\ \boldsymbol{0} & \boldsymbol{R}_n \end{bmatrix}. \tag{3.46}$$

The measurement model is then modified as

$$\boldsymbol{z}_n = \tilde{\boldsymbol{H}}_n \tilde{\boldsymbol{x}}_n, \tag{3.47}$$

which means the measurements contain no noise in the augmented system. As a result, the measurement noise covariance is removed. The state covariance matrices $\boldsymbol{P}_n^+$ and $\boldsymbol{P}_n^-$ in the Kalman filter are updated as

$$\begin{aligned} \boldsymbol{P}_n^- &= \tilde{\boldsymbol{\Phi}}_{n-1} \boldsymbol{P}_{n-1}^+ \tilde{\boldsymbol{\Phi}}_{n-1}^{\mathrm{T}} + \tilde{\boldsymbol{Q}}_{n-1}, \\ \boldsymbol{P}_n^+ &= \left(\mathbf{1} - \boldsymbol{P}_n^- \tilde{\boldsymbol{H}}_n^{\mathrm{T}} (\tilde{\boldsymbol{H}}_n \boldsymbol{P}_n^- \tilde{\boldsymbol{H}}_n^{\mathrm{T}})^{-1} \tilde{\boldsymbol{H}}_n \right) \boldsymbol{P}_n^-. \end{aligned} \tag{3.48}$$

It can be easily derived that $\tilde{\boldsymbol{H}}_n \boldsymbol{P}_n^+ \tilde{\boldsymbol{H}}_n^{\mathrm{T}} = 0$, i.e. $\boldsymbol{P}_n^+$ is singular. If the state transition matrix $\tilde{\boldsymbol{\Phi}}_n$ is near identity matrix, and the process noise covariance matrix $\tilde{\boldsymbol{Q}}_n$ is often very small, the prediction of the state covariance $\boldsymbol{P}_{n+1}^-$ would be near the a posteriori one $\boldsymbol{P}_n^+$, which leads also to a singular matrix $\boldsymbol{P}_{n+1}^-$ and thus the inverse in Eq. (3.48) does not exist [81]. Moreover, let the dimensions of $\boldsymbol{x}_n$ and $\boldsymbol{z}_n$ be a and b, the system is obviously rank-deficient, as there are $a + b$ augmented state variables and only b observations.

3.3.1 Time-differencing Approach

Bryson and Henrikson proposed a time-differencing approach for colored measurement noise in [81]. By time-differencing the measurements, a new type of measurement with white Gaussian noise is obtained as

$$\begin{aligned} \boldsymbol{z}_n^* &= \boldsymbol{z}_{n+1} - \boldsymbol{\Gamma}_n \boldsymbol{z}_n \\ &= \boldsymbol{H}_{n+1} \boldsymbol{x}_{n+1} + \boldsymbol{v}_{n+1} - \boldsymbol{\Gamma}_n \left(\boldsymbol{H}_n \boldsymbol{x}_n + \boldsymbol{v}_n \right) \\ &= \boldsymbol{H}_{n+1} \left(\boldsymbol{\Phi}_n \boldsymbol{x}_n + \boldsymbol{w}_n \right) + \boldsymbol{\Gamma}_n \boldsymbol{v}_n + \boldsymbol{\zeta}_n - \boldsymbol{\Gamma}_n \left(\boldsymbol{H}_n \boldsymbol{x}_n + \boldsymbol{v}_n \right) \\ &= \left(\boldsymbol{H}_{n+1} \boldsymbol{\Phi}_n - \boldsymbol{\Gamma}_n \boldsymbol{H}_n \right) \boldsymbol{x}_n + \boldsymbol{H}_{n+1} \boldsymbol{w}_n + \boldsymbol{\zeta}_n \\ &\triangleq \boldsymbol{H}_n^* \boldsymbol{x}_n + \boldsymbol{v}_n^*, \end{aligned} \tag{3.49}$$

with the transformed design matrix $\boldsymbol{H}_n^*$ and the transformed measurement noise $\boldsymbol{v}_n^*$ being

$$\begin{aligned} \boldsymbol{H}_n^* &= \boldsymbol{H}_{n+1} \boldsymbol{\Phi}_n - \boldsymbol{\Gamma}_n \boldsymbol{H}_n, \\ \boldsymbol{v}_n^* &= \boldsymbol{H}_{n+1} \boldsymbol{w}_n + \boldsymbol{\zeta}_n. \end{aligned} \tag{3.50}$$

Like $\boldsymbol{w}_n$ and $\boldsymbol{\zeta}_n$, the new noise $\boldsymbol{v}_n^*$ is also zero-mean white Gaussian distributed. The covariance is derived as

$$\begin{aligned} \mathrm{E}\{\boldsymbol{v}_n^* \boldsymbol{v}_m^{*\mathrm{T}}\} &= \mathrm{E}\left\{ \left(\boldsymbol{H}_{n+1} \boldsymbol{w}_n + \boldsymbol{\zeta}_n \right) \left(\boldsymbol{H}_{m+1} \boldsymbol{w}_m + \boldsymbol{\zeta}_m \right)^{\mathrm{T}} \right\} \\ &= \left(\boldsymbol{H}_{n+1} \boldsymbol{Q}_n \boldsymbol{H}_{n+1}^{\mathrm{T}} + \boldsymbol{R}_n \right) \delta_{nm} \triangleq \boldsymbol{R}_n^* \delta_{nm}, \end{aligned} \tag{3.51}$$

with

$$\boldsymbol{R}_n^* = \boldsymbol{H}_{n+1} \boldsymbol{Q}_n \boldsymbol{H}_{n+1}^{\mathrm{T}} + \boldsymbol{R}_n. \tag{3.52}$$

A new correlation is introduced between $\boldsymbol{v}_n^*$ and $\boldsymbol{w}_n$ as

$$\begin{aligned} \mathrm{E}\{\boldsymbol{w}_n \boldsymbol{v}_m^{*\mathrm{T}}\} &= \mathrm{E}\left\{ \boldsymbol{w}_n \left(\boldsymbol{H}_{m+1} \boldsymbol{w}_m + \boldsymbol{\zeta}_m \right)^{\mathrm{T}} \right\} \\ &= \left(\boldsymbol{Q}_n \boldsymbol{H}_{n+1}^{\mathrm{T}} \right) \delta_{nm} \triangleq \boldsymbol{S}_n \delta_{nm}, \end{aligned} \tag{3.53}$$

with

$$\boldsymbol{S}_n = \boldsymbol{Q}_n \boldsymbol{H}_{n+1}^{\mathrm{T}}. \tag{3.54}$$

In order to decouple the measurement and process noise, Bryson and Henrikson proposed a method to generate new process noise by adding a zero term into the state transition in Eq. (3.44), i.e.

$$\begin{aligned} \boldsymbol{x}_n &= \boldsymbol{\Phi}_{n-1}\boldsymbol{x}_{n-1} + \boldsymbol{w}_{n-1} + \boldsymbol{J}_{n-1} \cdot \left(\boldsymbol{z}_{n-1}^* - \boldsymbol{H}_{n-1}^* \boldsymbol{x}_{n-1} - \boldsymbol{v}_{n-1}^*\right) \\ &\triangleq \boldsymbol{\Phi}_{n-1}^* \boldsymbol{x}_{n-1} + \boldsymbol{w}_{n-1}^* + \boldsymbol{J}_{n-1}\boldsymbol{z}_{n-1}^*, \end{aligned} \tag{3.55}$$

where the transformed state transition matrix $\boldsymbol{\Phi}_n^*$ and process noise $\boldsymbol{w}_n^*$ are defined as

$$\begin{aligned} \boldsymbol{\Phi}_n^* &= \boldsymbol{\Phi}_n - \boldsymbol{J}_n \boldsymbol{H}_n^* \\ \boldsymbol{w}_n^* &= \boldsymbol{w}_n - \boldsymbol{J}_n \boldsymbol{v}_n^*. \end{aligned} \tag{3.56}$$

The weighting matrix $\boldsymbol{J}$ is determined by constraining $\boldsymbol{v}_n^*$ and $\boldsymbol{w}_n^*$ to be uncorrelated, i.e.

$$\begin{aligned} \mathrm{E}\{\boldsymbol{w}_n^* \boldsymbol{v}_m^{*\mathrm{T}}\} &= \mathrm{E}\left\{\left(\boldsymbol{w}_n - \boldsymbol{J}_n \boldsymbol{v}_n^*\right) \boldsymbol{v}_m^{*\mathrm{T}}\right\} \\ &= \left(\boldsymbol{S}_n - \boldsymbol{J}_n \boldsymbol{R}_n^*\right) \delta_{nm} \\ &\stackrel{!}{=} \boldsymbol{0}, \end{aligned} \tag{3.57}$$

which leads to

$$\boldsymbol{J}_n = \boldsymbol{S}_n \left(\boldsymbol{R}_n^*\right)^{-1}. \tag{3.58}$$

Applying Eq. (3.56) and (3.58), the covariance matrix of the decoupled process noise $\boldsymbol{w}_n^*$ is calculated as

$$\begin{aligned} \boldsymbol{Q}_n^* &= \mathrm{E}\{\boldsymbol{w}_n^* \boldsymbol{w}_n^{*\mathrm{T}}\} \\ &= \mathrm{E}\left\{(\boldsymbol{w}_n - \boldsymbol{J}_n \boldsymbol{v}_n^*)(\boldsymbol{w}_n - \boldsymbol{J}_n \boldsymbol{v}_n^*)^{\mathrm{T}}\right\} \\ &= \mathrm{E}\left\{(\boldsymbol{w}_n - \boldsymbol{S}_n (\boldsymbol{R}_n^*)^{-1} \boldsymbol{v}_n^*)(\boldsymbol{w}_n - \boldsymbol{S}_n (\boldsymbol{R}_n^*)^{-1} \boldsymbol{v}_n^*)^{\mathrm{T}}\right\} \\ &= \boldsymbol{Q}_n - \boldsymbol{S}_n (\boldsymbol{R}_n^*)^{-1} \boldsymbol{S}_n^{\mathrm{T}} - \boldsymbol{S}_n ((\boldsymbol{R}_n^*)^{-1})^{\mathrm{T}} \boldsymbol{S}_n^{\mathrm{T}} + \boldsymbol{S}_n (\boldsymbol{R}_n^*)^{-1} \boldsymbol{R}_n^* ((\boldsymbol{R}_n^*)^{-1})^{\mathrm{T}} \boldsymbol{S}_n^{\mathrm{T}} \\ &= \boldsymbol{Q}_n - \boldsymbol{S}_n (\boldsymbol{R}_n^*)^{-1} \boldsymbol{S}_n^{\mathrm{T}}. \end{aligned} \tag{3.59}$$

Now, the new measurement noise $\boldsymbol{v}_n^*$ and the new process noise $\boldsymbol{w}_n^*$ are Gaussian distributed with zero means, and are independent from each other. The standard Kalman filter can be applied with the transformed variables. The prediction step for the state vector and its covariance matrix is given by

$$\begin{aligned} \hat{\boldsymbol{x}}_n^- &= \boldsymbol{\Phi}_{n-1}^* \hat{\boldsymbol{x}}_{n-1}^+ + \boldsymbol{J}_{n-1} \boldsymbol{z}_{n-1}^* \\ \boldsymbol{P}_n^- &= \boldsymbol{\Phi}_{n-1}^* \boldsymbol{P}_{n-1}^+ \boldsymbol{\Phi}_{n-1}^{*\mathrm{T}} + \boldsymbol{Q}_{n-1}^*. \end{aligned} \tag{3.60}$$

They are updated, through the optimal Kalman gain, as

$$\begin{aligned} \boldsymbol{K}_n &= \boldsymbol{P}_n^- \boldsymbol{H}_n^{*\mathrm{T}} \left(\boldsymbol{H}_n^* \boldsymbol{P}_n^- \boldsymbol{H}_n^{*\mathrm{T}} + \boldsymbol{R}_n^*\right)^{-1} \\ \hat{\boldsymbol{x}}_n^+ &= \hat{\boldsymbol{x}}_n^- + \boldsymbol{K}_n \left(\boldsymbol{z}_n^* - \boldsymbol{H}_n^* \hat{\boldsymbol{x}}_n^-\right) \\ \boldsymbol{P}_n^+ &= \left(\boldsymbol{1} - \boldsymbol{K}_n \boldsymbol{H}_n^*\right) \boldsymbol{P}_n^-, \end{aligned} \tag{3.61}$$

where the transformed variables are summarized as

$$\begin{aligned}
\boldsymbol{z}_n^* &= \boldsymbol{z}_{n+1} - \boldsymbol{\Gamma}_n \boldsymbol{z}_n \\
\boldsymbol{H}_n^* &= \boldsymbol{H}_{n+1} \boldsymbol{\Phi}_n - \boldsymbol{\Gamma}_n \boldsymbol{H}_n \\
\boldsymbol{S}_n &= \boldsymbol{Q}_n \boldsymbol{H}_{n+1}^{\mathrm{T}} \\
\boldsymbol{R}_n^* &= \boldsymbol{H}_{n+1} \boldsymbol{Q}_n \boldsymbol{H}_{n+1}^{\mathrm{T}} + \boldsymbol{R}_n \\
\boldsymbol{J}_n &= \boldsymbol{S}_n \left(\boldsymbol{R}_n^*\right)^{-1} \\
\boldsymbol{Q}_n^* &= \boldsymbol{Q}_n - \boldsymbol{S}_n \left(\boldsymbol{R}_n^*\right)^{-1} \boldsymbol{S}_n^{\mathrm{T}} \\
\boldsymbol{\Phi}_n^* &= \boldsymbol{\Phi}_n - \boldsymbol{J}_n \boldsymbol{H}_n^*.
\end{aligned} \tag{3.62}$$

A numerical experiment

A simple numerical experiment is carried out to apply the Bryson's method in the Kalman filter. If the correlation of the measurements between epochs were small, the measurement noise $\boldsymbol{v}_n$ would be approximated by the white noise $\boldsymbol{\zeta}_n$. A standard Kalman filter would then provide a suboptimal solution [82]. In this experiment, to compare with the decoupled Kalman filter, a standard Kalman filter is used while ignoring the temporal correlation in the measurements. The state vector is generated with an initial vector $\boldsymbol{x}_1$, an identity transition matrix $\boldsymbol{\Phi}$ and a process noise vector $\boldsymbol{w}$. The process noise $\boldsymbol{w}$ is zero-mean Gaussian distributed with covariance matrix $\boldsymbol{Q}$, i.e.

$$\boldsymbol{x}_1 = \begin{bmatrix} 0.61 \\ 0.10 \\ 1.38 \end{bmatrix}, \quad \boldsymbol{Q} = \mathrm{diag}\left(\begin{bmatrix} 2.79 \cdot 10^{-4} \\ 1.17 \cdot 10^{-3} \\ 2.67 \cdot 10^{-4} \end{bmatrix} \right). \tag{3.63}$$

According to Eq. (3.43), the measurements are generated with a random design matrix $\boldsymbol{H}$, while the measurement noise is generated with $\boldsymbol{\Gamma}$. The matrices are chosen as

$$\boldsymbol{H} = \begin{bmatrix} 8.17 & -5.91 & 2.42 \\ -11.20 & -2.53 & 3.04 \\ -1.36 & -7.49 & -1.83 \\ 7.27 & 5.30 & -7.25 \end{bmatrix}, \quad \boldsymbol{\Gamma} = \begin{bmatrix} 0.17 & 0.26 & 0.17 & 0.04 \\ -0.19 & 0.47 & -0.32 & 0.40 \\ 0.05 & -0.05 & 0.33 & -0.25 \\ -0.13 & 0.73 & 0.45 & 0.58 \end{bmatrix}. \tag{3.64}$$

The covariance matrix of the white noise $\boldsymbol{\zeta}$ is chosen randomly as

$$\boldsymbol{R} = \mathrm{diag}\left(\begin{bmatrix} 3.60 \cdot 10^{-2} \\ 1.18 \cdot 10^{-3} \\ 3.16 \cdot 10^{-2} \\ 3.18 \cdot 10^{-4} \end{bmatrix} \right), \tag{3.65}$$

with $\mathrm{diag}(\cdot)$ converting a vector to a diagonal matrix.

Fig. 3.12 shows the result of decoupling the measurements with Bryson's method. The temporal correlation is neglected in Fig. 3.12(a), which causes the divergence of the estimates. After applying Bryson's method, the filter converged after the first few epochs.

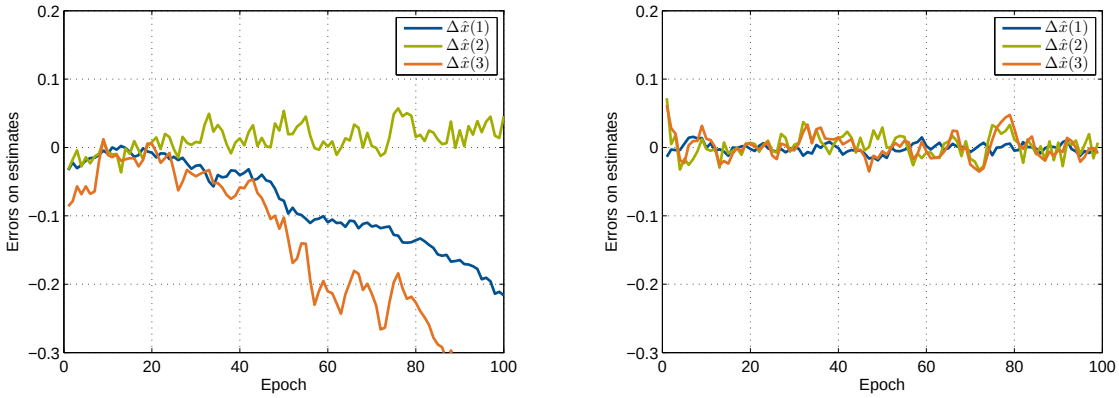

(a) The standard Kalman filter while neglecting the temporal correlation of the measurement noise.

(b) The proposed Bryson's method to decorrelate the measurement noise and process noise, which then satisfies the assumption for a Kalman filter.

Figure 3.12: The comparison of the estimation error from the standard Kalman filter and from the decoupled Kalman filter.

3.3.2 The Second-stage Kalman Filter

The geometric estimates $\Delta\hat{g}_r^k$ from the first-stage Kalman filter serve as measurements for the second-stage Kalman filter. The measurement model is given by

$$\Delta\hat{g}_r^k = (\vec{\boldsymbol{e}}_r^{\,k})^{\mathrm{T}}\Delta\vec{\boldsymbol{r}}^{\,k} + c\tilde{\tilde{\delta}}_r - c\Delta\tilde{\tilde{\delta}}^k + m_{\mathrm{T},r}^k T_{\mathrm{z},r} + \epsilon_r^k, \tag{3.66}$$

where $\Delta\vec{\boldsymbol{r}}^{\,k}$ denotes the orbital error, $c\tilde{\tilde{\delta}}_r$ denotes the receiver clock offset, $c\Delta\tilde{\tilde{\delta}}^k$ is a combination of the satellite geometric code bias and the residuals of the satellite clock offset, $T_{\mathrm{z},r}$ denotes the tropospheric zenith delay, and ϵ_r^k is the colored measurement noise. The residuals of the satellite clock offset arise from that we have subtracted a priori clock information in Eq. (3.4), e.g. the IGS final clock offset product $c\delta_{\mathrm{IGS}}^k$. Thus Eq. (3.4) becomes

$$c\Delta\tilde{\delta}^k = \underbrace{c\delta^k - c\delta_{\mathrm{IGS}}^k}_{c\Delta\delta_{\mathrm{IGS}}^k} - b_g^k. \tag{3.67}$$

It is noted that the two tildes on top of $c\tilde{\tilde{\delta}}_r$ and $c\Delta\tilde{\tilde{\delta}}^k$ come from mappings of geometric code biases and reference satellite bias, details see Section 3.1.

The state vector of the second-stage Kalman filter reads

$$\boldsymbol{x} = \left[\Delta\vec{\boldsymbol{r}}^{\,\mathrm{T}},\ \Delta\dot{\vec{\boldsymbol{r}}}^{\,\mathrm{T}},\ c\tilde{\tilde{\boldsymbol{\delta}}}_{\mathrm{R}}^{\mathrm{T}},\ c\Delta\tilde{\tilde{\boldsymbol{\delta}}}^{\mathrm{K,\,T}},\ \boldsymbol{T}_{\mathrm{z}}^{\mathrm{T}}\right]^{\mathrm{T}}, \tag{3.68}$$

with

$$\Delta\vec{\boldsymbol{r}} = \begin{bmatrix} \Delta\vec{\boldsymbol{r}}^{\,1} \\ \Delta\vec{\boldsymbol{r}}^{\,2} \\ \vdots \\ \Delta\vec{\boldsymbol{r}}^{\,K} \end{bmatrix},\quad c\tilde{\tilde{\boldsymbol{\delta}}}_{\mathrm{R}} = \begin{bmatrix} c\tilde{\tilde{\delta}}_1 \\ c\tilde{\tilde{\delta}}_2 \\ \vdots \\ c\tilde{\tilde{\delta}}_R \end{bmatrix},\quad \boldsymbol{T}_{\mathrm{z}} = \begin{bmatrix} T_{\mathrm{z},1} \\ T_{\mathrm{z},2} \\ \vdots \\ T_{\mathrm{z},R} \end{bmatrix}, \tag{3.69}$$

and the satellite code geometric bias vector being

$$c\Delta\tilde{\tilde{\boldsymbol{\delta}}}^{\mathrm{K}} = \left[c\Delta\tilde{\tilde{\delta}}^{1}, \ldots, c\Delta\tilde{\tilde{\delta}}^{\ell-1}, c\Delta\tilde{\tilde{\delta}}^{\ell+1}, \ldots, c\Delta\tilde{\tilde{\delta}}^{K}\right]^{\mathrm{T}}, \tag{3.70}$$

where R and K denote the number of available stations and satellites. One satellite bias $c\Delta\tilde{\delta}^{\ell}$ has been chosen as reference and is mapped away to form a full-rank system. The state vector of orbital error rate $\Delta\dot{\vec{\boldsymbol{r}}}$ has a similar structure with $\Delta\vec{\boldsymbol{r}}$.

The orbital error is assumed to follow a linear state space model, and its rate follows a random-walk process as

$$\begin{aligned} \Delta\vec{\boldsymbol{r}}_{n}^{\,k} &= \Delta\vec{\boldsymbol{r}}_{n-1}^{\,k} + \Delta t\Delta\dot{\vec{\boldsymbol{r}}}_{n-1}^{\,k} + \boldsymbol{w}_{\Delta\vec{\boldsymbol{r}}_{n-1}^{\,k}}, \\ \Delta\dot{\vec{\boldsymbol{r}}}_{n}^{\,k} &= \Delta\dot{\vec{\boldsymbol{r}}}_{n-1}^{\,k} + \boldsymbol{w}_{\Delta\dot{\vec{\boldsymbol{r}}}_{n-1}^{\,k}}, \end{aligned} \tag{3.71}$$

with Δt being the epoch interval. The process noise $\boldsymbol{w}_{\Delta\vec{\boldsymbol{r}}}$ and $\boldsymbol{w}_{\Delta\dot{\vec{\boldsymbol{r}}}}$ has zero mean, and their covariance matrix $\boldsymbol{\Sigma}_{\mathrm{Q},\Delta\vec{\boldsymbol{r}}\Delta\dot{\vec{\boldsymbol{r}}}}$ is calculated as

$$\boldsymbol{\Sigma}_{\mathrm{Q},\Delta\vec{\boldsymbol{r}}\Delta\dot{\vec{\boldsymbol{r}}}} = \sigma^{2}_{\Delta\dot{\vec{\boldsymbol{r}}}} \cdot \begin{bmatrix} \frac{1}{3}\Delta t^{4} & \frac{1}{2}\Delta t^{3} \\ \frac{1}{2}\Delta t^{3} & \Delta t^{2} \end{bmatrix} \otimes \mathbf{1}_{3K}. \tag{3.72}$$

The receiver clock offsets, the tropospheric zenith delays and the satellite geometric code biases are modelled as random walk variables, with the process noise standard deviation denoted as $\sigma_{c\tilde{\tilde{\delta}}_{\mathrm{R}}}$, $\sigma_{T_{\mathrm{z}}}$ and $\sigma_{c\Delta\tilde{\tilde{\delta}}^{\mathrm{K}}}$ respectively.

The method of Bryson and Henrikson is applied to decouple the colored measurement noise in Eq. (3.66). There are yet two unknowns in Eq. (3.62) to be determined, the $\boldsymbol{\Gamma}$ matrix describing the temporal relationship of the measurement noise and the covariance matrix $\boldsymbol{R}$ of the whitened noise $\boldsymbol{\zeta}$.

Because the measurement noise $\boldsymbol{v}_n$ of the second-stage comes from the first-stage geometric estimate $\Delta\hat{\boldsymbol{g}}_{n}^{+}$, the temporal covariance is defined by

$$\mathrm{E}\{\boldsymbol{v}_n\boldsymbol{v}_{n-1}^{\mathrm{T}}\} = \mathrm{E}\{(\Delta\hat{\boldsymbol{g}}_{n}^{+} - \Delta\boldsymbol{g}_n)(\Delta\hat{\boldsymbol{g}}_{n-1}^{+} - \Delta\boldsymbol{g}_{n-1})^{\mathrm{T}}\}. \tag{3.73}$$

Applying the state prediction and update equations from the first-stage Kalman filter, as well as the measurement model for $\boldsymbol{z}_n$ and the state transition model for $\boldsymbol{x}_n$, one obtains

$$\begin{aligned} &\mathrm{E}\{\boldsymbol{v}_n\boldsymbol{v}_{n-1}^{\mathrm{T}}\} \\ &= \mathrm{E}\{\left(\Delta\hat{\boldsymbol{g}}_{n}^{-} + \boldsymbol{K}_g(\boldsymbol{z}_n - \boldsymbol{H}_n\hat{\boldsymbol{x}}_{n}^{-}) - \Delta\boldsymbol{g}_n\right)\left(\Delta\hat{\boldsymbol{g}}_{n-1}^{+} - \Delta\boldsymbol{g}_{n-1}\right)^{\mathrm{T}}\} \\ &= \mathrm{E}\{\left(\boldsymbol{\Phi}_g\Delta\hat{\boldsymbol{g}}_{n-1}^{+} + \boldsymbol{K}_g(\boldsymbol{z}_n - \boldsymbol{H}_n\hat{\boldsymbol{x}}_{n}^{-}) - \Delta\boldsymbol{g}_n\right)\left(\Delta\hat{\boldsymbol{g}}_{n-1}^{+} - \Delta\boldsymbol{g}_{n-1}\right)^{\mathrm{T}}\} \\ &= \mathrm{E}\{\left(\boldsymbol{\Phi}_g\Delta\hat{\boldsymbol{g}}_{n-1}^{+} + \boldsymbol{K}_g(\boldsymbol{z}_n - \boldsymbol{H}_n\hat{\boldsymbol{x}}_{n}^{-}) - (\boldsymbol{\Phi}_g\Delta\boldsymbol{g}_{n-1} + \boldsymbol{w}_{n-1})\right)\left(\Delta\hat{\boldsymbol{g}}_{n-1}^{+} - \Delta\boldsymbol{g}_{n-1}\right)^{\mathrm{T}}\} \\ &= \mathrm{E}\{\left(\boldsymbol{\Phi}_g\Delta\hat{\boldsymbol{g}}_{n-1}^{+} + \boldsymbol{K}_g(\boldsymbol{H}_n\boldsymbol{x}_n + \boldsymbol{v}_n - \boldsymbol{H}_n\hat{\boldsymbol{x}}_{n}^{-}) - (\boldsymbol{\Phi}_g\Delta\boldsymbol{g}_{n-1} + \boldsymbol{w}_{n-1})\right)\left(\Delta\hat{\boldsymbol{g}}_{n-1}^{+} - \Delta\boldsymbol{g}_{n-1}\right)^{\mathrm{T}}\} \\ &= \mathrm{E}\{\left(\boldsymbol{\Phi}_g\Delta\hat{\boldsymbol{g}}_{n-1}^{+} + \boldsymbol{K}_g(\boldsymbol{H}_n(\boldsymbol{\Phi}\boldsymbol{x}_{n-1} + \boldsymbol{w}_{n-1}) + \boldsymbol{v}_n - \boldsymbol{H}_n\boldsymbol{\Phi}\hat{\boldsymbol{x}}_{n-1}^{+}) - (\boldsymbol{\Phi}_g\Delta\boldsymbol{g}_{n-1} + \boldsymbol{w}_{n-1})\right) \cdot \\ &\qquad \cdot \left(\Delta\hat{\boldsymbol{g}}_{n-1}^{+} - \Delta\boldsymbol{g}_{n-1}\right)^{\mathrm{T}}\}, \end{aligned} \tag{3.74}$$

where $\boldsymbol{K}_g$, $\boldsymbol{\Phi}_g$ denote the geometric parts of the Kalman gain matrix $\boldsymbol{K}$ and the state transition matrix $\boldsymbol{\Phi}$ respectively. As the process noise $\boldsymbol{w}_{n-1}$ and the measurement noise $\boldsymbol{v}_n$

do not occur until epoch n, there exists no correlation between the noise and the geometric estimate $\Delta\hat{\boldsymbol{g}}^{+}_{n-1}$ at epoch $n-1$. Therefore, the temporal covariance $\mathrm{E}\{\boldsymbol{v}_n\boldsymbol{v}^{\mathrm{T}}_{n-1}\}$ in Eq. (3.74) is further derived as

$$\begin{aligned}\mathrm{E}\{\boldsymbol{v}_n\boldsymbol{v}^{\mathrm{T}}_{n-1}\} &= \mathrm{E}\{\left(\boldsymbol{\Phi}_g(\Delta\hat{\boldsymbol{g}}^{+}_{n-1} - \Delta\boldsymbol{g}_{n-1}) - \boldsymbol{K}_g\boldsymbol{H}_n\boldsymbol{\Phi}(\hat{\boldsymbol{x}}^{+}_{n-1} - \boldsymbol{x}_{n-1})\right)\left(\Delta\hat{\boldsymbol{g}}^{+}_{n-1} - \Delta\boldsymbol{g}_{n-1}\right)^{\mathrm{T}}\} \\ &= \boldsymbol{\Phi}_g\boldsymbol{P}^{+}_{n-1,\,g} - \boldsymbol{K}_g\boldsymbol{H}_n\boldsymbol{\Phi}\boldsymbol{P}^{+}_{n-1,\,x,\,g}, \end{aligned} \tag{3.75}$$

where $\boldsymbol{P}^{+}_{n-1,\,g}$ denotes the a posteriori covariance matrix for geometric states, and $\boldsymbol{P}^{+}_{n-1,\,x,\,g}$ denotes the covariance matrix between all states and the geometric terms. Fig. 3.13 provides an illustrative overview for the selection of the state transition matrix $\boldsymbol{\Phi}_g$, of the Kalman gain matrix $\boldsymbol{K}_g$, and of the covariance matrix $\boldsymbol{P}^{+}_{g}$ and $\boldsymbol{P}^{+}_{x,\,g}$.

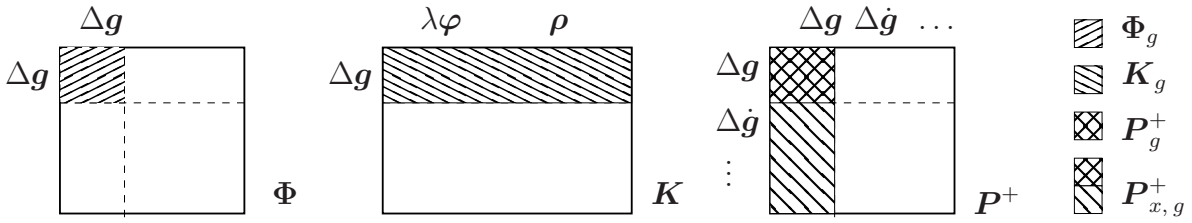

Figure 3.13: Illustration of the involved sub-matrices in the derivation for the temporal covariance matrix.

On the other hand, the matrix $\boldsymbol{\Gamma}_n$ in Eq. (3.43) also describes the relationship between $\boldsymbol{v}_n$ and $\boldsymbol{v}_{n-1}$, while no correlation exists between $\boldsymbol{v}_{n-1}$ and $\boldsymbol{\zeta}_{n-1}$ i.e.

$$\mathrm{E}\{\boldsymbol{v}_n\boldsymbol{v}^{\mathrm{T}}_{n-1}\} = \boldsymbol{\Gamma}_{n-1}\cdot\mathrm{E}\{\boldsymbol{v}_{n-1}\boldsymbol{v}^{\mathrm{T}}_{n-1}\} = \boldsymbol{\Gamma}_{n-1}\cdot\boldsymbol{P}^{+}_{n-1,\,g}. \tag{3.76}$$

Combining Eq. (3.75) and Eq. (3.76) yields

$$\boldsymbol{\Gamma}_n = \boldsymbol{\Phi}_g - \boldsymbol{K}_g\boldsymbol{H}_{n+1}\boldsymbol{\Phi}\boldsymbol{P}^{+}_{n,\,x,\,g}\cdot(\boldsymbol{P}^{+}_{n,\,g})^{-1} \tag{3.77}$$

The statistics for the noise $\boldsymbol{\zeta}_n$ in the transition equation (3.43) of the measurement noise can now be determined, namely the covariance $\boldsymbol{R}_n$ is calculated as

$$\begin{aligned}\boldsymbol{R}_n &= \mathrm{E}\{\boldsymbol{\zeta}_n\boldsymbol{\zeta}^{\mathrm{T}}_n\} \\ &= \mathrm{E}\{(\boldsymbol{v}_{n+1} - \boldsymbol{\Gamma}_n\boldsymbol{v}_n)((\boldsymbol{v}_{n+1} - \boldsymbol{\Gamma}_n\boldsymbol{v}_n)^{\mathrm{T}}\} \\ &= \boldsymbol{P}^{+}_{n+1,\,g} - \boldsymbol{\Gamma}_n\mathrm{E}\{\boldsymbol{v}_n\boldsymbol{v}^{\mathrm{T}}_{n+1}\} - \mathrm{E}\{\boldsymbol{v}_{n+1}\boldsymbol{v}^{\mathrm{T}}_n\}\boldsymbol{\Gamma}^{\mathrm{T}}_n + \boldsymbol{\Gamma}_n\boldsymbol{P}^{+}_{n,\,g}\boldsymbol{\Gamma}^{\mathrm{T}}_n \\ &= \boldsymbol{P}^{+}_{n+1,\,g} - \boldsymbol{\Gamma}_n\boldsymbol{P}^{+}_{n,\,g}\boldsymbol{\Gamma}^{\mathrm{T}}_n, \end{aligned} \tag{3.78}$$

where the last step is realized by Eq. (3.76).

3.3.3 Real Data Analysis

Using the results from the global IGS network of 40 reference stations in Section 3.2.4, we apply Bryson's method to decouple the colored measurement noise on the geometric estimates. The state estimates include the along- and cross-track orbital errors, the receiver clock offsets, the geometric code biases and the tropospheric zenith delays. Due to the high

correlation of the radial orbital error and the satellite clock offset, the radial component is assumed to be corrected precisely. The IGS final satellite orbits and satellite clock offsets are corrected in the first-stage Kalman filter. The accuracies of the products are used as a priori information for the second-stage Kalman filter, i.e. 2 cm for the orbital corrections and clock offsets.

The orbital drifts are modelled as random-walk processes, while the standard deviation of the process noise is set to 1 cm/s. The process noise for the receiver clock offsets, the geometric code biases and the tropospheric zenith delays is assumed to follow zero-mean Gaussian distributions, having standard deviations of 1 m, 2 cm and 1 mm.

The geometric code bias estimates are shown in Fig. 3.14. The most bias estimates converge to within ± 30cm. The variations of most bias estimates are around 5 cm, very few up to several tens of centimeters. It is expected that, by increasing the number of reference stations (e.g. to 100 stations) the station geometry can be improved to better model the satellite orbits. Thus the bias estimation and stability can be improved.

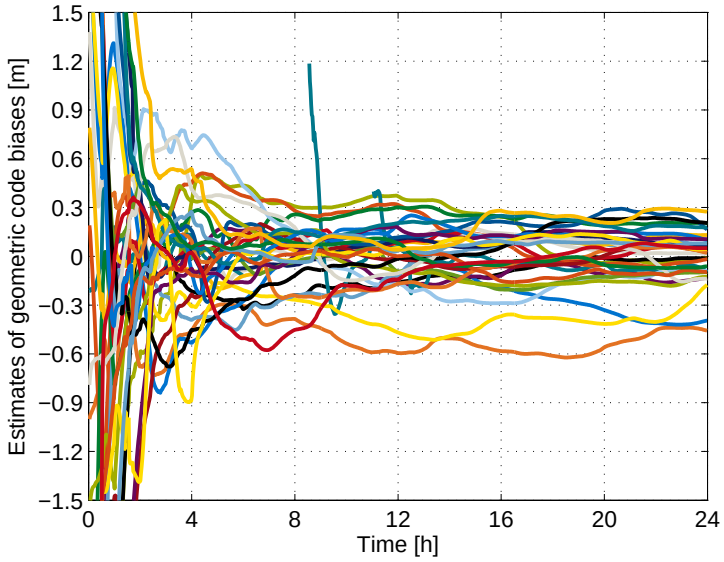

Figure 3.14: The geometric code bias estimates over 24 hours, with the most of them converging within ±30 cm. The "outlier" after the 8th hour represents PRN 8, while before that the satellite was not visible to any stations and was re-introduced to the system.

Tab. 3.5 lists the estimates of orbital errors and geometric code biases. The PRN 1 was chosen as the reference satellite, therefore no entries are existed for the code biases of PRN 1. Most of the along- and cross-track orbital errors lie within ±5 cm, with two outliers from PRN 9 and PRN 19 having errors up to 20 cm. The code geometric bias estimates lie within ±30 cm with outliers of PRN 3 and PRN 6. The reason to this is unclear and can unfortunately not be clarified in this thesis.

It is noted that the quality of the bias estimates indicates an accuracy of 1mm. However, this is believed to be too optimistic. The measurement noise covariance matrix comes from the the state covariance matrix of the first-stage Kalman filter. It has experienced two filters to obtain the covariance output.

k	$\Delta\hat{r}^k_{\text{Along}}$ [m]	$\Delta\hat{r}^k_{\text{Cross}}$ [m]	$c\Delta\hat{\tilde{\delta}}^k$ [m]	$\sigma_{c\Delta\hat{\tilde{\delta}}^k}$ [m]
1	0.001	-0.028	-	-
2	0.004	-0.01	-0.009	0.001
3	-0.04	-0.043	-0.457	0.001
4	-0.012	0.016	-0.014	0.001
5	-0.01	-0.013	0.02	0.001
6	0.038	-0.027	-0.395	0.001
7	0.025	0.001	-0.13	0.001
8	-0.013	0.019	-0.097	0.002
9	0.082	0.201	-0.174	0.001
10	0.005	-0.001	-0.018	0.001
11	0.052	-0.067	0.081	0.001
12	0.011	0.009	0.206	0.001
13	-0.01	0.001	0.131	0.001
14	-0.019	-0.013	0.059	0.001
15	0.005	-0.005	0.06	0.001
16	0.001	0.036	-0.089	0.001
17	0.021	-0.017	-0.097	0.001
18	-0.033	0.001	0.024	0.001
19	-0.204	0.012	0.164	0.001
20	0.011	0.017	-0.125	0.001
21	-0.021	-0.011	0.021	0.001
22	0.001	-0.007	0.205	0.001
23	0.001	-0.038	-0.137	0.001
24	-0.025	0.016	0.1	0.001
25	0.03	-0.024	0.106	0.001
26	0.001	0.001	0.178	0.001
27	-0.031	-0.016	0.044	0.001
28	0.008	0.019	-0.097	0.001
29	0.001	0.001	0.079	0.001
30	0.025	-0.011	-0.06	0.001
31	-0.025	0.002	0.274	0.001
32	0.004	-0.002	0.05	0.001

Table 3.5: Estimates from the second-stage Kalman filter at the last epoch. Columns from left to right: the satellite PRN numbers, the orbital error estimates, the geometric code bias estimates and the standard deviations of the code biases.

3.4 Conclusions

In this chapter, we have proposed a new method to estimate the satellite phase and code biases. The geometric and ionospheric terms were estimated as whole parameters and were split in a separate next stage. The first-stage output the satellite phase bias estimates, while the geometric code biases are obtained from the second filter. Bryson's method

was introduced to decouple the colored measurement noise. Additionally, code multipath from GPS signals can be strongly suppressed by sidereal filtering in static scenarios, i.e. averaging code residuals over multiple sidereal days. The proposed algorithms were tested with real GPS data, from both a regional SAPOS network and a global IGS network. The bias estimation accuracy was shown to be at centimeter to millimeter level. In the next chapter, we will focus on the other part of the second stage, namely the ionospheric estimation. The slant ionospheric estimates from the first-stage will be used to determine the ionospheric code biases.

Chapter 4

Estimation of Ionospheric Code Biases

The propagation delay in the ionosphere is one of the largest error sources in GNSS positioning. Besides, the ionospheric delay observables are often coupled with unknown inter-frequency biases due to the transmitting and receiving hardware, or known as differential code biases or ionospheric biases. The research on ionospheric estimation is of great importance. Single-frequency receivers rely highly on modelling or external inputs on ionospheric delays and biases. Dual-frequency receivers normally form an ionosphere-free combination, however, ionospheric biases need to be free from the choice of linear combinations. Uncombined ionospheric biases are beneficial for multi-frequency approaches. Besides, the ionospheric delays can also be brought in as a priori information. Last but not least, the ionospheric estimation can potentially provide higher order corrections.

The ionospheric delay is proportional to the total electron density, which is mostly concentrated between 250 and 400 km. The ionosphere is usually modelled as a thin shell at a reference height h being $h = 350\,\mathrm{km}$. This is fulfilled under sufficiently homogeneous and isotropic ionosphere [1]. The thin shell assumes the total electron content a scalar at each point instead of a distribution along the path, which significantly reduces the complexity. The slant ionospheric delay $I^k_{1,r}$ is associated to the vertical delay $I^k_{1,\mathrm{v},r}$ by a mapping function $m^k_{\mathrm{I},r}$, i.e.

$$I^k_{1,r} = m^k_{\mathrm{I},r} \cdot I^k_{1,\mathrm{v},r}, \tag{4.1}$$

where the index "1" indicates the frequency and is omitted from now on for simplicity. A simplified illustration of the single layer model is seen in Fig. 4.1. The vertical delay $I^k_{\mathrm{v},r}$ is calculated at the ionospheric pierce point (IPP), the intersection between the path and the single layer. The latitude and longitude of the IPP is denoted by (ϕ^k_r, λ^k_r).

The coordinates of the IPP can be calculated from the receiver coordinates $\vec{\boldsymbol{r}}_r$ and the unit vector $\vec{\boldsymbol{e}}_r^{\,k}$ as

$$\vec{\boldsymbol{r}}_{\mathrm{IPP}} = \vec{\boldsymbol{r}}_r - d^k_r \cdot \vec{\boldsymbol{e}}_r^{\,k}, \tag{4.2}$$

where the distance d^k_r between the receiver and the pierce point is obtained from cosine's law as

$$d^k_r = -R_\mathrm{e} \sin E^k_r + \sqrt{R^2_\mathrm{e} \sin^2 E^k_r - (R^2_\mathrm{e} - (R_\mathrm{e} + h)^2)}. \tag{4.3}$$

The mapping function $m^k_{\mathrm{I},r}$ depends on the elevation angle E^k_r and is determined as

$$m^k_{\mathrm{I},r} = \frac{1}{\sqrt{1 - \dfrac{\cos^2 E^k_r}{(1 + h/R_\mathrm{e})^2}}}, \tag{4.4}$$

with R_e being the radius of the earth.

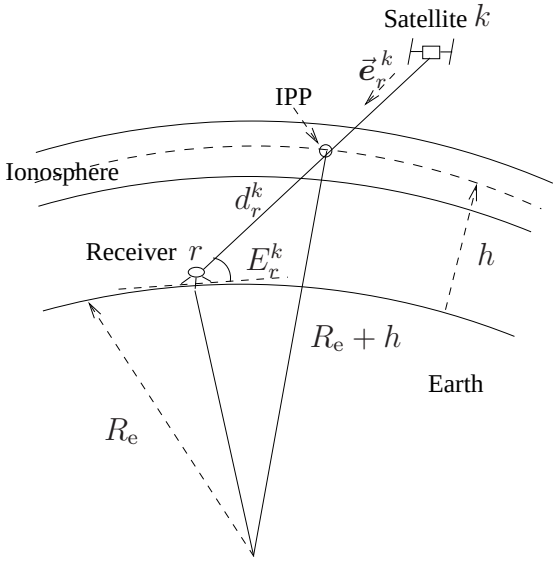

Figure 4.1: The single layer model for the ionosphere. The slant delay on the path is represented by the vertical delay at the IPP and a mapping function.

According to Eq. (3.4), the raw slant ionospheric delay measurements have absorbed the receiver and satellite code ionospheric biases $b_{I,r}$ and b_I^k. The measurement model is given by

$$\tilde{I}_r^k = m_{\mathrm{I},r}^k I_{\mathrm{v},r}^k + b_{I,r} + b_I^k + \epsilon_{\mathrm{I},r}^k, \tag{4.5}$$

with $\epsilon_{\mathrm{I},r}^k$ denoting the measurement noise. As implied in Eq. (3.3), the ionospheric biases $b_{I,r}$ and b_I^k are obtained from the absolute biases by

$$b_{I,r} = \frac{f_2^2}{f_1^2 - f_2^2} \cdot (b_{2,r} - b_{1,r}), \quad b_I^k = \frac{f_2^2}{f_1^2 - f_2^2} \cdot (b_2^k - b_1^k). \tag{4.6}$$

Eq. (4.5) implies that there are as many vertical delays as slant delays. The system is thus rank-deficient to solve all vertical delays and the code biases. Therefore, a proper modelling for the vertical ionospheric delay is needed for the joint estimation. The Klobuchar model [40] is a simple way to model the vertical delay, but is only capable of accounting for about 50% of the ionospheric delay under nominal conditions. Several conventional methods are presented in the following section, including the least-squares planar fit, the bicubic splines interpolation, the NTCM-GL model, and the Kriging method. In section 4.2, a new ionospheric estimation method is introduced with the Kriging method used to model the ionospheric TEC. Results from simulation and real GPS data are presented in the last section.

4.1 Conventional Strategies

In this section some state-of-the-art ionospheric models are presented, such as planar fitting, spherical harmonics and splines fitting, and Neustrelitz TEC Global Model. The models are described in details in the following sub-sections.

4.1.1 Planar Fit

The Wide Area Augmentation System (WAAS) has initially adopted a least-squares planar fit method as the ionospheric total electron content (TEC) model . The TECV (vertical TEC) at a grid point is estimated by fitting the vertical delays at the surrounding pierce points to a plane, which is centered around the grid point. Assume the grid point is located at geomagnetic latitude ϕ_0 and longitude λ_0, the vertical delay at the pierce point, with geomagnetic latitude and longitude $(\phi^k_{\mathrm{m},r}, \lambda^k_{\mathrm{m},r})$, can be expressed by

$$I^k_{\mathrm{v},r} = I_0 + i_{\phi_0}(\phi^k_{\mathrm{m},r} - \phi_0) + i_{\lambda_0}(\lambda^k_{\mathrm{m},r} - \lambda_0), \tag{4.7}$$

with I_0 being the vertical delay at the grid point, i_{ϕ_0} and i_{λ_0} denoting the latitudinal and longitudinal gradient of the plane respectively. The coefficients I_0, i_{ϕ_0} and i_{λ_0} are determined in a least-squares estimation as

$$\begin{bmatrix} \hat{I}_0 \\ \hat{i}_{\phi_0} \\ \hat{i}_{\lambda_0} \end{bmatrix} = \underset{\begin{bmatrix} I_0 \\ i_{\phi_0} \\ i_{\lambda_0} \end{bmatrix}}{\operatorname{argmin}} \left\| \boldsymbol{I}_v - \boldsymbol{H}_{I_0} \cdot \begin{bmatrix} I_0 \\ i_{\phi_0} \\ i_{\lambda_0} \end{bmatrix} \right\|^2_{\boldsymbol{\Sigma}^{-1}}, \tag{4.8}$$

where the included pierce points are constrained to the surrounding region of the grid point by the radius R_{fit}

$$\left\| \vec{\boldsymbol{r}}^{\,k}_{\mathrm{IPP},r} - \vec{\boldsymbol{r}}_0 \right\| \leq R_{\mathrm{fit}}. \tag{4.9}$$

The vertical delay measurement vector $\boldsymbol{I}_v$ is obtained from the bias-corrected slant delays projected to the vertical direction, and reads

$$\boldsymbol{I}_v = \begin{bmatrix} \frac{1}{m^1_{\mathrm{I},1}} & & \\ & \ddots & \\ & & \frac{1}{m^K_{\mathrm{I},R}} \end{bmatrix} \cdot \begin{bmatrix} \tilde{I}^1_1 - \hat{b}_{\mathrm{I},1} - \hat{b}^1_{\mathrm{I}} \\ \vdots \\ \tilde{I}^K_R - \hat{b}_{\mathrm{I},R} - \hat{b}^K_{\mathrm{I}} \end{bmatrix}, \tag{4.10}$$

where R receivers and K visible satellites are assumed to contribute to the fit. In the WAAS estimation scheme, the differential biases have been estimated with a global network approach, where the TECV is modelled with bicubic splines [17]. The design matrix is obtained straightforward from Eq. (4.7) as

$$\boldsymbol{H}_{I_0} = \begin{bmatrix} 1 & \phi^1_1 - \phi_0 & \lambda^1_1 - \lambda_0 \\ \vdots & \vdots & \vdots \\ 1 & \phi^K_R - \phi_0 & \lambda^K_R - \lambda_0 \end{bmatrix}. \tag{4.11}$$

The quality of the planar fit relies apparently on the fit radius R_{fit}. When the ionospheric spatial gradients are large (e.g. ionosphere at low latitudes), the fit radius is expected to be smaller to improve the accuracy. However, smaller radius means less pierce points used for the planar fit, which may lower the integrity of the corrections. The fit radius is set to around 2000 km for WAAS [17].

The planar fit approach can be further applied to the joint estimation of the TECVs and biases, as we fit one or multiple planes around pre-selected grid points to cover the ionosphere. The number of unknowns is reduced from the number of IPPs to three coefficients for each plane. If there exists intersection between different fitting planes, a transition plane can be introduced which is a weighted sum over the involved planes. Therefore, the model for the vertical delay is described by

$$I^k_{\mathrm{v},r} = \sum_{\ell=1}^{L^k_r} \alpha^k_{\ell,r} \left(I_\ell + i_{\phi_\ell}(\phi^k_{\mathrm{m},r} - \phi_\ell) + i_{\lambda_\ell}(\lambda^k_{\mathrm{m},r} - \lambda_\ell) \right), \quad \text{s.t.} \sum_{\ell=1}^{L^k_r} \alpha^k_{\ell,r} = 1, \tag{4.12}$$

with L^k_r representing the number of involved fit planes for the pierce point from satellite k to receiver r. The weights can be chosen based on the distance between the pierce point and the grid points. As normally the planes would not intersect too much with each other, the weights can be selected equally in the practice, i.e. $\alpha^k_{\ell,r} = 1/L^k_r$.

The measurement model for the joint estimation is given by

$$\tilde{\boldsymbol{I}} = \boldsymbol{M} \cdot \boldsymbol{H}_I \cdot \boldsymbol{i} + \boldsymbol{H}_{b_{\mathrm{I,R}}} \cdot \boldsymbol{b}_{\mathrm{I,R}} + \boldsymbol{H}_{b^{\mathrm{K}}_{\mathrm{I}}} \cdot \boldsymbol{b}^{\mathrm{K}}_{\mathrm{I}} + \boldsymbol{\epsilon}_{\mathrm{I}}, \tag{4.13}$$

where the state vectors for the fit planes and the biases are constructed by

$$\begin{aligned} \boldsymbol{i} &= [I_1,\, i_{\phi_1},\, i_{\lambda_1}, \ldots,\, I_L,\, i_{\phi_L},\, i_{\lambda_L}]^{\mathrm{T}}, \\ \boldsymbol{b}_{\mathrm{I,R}} &= [b_{\mathrm{I},1},\, b_{\mathrm{I},2}, \ldots,\, b_{\mathrm{I},R}]^{\mathrm{T}}, \\ \boldsymbol{b}^{\mathrm{K}}_{\mathrm{I}} &= \left[b^1_{\mathrm{I}}, \ldots,\, b^{\ell-1}_{\mathrm{I}},\, b^{\ell+1}_{\mathrm{I}}, \ldots,\, b^K_{\mathrm{I}}\right]^{\mathrm{T}}, \end{aligned} \tag{4.14}$$

with L being the total number of grid points. The measurement noise vector is denoted by $\boldsymbol{\epsilon}_{\mathrm{I}}$. Similar with the estimation of phase biases, one satellite bias b^ℓ_{I} is mapped away. The matrix $\boldsymbol{M}$ is a diagonal matrix with the mapping functions on the diagonal. The design matrix $\boldsymbol{H}_I$ has now $3L$ columns, while each row $\boldsymbol{h}^{k,\mathrm{T}}_r$ represents the coefficients for the TECV at one pierce point and has the form of

$$\boldsymbol{h}^{k,\mathrm{T}}_r = \left[\boldsymbol{a}^{\mathrm{T}}_1,\, \boldsymbol{a}^{\mathrm{T}}_2, \ldots,\, \boldsymbol{a}^{\mathrm{T}}_L\right]. \tag{4.15}$$

The coefficient vector $\boldsymbol{a}^{\mathrm{T}}_\ell$ at one grid point ℓ is given by

$$\boldsymbol{a}^{\mathrm{T}}_\ell = \begin{cases} \left[\dfrac{1}{L^k_r},\, \dfrac{1}{L^k_r}(\phi^k_r - \phi_\ell),\, \dfrac{1}{L^k_r}(\lambda^k_r - \lambda_\ell)\right], & \left\| \vec{\boldsymbol{r}}^{\,k}_{\mathrm{IPP},r} - \vec{\boldsymbol{r}}_\ell \right\| \le R_{\mathrm{fit}}, \\ [0,\, 0,\, 0], & \text{else.} \end{cases} \tag{4.16}$$

The state vector can be estimated in a least-squares method or a Kalman filter.

Furthermore, Coco et al. have proposed a second-order polynomial fitting in [83], where the vertical TEC is represented by a two-dimensional quadratic model as

$$\begin{aligned} I^k_{v,r} = {} & c_1 + c_2 \cdot (\phi^k_{\mathrm{m},r} - \phi_0) + c_3 \cdot (\lambda^k_{\mathrm{cr},r} - \lambda_{\mathrm{cr},0}) + c_4 \cdot (\phi^k_{\mathrm{m},r} - \phi_0)^2 + c_5 \cdot (\lambda^k_{\mathrm{cr},r} - \lambda_{\mathrm{cr},0})^2 + \\ & c_6 \cdot (\phi^k_{\mathrm{m},r} - \phi_0) \cdot (\lambda^k_{\mathrm{cr},r} - \lambda_{\mathrm{cr},0}), \end{aligned} \tag{4.17}$$

with $\lambda^k_{\mathrm{cr},r}$ being the longitude of the pierce point in the co-rotating reference frame, and c_1 through c_6 are the coefficients to be determined. The differential biases as well as the six coefficients can be determined by a least-squares estimation process.

The longitude in the co-rotating frame depends on both the longitude in the ECEF frame and the rotation of the ECEF frame relative to the sun, i.e.

$$\lambda^k_{\mathrm{cr},r} = \lambda^k_r + \omega_\mathrm{e} \cdot T, \tag{4.18}$$

with ω_e denoting the angular velocity of the earth and T being the time of day.

4.1.2 Global Ionospheric Mapping Approach

In the IGS ionospheric estimation process, the ionosphere is modelled globally in a solar-geomagnetic frame with around 200 stations, while the receiver and satellite differential biases are estimated as daily constants [84]. Different strategies have been applied by several ionospheric analysis centers, where a generalized model for the global ionospheric TEC and bias estimation is proposed in [19, 20] as

$$\tilde{I}^k_r = m^k_{\mathrm{I},r} \cdot \sum_i c_i B_i(\phi^k_{\mathrm{m},r}, \lambda^k_{\mathrm{m},r}) + b_{I,r} + b^k_I + \epsilon^k_{\mathrm{I},r}, \tag{4.19}$$

with $B_i(\phi^k_{\mathrm{m},r}, \lambda^k_{\mathrm{m},r})$ denoting the horizontal basis function evaluated at the pierce point having geomagnetic latitude and longitude $(\phi^k_{\mathrm{m},r}, \lambda^k_{\mathrm{m},r})$, and c_i being the coefficients to be determined together with the differential biases. The basis function could be based on bilinear interpolation or bicubic splines. A Kalman filter can be employed to solve the coefficients and the biases which are assumed to vary as random walk processes. The vector of the fit coefficient estimates combined with the basis functions defines a global TEC distribution that provides interpolated values covering the entire sphere.

The model used by the Jet Propulsion Laboratory (JPL) covers the ionosphere with spherical triangles, where bicubic splines are used as basis functions and the vertex TEC values are the estimated coefficients. The construction of the triangular tiling is presented by Mannucci et al. in [85]. First, an icosahedron is projected onto the sphere, with two of the 12 vertices aligned at the north and south pole. The 12 vertices define 20 equilateral spherical triangles on the sphere. Each triangle is then subdivided into four smaller spherical triangles, by bisecting all three sides of the triangle and connecting the new vertices. The subdivision procedure could be performed repeatedly. The current used model for the global TEC map at JPL has 1280 spherical triangles.

Other analysis centers such as the Center for Orbit Determination in Europe (CODE) and European Space Operation Center (ESOC), applies a series of spherical harmonic expansions up to degree and order 15 to model the global TEC [86, 87], i.e.

$$I^k_{\mathrm{v},r} = \sum_{n=0}^{15} \sum_{m=0}^{n} \bar{P}_{nm}(\sin \phi^k_{\mathrm{m},r}) \left(C_{nm} \cos(m\lambda^k_{\mathrm{m},r}) + S_{nm} \sin(m\lambda^k_{\mathrm{m},r}) \right), \tag{4.20}$$

where $\bar{P}_{nm}$ denotes the normalized associated Legendre function for degree n and order m, and C_{nm} and S_{nm} represent the unknown spherical harmonic coefficients.

4.1.3 Neustrelitz TEC Model

Jakowski, Hoque and Mayer have recently proposed [18] an empirical ionospheric model, namely the Global Neustrelitz TEC model (NTCM-GL). It describes an average behavior

of a nominal ionosphere, and models the spatial and temporal variations of the ionosphere on a global scale. The model has comparable performance to the NeQuick model, which is an ionospheric electron density model developed for the Galileo system. However, the NTCM-GL model has a great advantage that it does not require numerical integrations and has a much smaller set of parameters. It is thus easily accessible.

The NTCM-GL model describes the vertical TEC by a product of five factors, i.e.

$$I_{\mathrm{v}} = F_1(\phi, \delta, t) \cdot F_2(t_d) \cdot F_3(\phi_m) \cdot F_4(\phi_m) \cdot F_5(F_{10.7}), \tag{4.21}$$

in units of TECU. The factors indicate different dependencies and are given by

$$\begin{aligned}
F_1(\phi, \delta, t) &= 0.4 + \cos(\phi - \delta) + (c_1 \cos V_{\mathrm{D}} + c_2 \cos V_{\mathrm{SD}} + c_3 \sin V_{\mathrm{SD}} + c_4 \cos V_{\mathrm{TD}} + \\
&\quad + c_5 \sin V_{\mathrm{TD}}) \cdot \left(\cos(\phi - \delta) - \frac{2\phi}{\pi} \sin \delta \right) \\
F_2(t_d) &= 1 + c_6 \cos V_{\mathrm{A}} + c_7 \sin V_{\mathrm{SA}} \\
F_3(\phi_m) &= 1 + c_8 \cos \phi_{\mathrm{m}} \\
F_4(\phi_m) &= 1 + c_9 \exp\left(-\frac{(\phi_{\mathrm{m}} - \phi_{\mathrm{ic1}})^2}{2\sigma_{\mathrm{ic1}}^2} \right) + c_{10} \exp\left(-\frac{(\phi_{\mathrm{m}} - \phi_{\mathrm{ic2}})^2}{2\sigma_{\mathrm{ic2}}^2} \right) \\
F_5(F_{10.7}) &= c_{11} + c_{12} F_{10.7},
\end{aligned} \tag{4.22}$$

with the latitude ϕ and the geomagnetic latitude ϕ_m of the pierce point, the declination δ of the sun; the diurnal, semi-diurnal and ter-diurnal variations V_{D}, V_{SD}, and V_{TD} depending on the local solar time t; the annual and semi-annual variations V_{A} and V_{SA} depending on the day of year t_d, the latitudes of the north- and south-ward ionisation crests ϕ_{ic1} and ϕ_{ic2}, their corresponding half widths σ_{ic1} and σ_{ic2}, and the solar flux index $F_{10,7}$.

The 12 coefficients c_1 through c_{12} have been determined by Jakowski et al. with non-linear least-squares estimation. An optimal set of values with 95% confidence intervals is listed in Tab. 4.1 [18]. The units of c_{11} and c_{12} are TECU and TECU/sfu [1], while the other coefficients are unit-less. Fig. 4.2 shows a global TECV map generated by the NTCM-GL model for one snapshot.

Given the latitude and longitude of an IPP and the observation time, the vertical TEC only depends on the solar flux index $F_{10.7}$, i.e.

$$I_{\mathrm{v}} = a_1(\phi, \delta, \phi_{\mathrm{m}}, t, t_d) + a_2(\phi, \delta, \phi_{\mathrm{m}}, t, t_d) F_{10.7}, \tag{4.23}$$

with $a_1 = F_1 \cdot F_2 \cdot F_3 \cdot F_4 \cdot c_{11}$, and $a_2 = F_1 \cdot F_2 \cdot F_3 \cdot F_4 \cdot c_{12}$. This enables the joint estimation of the vertical TEC and the differential biases. The measurement model is expressed by

$$\tilde{\boldsymbol{I}} - \boldsymbol{M} \cdot \boldsymbol{a}_1 q = \boldsymbol{M} \cdot \boldsymbol{a}_2 \cdot F_{10.7} + \boldsymbol{H}_{b_{\mathrm{I,R}}} \cdot \boldsymbol{b}_{\mathrm{I,R}} + \boldsymbol{H}_{b_{\mathrm{I}}^{\mathrm{K}}} \cdot \boldsymbol{b}_{\mathrm{I}}^{\mathrm{K}} + \boldsymbol{\epsilon}_{\mathrm{I}}, \tag{4.24}$$

where q converts the unit from TECU to meter, i.e. $q = 1\mathrm{m/TECU} = 40.3 \cdot 10^{16}/f^2$ with f being the frequency. The mapping matrix $\boldsymbol{M}$, the bias state vectors $\boldsymbol{b}_{\mathrm{I,R}}$ and $\boldsymbol{b}_{\mathrm{I}}^{\mathrm{K}}$, and their design matrices $\boldsymbol{H}_{b_{\mathrm{I,R}}}$ and $\boldsymbol{H}_{b_{\mathrm{I}}^{\mathrm{K}}}$ are defined in the same way as in Section 4.1.1. The vectors $\boldsymbol{a}_1$ and $\boldsymbol{a}_2$ stack the values from all pierce points. The solar flux index is the only unknown to describe the global ionosphere, and can be estimated in a Kalman filter along with the other bias states.

[1] $1\ \mathrm{sfu} = 10^{-22}\mathrm{Wm}^{-2}\mathrm{Hz}^{-1}$.

Coefficient	Estimated value	95% Confidence interval
c_1	0.89656	±0.0011
c_2	0.16984	±0.0010
c_3	-0.02166	±0.0010
c_4	0.05928	±0.0010
c_5	0.00738	±0.0010
c_6	0.13912	±0.0007
c_7	-0.17593	±0.0006
c_8	-0.34545	±0.0043
c_9	1.11670	±0.0074
c_{10}	1.15730	±0.0083
c_{11}	-4.33560	±0.0350
c_{12}	0.17775	±0.0006

Table 4.1: Coefficients for the NTCM-GL model with 95% confidence intervals [18].

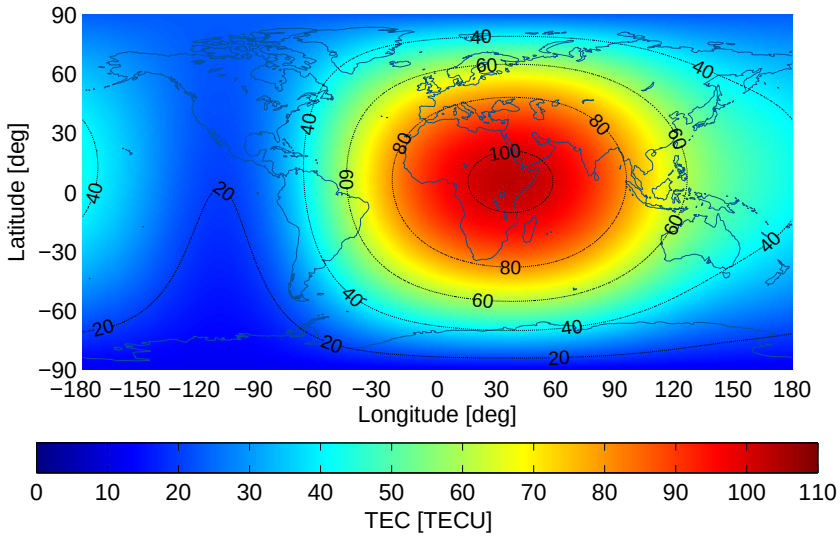

Figure 4.2: Vertical TEC map based on the NTCM-GL model at 11:00 on March 1st, 2014. The solar flux index is set to 165 sfu [88].

4.1.4 Kriging

Kriging was initially applied in mining and helped estimate metal concentrations precisely based on sample data. Blanch et al. introduced the Kriging method into ionospheric estimation, which is currently employed in WAAS [89–92].

In geostatistics, a function $Z(\boldsymbol{x})$ at a given location $\boldsymbol{x}$ depends on some incomplete or unpredictable knowledge, and is thus usually treated as a random variable resulting from a random process [93]. A classical assumption in geostatistics is the intrinsic stationarity.

It states that for any two neighboring points $\boldsymbol{x}_i$ and $\boldsymbol{x}_j$, we have

$$\begin{aligned} &\mathrm{E}\{Z(\boldsymbol{x}_i) - Z(\boldsymbol{x}_j)\} = 0, \\ &\mathrm{Var}\{Z(\boldsymbol{x}_i) - Z(\boldsymbol{x}_j)\} = 2\gamma(\|\boldsymbol{x}_i - \boldsymbol{x}_j\|). \end{aligned} \tag{4.25}$$

The first property states the random variable $Z(\boldsymbol{x})$ has the same mean over a small area, while the second one interprets the variance of the difference as a function describing the spatial relation of the field. The function $2\gamma(d)$ depends solely on the relative distance d rather than the absolute locations, and is known as the variogram.

Kriging estimates the value at a given point based on the known values at sampled locations. The most common variant of Kriging estimator is ordinary Kriging. Consider a random variable $Z(\boldsymbol{x}_0)$ at location $\boldsymbol{x}_0$, its estimate $\hat{Z}(\boldsymbol{x}_0)$ is expressed by a weighted sum of the existing data in the neighborhood, i.e.

$$\hat{Z}(\boldsymbol{x}_0) = \sum_{i=1}^{n} \alpha_i Z(\boldsymbol{x}_i), \quad \text{s.t.} \quad \sum_{i=1}^{n} \alpha_i = 1, \tag{4.26}$$

with n denoting the number of existing data contributed to the interpolation. The variance of the estimation error is derived in [1] as

$$\begin{aligned} \mathrm{Var}\{\hat{Z}(\boldsymbol{x}_0) - Z(\boldsymbol{x}_0)\} &= 2\sum_{i=1}^{n} \alpha_i \gamma(\|\boldsymbol{x}_0 - \boldsymbol{x}_i\|) - \sum_{i=1}^{n}\sum_{j=1}^{n} \alpha_i \alpha_j \gamma(\|\boldsymbol{x}_i - \boldsymbol{x}_j\|) \\ &= 2\boldsymbol{A}^{\mathrm{T}}\boldsymbol{\Gamma} - \boldsymbol{A}^{\mathrm{T}}\boldsymbol{G}\boldsymbol{A}, \end{aligned} \tag{4.27}$$

with the matrices expressed in

$$\boldsymbol{A} = \begin{bmatrix} \alpha_1 \\ \vdots \\ \alpha_n \end{bmatrix}, \boldsymbol{G} = \begin{bmatrix} \gamma(\|\boldsymbol{x}_1 - \boldsymbol{x}_1\|) & \dots & \gamma(\|\boldsymbol{x}_1 - \boldsymbol{x}_n\|) \\ \vdots & \ddots & \vdots \\ \gamma(\|\boldsymbol{x}_n - \boldsymbol{x}_1\|) & \dots & \gamma(\|\boldsymbol{x}_n - \boldsymbol{x}_n\|) \end{bmatrix}, \boldsymbol{\Gamma} = \begin{bmatrix} \gamma(\|\boldsymbol{x}_0 - \boldsymbol{x}_1\|) \\ \vdots \\ \gamma(\|\boldsymbol{x}_0 - \boldsymbol{x}_n\|) \end{bmatrix}. \tag{4.28}$$

The coefficient vector $\boldsymbol{A}$ is obtained such that the variance of the estimation error is minimized, i.e.

$$\hat{\boldsymbol{A}} = \underset{\boldsymbol{A}}{\mathrm{argmin}}\, \mathrm{Var}\{\hat{Z}(\boldsymbol{x}_0) - Z(\boldsymbol{x}_0)\}, \quad \text{s.t.} \;\; \boldsymbol{A}^{\mathrm{T}}\mathbf{I} = 1, \tag{4.29}$$

with $\mathbf{I}$ denoting an all-ones column vector with n elements. The optimum is solved by introducing a Lagrange multiplier μ in

$$\frac{\partial}{\partial \boldsymbol{A}} \left(2\boldsymbol{A}^{\mathrm{T}}\boldsymbol{\Gamma} - \boldsymbol{A}^{\mathrm{T}}\boldsymbol{G}\boldsymbol{A} - 2\mu(\boldsymbol{A}^{\mathrm{T}}\mathbf{I} - 1)\right) = 0, \quad \text{and} \quad \boldsymbol{A}^{\mathrm{T}}\mathbf{I} = 1, \tag{4.30}$$

which yields

$$\begin{aligned} &2\boldsymbol{\Gamma} - 2\boldsymbol{G}\boldsymbol{A} - 2\mu\mathbf{I} = 0, \quad \text{and} \quad \boldsymbol{A}^{\mathrm{T}}\mathbf{I} = 1, \\ &\begin{bmatrix} \boldsymbol{G} & \mathbf{I} \\ \mathbf{I}^{\mathrm{T}} & \mathbf{0} \end{bmatrix} \cdot \begin{bmatrix} \boldsymbol{A} \\ \mu \end{bmatrix} = \begin{bmatrix} \boldsymbol{\Gamma} \\ 1 \end{bmatrix}, \end{aligned} \tag{4.31}$$

The estimate is obtained by

$$\hat{\tilde{\boldsymbol{A}}} \triangleq \begin{bmatrix} \hat{\boldsymbol{A}} \\ \hat{\mu} \end{bmatrix} = \underbrace{\begin{bmatrix} \boldsymbol{G} & \mathbf{I} \\ \mathbf{I}^{\mathrm{T}} & \mathbf{0} \end{bmatrix}^{-1}}_{\tilde{\boldsymbol{G}}^{-1}} \cdot \underbrace{\begin{bmatrix} \boldsymbol{\Gamma} \\ 1 \end{bmatrix}}_{\tilde{\boldsymbol{\Gamma}}} \tag{4.32}$$

The estimation variance is derived from Eq. (4.27) and Eq. (4.32) as

$$\mathrm{Var}\{\hat{Z}(\boldsymbol{x}_0) - Z(\boldsymbol{x}_0)\} = \tilde{\boldsymbol{\Gamma}}^{\mathrm{T}} \tilde{\boldsymbol{G}}^{-1} \tilde{\boldsymbol{\Gamma}}. \tag{4.33}$$

Eq. (4.32) and (4.33) summarizes the solution from Kriging, which is a best linear unbiased estimator in the sense of minimizing the estimation variance. The unbiasedness is directly guaranteed under the constraint of the coefficients. The weighting coefficients depend on the variogram γ evaluated at the distance between the point of interest and the pierce point associated with the measurement. The points which are nearer to the point of interest contribute more to the interpolation than the ones farther.

Blanch used Kriging to estimate the ionospheric delay at arbitrary pierce points after subtracting the satellite and receiver differential biases from the measurements, where confidence bounds are also developed. In this thesis, the Kriging method is used for the joint estimation of the vertical delays and biases.

4.2 Joint Estimation of TECVs and Biases Using Kriging

Kriging provides an optimal way of representing a subset of sample points by another subset. It overcomes the rank-deficiency in Eq. (4.5). In the case of R receivers with totally K satellites in view, the number of receiver and satellite biases is $R+K-1$. There are thus at least $R+K-1$ vertical delay states that have to be mapped away. These mapped vertical delays do not appear in the state vector, instead they are interpolated with Kriging using the remaining subset of vertical delays.

The measurement model is given by

$$\tilde{\boldsymbol{I}} = \left[\boldsymbol{H}_{I_{\mathrm{v}}},\ \boldsymbol{H}_{b_{\mathrm{I,R}}},\ \boldsymbol{H}_{b_{\mathrm{I}}^{\mathrm{K}}}\right] \cdot \begin{bmatrix} \boldsymbol{I}_{\mathrm{v}}^{\mathrm{s}} \\ \boldsymbol{b}_{\mathrm{I,R}} \\ \boldsymbol{b}_{\mathrm{I}}^{\mathrm{K}} \end{bmatrix} + \boldsymbol{\epsilon}_I, \tag{4.34}$$

where the estimated subset $\boldsymbol{S}$ is denoted by an upper index s, and the mapped (complement) subset $\bar{\boldsymbol{S}}$ to be interpolated is denoted by $\bar{\mathrm{s}}$. The design matrix for the vertical delays $\boldsymbol{H}_{I_{\mathrm{v}}}$ contains two parts, i.e. the mapping functions alone representing the estimated subset and the functions multiplied with the Kriging coefficients representing the mapped subset:

$$\boldsymbol{H}_{I_{\mathrm{v}}} = \begin{bmatrix} m_{\mathrm{I},1}^{\bar{\mathrm{s}}} \hat{\alpha}_{1,1} & \dots & \dots & \dots & \dots & m_{\mathrm{I},1}^{\bar{\mathrm{s}}} \hat{\alpha}_{1,n_s} \\ m_{\mathrm{I},1}^{\mathrm{s}} & 0 & \dots & \dots & \dots & 0 \\ \vdots & \vdots & \vdots & \vdots & \vdots & \vdots \\ m_{\mathrm{I},j}^{\bar{\mathrm{s}}} \hat{\alpha}_{j,1} & \dots & \dots & \dots & \dots & m_{\mathrm{I},j}^{\bar{\mathrm{s}}} \hat{\alpha}_{j,n_{\mathrm{s}}}, \\ 0 & \dots & 0 & m_{\mathrm{I},i}^{\mathrm{s}} & \dots & 0 \\ \vdots & \vdots & \vdots & \vdots & \vdots & \vdots \\ m_{\mathrm{I},n_{\bar{\mathrm{s}}}}^{\bar{\mathrm{s}}} \hat{\alpha}_{n_{\bar{\mathrm{s}}},1} & \dots & \dots & \dots & \dots & m_{\mathrm{I},n_{\bar{\mathrm{s}}}}^{\bar{\mathrm{s}}} \hat{\alpha}_{n_{\bar{\mathrm{s}}},n_{\mathrm{s}}} \end{bmatrix}, \tag{4.35}$$

with n_s and $n_{\bar{s}}$ being the number of pierce points in the estimated subset and the mapped subset respectively. For each pierce point j belonging to $\bar{\boldsymbol{S}}$, the vertical delay is interpreted by a linear combination of vertical delays in $\boldsymbol{S}$. The weighting coefficients are determined by Kriging method and are combined in the vector $\hat{\boldsymbol{\alpha}}_j$ as

$$\hat{\boldsymbol{\alpha}}_j = [\hat{\alpha}_{j,1}, \hat{\alpha}_{j,2}, \ldots, \hat{\alpha}_{j,n_s}]^{\mathrm{T}}, \text{ with } j \in \{1, \ldots, n_{\bar{\mathrm{s}}}\}. \tag{4.36}$$

The design matrix can be better visualized by re-arranging the rows to separate the estimated subset and the mapped subset, so that the Kriging solution in Eq. (4.32) can be included in Eq. (4.35). Let the re-arranged design matrix for the vertical delays be denoted by $\tilde{\boldsymbol{H}}_{I_\mathrm{v}}$, which reads

$$\tilde{\boldsymbol{H}}_{I_\mathrm{v}} = \begin{bmatrix} \mathrm{diag}(\boldsymbol{m}_\mathrm{I}^{\mathrm{s}}) \\ \mathrm{diag}(\boldsymbol{m}_\mathrm{I}^{\bar{\mathrm{s}}}) \cdot \begin{bmatrix} \hat{\boldsymbol{\alpha}}_1^{\mathrm{T}} \\ \vdots \\ \hat{\boldsymbol{\alpha}}_{n_{\bar{\mathrm{s}}}}^{\mathrm{T}} \end{bmatrix} \end{bmatrix} = \begin{bmatrix} \mathrm{diag}(\boldsymbol{m}_\mathrm{I}^{\mathrm{s}}) \\ \mathrm{diag}(\boldsymbol{m}_\mathrm{I}^{\bar{\mathrm{s}}}) \cdot \begin{bmatrix} \left(\boldsymbol{D} \cdot \tilde{\boldsymbol{G}}^{\mathrm{s},-1} \cdot \tilde{\boldsymbol{\Gamma}}_1\right)^{\mathrm{T}} \\ \vdots \\ \left(\boldsymbol{D} \cdot \tilde{\boldsymbol{G}}^{\mathrm{s},-1} \cdot \tilde{\boldsymbol{\Gamma}}_{n_{\bar{\mathrm{s}}}}\right)^{\mathrm{T}} \end{bmatrix} \end{bmatrix}, \tag{4.37}$$

with $\tilde{\boldsymbol{G}}^{\mathrm{s}}$ and $\tilde{\boldsymbol{\Gamma}}_j$ ($\forall j \in \{1, \ldots, n_{\bar{\mathrm{s}}}\}$) defined in Eq. (4.32) as

$$\tilde{\boldsymbol{G}}^{\mathrm{s}} = \begin{bmatrix} \gamma(\|\boldsymbol{x}_1^{\mathrm{s}} - \boldsymbol{x}_1^{\mathrm{s}}\|) & \ldots & \gamma(\|\boldsymbol{x}_1^{\mathrm{s}} - \boldsymbol{x}_{n_\mathrm{s}}^{\mathrm{s}}\|) & 1 \\ \vdots & \ddots & \vdots & \vdots \\ \gamma(\|\boldsymbol{x}_{n_\mathrm{s}}^{\mathrm{s}} - \boldsymbol{x}_1^{\mathrm{s}}\|) & \ldots & \gamma(\|\boldsymbol{x}_{n_\mathrm{s}}^{\mathrm{s}} - \boldsymbol{x}_{n_\mathrm{s}}^{\mathrm{s}}\|) & 1 \\ 1 & \ldots & 1 & 0 \end{bmatrix}, \quad \tilde{\boldsymbol{\Gamma}}_j = \begin{bmatrix} \gamma(\|\boldsymbol{x}_j^{\bar{\mathrm{s}}} - \boldsymbol{x}_1^{\mathrm{s}}\|) \\ \vdots \\ \gamma(\|\boldsymbol{x}_j^{\bar{\mathrm{s}}} - \boldsymbol{x}_{n_\mathrm{s}}^{\mathrm{s}}\|) \\ 1 \end{bmatrix}, \tag{4.38}$$

and $\boldsymbol{D}$ being a selection matrix to exclude the Lagrange multiplier μ, i.e. $\boldsymbol{D} = [\mathbf{1}_{n_\mathrm{s}}, \mathbf{0}_{n_\mathrm{s} \times 1}]$.

Now, the measurement noise for the ionospheric delays from the mapped subset points shall be updated, as additional modelling error is introduced from the Kriging estimator. The covariance matrix can be expressed in four sub-matrices as

$$\boldsymbol{\Sigma}_\mathrm{R} = \begin{bmatrix} \boldsymbol{\Sigma}_\mathrm{R}^{\mathrm{ss}} & \boldsymbol{\Sigma}_\mathrm{R}^{\mathrm{s}\bar{\mathrm{s}}} \\ \boldsymbol{\Sigma}_\mathrm{R}^{\bar{\mathrm{s}}\mathrm{s}} & \boldsymbol{\Sigma}_\mathrm{R}^{\bar{\mathrm{s}}\bar{\mathrm{s}}} \end{bmatrix}, \tag{4.39}$$

with the upper left one representing the noise for the slant delays in the estimated subset, which is not affected by Kriging. The covariance $\boldsymbol{\Sigma}_\mathrm{R}^{\mathrm{s}j}$ in the cross term of the point j in the mapped subset with the estimated subset are obtained by the interpolating coefficient vector $\hat{\boldsymbol{\alpha}}_j$, i.e.

$$\boldsymbol{\Sigma}_\mathrm{R}^{\mathrm{s}j} = \boldsymbol{\Sigma}_\mathrm{R}^{\mathrm{ss}} \hat{\boldsymbol{\alpha}}_j. \tag{4.40}$$

The lower right matrix in Eq. (4.39) represents the combined measurement noise and Kriging error, where a term $\sigma_{\mathrm{R},ij}$ in the sub-matrix is expressed by

$$\sigma_{\mathrm{R},ij} = \sigma_{\mathrm{I},ij}\delta_{ij} + \hat{\boldsymbol{\alpha}}_i^{\mathrm{T}} \boldsymbol{\Gamma}_i + \hat{\boldsymbol{\alpha}}_j^{\mathrm{T}} \boldsymbol{\Gamma}_j - \hat{\boldsymbol{\alpha}}_j^{\mathrm{T}} \boldsymbol{G}^s \hat{\boldsymbol{\alpha}}_i - \gamma_{ij}\delta_{ij}, \tag{4.41}$$

with $\sigma_{\mathrm{I},ij}$ being the standard deviation from the raw slant delay measurement, δ being the dirac function, the vectors $\hat{\boldsymbol{\alpha}}_i$ and $\hat{\boldsymbol{\alpha}}_j$ representing the estimated Kriging coefficients, $\boldsymbol{\Gamma}$

and $\boldsymbol{G}^s$ defined in Eq. (4.28), and γ_{ij} being the variogram valued between point i and j. The detailed derivation can be found in Appendix D.

With the descriptions on the design matrices and the measurement noise covariance matrix, the states in Eq. (4.34) can be estimated in a Kalman filter. Random walk processes are assumed to the vertical delays and the biases. Two important aspects are presented in the following sections, which are the modelling for the variogram and the selection of the estimated subset.

4.2.1 Experimental and Theoretical Variograms

The variogram describes the spatial dependence of a random field, and is defined as the expectation of the squared difference between data at different sample points [93]. It can be represented as a function of the distance between the locations. According to the definition in Eq. (4.25):

$$\gamma(d) = \frac{1}{2}\mathrm{E}\left\{(Z(\boldsymbol{x}_i) - Z(\boldsymbol{x}_j))^2\right\}, \quad \text{s.t. } \|\boldsymbol{x}_i - \boldsymbol{x}_j\| = d, \tag{4.42}$$

where the expectation is computed from all pairs of observations having the distance d. It is however hard to realize due to the exact distance, thus an interval Δd is allowed to obtain the experimental variogram for a certain distance d as suggested by Blanch in [92], i.e.

$$\gamma(d) = \frac{1}{2m(d)} \sum_{\|\boldsymbol{x}_i - \boldsymbol{x}_j\| \in [d-\frac{1}{2}\Delta d, d+\frac{1}{2}\Delta d]} (Z(\boldsymbol{x}_i) - Z(\boldsymbol{x}_j))^2, \tag{4.43}$$

with $m(d)$ denoting the number of pairs whose distances fall into the range of $[d-\frac{1}{2}\Delta d, d+\frac{1}{2}\Delta d]$.

First, an experimental variogram is calculated. A set of vertical ionospheric delays are collected from the IGS final TEC grid product on Jan. 1, 2011. The resolution of the map is refined to $1^\circ \times 1^\circ$ through bilinear interpolation. A mean ionosphere is obtained by averaging the TEC maps over sun-synchronous locations over one day, as shown in Fig. 4.3. The 0° longitude in the figure represents $12:00$ UTC time.

The averaged ionosphere is subtracted to obtain the residual field. The region of interest covers most of Europe with latitude from 30° to 87.5° and longitude from -30° to 75°. Fig. 4.4 shows the experimental variogram (points with blue circles) as a function of distance with the distance step being $\Delta d = 50\,\mathrm{km}$.

Various models, such as linear, spherical and exponential models, can be used to represent a theoretical variogram. A widely-used exponential function is given by

$$\gamma(d) = c_0(1 - e^{-d/a_0}) + c_n, \tag{4.44}$$

where d represents the distance and the parameter c_n represents the nugget effect. The value $c_0 + c_n$ denotes the saturation of the variogram when the distance approaches infinity, while a_0 controls that the variogram increases linearly near the origin as the experimental one suggests. The reason for the nugget effect is to represent the spatial discontinuity in practice. The variogram equals zero at zero distance by definition, but approaches some positive value immediately away from the origin.

In this thesis, as we have already subtracted an average ionosphere and are only modelling the residuals field, the nugget effect is not observed from the experimental variogram.

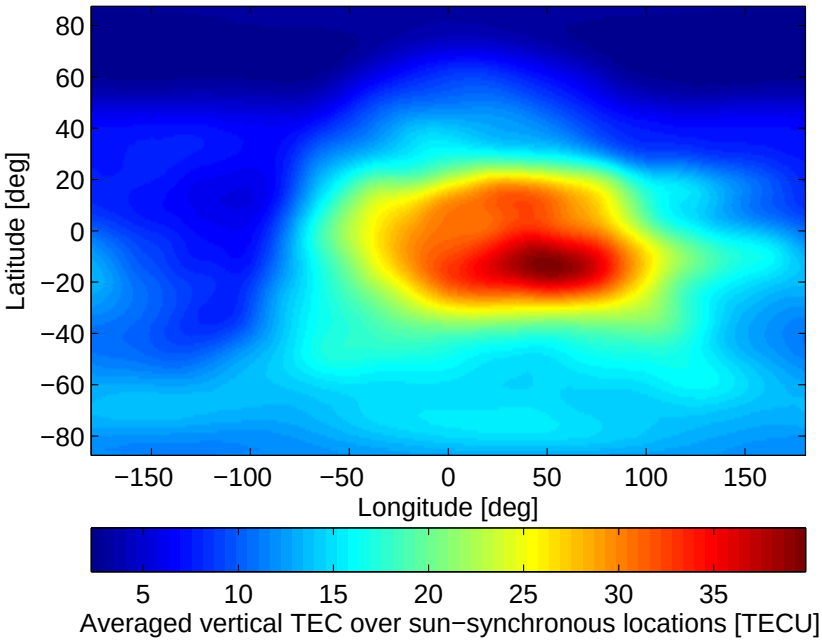

Figure 4.3: The averaged vertical TEC map on Jan. 1, 2011. The TECV products every 2 hours have been summed together after adjusted to synchronous locations with respect to the sun.

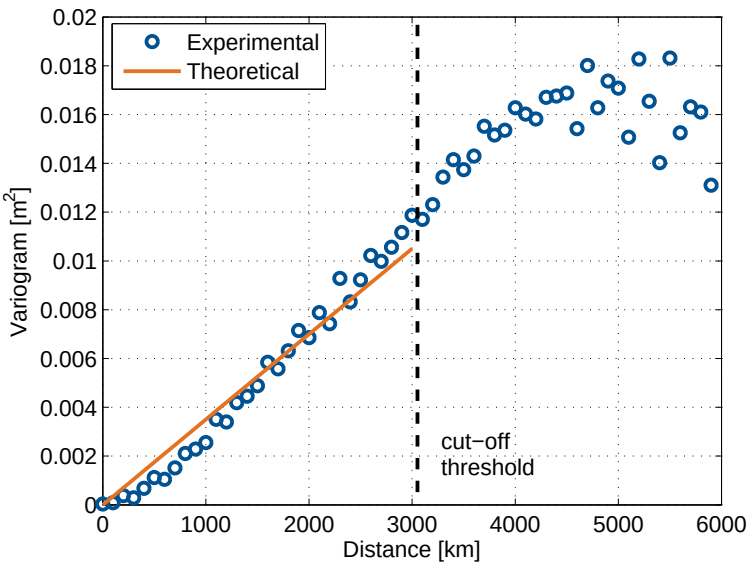

Figure 4.4: The calculated experimental and fitted exponential variograms in the night for the region of latitude from 30° to 87.5° and longitude from −30° to 75°. A cut-off threshold is introduced to neglect the points, whose ionospheric delays have negligible contribution.

Additionally, we have set 3000 km as the cut-off threshold, because the ionospheric delays at points farther than the threshold have even negligible influence on the point of interest.

Within the threshold, the saturation has not yet reached, therefore we have chosen a linear fitting for the variogram. Fig. 4.4 shows the fitted variogram as an orange line. The fitted line starts at the origin and the slope is obtained as $3.5 \times 10^{-6}\mathrm{m}^2/\mathrm{km}$.

4.2.2 Iterative Greedy Algorithm

Observing the measurement model in Eq. (4.34), the system would be straightforward to solve if the estimated subset $\boldsymbol{S}$ were known a priori. However, both the number of vertical delays contained in the mapped subset and the choice of the subset remain open points.

Intuitively the more pierce points included in the estimated subset, the better the interpolation would be. However, the improvement of the interpolation would be little when sufficient vertical delays have already been included in the state vector. The convergence of the estimation would also be slower in general if there are more unknowns. A brute-force search would find the optimum subset by examining all possible options. This would however be computationally infeasible for a typical scenario of hundreds to thousands of ionospheric pierce points.

We propose an efficient Greedy algorithm to obtain a sub-optimal solution, which constructs the estimated subset of vertical delays in a sequential manner [94]. The initial point to start with is selected geographically in the center of the map, i.e.

$$\hat{\boldsymbol{x}}_1 = \arg\min_{\boldsymbol{x}_1}(|\phi(\boldsymbol{x}_1) - \bar{\phi}| + |\lambda(\boldsymbol{x}_1) - \bar{\lambda}|), \tag{4.45}$$

where $\phi(\boldsymbol{x})$ and $\lambda(\boldsymbol{x})$ denote the latitude and longitude of pierce point $\boldsymbol{x}$, and $\bar{\phi}$ and $\bar{\lambda}$ denote the average latitude and longitude of the studied region. Then all other points are "interpolated" by the first one by Kriging. Consequently they will all have a weighting coefficient 1 but different variances. The next point to be included has the largest error as compared to its representation by Kriging, i.e.

$$\hat{\boldsymbol{x}}_i = \arg\max_{\boldsymbol{x}_i}\left\{\mathrm{Var}\left[\hat{Z}(\boldsymbol{x}_i) - Z(\boldsymbol{x}_i)\right]\right\}, \quad \text{s.t. } \hat{Z}(\boldsymbol{x}_i) = \sum_{j=1}^{i-1}\lambda_j Z(\boldsymbol{x}_j), \quad i > 1. \tag{4.46}$$

The selection procedure stops until the Kriging variances of the remaining points are below a given threshold, which means the selected points can well represent the area.

We apply a Kalman filter to solve the measurement model in Eq. (4.34). The state vector includes the estimated subset of vertical delays $\boldsymbol{I}_{\mathrm{v}}^{\mathrm{s}}$ and the satellite and receiver ionospheric biases $\boldsymbol{b}_{\mathrm{I}}^{\mathrm{K}}$ and $\boldsymbol{b}_{\mathrm{I,R}}$. The biases are referenced to one satellite bias in order to remove rank-deficiency. The state transition from epoch $t-1$ to epoch t is given by

$$\begin{aligned}\boldsymbol{I}_{\mathrm{v}}^{\mathrm{s}}(t) &= \boldsymbol{I}_{\mathrm{v}}^{\mathrm{s}}(t-1) + \boldsymbol{\omega}_{\boldsymbol{I}}(t-1)\\ \boldsymbol{b}_{\mathrm{I}}(t) &= \boldsymbol{b}_{\mathrm{I}}(t-1) + \boldsymbol{\omega}_{\boldsymbol{b}_{\mathrm{I}}}(t-1),\end{aligned} \tag{4.47}$$

where $\boldsymbol{b}_{\mathrm{I}}$ represents both for satellite and receiver biases. Due to the estimation in the night, the standard deviations of the Gaussian-distributed process noise $\boldsymbol{\omega}_{\boldsymbol{I}}$ and $\boldsymbol{\omega}_{\boldsymbol{b}_{\mathrm{I}}}$ are set to 5 mm and 1 mm, respectively.

Subset reselection

As time evolves, the pierce points change their positions because of change of satellite geometry. The estimated subset needs to be updated during the estimation.

If a point in the subset is no longer included, the corresponding entries from that point are deleted. If a new point is included, its vertical delay as well as its variance and covariance with other points need to be initialized for the Kalman filter. The vertical delay is initialized with the interpolated value based on the previous subset used for Kriging:

$$\hat{I}^{\tilde{\mathrm{s}},-}_{\mathrm{v},\bar{s}_j}(t_n) = \hat{\boldsymbol{\alpha}}_j^{\mathrm{T}} \cdot \hat{\boldsymbol{I}}^{\mathrm{s},+}_{\mathrm{v}}(t_{n-1}), \tag{4.48}$$

where the new point $\bar{s}_j$ belonged to the mapped subset at epoch t_{n-1}. Assume the previous estimated subset contains pierce points $\boldsymbol{S} = \{s_1, \ldots, s_{n_\mathrm{s}}\}$, then the new estimated subset is $\tilde{\boldsymbol{S}} = \{s_1, \ldots, s_{n_\mathrm{s}}, \bar{s}_j\}$. At epoch t_n, the a priori covariance matrix $\boldsymbol{P}^-$ is calculated as

$$\boldsymbol{P}^-_{\tilde{\boldsymbol{S}}\tilde{\boldsymbol{S}}}(t_n) = \begin{bmatrix} \boldsymbol{P}^-_{\boldsymbol{S}\boldsymbol{S}}(t_n) & \boldsymbol{P}^-_{\boldsymbol{S}\bar{s}_j}(t_n) \\ \boldsymbol{P}^-_{\bar{s}_j\boldsymbol{S}}(t_n) & \boldsymbol{P}^-_{\bar{s}_j\bar{s}_j}(t_n) \end{bmatrix}, \tag{4.49}$$

where the upper left element comes from the prediction step of Kalman filtering, and the other three terms need to be initialized. The variance of the new vertical delay estimate $\boldsymbol{P}^-_{\bar{s}_j\bar{s}_j}(t_n)$ is initialized from the Kriging variance as

$$\begin{aligned} \boldsymbol{P}^-_{\bar{s}_j\bar{s}_j}(t_n) &= \mathrm{E}\left\{ \left(\hat{I}^{\tilde{\mathrm{s}},-}_{\mathrm{v},\bar{s}_j}(t) - I^{\tilde{\mathrm{s}},-}_{\mathrm{v},\bar{s}_j}(t) \right)^2 \right\} \\ &= \hat{\boldsymbol{\alpha}}_j^{\mathrm{T}} \hat{\boldsymbol{P}}^+_{\boldsymbol{S}\boldsymbol{S}}(t_{n-1}) \hat{\boldsymbol{\alpha}}_j. \end{aligned} \tag{4.50}$$

The off-diagonal terms are calculated by

$$\boldsymbol{P}^-_{\boldsymbol{S}\bar{s}_j}(t_n) = \left(\boldsymbol{P}^-_{\bar{s}_j\boldsymbol{S}}(t_n) \right)^{\mathrm{T}} = \boldsymbol{P}^+_{\boldsymbol{S}\boldsymbol{S}}(t_{n-1}) \hat{\boldsymbol{\alpha}}_j \tag{4.51}$$

4.3 Real Data Analysis

We have applied the joint estimation algorithm to some real GPS data. A regional network is selected including 24 IGS stations mostly in Europe. The station coordinates are found in Tab. 4.2 and Fig. 4.5 shows the locations of the stations. The code and carrier phase measurements on L1 and L2 were taken on Jan. 1, 2011, from 20:00 to 00:00 during the night. Possible code multipath effects are reduced by sidereal filtering over 2 weeks, which is described in section 3.2.3.

The Kriging method is applied to jointly estimate the vertical delays and the differential biases using a Kalman filter. The measurement noise for the Kalman filter is configured that the standard deviation follows an exponential function of elevation angle, with 10 cm at 20° and 2 cm at 70°. The standard deviations of the process noise for the vertical delays and the biases are set to 5 mm and 1 mm respectively.

Station	Lat.	Long.	Station	Lat.	Long.	Station	Lat.	Long.
bor1	52.10°	17.07°	hert	50.87°	0.33°	rabt	34.00°	−6.85°
brst	48.38°	−4.50°	joz2	52.10°	21.03°	redu	50.00°	5.14°
bucu	44.46°	26.13°	mad2	40.43°	−4.25°	sofi	42.56°	23.39°
bzrg	46.50°	11.34°	mate	40.65°	16.70°	vill	40.44°	−3.95°
cebr	40.45°	16.87°	mobn	55.11°	36.57°	wroc	51.11°	17.06°
crao	44.41°	33.99°	nico	35.14°	33.40°	wtzr	49.14°	12.88°
ebre	40.82°	0.49◦	pado	45.41°	11.90°	yebe	40.52°	−3.09°
graz	47.07°	15.49°	pots	52.38°	13.07°	zim2	46.88°	7.47°

Table 4.2: Coordinates of the selected 24 IGS stations.

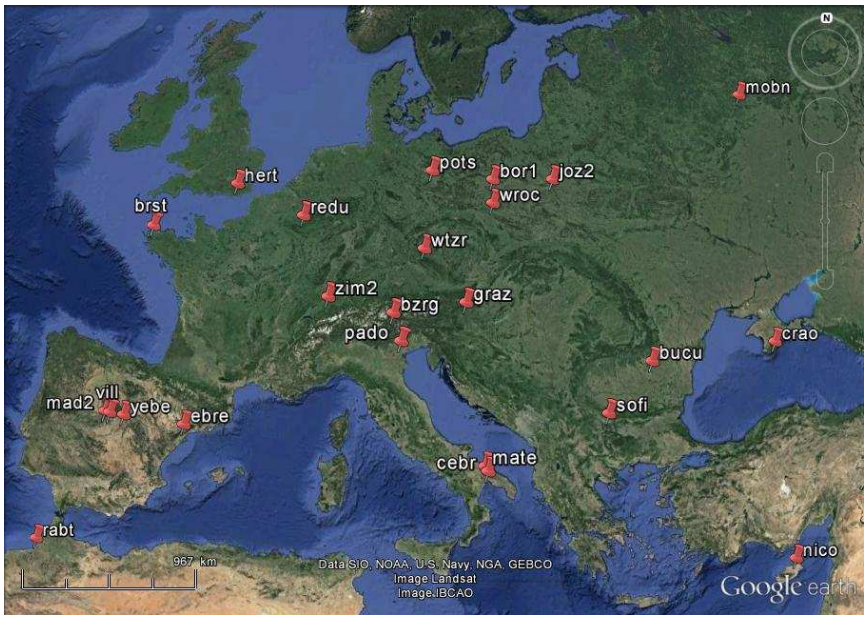

Figure 4.5: The network of the 24 IGS stations, shown in red pins.

4.3.1 Bias Estimates and Residuals

The slant delay measurements to estimate the vertical delays and biases are obtained from the first-stage Kalman filter estimating phase biases, while descriptions are found in Section 3.2.1. The estimates after the first-stage filter include the geometry term, the ionospheric slant delays, the ambiguities and the phase biases. The slant delay estimates and the state covariance matrix are taken as measurements for the second-stage estimation.

The outcome from the first-stage filter is listed in Tab. 4.3. The PRN 8 was selected as the reference satellite, as it was visible throughout the measurement period. The accuracy of the phase biases ranges from 1cm to 5cm, which is mainly due to different convergence times.

In the second-stage Kalman filter, the number of ionospheric vertical delays included in the estimated subset starts with 30. The satellite geometry changes as time evolves. Every pierce point affected by satellite risings and settings is checked. In case of rising, the relative location of a new pierce point determines whether the new pierce point should be included

PRN k	$\lambda_1\hat{\tilde{\tilde{\beta}}}_1^k$ [m]	$\sigma_{\lambda_1\hat{\tilde{\tilde{\beta}}}_1^k}$ [m]	$\lambda_2\hat{\tilde{\tilde{\beta}}}_2^k$ [m]	$\sigma_{\lambda_2\hat{\tilde{\tilde{\beta}}}_2^k}$ [m]
5	0.031	0.041	0.036	0.052
7	0.136	0.022	-0.159	0.028
9	0.146	0.013	-0.017	0.016
10	0.112	0.024	-0.151	0.03
12	0.088	0.023	-0.071	0.029
13	0.015	0.045	-0.074	0.057
15	0.07	0.013	0.002	0.017
17	0.052	0.014	-0.091	0.017
18	0.158	0.016	0.008	0.02
19	0.091	0.038	-0.048	0.048
21	0.113	0.037	-0.097	0.047
26	0.017	0.013	-0.12	0.016
27	0.14	0.011	-0.022	0.014
28	0.047	0.01	-0.156	0.012

Table 4.3: The phase bias estimates and their standard deviations from the first-stage Kalman filter.

in the estimated subset or mapped subset. If there are no more than 2 estimated pierce points in the neighborhood (e.g. a radius of 1000km), the new point is included in the subset. In case of satellite setting, the pierce points are removed from their corresponding subsets. The changes in the Kriging variances for the remaining points are monitored. If the change is more than $10^{-5}\,\mathrm{m}^2$, these points are included additionally to the estimated subset.

Every 30 minutes, a new subset is selected using the iterative Greedy algorithm, where at each iteration the point with largest Kriging variance is selected in the estimated subset. Fig. 4.6 illustrates the change of subsets due to setting measurements and change of geometry. Fig. 4.6(a) shows the setting IPPs at the 30-th minute, while Fig. 4.6(b) shows the adjusted subset selection.

In order to compare Fig. 4.6(a) and Fig. 4.6(b), we have a closer look at two examples, which locate at the upper right and lower left corners, respectively. The point "1" belonged to the estimated subset, and its setting directly affects the neighboring points "2" and "3". In the new selected subset, the points "2" and "3" are included, which benefits also points "4" and "5". Then the point "5" is moved from the estimated subset to the mapped subset. Similarly, at the lower left corner, the setting of estimated subset point "6" and "7" leads to the inclusion of the points "8" and "9".

The histograms of the residuals are plotted in Fig. 4.7, where the blue peak comes from the Kriging method and the iterative subset selection algorithm. Comparisons have been made among different estimation strategies. In the planar fit method, the region is suggested to be covered by three planes around the grid points at latitudes and longitudes $(45°, 10°)$ and $(50°, 25°)$, with the fit radius being 2500 km. In the NTCM-GL model, the solar flux index is estimated, while the standard deviation of the process noise is set to 0.01. Although only one state is representing the ionosphere, the global NTCM model

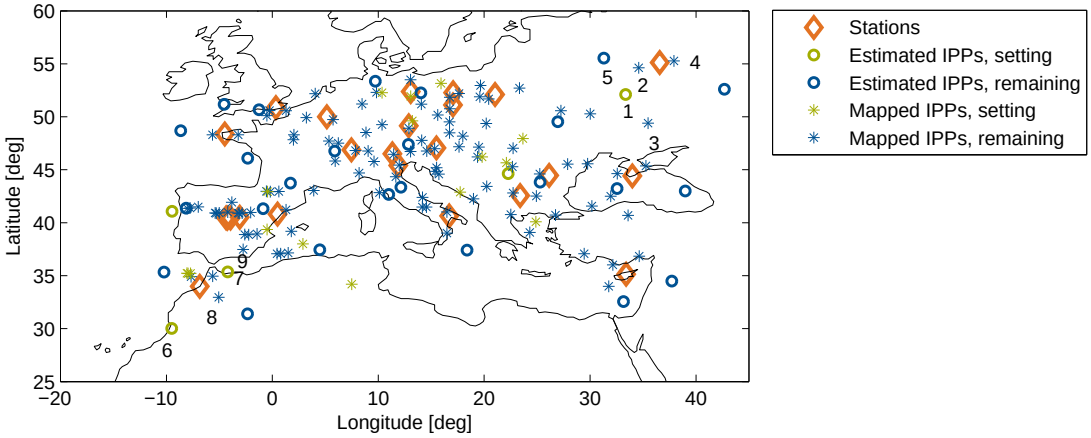

(a) At the 30-th minute, the setting satellites/measurements are processed, which are indicated in green.

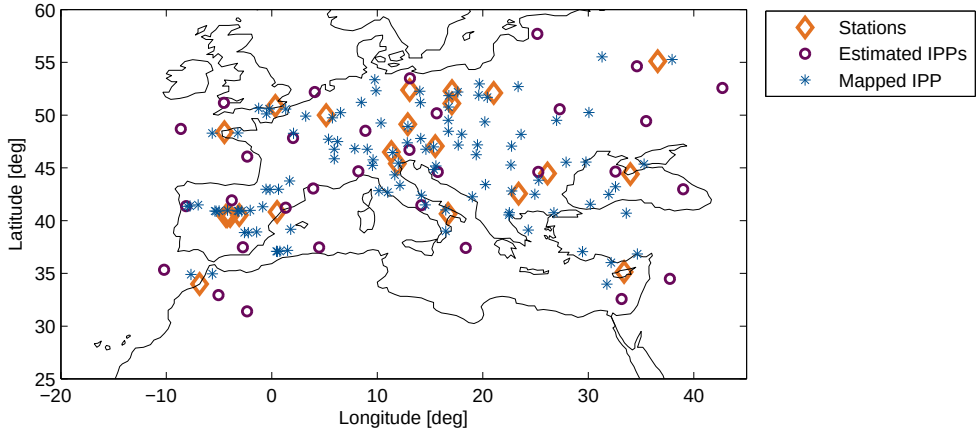

(b) A new IPP subset (shown with purple cycles) to be estimated is obtained with the proposed iterative Greedy algorithm.

Figure 4.6: The change of subsets due to satellite movements and pierce point changes. Orange diamonds represent the reference stations, circles and asterisks represent estimated and mapped IPPs, respectively.

performs well as compared to the planar fit method, see Fig. 4.7. The last comparison is to subtract the IGS final TEC product and the P1P2 differential bias products. The residuals are biased from zero having the largest error. However it should be noted that, the IGS final ionospheric products are provided with 2 h update frequency while the bias products are obtained averaging over hundreds of stations and one month's time. That is partly the reason why the code residuals correcting the IGS products are larger than the ones from other methods.

The geometric and ionospheric code biases estimated from the second-stage Kalman filters are shown in Tab. 4.4. The same PRN 8 was chosen in both cases as reference satellite, so that the results can be combined with the phase bias estimates from the first-stage filter. In the geometric bias estimation, the IGS final satellite orbit and clock offset products are subtracted as a priori information. The state vector includes the receiver

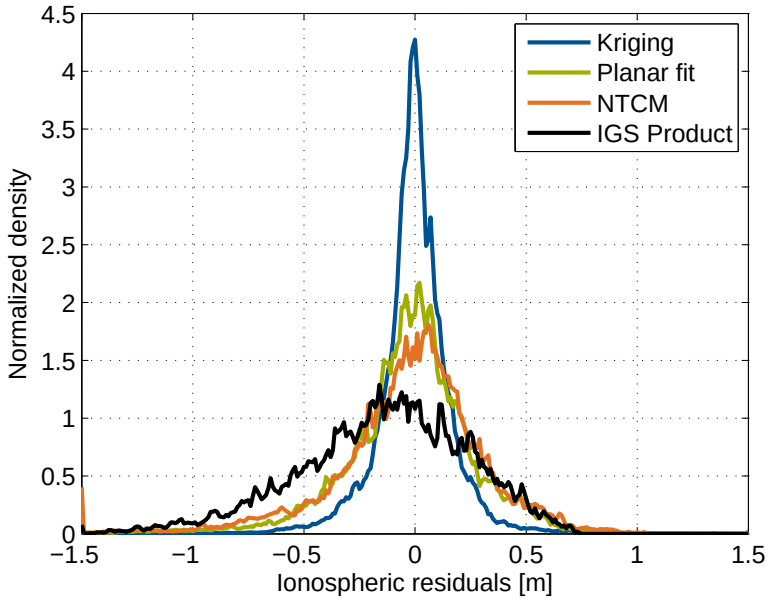

Figure 4.7: Comparison of the histograms on the estimation residuals for all stations on Jan. 1 2011. Different methods have been applied, including the proposed Kriging method, the planar fit model, the NTCM-GL model and subtracting the IGS products. The Kriging method outperforms with the smallest variance while the IGS products result in a bias and the least accuracy.

clock offsets, the satellite geometric code biases, the tropospheric zenith delays, while the orbital errors are assumed negligible.

Additionally, the original phase bias estimates are derived by subtracting the code biases from the phase biases in Tab. 4.3. Recalling Eq. (3.7) in the chapter determining phase biases, the phase biases are compensated with the code biases, which were absorbed into geometric and ionospheric states. After the second-stage Kalman filters, the original phase biases can be calculated by

$$\begin{aligned}\lambda_1\hat{\beta}_1^k &= \lambda_1\hat{\tilde{\tilde{\beta}}}_1^k + \hat{b}_{\mathrm{g}}^k - \quad \hat{b}_{\mathrm{I}}^k,\\ \lambda_2\hat{\beta}_2^k &= \lambda_2\hat{\tilde{\tilde{\beta}}}_2^k + \hat{b}_{\mathrm{g}}^k - \frac{f_1^2}{f_2^2}\hat{b}_{\mathrm{I}}^k.\end{aligned} \tag{4.52}$$

These biases are referenced to one common satellite bias on each frequency, i.e. $\lambda_1\hat{\beta}_1^\ell$ and $\lambda_1\hat{\beta}_1^\ell$. In the second-stage estimation of geometric terms, the code biases and the clock residuals are not separable, see Eq. (3.67). Applying Eq. (3.67) in Eq. (4.52), we obtain

$$\begin{aligned}\lambda_1\Delta\hat{\beta}_1^k &\triangleq \lambda_1\hat{\beta}_1^k - (c\delta^k - c\hat{\delta}_{\mathrm{IGS}}^k) = \lambda_1\hat{\tilde{\tilde{\beta}}}_1^k - c\Delta\hat{\tilde{\tilde{\delta}}}^k - \quad \hat{b}_{\mathrm{I}}^k,\\ \lambda_2\Delta\hat{\beta}_2^k &\triangleq \lambda_2\hat{\beta}_2^k - (c\delta^k - c\hat{\delta}_{\mathrm{IGS}}^k) = \lambda_2\hat{\tilde{\tilde{\beta}}}_2^k - c\Delta\hat{\tilde{\tilde{\delta}}}^k - \frac{f_1^2}{f_2^2}\hat{b}_{\mathrm{I}}^k.\end{aligned} \tag{4.53}$$

The clock residuals $(c\delta^k - c\hat{\delta}_{\mathrm{IGS}}^k)$ however do not affect the usage of phase bias estimates. As long as the user applies the same prior corrections on satellite clock offsets, e.g. the

IGS final clock offset product $c\hat{\delta}^k_{\mathrm{IGS}}$, the clock residuals in the phase bias estimates will compensate the clock products.

In this way, we have obtained the estimation of the full set of satellite phase and code biases. The receiver biases can be obtained similarly. However, they stay less in the focus, because the satellite biases can be broadcast and used for a variety of receivers.

PRN k	$c\Delta\hat{\tilde{\delta}}^k$ [m]	$\sigma_{c\Delta\hat{\tilde{\delta}}^k}$ [m]	$\hat{b}^k_1$ [m]	$\sigma_{\hat{b}^k_1}$ [m]	$\lambda_1\Delta\hat{\beta}^k_1$ [m]	$\lambda_2\Delta\hat{\beta}^k_2$ [m]
5	-0.789	0.006	-0.41	0.023	1.23	1.5
7	0.29	0.001	-2.213	0.021	2.059	3.196
9	-0.865	0.001	-0.677	0.013	1.688	1.963
10	-0.352	0.001	1.122	0.019	-0.658	-1.647
12	-0.35	0.004	-1.991	0.018	2.429	3.558
13	0.177	0.007	-1.249	0.019	1.087	1.806
15	-0.987	0.001	-1.868	0.012	2.925	4.065
17	-0.641	0.002	-2.139	0.014	2.832	4.073
18	-1.077	0.003	-2.46	0.017	3.695	5.136
19	0.132	0.006	-4.139	0.023	4.098	6.637
21	0.052	0.009	-3.263	0.026	3.324	5.225
26	-0.773	0.001	-0.137	0.013	0.927	0.879
27	-0.565	0.001	-0.15	0.012	0.855	0.79
28	-0.222	0.001	-2.203	0.016	2.472	3.694

Table 4.4: Bias estimates from the second-stage Kalman filters. Columns from left to right represent satellite PRN number, geometric code bias estimates and their standard deviations, ionospheric code biases on L1 and their standard deviations, derived satellite phase bias estimates on L1 and L2 without mapped code biases, respectively.

4.3.2 Repeatability and Validation

In this section, long-term bias repeatability is analysed. The ionospheric bias estimates are also compared with IGS differential code bias products to validate the algorithm.

The GPS code and carrier phase measurements were taken from Jan. 1st to Jan. 14th, 2011, each day with 6 hours from 20:00 to 02:00(+1). The code multipath effects are reduced by sidereal filtering over 2 weeks, which is described in section 3.2.3. In this section, the slant delay measurements are generated by the code-aligned phase ionospheric-preserving combination. This does not affect the application and validation of the Kriging method with the iterative Greedy algorithm. After the first-stage Kalman filter estimation, a comparison of the ionospheric estimates against the code-aligned phase ionospheric-preserving combination can be performed. The comparison shows that the two measurement sources match well with each other. Therefore, the repeatability and validation analysis is seen valid with the measurements from ionospheric combination as well.

The code-aligned carrier phase combination, as suggested by Sardon et al. in [95], is applied to obtain first-order slant ionospheric delays. The alignment is done for each

receiver-satellite link by determining the constant offset between the code combination and the phase one. In the end, the slant ionospheric delay is obtained as

$$\tilde{\boldsymbol{I}}_r^k = \boldsymbol{I}_{\varphi,r}^k - \mathrm{E}_t\left\{\boldsymbol{I}_{\varphi,r}^k - \boldsymbol{I}_{\rho,r}^k\right\}, \tag{4.54}$$

where the vectors $\tilde{\boldsymbol{I}}_r^k$, $\boldsymbol{I}_r^k$ stack a continuous time series of slant delays for the same satellite-receiver pair, and the indices φ and ρ denote phase and code combination respectively.

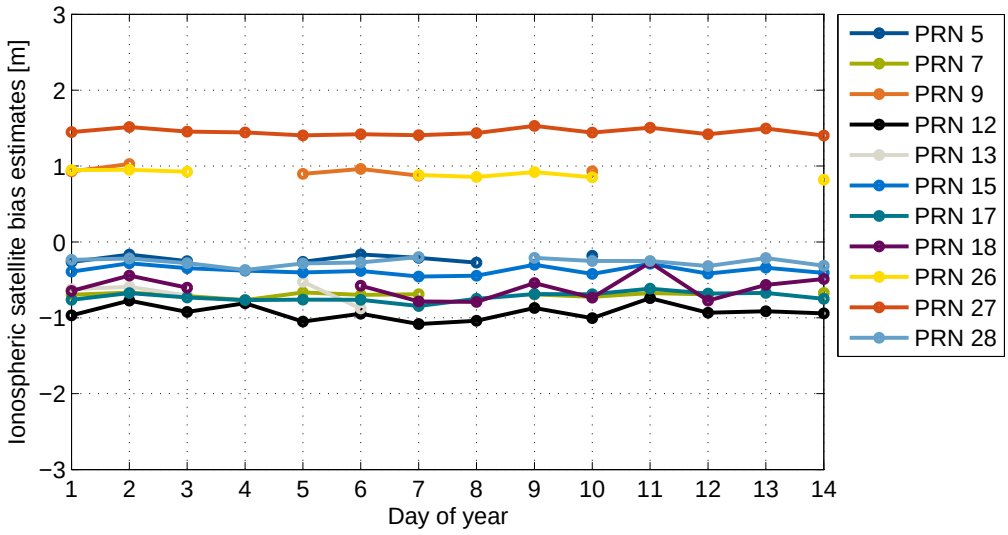

Figure 4.8: The satellite ionospheric bias estimates show a high repeatability over 2 weeks. The smallest variation is seen on the bias estimate from PRN 9 with about 6 cm per 14 days.

Fig. 4.8 depicts the satellite bias estimates over 2 weeks. All satellite bias estimates have been aligned to the zero-sum condition, which is consistent with the reference of the IGS differential code bias products [96]. A high repeatability is observed on each bias estimate, where the most stable one varies about 6 cm per 14 days. The bias estimates are also compared with the IGS DCBs, in order to validate the correctness of the biases. The differences over the consecutive 14 days are shown in Fig. 4.9, where most of the differences on the bias estimates remain below 20 cm.

Fig. 4.10 shows the ground trajectories for the plotted satellites. The bigger variations observed from the satellite bias estimates in Fig. 4.8 and 4.9 can be well explained by the satellite geometries, where the worst ones PRN 12 and PRN 18 are seen with low elevations from the region of Europe (marked with a dashed rectangular) throughout the whole period.

4.4 Conclusions

In this chapter, a new algorithm was proposed for joint estimation of ionospheric vertical delays and code biases. Kriging method was applied to remove the rank-deficiency by

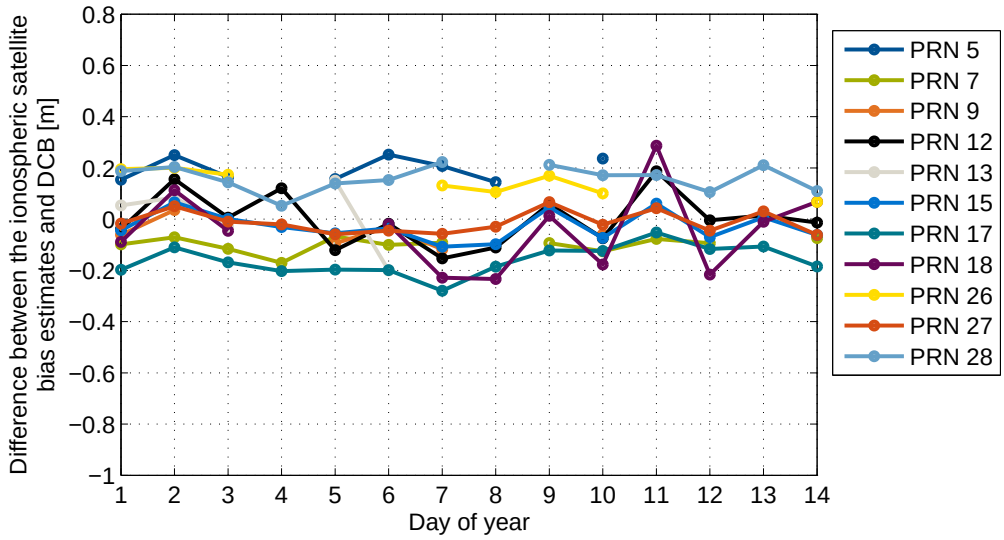

Figure 4.9: Difference between the satellite ionospheric biases and the IGS differential code biases over 2 weeks.

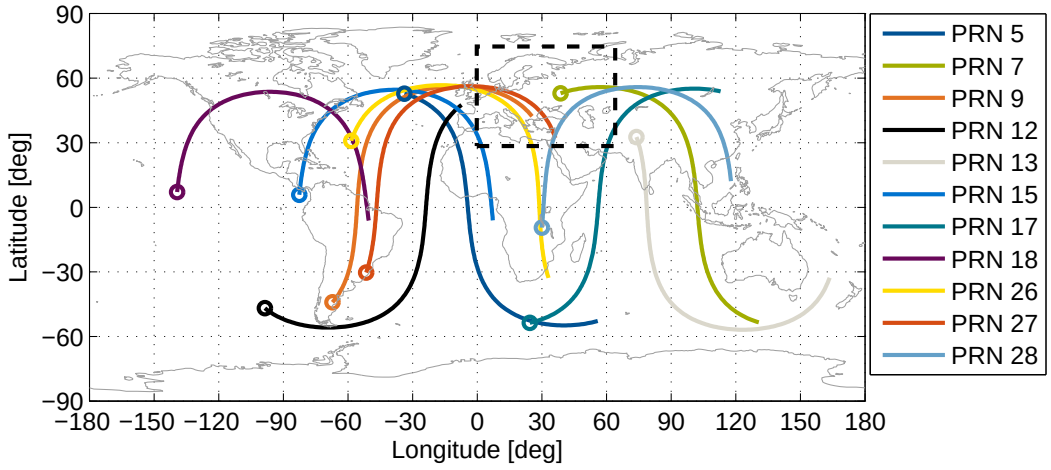

Figure 4.10: The ground tracks for the selected satellites between 20:00 and 2:00(+1) on Jan. 1, 2011. The starting point for each track is marked with a circle.

representing a subset of vertical delays with the remaining ones. The key to a successful representation is a minimum loss of information, which is made possible by the best linear unbiased Kriging estimator. It exploits the spatial correlation of the ionosphere through the variogram. An iterative Greedy algorithm was introduced to determine the selection of the estimated subset. Real data results have shown centimeter-accurate vertical delay and bias estimates, while the comparison to the IGS differential code biases confirms the correctness of the bias estimates. Most importantly, the estimation of code ionospheric biases completed the estimation of the full set of phase and code bias estimates. The bias mappings introduced in Chapter 3 were resolved by cascaded Kalman filtering.

It should be mentioned that the experiment data was selected in the night when the ionosphere is quiet. However the algorithm always estimates a subset of vertical delays which relate directly to the instant measurements. Thus it is reasonable to expect a similar accuracy during the daytime, as long as the variogram could well describe the field.

Chapter 5

Assisted GPS with Precise Ephemerides

Most commercial receivers decode broadcast navigation messages in order to obtain satellite coordinates. In the case of a cold-start, the receiver needs to perform a full search in frequency and time delay to acquire the satellites, which may take quite some time. Assisted-GPS (A-GPS) provides the receiver with assistance information, which reduces the time and effort for the receiver to obtain satellite coordinates and start tracking. The assistance data includes four main elements: namely orbits, time, frequency, and position [97].

This mechanism could also be used to provide precise orbit to the receiver. IGS rapid products provide precise satellite orbits and are also suitable for real-time applications. They are however in forms of Cartesian coordinates referred to the satellite's center of mass. Kosola et al., González and Reid et al. have studied the conversion of Cartesian coordinates to GPS-compatible formats [98–100]. This chapter presents a similar method to generate broadcast-like orbit parameters from precise orbits. In addition to estimating conventional broadcast ephemerides, the method also presents non-singular orbital elements as alternative state estimates. Moreover, long time evaluation of the algorithm is performed and statistics for all PRNs are presented.

5.1 Curve Fit Algorithm

A set of six independent Keplerian parameters $(a, e, i, \omega, \Omega, M)$ uniquely defines the position of a satellite in the space [101]. The GPS broadcast ephemerides are calculated by predicting orbits forward on the basis of a curve fit interval of 4 to 6 hours. They include the Keplerian parameters at reference epoch and a series of corrections, i.e.

$\sqrt{a}$	square root of semi-major axis,
Δn	correction to mean motion,
M_0	mean anomaly at reference time,
e	eccentricity,
Ω_0	longitude of ascending node at reference time,
i_0	inclination angle at reference time,
ω	argument of perigee,
$\dot{\Omega}$	rate of right ascension,
$\dot{i}$	rate of inclination angle,
t_{oe}	reference time ephemeris,
C_{us}, C_{uc}	amplitude of the sine, cosine harmonic correction term to the latitude,
C_{rs}, C_{rc}	amplitude of the sine, cosine harmonic correction term to the orbit radius,

C_{is}, C_{ic} amplitude of the sine, cosine harmonic correction term to the inclination.

We determine the broadcast ephemerides based on curve fit of the Cartesian coordinates in a time window. The Cartesian coordinates at epochs t_1 to t_m are gathered in a measurement vector $\boldsymbol{z}$ as

$$\boldsymbol{z} = \left[\vec{\boldsymbol{r}}_{t_1},\ \vec{\boldsymbol{r}}_{t_2},\ \ldots, \vec{\boldsymbol{r}}_{t_m}\right]^{\mathrm{T}}, \tag{5.1}$$

with m being the number of epochs in the fit interval.

The broadcast-like state vector, denoted by $\boldsymbol{x}$, includes 6 Keplerian parameters and 9 correction terms, i.e.

$$\boldsymbol{x} = \left[a,\ e,\ i_0,\ \Omega_0,\ \omega,\ M_0,\ \Delta n,\ \dot{i},\ \dot{\Omega},\ C_{\mathrm{us}},\ C_{\mathrm{uc}},\ C_{\mathrm{rs}},\ C_{\mathrm{rc}},\ C_{\mathrm{is}},\ C_{\mathrm{ic}}\right]^{\mathrm{T}}. \tag{5.2}$$

The ephemeris vector is solved by a non-linear least-squares problem, which minimizes the weighted quadratic error norm of the fitting, i.e.

$$\hat{\boldsymbol{x}} = \underset{\boldsymbol{x}}{\operatorname{argmin}} \left\|\boldsymbol{z} - \boldsymbol{z}(\boldsymbol{x})\right\|_{\boldsymbol{W}}^2, \tag{5.3}$$

where $\boldsymbol{z}(\boldsymbol{x})$ denotes the vector of satellite coordinates evaluated with the ephemeris vector $\boldsymbol{x}$, and the weighting matrix $\boldsymbol{W}$ is the inverse of the measurement noise covariance matrix.

The non-linear least-squares problem in Eq. (5.3) can be solved by Gauss-Newton algorithm. First, the ephemeris vector $\boldsymbol{x}$ is initialized with a guess as $\boldsymbol{x}^{(0)}$

$$\hat{\boldsymbol{x}}^{(0)} = \left[a,\ e,\ i_0,\ \Omega_0,\ \omega,\ M_0,\ 0,\ 0,\ 0,\ 0,\ 0,\ 0,\ 0,\ 0,\ 0\right]^{\mathrm{T}}. \tag{5.4}$$

The harmonic corrections terms are assumed to be zero, while the initial Keplerian parameters come from the broadcast ephemerides.

At $(i+1)$-th iteration step, the state vector is updated by minimizing the norm of current measurement residuals based on the state vector $\hat{\boldsymbol{x}}^{(i)}$, i.e.

$$\hat{\boldsymbol{x}}^{(i+1)} = \hat{\boldsymbol{x}}^{(i)} + \left(\boldsymbol{J}^{(i),\,\mathrm{T}}\boldsymbol{W}\boldsymbol{J}^{(i)}\right)^{-1}\boldsymbol{J}^{(i),\,\mathrm{T}}\boldsymbol{W}\left(\boldsymbol{z} - \boldsymbol{z}(\hat{\boldsymbol{x}}^{(i)})\right). \tag{5.5}$$

The Jacobian matrix $\boldsymbol{J}^{(i)}$ at the i-th step has a dimension of $3m \times 15$, and is expressed as

$$\boldsymbol{J} = \begin{bmatrix} \dfrac{\partial \vec{\boldsymbol{r}}_{t_1}(\hat{\boldsymbol{x}}^{(i)})}{\partial a} & \dfrac{\partial \vec{\boldsymbol{r}}_{t_1}(\hat{\boldsymbol{x}}^{(i)})}{\partial e} & \dfrac{\partial \vec{\boldsymbol{r}}_{t_1}(\hat{\boldsymbol{x}}^{(i)})}{\partial i_0} & \dfrac{\partial \vec{\boldsymbol{r}}_{t_1}(\hat{\boldsymbol{x}}^{(i)})}{\partial \Omega_0} & \cdots & \dfrac{\partial \hat{\vec{\boldsymbol{r}}}_{t_1}(\hat{\boldsymbol{x}}^{(i)})}{\partial C_{\mathrm{is}}} & \dfrac{\partial \vec{\boldsymbol{r}}_{t_1}(\hat{\boldsymbol{x}}^{(i)})}{\partial C_{\mathrm{ic}}} \\ \dfrac{\partial \vec{\boldsymbol{r}}_{t_2}(\hat{\boldsymbol{x}}^{(i)})}{\partial a} & \dfrac{\partial \vec{\boldsymbol{r}}_{t_2}(\hat{\boldsymbol{x}}^{(i)})}{\partial e} & \dfrac{\partial \vec{\boldsymbol{r}}_{t_2}(\hat{\boldsymbol{x}}^{(i)})}{\partial i_0} & \dfrac{\partial \vec{\boldsymbol{r}}_{t_2}(\hat{\boldsymbol{x}}^{(i)})}{\partial \Omega_0} & \cdots & \dfrac{\partial \vec{\boldsymbol{r}}_{t_2}(\hat{\boldsymbol{x}}^{(i)})}{\partial C_{\mathrm{is}}} & \dfrac{\partial \vec{\boldsymbol{r}}_{t_2}(\hat{\boldsymbol{x}}^{(i)})}{\partial C_{\mathrm{ic}}} \\ \vdots & \vdots & \vdots & \vdots & \ddots & \vdots & \vdots \\ \dfrac{\partial \vec{\boldsymbol{r}}_{t_m}(\hat{\boldsymbol{x}}^{(i)})}{\partial a} & \dfrac{\partial \vec{\boldsymbol{r}}_{t_m}(\hat{\boldsymbol{x}}^{(i)})}{\partial e} & \dfrac{\partial \vec{\boldsymbol{r}}_{t_m}(\hat{\boldsymbol{x}}^{(i)})}{\partial i_0} & \dfrac{\partial \vec{\boldsymbol{r}}_{t_m}(\hat{\boldsymbol{x}}^{(i)})}{\partial \Omega_0} & \cdots & \dfrac{\partial \vec{\boldsymbol{r}}_{t_m}(\hat{\boldsymbol{x}}^{(i)})}{\partial C_{\mathrm{is}}} & \dfrac{\partial \vec{\boldsymbol{r}}_{t_m}(\hat{\boldsymbol{x}}^{(i)})}{\partial C_{\mathrm{ic}}} \end{bmatrix}, \tag{5.6}$$

with the partial derivatives explicitly computed in Appendix E.

It is noted that, the states have large differences to several orders of magnitude in the absolute values, e.g. the semi-major axis is in the order of 10^7, while the rate of inclination $\dot{i}$ is around 10^{-10}. This results in a badly conditioned Jacobian matrix. In order to enhance

numerical stability, a scale vector is multiplied to the Jacobian matrix, and subsequently removed from the state vector. The scale vector $\boldsymbol{s}$ is given by

$$\boldsymbol{s} = \left[1, 10^{-7}, 10^{-7}, 10^{-7}, 10^{-7}, 10^{-7}, 10^{-11}, 10^{-11}, 10^{-11}, 10^{-7}, 10^{-7}, 1, 1, 10^{-7}, 10^{-7}\right]^{\mathrm{T}}. \quad (5.7)$$

The modified estimation algorithm is suggested as

$$\tilde{\boldsymbol{J}}^{(i)} = \boldsymbol{J}^{(i)} \cdot \mathrm{diag}(\boldsymbol{s}), \quad (5.8)$$

$$\hat{\boldsymbol{x}}^{(i+1)} = \hat{\boldsymbol{x}}^{(i)} + \mathrm{diag}(\boldsymbol{s}) \cdot \left(\tilde{\boldsymbol{J}}^{(i),\,\mathrm{T}} \boldsymbol{W} \tilde{\boldsymbol{J}}^{(i)}\right)^{-1} \tilde{\boldsymbol{J}}^{(i),\,\mathrm{T}} \boldsymbol{W} \left(\boldsymbol{z} - \boldsymbol{z}(\hat{\boldsymbol{x}}^{(i)})\right), \quad (5.9)$$

with $\mathrm{diag}(\cdot)$ transforming a vector into a diagonal matrix.

Moreover, if the satellite orbits tend to be near-circular, the eccentricity is close to zero, which leads to a singularity problems may arise as the argument of perigee is difficult to be defined for small eccentricities. Similar applies for the difficulty in determining the longitude of ascending node Ω when the inclination is small [101]. In the case of GPS orbits, the eccentricity is quite small, therefore, a possible set of non-singular orbital elements is introduced in [102] as

$$a, \;\; i_0, \;\; \Omega_0, \;\; \xi = e\cos\omega, \;\; \eta = -e\sin\omega, \;\; \lambda = M_0 + \omega. \quad (5.10)$$

The traditional Keplerian parameters can be easily retrieved by

$$\begin{aligned} e &= \sqrt{\xi^2 + \eta^2}, \\ \omega &= -\arg(\xi + i\eta), \\ M_0 &= \lambda - \omega, \end{aligned} \quad (5.11)$$

where $\arg(\cdot)$ denotes the argument operator. The derivation of the partial derivatives to the transformed ephemerides are found in Appendix E.

5.2 Estimation of Precise Broadcast Ephemerides

In order to validate the curve fit algorithms, we first use measurements from known broadcast ephemerides, which can be compared with the orbital estimates. The GPS ephemerides from a randomly chosen PRN 9 are collected on October 6th, 2013. The satellite Cartesian coordinates are then generated with an epoch interval of 15 minutes. The fit interval is set to 2 hours. There are thus 8 sets of coordinates to determine each set of unknown orbital parameters.

The state vector consists of the traditional 6 Keplerian and 9 correction terms, while the use of the non-singular set brings limited improvement in this case. Fig. 5.1 shows the errors on the scaled orbital states using Gauss-Newton method. The scaling factors in the plot are chosen such that a ratio of 1 represents meter-level error on the coordinates. It can be seen that the state estimates have at least one order of magnitude smaller than millimeter-level impact.

Furthermore, a correlation is observed between the argument of perigee ω and the mean anomaly M_0 at reference epoch. The reason for this is under small eccentricity, the

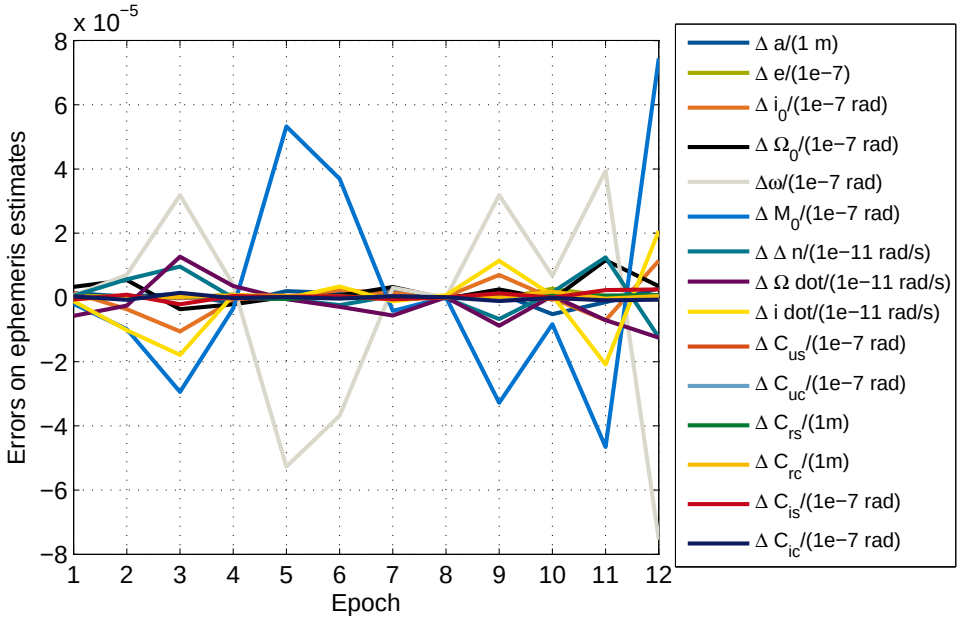

Figure 5.1: The estimation error on the 6 Keplerian parameters and 9 correction terms. The scaling factors indicate the orders of magnitude of the states causing meter-level error on the satellite coordinates.

argument of perigee could not be well defined, while the mean anomaly M approaches the true anomaly ν. The argument of latitude thus becomes

$$\Phi = \nu + \omega \simeq M + \omega = M_0 + n \cdot \Delta t + \omega, \tag{5.12}$$

which indicates that M_0 and ω are difficult to be separated.

Next, precise real-time orbit serves as measurements in order to estimate a set of precise ephemerides for PRN 9. We use the IGS ultra-rapid orbit product (with predicted half), which is updated every six hours with prediction of 24 hours. The accuracy of the orbit is given as 5 cm [22]. Like in the previous experiment, the epoch interval and fit interval have been set to 15 minutes and 2 hours, respectively. The IGS phase center offsets are applied to the orbit products to shift the positions to the phase centers.

The observation duration is one week, spanning from October 6th to October 12th, 2013. To evaluate the results, the reconstructed Cartesian coordinates are compared with the reference orbits, based on the estimated ephemeris vector with a smaller interval of 3 minutes. The reference coordinates are obtained from 12-order polynomial fitting of the 15-minute-spaced precise IGS ultra-rapid orbit. Fig. 5.2 depicts the measurement residuals. The variations of the residuals show different accuracies in different fit intervals of 2 hours. In some fit intervals, the estimated ephemerides match with the reference orbits with residuals below 1 cm. Other periods have residuals being up to ±5 cm. It is believed to be dependant on the initialization for the Newton's method.

Now the IGS final orbit is taken as a true reference, while the errors of the Cartesian coordinates are shown in Fig. 5.3. The coordinates are computed from the precise ephemerides and from the broadcast ephemerides respectively. The benefit of the precise

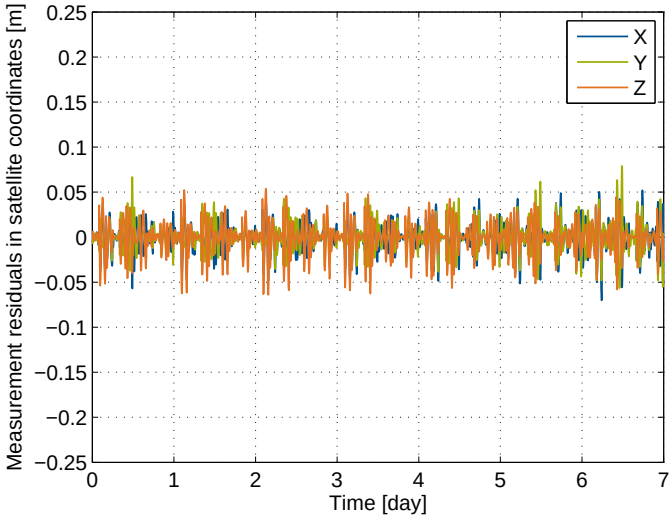

Figure 5.2: The difference between the ultra-rapid orbit and the computed coordinates, which are evaluated based on the estimated ephemerides with 3-minute interval.

ephemerides is clearly seen, with a reduction factor of about 50 times in terms of measurement residuals. When using the broadcast ephemerides in Fig. 5.3(a), all three coordinates have errors of up to 2 m. The precise ephemerides indicate only coordinates errors of 5 cm despite a larger variation on day 1 and day 2.

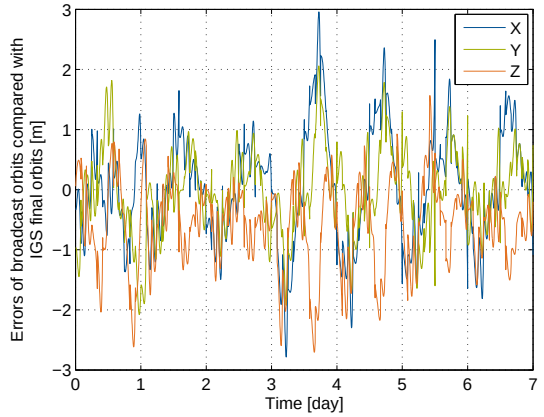

(a) The broadcast orbits have meter-level accuracy.

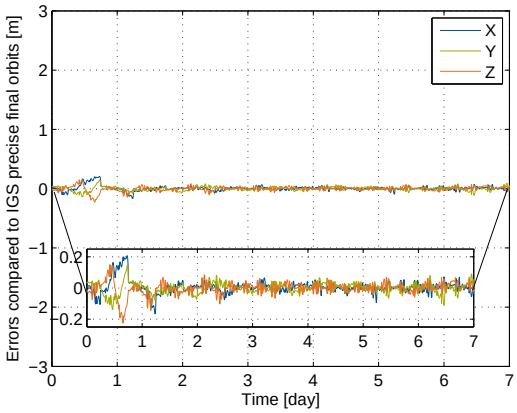

(b) The orbits generated from the estimated precise ephemerides are accurate to 5 cm.

Figure 5.3: Benefit of the precise ephemerides compared with the broadcast ephemerides, where the accuracy is improved by almost 50 times.

The large variations up to 20 cm on day 1 and 2 are analyzed, where the error does not lie in the curve fitting algorithm according to the residuals plot in Fig. 5.2. Instead, it comes from the quality of the predicted orbit for PRN 9 in the IGS ultra-rapid product. Using the "observed half" orbit measurements which have a few hours latency instead of the real-time "predicted half", the quality of the orbits are improved, shown in Fig. 5.4.

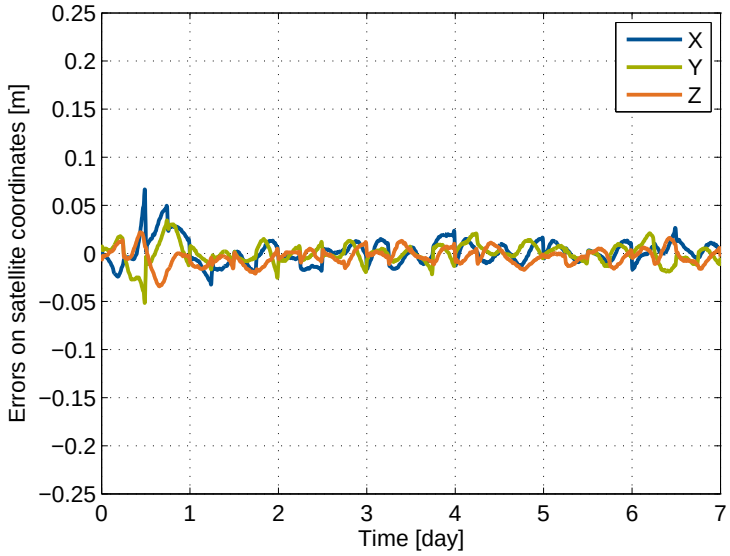

Figure 5.4: The errors of the IGS ultra-rapid "observed half" (post-processed) orbit, where the orbits accuracy has much improved from the real-time "predicted half" orbits.

It is seen that the large variations on day 1 and 2 are mostly vanished, while the errors on the other days are even below 2 cm.

Until now, the error analysis of the precise ephemerides is studied only for one satellite, i.e. PRN 9, and one week. To obtain reasonable statistics, longer observation time and more satellites are suggested, where the measurements for all PRNs are gathered from the IGS ultra-rapid predicted orbit for 31 days in October, 2013. The Cartesian coordinates are reconstructed at an interval of 5 minutes and compared with the reference IGS final orbit, with a total of 267264 samples for each coordinate. Finally the coordinates are transformed from ECEF frame to satellite RAC frame, see Eq. (2.7). The steps to calculate the satellite velocities from the ephemeris parameters are described in Appendix F.

The histograms are drawn in Fig. 5.5, which indicates the standard deviations of the orbital errors for the radial, along- and cross-track are around 2 cm, 2 cm and 3 cm respectively. Note that the bell-shaped histogram for the radial component are centered at around 1 cm, however the offset appears the same for all satellites (not shown in the figure). This non-zero mean could indicate that the satellite clock offsets are slightly different when determining the predicted orbit and the final orbit.

Differences among the satellite types can be observed if we zoom in the histograms at the edges. Fig. 5.6 shows the comparison of the Block IIA, IIR, IIRM, and IIF, where more accurate predicted orbits can be obtained for more modernized satellite type.

5.3 Round-off Error Analysis

We study in this section, whether the representation of the orbital elements in the navigation message would result in a non-negligible error. In the transmission of the navigation message, the allocated bits for the ephemerides with scale factors guarantees more than

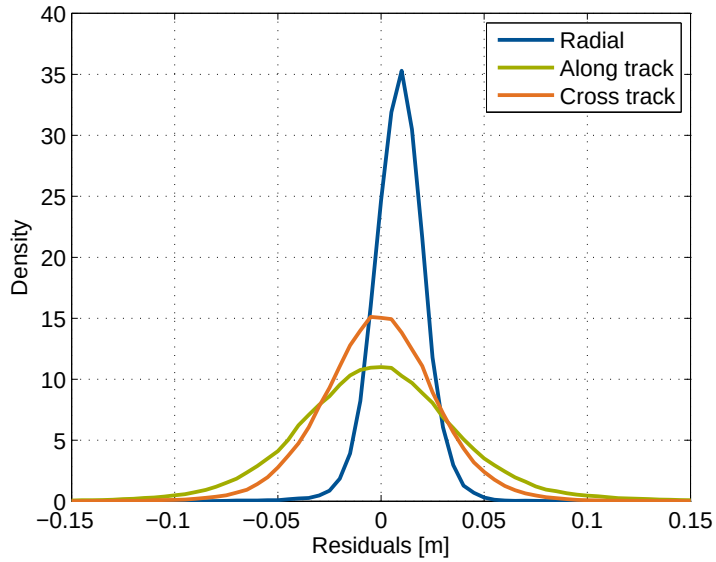

Figure 5.5: Histograms of the radial, along- and cross-track errors using estimated precise ephemerides for one month, which indicate accuracies of less than 3 cm.

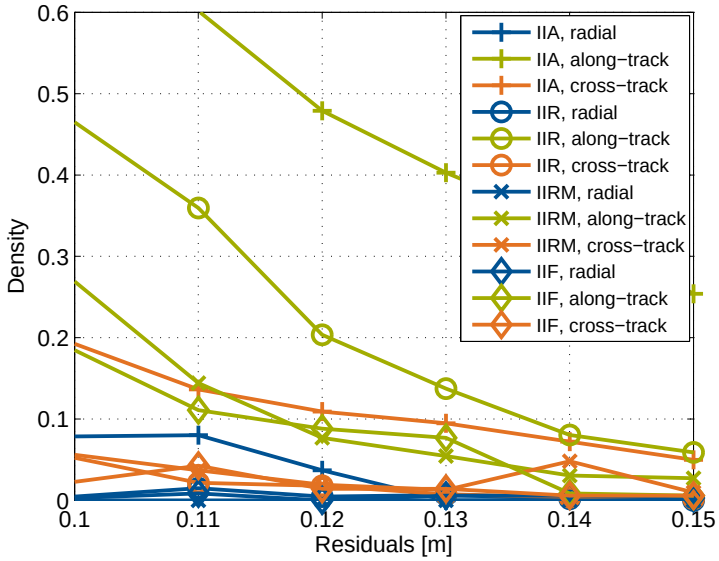

Figure 5.6: Comparison of the normalized density between different satellite types. The Block IIA has the worst performance, then follows IIR, while IIRM and IIF have the most accurate predicted orbit.

sufficient accuracy [26]. Table 5.1 lists the 6 Keplerian parameters with their effective ranges, and the worst-case representation errors.

Now the last digit of one or multiple Keplerian parameters are adjusted, for PRN 9 from the broadcast navigation file on October 6th, 2013. The new orbits are compared with the original broadcast orbits, and the errors of the 3D positions are plotted in Fig. 5.7. It

Parameter	Number of bits	Scale factor (LSB)	Effective range	Worst-case error	Units
$\sqrt{a}$	32	2^{-19}	0 to $8193 - 2^{-19}$	10^{-8}	$(\text{meter})^{1/2}$
e	32	2^{-33}	0 to $1 - 2^{-33}$	10^{-13}	unitless
i_0	32*	$2^{-31}\pi$**	$(2^{-31} - 1)\pi$ to $(1 - 2^{-31})\pi$	10^{-12}	radians
Ω_0	32*	$2^{-31}\pi$	$(2^{-31} - 1)\pi$ to $(1 - 2^{-31})\pi$	10^{-11}	radians
ω	32*	$2^{-31}\pi$	$(2^{-31} - 1)\pi$ to $(1 - 2^{-31})\pi$	10^{-11}	radians
M_0	32*	$2^{-31}\pi$	$(2^{-31} - 1)\pi$ to $(1 - 2^{-31})\pi$	10^{-11}	radians

* means the sign bit (+ or −) occupies the most-significant-bit (MSB).
** The conversion from semi-circles to radians: 1 semi-circles= π radians.

Table 5.1: Keplerian ephemerides parameters.

is clearly seen that the effect of round-off error on a single parameter is well negligible. Moreover, simultaneous round-off errors on all Keplerian parameters only affect the satellite positions at millimeter-level, which is comparable to or less than the noise of phase measurements.

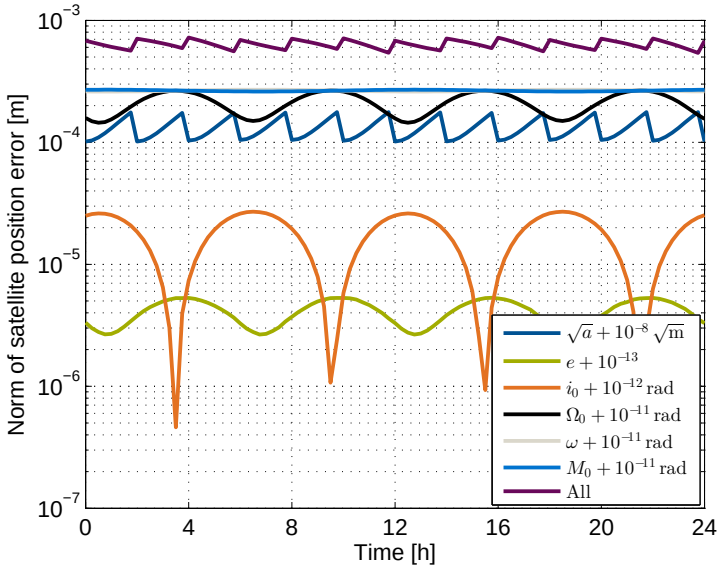

Figure 5.7: Impact of round-off errors of the Keplerian parameters on the satellite orbits. Even if all 6 parameters have round-off errors (shown in magenta), the effect is at sub-millimeter level.

The analysis for the impact of representation errors of the other correction terms, e.g. the correction to mean motion, the rate of inclination, the rate of right ascension and the harmonic corrections, etc., can be performed similarly and is thus omitted here.

Chapter 6

Conclusions

In this work, precise point positioning has been performed with absolute carrier phase and code measurements, where most of above cm-level effects have been either modelled or estimated. The code multipath and the high correlation between the tropospheric zenith delay and the receiver height coordinate belong to most challenging tasks for PPP. Therefore, improvements have been made on the coordinate estimates, by augmenting the state vector with a subset of code multipath and by estimating the tropospheric zenith delay with intervals. The proposed algorithms were tested with real GPS data, where the variations on the coordinates errors were significantly reduced. Moreover, the PPP algorithm has been extended for a multi-GNSS system, by assigning different receiver clock offsets for different systems.

New algorithms were proposed for estimation of satellite phase and code biases. The system of equations was made solvable after removing rank-deficiencies in the code biases, phase biases and integer ambiguities. The parameter mappings include mapping the code biases into the geometric and ionospheric parameters, mapping one satellite phase bias into receiver phase bias, and mapping a subset of ambiguities into the phase biases and other ambiguities. Cascaded Kalman filters were introduced to estimate the phase biases and the code biases in two-steps. Real measurements from a regional SAPOS network as well as a global IGS network have been processed for a continuous period of 24 hours. It has shown a remarkable stability of the phase bias estimates over hours. The phase bias estimates were also observed to converge to identical values when the satellite geometry repeated itself. Furthermore, the code multipath was substantially removed by sidereal filtering for each reference station, as the GPS satellite geometry returns the same after each revolution.

The geometric code biases are estimated together with the orbital errors in the second-stage Kalman filter. The first-stage outcome from the global reference network was used, while Bryson and Henrikson's method has been applied to decouple the colored measurement noise. A table of orbital errors geometric code bias estimates was obtained. The accuracy of the bias estimates is expected to be improved by an augmented network with more reference stations.

A new algorithm for joint estimation of ionospheric delays and ionospheric code biases has been proposed, where a subset of vertical delays was estimated and the remaining vertical delays were represented by the subset. The key to a successful representation was a minimum loss of information, which was made possible by the best linear unbiased Kriging estimator. It exploited the spatial correlation of the ionosphere through the variogram. The real data results have shown accurate vertical delay and bias estimates, while the comparison to the IGS differential code biases confirmed the correctness of our bias estimates. Although the experiment data was selected in the night with a quiet ionosphere, however

a similar accuracy is expected also during the daytime. The reason is the algorithm always estimates a subset of vertical delays which relates directly to the instant measurements. As long as the background knowledge, i.e. the variogram, well describes the field, the ionosphere can be well modelled by the Kriging estimator. Moreover, the precise ionospheric estimates would enable a single-frequency receiver to position itself with better accuracy.

The first-stage phase bias estimates, the geometric code bias estimates and the ionospheric code bias estimates from the second-stage filter, together form a full table of phase and code bias estimates. This completes the estimation for the needed satellite biases for PPP.

Last but not least, the concept of assisted-GPS has been further developed, where real-time precise satellite ephemerides were provided to the user following to the established broadcast description. A receiver could thus perform the stand-alone positioning correcting satellite orbits at centimeter-level, rather than the current meter-level from the broadcast ephemerides. Least-squares curve fit algorithms were presented with iterative Gauss-Newton method, fitting real-time precise Cartesian coordinates into a set of Keplerian parameters and harmonic corrections. Furthermore, the ionospheric delay could be similarly aided to the receiver, by fitting local ionospheric corrections into Klobuchar model coefficients that have been broadcast by the satellites. This would bring the same benefit as the precise ephemerides, as the local ionospheric corrections could be much more precise than the ionosphere derived from the blind Klobuchar model. Besides, the round-off representation errors of the broadcast ephemerides were evaluated, which showed negligible (millimeter-level) effect on the satellite coordinates.

Appendix A

Satellite Antenna Phase Center Offset

The satellite antenna phase center offset (PCO) describes the offset from the satellite center of mass to the mean phase center. The PCOs determined by different organisations are listed in Table A.1, i.e. from the IGS and the National Geospatial Intelligence Agency (NGA, which represents the GPS control segment). The satellite PCOs are grouped by satellite types, with small differences within each group. It is also observed that the horizontal offsets from the two sources agree on the millimeter level with each other, while the vertical component differs a lot. This implies the satellite clock products would also be different from each other, since the vertical offset correlates highly with the satellite clock. Therefore, a consistent set of orbit corrections is always recommended, including satellite PCO and satellite clock offset.

Table A.1: Comparison between IGS and NGA published PCO values in satellite local coordinate frame [27, 103]. (Effective date: Oct. 6, 2013)

		$\vec{r}_{\mathrm{PCO,IGS}}$			$\vec{r}_{\mathrm{PCO,NGA}}$		
Satellite Type	PRN	r_x (m)	r_y (m)	r_z (m)	r_x (m)	r_y (m)	r_z (m)
Block IIA	3	0.2790	0	2.7926	0.2794	0	0.9519
Block IIA	4	0.2790	0	2.4200	0.2794	0	0.9519
Block IIA	6	0.2790	0	2.8786	0.2794	0	0.9519
Block IIA	8	0.2790	0	2.5781	0.2794	0	0.9519
Block IIA	9	0.2790	0	2.4614	0.2794	0	0.9519
Block IIA	10	0.2790	0	2.5465	0.2794	0	0.9519
Block IIA	26	0.2790	0	2.4594	0.2794	0	0.9519
Block IIA	30	0.2790	0	2.3522	0.2794	0	0.9519
Block IIA	32	0.2790	0	2.7772	0.2794	0	0.9519
Block IIR-A	11	0	0	1.1413	0.0019	0.0011	1.5141
Block IIR-A	13	0	0	1.3895	0.0024	0.0025	1.6140
Block IIR-A	14	0	0	1.3454	0.0018	0.0002	1.6137
Block IIR-A	16	0	0	1.5064	-0.0098	0.0060	1.6630
Block IIR-A	18	0	0	1.2909	-0.0098	0.0060	1.5923
Block IIR-A	20	0	0	1.3436	0.0022	0.0014	1.6140
Block IIR-A	21	0	0	1.4054	0.0023	-0.0006	1.5840
Block IIR-A	28	0	0	1.0428	0.0019	0.0007	1.5131
Block IIR-B	2	0	0	0.7786	-0.0099	0.0061	-0.0820
Block IIR-B	19	0	0	0.8496	-0.0079	0.0046	-0.0180
Block IIR-B	22	0	0	0.9058	0.0018	-0.0009	0.0598

Table A.1 – continued from previous page

		$\vec{r}_{\mathrm{PCO,IGS}}$			$\vec{r}_{\mathrm{PCO,NGA}}$		
Satellite Type	PRN	r_x (m)	r_y (m)	r_z (m)	r_x (m)	r_y (m)	r_z (m)
Block IIR-B	23	0	0	0.8082	-0.0088	0.0035	0.0004
Block IIR-M	5	0	0	0.8226	0.00292	-0.00005	-0.01671
Block IIR-M	7	0	0	0.8529	0.00127	0.00025	0.00056
Block IIR-M	12	0	0	0.8408	-0.01016	0.00587	-0.09355
Block IIR-M	15	0	0	0.6811	-0.00996	0.00579	-0.01227
Block IIR-M	17	0	0	0.8271	-0.00996	0.00599	-0.10060
Block IIR-M	29	0	0	0.8571	-0.01012	0.00591	-0.01512
Block IIR-M	31	0	0	0.9714	0.00160	0.00033	-0.05750
Block IIF	1	0.3940	0	1.6500	0.39100	0	1.09100
Block IIF	24	0.3940	0	1.6000	0.39200	0.00200	1.09300
Block IIF	25	0.3940	0	1.5973	0.39200	0.00200	1.09300
Block IIF	27	0.3940	0	1.6000	0.39140	0.00030	1.09040

Appendix B

Ocean Tidal Loading

Various methods can be used to compute ocean tidal loading, where the Green's function method belongs to one of them. Agnew proposed in [104] to calculate the tidal loading by multiplying an ocean tide model with the impulse Green's function, and by integrating over all surface elements. The displacement vector $\vec{\boldsymbol{r}}_{\mathrm{ol}}$ in vertical, south and west directions at time t reads

$$\Delta\vec{\boldsymbol{r}}_{\mathrm{ol}}(\varphi,\lambda,t) = \int_0^{2\pi}\int_0^{\pi} \rho h(\varphi',\lambda',t)\boldsymbol{G}(\theta,A)R^2\sin\varphi'\,\mathrm{d}\varphi'\,\mathrm{d}\lambda', \tag{B.1}$$

where (φ,λ) and (φ',λ') are the geographical coordinates of the observation point and the tidal point, ρ denotes ocean water density, h is the instantaneous tidal height at tidal point, R is the radius of the earth, $R^2\sin(\varphi')d\varphi' d\lambda'$ denotes spherical surface element.

The mass loading Green's function $\boldsymbol{G}(\theta,A)$ mainly depends on the spherical distance between the observation point and the tidal point, which is represented by the central angle θ, and depends on the azimuth angle A. The Green's function is expressed in three directions (vertical, south and west) [105] as

$$\boldsymbol{G}(\theta,A) = \begin{bmatrix} u(\theta) \\ v(\theta)\cos(A) \\ v(\theta)\sin(A) \end{bmatrix}. \tag{B.2}$$

The components $u(\theta)$ and $v(\theta)$ are sums of Legendre functions $P_n(\cos\theta)$ and their derivatives respectively, with h_n and l_n being the Love numbers, i.e.

$$\begin{aligned} u(\theta) &= \frac{a}{m_e}\sum_{n=0}^{\infty} h_n P_n(\cos\theta) \\ v(\theta) &= \frac{a}{m_e}\sum_{n=1}^{\infty} l_n \frac{\partial P_n(\cos\theta)}{\partial\theta}. \end{aligned} \tag{B.3}$$

where θ is obtained by spherical law of cosines as

$$\cos\theta = \sin\varphi\sin\varphi' + \cos\varphi\cos\varphi'\cos(\lambda-\lambda'). \tag{B.4}$$

The instantaneous tidal height $h(\varphi',\lambda',t)$ is decomposed by a sum of the tidal harmonic constituents as

$$\begin{aligned} h(\varphi',\lambda',t) &= \sum_{j=1}^{N}\zeta_j(\varphi',\lambda')\cos(\omega_j t+\chi_j-\delta_j) \\ &= \sum_{j=1}^{N}\left(h_{j,\mathrm{c}}(\varphi',\lambda')\cos(\omega_j t+\chi_j) + h_{j,\mathrm{s}}(\varphi',\lambda')\sin(\omega_j t+\chi_j)\right), \end{aligned} \tag{B.5}$$

where $N = 11$ main tidal waves including long-period, diurnal and semidiurnal ones are considered in practice without actual loss of accuracy. The cosine and sine parts are defined by

$$\begin{aligned} h_{j,\mathrm{c}}(\varphi', \lambda') &= \zeta_j(\varphi', \lambda') \cos(\delta_j) \\ h_{j,\mathrm{s}}(\varphi', \lambda') &= \zeta_j(\varphi', \lambda') \sin(\delta_j). \end{aligned} \tag{B.6}$$

Applying the above equations in Eq. (B.1) yields

$$\begin{aligned} \Delta\vec{\boldsymbol{r}}_{\mathrm{ol}}(\varphi, \lambda, t) = \int_0^{2\pi} \int_0^{\pi} \rho \sum_{j=1}^{N} \left(h_{j,\mathrm{c}}(\varphi', \lambda') \cos(\omega_j t + \chi_j) + h_{j,\mathrm{s}}(\varphi', \lambda') \sin(\omega_j t + \chi_j) \right) \boldsymbol{G}(\theta, A) \cdot \\ \cdot R^2 \sin\varphi' \, \mathrm{d}\varphi' \, \mathrm{d}\lambda' \\ = \sum_{j=1}^{N} \left(\left(\rho R^2 \int_0^{2\pi} \int_0^{\pi} h_{j,\mathrm{c}}(\varphi', \lambda') \boldsymbol{G}(\theta, A) \sin\varphi' \, \mathrm{d}\varphi' \, \mathrm{d}\lambda' \right) \cdot \cos(\omega_j t + \chi_j) + \right. \\ \left. + \left(\rho R^2 \int_0^{2\pi} \int_0^{\pi} h_{j,\mathrm{s}}(\varphi', \lambda') \boldsymbol{G}(\theta, A) \sin\varphi' \, \mathrm{d}\varphi' \, \mathrm{d}\lambda' \right) \cdot \sin(\omega_j t + \chi_j) \right), \end{aligned} \tag{B.7}$$

Eq. (B.7) can be transformed using trigonometric addition formula to a much simplified form of Eq. (2.27), i.e.

$$\Delta r_{\mathrm{ol},i} = \sum_{j=1}^{N} a_{j,i} \cos(\omega_j t + \chi_j - \phi_{j,i}), \tag{B.8}$$

where the j-th amplitude and phase components for each x-, y- and z-coordinate of the displacement vector (denoted by $i = 1, 2, 3$) are given by

$$\begin{aligned} a_{j,i}^2(\varphi, \lambda) = \left(\rho R^2 \int_0^{2\pi} \int_0^{\pi} \rho h_{j,\mathrm{c}}(\varphi', \lambda') G_i(\theta, A) \sin\varphi' \, \mathrm{d}\varphi' \, \mathrm{d}\lambda' \right)^2 + \\ + \left(\rho R^2 \int_0^{2\pi} \int_0^{\pi} \rho h_{j,\mathrm{s}}(\varphi', \lambda') G_i(\theta, A) \sin\varphi' \, \mathrm{d}\varphi' \, \mathrm{d}\lambda' \right)^2 \\ \tan\phi_{j,i} = \frac{\int_0^{2\pi} \int_0^{\pi} h_{j,\mathrm{s}}(\varphi', \lambda') G_i(\theta, A) \sin\varphi' \, \mathrm{d}\varphi' \, \mathrm{d}\lambda'}{\int_0^{2\pi} \int_0^{\pi} h_{j,\mathrm{c}}(\varphi', \lambda') G_i(\theta, A) \sin\varphi' \, \mathrm{d}\varphi' \, \mathrm{d}\lambda'}. \end{aligned} \tag{B.9}$$

Appendix C

Site Displacements due to Polar Motion

The earth's rotation generates a centrifugal force, which causes the earth to deform. Change in the instantaneous rotation axis would result in variations in the centrifugal potential, which then translate into variations in the earth deformation. The variations in the rotation axis includes deviations of the location of the pole, i.e. polar motion, and variations in the rotation rate.

Let us assume the instantaneous rotation vector as $\vec{\mathbf{\Omega}} = \Omega(m_1\vec{\boldsymbol{e}}_x + m_2\vec{\boldsymbol{e}}_y + (1 + m_3\vec{\boldsymbol{e}}_z)$, where Ω denotes the mean angular velocity of the earth. The fixed body frame is chosen as: the z-axis is aligned to the mean rotation axis, the x-axis points to the adopted zero longitude (e.g. Greenwich meridian) and the y-axis completes the right-hand system. The parameters m_1, m_2, and m_3 describe the variations, where m_3 denotes the variation in the rotation rate, and m_1 and m_2 describe the polar motion, i.e.

$$m_1 = x_p - \bar{x}_p, \quad m_2 = -(y_p - \bar{y}_p), \tag{C.1}$$

with (x_p, y_p) and $(\bar{x}_p, \bar{y}_p)$ being the instantaneous and mean pole positions, respectively. Note that the minus sign in m_2 comes from the representation of the celestial intermediate pole (CIP) in the terrestrial coordinate frame. The coordinate x_p is measured along the 0° longitude meridian, while y_p refers to the 90° longitude meridian [106].

The centrifugal potential at location $\vec{\boldsymbol{r}} = (r_x,\, r_y,\, r_z)$ is calculated as, i.e.

$$\begin{aligned} V(\vec{\boldsymbol{r}}) &= \frac{1}{2}\left(|\vec{\boldsymbol{r}}|^2|\vec{\mathbf{\Omega}}|^2 - (\vec{\boldsymbol{r}}\cdot\vec{\mathbf{\Omega}})^2\right) \\ &= \frac{\Omega^2}{2}\left((m_1^2 + m_2^2 + (1+m_3)^2)\cdot(r_x^2 + r_y^2 + r_z^2) - (m_1 r_x + m_2 r_y + (1+m_3)r_z)^2\right) \\ &= \frac{\Omega^2}{2}\left(m_1^2(r_y^2 + r_z^2) + m_2^2(r_x^2 + r_z^2) + (1+m_3)^2(r_x^2 + r_y^2) - 2m_1m_2r_xr_y - \right. \\ &\qquad \left. -2m_1(1+m_3)r_xr_z - 2m_2(1+m_3)r_yr_z\right) \\ &\simeq \frac{\Omega^2}{2}\left((1+2m_3)(r_x^2 + r_y^2) - 2(m_1r_x + m_2r_y)r_z\right) \end{aligned} \tag{C.2}$$

The approximation that the second-orders in m_i $(i = 1, 2, 3)$ are neglected, is because m_i is much smaller than 1 [107].

Let m_i in Eq. (C.2) be zero, the centrifugal potential that corresponds to the mean rotation vector is obtained from

$$\bar{V}(\vec{\boldsymbol{r}}) = \frac{\Omega^2}{2}(r_x^2 + r_y^2). \tag{C.3}$$

The difference between Eq. (C.2) and Eq. (C.3) gives the perturbation in the centrifugal potential due to the variations of the rotation vector, i.e.

$$\Delta V(\vec{\boldsymbol{r}}) = \frac{\Omega^2}{2}\left(2m_3(r_x^2 + r_y^2) - 2(m_1 r_x + m_2 r_y) r_z\right). \tag{C.4}$$

Variations in the rotation rate, described by m_3, are at least two orders of magnitude smaller than the polar motion, and induce displacements that are below millimeter-level [107]. Thus the first term in Eq. (C.4) is neglected.

The position can also be expressed as $\vec{\boldsymbol{r}} = R_\mathrm{e}(\cos\phi\cos\lambda,\ \cos\phi\sin\lambda,\ \sin\phi)$ with the radius of the earth R_e, latitude ϕ and longitude λ. The differential centrifugal potential is finally derived as

$$\Delta V(\vec{\boldsymbol{r}}) = -\frac{\Omega^2 R_\mathrm{e}^2}{2}\sin(2\phi)(m_1\cos\lambda + m_2\sin\lambda). \tag{C.5}$$

The variations of the station coordinates caused by the pole tide are obtained using the formulation of the tidal Love numbers h_2 and l_2 [108], i.e.

$$\begin{aligned}
\Delta r_\mathrm{u} &= h_2\frac{\Delta V}{g} = -\frac{h_2\Omega^2 R_\mathrm{e}^2}{2g}\sin(2\phi)(m_1\cos\lambda + m_2\sin\lambda),\\
\Delta r_\mathrm{e} &= \frac{l_2}{g\cos\phi}\frac{\partial}{\partial\lambda}\Delta V = -\frac{l_2\Omega^2 R_\mathrm{e}^2}{g}\cos(\phi)(-m_1\sin\lambda + m_2\cos\lambda),\\
\Delta r_\mathrm{n} &= \frac{l_2}{g}\frac{\partial}{\partial\phi}\Delta V = -\frac{l_2\Omega^2 R_\mathrm{e}^2}{g}\cos(2\phi)(m_1\cos\lambda + m_2\sin\lambda).
\end{aligned} \tag{C.6}$$

Setting the Love numbers $h_2 = 0.6207$ and $l_2 = 0.0836$ [36],and the radius $R_\mathrm{e} = 6378\,\mathrm{km}$, Eq. (2.28) is obtained.

Appendix D

Error Covariance of Kriging Estimates

In the ionospheric estimation proposed in this work, a subset of vertical ionospheric delays is mapped away and represented with the other estimated subset by the Kriging method. The measurements are thus grouped accordingly, where the measurements from the mapped subset contains not only the noise from the ionospheric measurement model, but also the Kriging interpolation error. Therefore, the error covariance between the Kriging estimates is required.

Let x and y denote two pierce points belonging to the mapped subset, which is denoted by an upper index "s", the error covariance is calculated as

$$\begin{aligned}
&\mathrm{Cov}\{\epsilon_{\hat{I}^{\bar{s}}_{\mathrm{v},x}}\epsilon_{\hat{I}^{\bar{s}}_{\mathrm{v},y}}\} = \mathrm{E}\left\{(\hat{I}^{\bar{s}}_{\mathrm{v},x} - I^{\bar{s}}_{\mathrm{v},x})(\hat{I}^{\bar{s}}_{\mathrm{v},y} - I^{\bar{s}}_{\mathrm{v},y})\right\} \\
&= \mathrm{E}\left\{(\sum_{i=1}^{n_s}\alpha_i\hat{I}^{s}_{\mathrm{v},i} - I^{\bar{s}}_{\mathrm{v},x})(\sum_{j=1}^{n_s}\beta_j\hat{I}^{s}_{\mathrm{v},j} - I^{\bar{s}}_{\mathrm{v},y})\right\} \\
&= \sum_{i=1}^{n_s}\sum_{j=1}^{n_s}\alpha_i\beta_j\mathrm{E}\{\hat{I}^{s}_{\mathrm{v},i}\hat{I}^{s}_{\mathrm{v},j}\} - \sum_{i=1}^{n_s}\alpha_i\mathrm{E}\{\hat{I}^{s}_{\mathrm{v},i}I^{\bar{s}}_{\mathrm{v},y}\} - \sum_{j=1}^{n_s}\beta_j\mathrm{E}\{\hat{I}^{s}_{\mathrm{v},j}I^{\bar{s}}_{\mathrm{v},x}\} + \mathrm{E}\{I^{\bar{s}}_{\mathrm{v},x}I^{\bar{s}}_{\mathrm{v},x}\}, \qquad \text{(D.1)}
\end{aligned}$$

where n_s represents the number of points in the estimated subset, α_i and β_j are the Kriging coefficients for point x and y respectively.

We apply a similar identity like in the derivation for the variance of the Kriging estimation error at one location by Günther in [1], i.e.

$$\begin{aligned}
&\frac{1}{2}\left(\mathrm{Var}\{\hat{I}^{s}_{\mathrm{v},j} - I^{\bar{s}}_{\mathrm{v},x}\} + \mathrm{Var}\{\hat{I}^{s}_{\mathrm{v},i} - I^{\bar{s}}_{\mathrm{v},y}\} - \mathrm{Var}\{\hat{I}^{s}_{\mathrm{v},i} - \hat{I}^{s}_{\mathrm{v},j}\} - \mathrm{Var}\{I^{\bar{s}}_{\mathrm{v},x} - I^{\bar{s}}_{\mathrm{v},y}\}\right) \\
&= -\mathrm{E}\{\hat{I}^{s}_{\mathrm{v},j}I^{\bar{s}}_{\mathrm{v},x}\} - \mathrm{E}\{\hat{I}^{s}_{\mathrm{v},i}I^{\bar{s}}_{\mathrm{v},y}\} + \mathrm{E}\{\hat{I}^{s}_{\mathrm{v},i}\hat{I}^{s}_{\mathrm{v},i}\} + \mathrm{E}\{I^{\bar{s}}_{\mathrm{v},x}I^{\bar{s}}_{\mathrm{v},y}\}, \qquad \text{(D.2)}
\end{aligned}$$

which comes from

$$\mathrm{Var}\{a-b\} = \mathrm{E}\{a^2\} - 2\mathrm{E}\{ab\} + \mathrm{E}\{b^2\}. \qquad \text{(D.3)}$$

Multiply the both sides of Eq. (D.2) with α_i and β_j, and sum over i, j yields

$$\begin{aligned}
\mathrm{Cov}\{\epsilon_{\hat{I}^{\bar{s}}_{\mathrm{v},x}}\epsilon_{\hat{I}^{\bar{s}}_{\mathrm{v},y}}\} &= \frac{1}{2}\left(\sum_{j=1}^{n_s}\beta_j\mathrm{Var}\{\hat{I}^{s}_{\mathrm{v},j} - I^{\bar{s}}_{\mathrm{v},x}\} + \sum_{i=1}^{n_s}\alpha_i\mathrm{Var}\{\hat{I}^{s}_{\mathrm{v},i} - I^{\bar{s}}_{\mathrm{v},y}\} - \right. \\
&\qquad \left. - \sum_{i=1}^{n_s}\alpha_i\sum_{j=1}^{n_s}\beta_j\mathrm{Var}\{\hat{I}^{s}_{\mathrm{v},i} - \hat{I}^{s}_{\mathrm{v},j}\} - \mathrm{Var}\{I^{\bar{s}}_{\mathrm{v},x} - I^{\bar{s}}_{\mathrm{v},y}\}\right) \\
&= \boldsymbol{B}^{\mathrm{T}}\boldsymbol{\Gamma}_x + \boldsymbol{A}^{\mathrm{T}}\boldsymbol{\Gamma}_y - \boldsymbol{A}^{\mathrm{T}}\boldsymbol{G}^s\boldsymbol{B} - \gamma_{xy} \qquad \text{(D.4)}
\end{aligned}$$

with

$$\boldsymbol{A} = \begin{bmatrix} \alpha_1 \\ \vdots \\ \alpha_{n_s} \end{bmatrix}, \boldsymbol{B} = \begin{bmatrix} \beta_1 \\ \vdots \\ \beta_{n_s} \end{bmatrix}, \boldsymbol{\Gamma}_x = \begin{bmatrix} \gamma(\|\boldsymbol{r}_1 - \boldsymbol{r}_x\|) \\ \vdots \\ \gamma(\|\boldsymbol{r}_{n_s} - \boldsymbol{r}_x\|) \end{bmatrix}, \boldsymbol{\Gamma}_j = \begin{bmatrix} \gamma(\|\boldsymbol{r}_1 - \boldsymbol{r}_y\|) \\ \vdots \\ \gamma(\|\boldsymbol{r}_{n_s} - \boldsymbol{r}_y\|) \end{bmatrix}, \quad \text{(D.5)}$$

and $\boldsymbol{G}^s$ represents the variogram matrix containing all pairs in the estimated subset of vertical delays, i.e.

$$\boldsymbol{G}^s = \begin{bmatrix} \gamma(\|\boldsymbol{r}_1^{\mathrm{s}} - \boldsymbol{r}_1^{\mathrm{s}}\|) & \dots & \gamma(\|\boldsymbol{r}_1^{\mathrm{s}} - \boldsymbol{r}_{n_{\mathrm{s}}}^{\mathrm{s}}\|) \\ \vdots & \ddots & \vdots \\ \gamma(\|\boldsymbol{r}_{n_{\mathrm{s}}}^{\mathrm{s}} - \boldsymbol{r}_1^{\mathrm{s}}\|) & \dots & \gamma(\|\boldsymbol{r}_{n_{\mathrm{s}}}^{\mathrm{s}} - \boldsymbol{r}_{n_{\mathrm{s}}}^{\mathrm{s}}\|) \end{bmatrix}. \quad \text{(D.6)}$$

Blanch et al. have given the expression for the variance of the Kriging estimation error in [90]. It is noted Eq. (D.4) is a general form, which transforms to the error variance from Blanch in Eq. (4.33) when point x and y represent the same point.

Appendix E

Partial Derivatives for Orbit Fitting

The steps to obtain the earth-centered earth-fixed satellite coordinates from the broadcast ephemerides are described in [26] as

Corrected mean motion	$n = \sqrt{\frac{\mu}{a^3}} + \Delta n,$
Time difference between current time and reference epoch time	$\Delta t = t - t_{\mathrm{oe}},$
Mean anomaly	$M = M_0 + n \cdot \Delta t,$
Iterative solution for eccentric anomaly	$M = E - e \cdot \sin E,$
True anomaly	$\nu = \arctan \frac{\sqrt{1-e^2}\sin E}{\cos E - e},$
Argument of latitude	$\Phi = \nu + \omega,$
Corrected longitude of ascending node	$\Omega = \Omega_0 + (\dot{\Omega} - \dot{\Omega}_{\mathrm{e}})\Delta t - \dot{\Omega}_{\mathrm{e}} t_{\mathrm{oe}},$
Corrected argument of latitude	$u = \Phi + C_{\mathrm{us}} \sin(2\Phi) + C_{\mathrm{uc}} \cos(2\Phi),$
Corrected radius	$r = a \cdot (1 - e\cos E) + C_{\mathrm{rs}} \sin(2\Phi) + C_{\mathrm{rc}} \cos(2\Phi),$
Corrected inclination angle	$i = i_0 + \dot{i} \cdot \Delta t + C_{\mathrm{is}} \sin(2\Phi) + C_{\mathrm{ic}} \cos(2\Phi),$
Earth-centered earth-fixed coordinates	$x = r\cos u \cos\Omega - r \sin u \cos i \sin\Omega,$
	$y = r\cos u \sin\Omega + r \sin u \cos i \cos\Omega,$
	$z = r \sin u \sin i,$

where μ denotes the gravitational constant.

The Jacobian matrix $\boldsymbol{J}$ for determining the broadcast ephemerides requires the partial derivatives over the Keplerian parameters and correction terms. The basis is the orbit calculation in section 5.1.

Let $\boldsymbol{P}$ denote the unit vector of the satellite position, which is given by

$$\boldsymbol{P} = \begin{bmatrix} \cos u \cos\Omega - \sin u \cos i \sin\Omega \\ \cos u \sin\Omega + \sin u \cos i \cos\Omega \\ \sin u \sin i \end{bmatrix}. \tag{E.1}$$

Additionally, three auxiliary vectors are introduced as

$$\boldsymbol{Q} = \frac{\partial \boldsymbol{P}}{\partial u} = \begin{bmatrix} -\sin u \cos\Omega - \cos u \cos i \sin\Omega \\ -\sin u \sin\Omega + \cos u \cos i \cos\Omega \\ \cos u \sin i \end{bmatrix}, \tag{E.2}$$

$$\boldsymbol{R} = \frac{\partial \boldsymbol{P}}{\partial i} = \begin{bmatrix} \sin u \sin i \sin\Omega \\ -\sin u \sin i \cos\Omega \\ \sin u \cos i \end{bmatrix}, \tag{E.3}$$

$$\boldsymbol{V} = \frac{\partial \boldsymbol{P}}{\partial \Omega} = \begin{bmatrix} -\cos u \sin \Omega - \sin u \cos i \cos \Omega \\ \cos u \cos \Omega - \sin u \cos i \sin \Omega \\ 0 \end{bmatrix}. \tag{E.4}$$

Using the chain rule, the partial derivatives with respect to the 6 Keplerian parameters a, e, i_0, ω, Ω, M_0 are calculated by

$$\frac{\partial \vec{\boldsymbol{r}}}{\partial a} = \frac{\partial r}{\partial a} \cdot \boldsymbol{P} + r \cdot \left(\frac{\partial u}{\partial a} \cdot \boldsymbol{Q} + \frac{\partial i}{\partial a} \cdot \boldsymbol{R} \right), \tag{E.5}$$

$$\frac{\partial \vec{\boldsymbol{r}}}{\partial e} = \frac{\partial r}{\partial e} \cdot \boldsymbol{P} + r \cdot \left(\frac{\partial u}{\partial e} \cdot \boldsymbol{Q} + \frac{\partial i}{\partial e} \cdot \boldsymbol{R} \right), \tag{E.6}$$

$$\frac{\partial \vec{\boldsymbol{r}}}{\partial i_0} = r \cdot \boldsymbol{R} \cdot \frac{\partial i}{\partial i_0} = r \cdot \boldsymbol{R}, \tag{E.7}$$

$$\frac{\partial \vec{\boldsymbol{r}}}{\partial \omega} = \frac{\partial r}{\partial \omega} \cdot \boldsymbol{P} + r \cdot \left(\frac{\partial u}{\partial \omega} \cdot \boldsymbol{Q} + \frac{\partial i}{\partial \omega} \cdot \boldsymbol{R} \right), \tag{E.8}$$

$$\frac{\partial \vec{\boldsymbol{r}}}{\partial \Omega_0} = r \cdot \boldsymbol{V} \cdot \frac{\partial \Omega}{\partial \Omega_0} = r \cdot \boldsymbol{V}, \tag{E.9}$$

$$\frac{\partial \vec{\boldsymbol{r}}}{\partial M_0} = \frac{\partial r}{\partial M_0} \cdot \boldsymbol{P} + r \cdot \left(\frac{\partial u}{\partial M_0} \cdot \boldsymbol{Q} + \frac{\partial i}{\partial M_0} \cdot \boldsymbol{R} \right), \tag{E.10}$$

with

$$\frac{\partial r}{\partial a} = 1 - e\cos E + ae \sin E \frac{\partial E}{\partial M}\frac{\partial M}{\partial a} + 2(C_{\mathrm{rs}} \cos(2\Phi) - 2C_{\mathrm{rc}} \sin(2\Phi)) \cdot \frac{\partial \Phi}{\partial a}, \tag{E.11}$$

$$\frac{\partial E}{\partial M} = \frac{1}{1 - e\cos E}, \tag{E.12}$$

$$\frac{\partial M}{\partial a} = -\frac{3}{2}\sqrt{\frac{\mu}{a^5}} \cdot \Delta t, \tag{E.13}$$

$$\frac{\partial \Phi}{\partial E} = \frac{\partial \Phi}{\partial \nu} \cdot \frac{\partial \nu}{\partial E} = 1 \cdot \frac{(\cos E - e)^2}{(1 - e\cos E)^2} \cdot \frac{\sqrt{1 - e^2} \cdot (1 - e\cos E)}{(\cos E - e)^2} = \frac{\sqrt{1 - e^2}}{1 - e\cos E}, \tag{E.14}$$

$$\frac{\partial \Phi}{\partial a} = \frac{\partial \Phi}{\partial E} \cdot \frac{\partial E}{\partial M} \cdot \frac{\partial M}{\partial a} = \frac{\sqrt{1 - e^2}}{(1 - e\cos E)^2} \cdot \left(-\frac{3}{2}\sqrt{\frac{\mu}{a^5}} \right) \cdot \Delta t, \tag{E.15}$$

$$\frac{\partial u}{\partial a} = (1 + 2(C_{\mathrm{us}} \cos(2\Phi) - C_{\mathrm{uc}} \sin(2\Phi))) \cdot \frac{\partial \Phi}{\partial a}, \tag{E.16}$$

$$\frac{\partial i}{\partial a} = 2(C_{\mathrm{is}} \cos(2\Phi) - C_{\mathrm{ic}} \sin(2\Phi)) \cdot \frac{\partial \Phi}{\partial a}, \tag{E.17}$$

$$\frac{\partial r}{\partial e} = -a\cos E + ae \sin E \frac{\partial E}{\partial e} + 2(C_{\mathrm{rs}} \cos(2\Phi) - C_{\mathrm{rc}} \sin(2\Phi)) \cdot \frac{\partial \Phi}{\partial e}, \tag{E.18}$$

$$\frac{\partial E}{\partial e} = \frac{\sin E}{1 - e\cos E}, \tag{E.19}$$

$$\frac{\partial \Phi}{\partial e} = \frac{\partial \nu}{\partial e} = \frac{(\cos E - e)^2}{(1 - e\cos E)^2} \cdot \left(\frac{-e\sin E + (1 - e^2)\cos E \dfrac{\partial E}{\partial e}}{\sqrt{1 - e^2} \cdot (\cos E - e)} + + \frac{\sqrt{1 - e^2} \sin E \cdot \left(1 + \sin E \dfrac{\partial E}{\partial e} \right)}{(\cos E - e)^2} \right), \tag{E.20}$$

$$\frac{\partial u}{\partial e} = (1 + 2(C_{\mathrm{us}}\cos(2\Phi) - C_{\mathrm{uc}}\sin(2\Phi))) \cdot \frac{\partial \Phi}{\partial e}, \tag{E.21}$$

$$\frac{\partial i}{\partial e} = 2(C_{\mathrm{is}}\cos(2\Phi) - C_{\mathrm{ic}}\sin(2\Phi)) \cdot \frac{\partial \Phi}{\partial e}, \tag{E.22}$$

$$\frac{\partial r}{\partial \omega} = 2(C_{\mathrm{rs}}\cos(2\Phi) - C_{\mathrm{rc}}\sin(2\Phi)), \tag{E.23}$$

$$\frac{\partial u}{\partial \omega} = 1 + 2(C_{\mathrm{us}}\cos(2\Phi) - C_{\mathrm{uc}}\sin(2\Phi)), \tag{E.24}$$

$$\frac{\partial i}{\partial \omega} = 2(C_{\mathrm{is}}\cos(2\Phi) - C_{\mathrm{ic}}\sin(2\Phi)), \tag{E.25}$$

$$\frac{\partial r}{\partial M_0} = ae\sin E\frac{\partial E}{\partial M_0} + 2(C_{\mathrm{rs}}\cos(2\Phi) - C_{\mathrm{rc}}\sin(2\Phi)) \cdot \frac{\partial \Phi}{\partial M_0}, \tag{E.26}$$

$$\frac{\partial E}{\partial M_0} = \frac{1}{1 - e\cos E}, \tag{E.27}$$

$$\frac{\partial \Phi}{\partial M_0} = \frac{\partial \Phi}{\partial \nu} \cdot \frac{\partial \nu}{\partial E} \cdot \frac{\partial E}{\partial M_0} = \frac{\sqrt{1 - e^2}}{(1 - e\cos E)^3}, \tag{E.28}$$

$$\frac{\partial u}{\partial M_0} = (1 + 2(C_{\mathrm{us}}\cos(2\Phi) - C_{\mathrm{uc}}\sin(2\Phi))) \cdot \frac{\partial \Phi}{\partial M_0}, \tag{E.29}$$

$$\frac{\partial i}{\partial M_0} = 2(C_{\mathrm{is}}\cos(2\Phi) - C_{\mathrm{ic}}\sin(2\Phi)) \cdot \frac{\partial \Phi}{\partial M_0}. \tag{E.30}$$

Similarly, the partial derivatives with respect to the correction terms are calculated by

$$\frac{\partial \vec{\boldsymbol{r}}}{\partial \Delta n} = \frac{\partial r}{\partial \Delta n} \cdot \boldsymbol{P} + r \cdot \left(\frac{\partial u}{\partial \Delta n} \cdot \boldsymbol{Q} + \frac{\partial i}{\partial \Delta n} \cdot \boldsymbol{R} \right), \tag{E.31}$$

$$\frac{\partial \vec{\boldsymbol{r}}}{\partial i} = r \cdot \Delta t \cdot \boldsymbol{R}, \tag{E.32}$$

$$\frac{\partial \vec{\boldsymbol{r}}}{\partial \dot{\Omega}} = r \cdot \Delta t \cdot \boldsymbol{V}, \tag{E.33}$$

$$\frac{\partial \vec{\boldsymbol{r}}}{\partial C_{\mathrm{us}}} = r\sin(2\Phi) \cdot \boldsymbol{Q}, \tag{E.34}$$

$$\frac{\partial \vec{\boldsymbol{r}}}{\partial C_{\mathrm{uc}}} = r\cos(2\Phi) \cdot \boldsymbol{Q}, \tag{E.35}$$

$$\frac{\partial \vec{\boldsymbol{r}}}{\partial C_{\mathrm{rs}}} = \sin(2\Phi) \cdot \boldsymbol{P}, \tag{E.36}$$

$$\frac{\partial \vec{\boldsymbol{r}}}{\partial C_{\mathrm{rc}}} = \cos(2\Phi) \cdot \boldsymbol{P}, \tag{E.37}$$

$$\frac{\partial \vec{\boldsymbol{r}}}{\partial C_{\mathrm{is}}} = r\sin(2\Phi) \cdot \boldsymbol{R}, \tag{E.38}$$

$$\frac{\partial \vec{\boldsymbol{r}}}{\partial C_{\mathrm{ic}}} = r\cos(2\Phi) \cdot \boldsymbol{R}, \tag{E.39}$$

with

$$\frac{\partial r}{\partial \Delta n} = ae\sin E\frac{\partial E}{\partial \Delta n} + 2(C_{\mathrm{rs}}\cos(2\Phi) - C_{\mathrm{rc}}\sin(2\Phi)) \cdot \frac{\partial \Phi}{\partial \Delta n}, \tag{E.40}$$

$$\frac{\partial E}{\partial \Delta n} = \frac{\partial E}{\partial M} \cdot \frac{\partial M}{\partial \Delta n} = \frac{\Delta t}{1 - e\cos E}, \tag{E.41}$$

$$\frac{\partial \Phi}{\partial \Delta n} = \frac{\partial \Phi}{\partial E} \cdot \frac{\partial E}{\partial \Delta n} = \frac{\Delta t \cdot \sqrt{1-e^2}}{(1 - e\cos E)^2}, \tag{E.42}$$

$$\frac{\partial u}{\partial \Delta n} = (1 + 2(C_{\mathrm{us}}\cos(2\Phi) - C_{\mathrm{uc}}\sin(2\Phi))) \cdot \frac{\partial \Phi}{\partial \Delta n}, \tag{E.43}$$

$$\frac{\partial i}{\partial \Delta n} = 2(C_{\mathrm{is}}\cos(2\Phi) - C_{\mathrm{ic}}\sin(2\Phi)) \cdot \frac{\partial \Phi}{\partial \Delta n}. \tag{E.44}$$

If the transformed set of non-singular orbital elements $(a, i_0, \Omega_0, \xi, \eta, \lambda)$ instead of the 6 Keplerian parameters is used, i.e.

$$\xi = e\cos\omega, \;\; \eta = -e\sin\omega, \;\; \lambda = M_0 + \omega, \tag{E.45}$$

the partial derivatives with respect to ξ, η, and λ are obtained by

$$\frac{\partial \vec{\boldsymbol{r}}}{\partial \xi} = \frac{\partial r}{\partial \xi} \cdot \boldsymbol{P} + r \cdot \left(\frac{\partial u}{\partial \xi} \cdot \boldsymbol{Q} + \frac{\partial i}{\partial \xi} \cdot \boldsymbol{R} \right), \tag{E.46}$$

$$\frac{\partial \vec{\boldsymbol{r}}}{\partial \eta} = \frac{\partial r}{\partial \eta} \cdot \boldsymbol{P} + r \cdot \left(\frac{\partial u}{\partial \eta} \cdot \boldsymbol{Q} + \frac{\partial i}{\partial \eta} \cdot \boldsymbol{R} \right), \tag{E.47}$$

$$\frac{\partial \vec{\boldsymbol{r}}}{\partial \lambda} = \frac{\partial r}{\partial \lambda} \cdot \boldsymbol{P} + r \cdot \left(\frac{\partial u}{\partial \lambda} \cdot \boldsymbol{Q} + \frac{\partial i}{\partial \lambda} \cdot \boldsymbol{R} \right), \tag{E.48}$$

where

$$\frac{\partial e}{\partial \xi} = \frac{\xi}{\sqrt{\xi^2 + \eta^2}}, \quad \frac{\partial \omega}{\partial \xi} = \frac{\eta}{\xi^2 + \eta^2}, \tag{E.49}$$

$$\frac{\partial \Phi}{\partial \xi} = \frac{\partial \nu}{\partial e} \cdot \frac{\partial e}{\partial \xi} + \frac{\partial \omega}{\partial \xi}, \tag{E.50}$$

$$\frac{\partial r}{\partial \xi} = \left(-a\cos E + a\sqrt{\xi^2 + \eta^2}\sin E \frac{\partial E}{\partial e} + 2(C_{\mathrm{rs}}\cos(2\Phi) - C_{\mathrm{rc}}\sin(2\Phi)) \cdot \frac{\partial \Phi}{\partial e} \right) \frac{\partial e}{\partial \xi}, \tag{E.51}$$

$$\frac{\partial u}{\partial \xi} = (1 + 2(C_{\mathrm{us}}\cos(2\Phi) - C_{\mathrm{uc}}\sin(2\Phi))) \cdot \frac{\partial \Phi}{\partial \xi}, \tag{E.52}$$

$$\frac{\partial i}{\partial \xi} = 2(C_{\mathrm{is}}\cos(2\Phi) - C_{\mathrm{ic}}\sin(2\Phi)) \cdot \frac{\partial \Phi}{\partial \xi}, \tag{E.53}$$

$$\frac{\partial e}{\partial \eta} = \frac{\eta}{\sqrt{\xi^2 + \eta^2}}, \quad \frac{\partial \omega}{\partial \eta} = -\frac{\xi}{\xi^2 + \eta^2}, \tag{E.54}$$

$$\frac{\partial \Phi}{\partial \eta} = \frac{\partial \nu}{\partial e} \cdot \frac{\partial e}{\partial \eta} + \frac{\partial \omega}{\partial \eta}, \tag{E.55}$$

$$\frac{\partial r}{\partial \eta} = \left(-a\cos E + a\sqrt{\xi^2 + \eta^2}\sin E \frac{\partial E}{\partial e} + 2(C_{\mathrm{rs}}\cos(2\Phi) - C_{\mathrm{rc}}\sin(2\Phi)) \cdot \frac{\partial \Phi}{\partial e} \right) \frac{\partial e}{\partial \eta}, \tag{E.56}$$

$$\frac{\partial u}{\partial \eta} = (1 + 2(C_{\mathrm{us}}\cos(2\Phi) - C_{\mathrm{uc}}\sin(2\Phi))) \cdot \frac{\partial \Phi}{\partial \eta}, \tag{E.57}$$

$$\frac{\partial i}{\partial \eta} = 2(C_{\mathrm{is}}\cos(2\Phi) - C_{\mathrm{ic}}\sin(2\Phi)) \cdot \frac{\partial \Phi}{\partial \eta}, \tag{E.58}$$

$$\frac{\partial E}{\partial \lambda} = \frac{1}{1 - e\cos E}, \quad \frac{\partial \omega}{\partial \lambda} = 1, \tag{E.59}$$

$$\frac{\partial r}{\partial \lambda} = 2(C_{\mathrm{rs}}\cos(2\Phi) - C_{\mathrm{rc}}\sin(2\Phi)) \cdot \left(\frac{\partial \nu}{\partial E} \cdot \frac{\partial E}{\partial \lambda} + \frac{\partial \omega}{\partial \lambda}\right), \tag{E.60}$$

$$\frac{\partial u}{\partial \lambda} = (1 + 2(C_{\mathrm{us}}\cos(2\Phi) - C_{\mathrm{uc}}\sin(2\Phi))) \cdot \left(\frac{\partial \nu}{\partial E} \cdot \frac{\partial E}{\partial \lambda} + \frac{\partial \omega}{\partial \lambda}\right), \tag{E.61}$$

$$\frac{\partial i}{\partial \lambda} = 2(C_{\mathrm{is}}\cos(2\Phi) - C_{\mathrm{ic}}\sin(2\Phi)) \cdot \left(\frac{\partial \nu}{\partial E} \cdot \frac{\partial E}{\partial \lambda} + \frac{\partial \omega}{\partial \lambda}\right). \tag{E.62}$$

Appendix F

Calculation of Satellite Velocity from Broadcast Ephemerides

The transformation from the ECEF frame to the satellite RAC frame requires the satellite velocity vector. It can be easily derived from the calculation of satellite positions, which is described in the GPS ICD [26]. The position vector reads

$$\vec{\boldsymbol{r}} = \boldsymbol{R}_3(-\Omega)\boldsymbol{R}_1(-i)\begin{bmatrix} r_x \\ r_y \\ 0 \end{bmatrix} = \begin{bmatrix} r_x\cos\Omega - r_y\cos i\sin\Omega \\ r_x\sin\Omega + r_y\cos i\cos\Omega \\ r_y\sin i \end{bmatrix}, \tag{F.1}$$

with the rotation matrices $\boldsymbol{R}_3$ along the z-axis and $\boldsymbol{R}_1$ along the x-axis. The coordinates in the orbital plane is given by

$$\begin{bmatrix} r_x \\ r_y \\ 0 \end{bmatrix} = \begin{bmatrix} r\cos u \\ r\sin u \\ 0 \end{bmatrix}. \tag{F.2}$$

The first-order derivative with respect to time yields the velocity as

$$\begin{aligned} \dot{\vec{\boldsymbol{r}}} &= \frac{\partial}{\partial t}\begin{bmatrix} r_x\cos\Omega - r_y\cos i\sin\Omega \\ r_x\sin\Omega + r_y\cos i\cos\Omega \\ r_y\sin i \end{bmatrix} \\ &= \begin{bmatrix} (\dot{r}_x - r_y\dot{\Omega}\cos i)\cdot\cos\Omega - (r_x\dot{\Omega} + \dot{r}_y\cos i - r_y\dot{i}\sin i)\cdot\sin\Omega \\ (\dot{r}_x - r_y\dot{\Omega}\cos i)\cdot\sin\Omega + (r_x\dot{\Omega} + \dot{r}_y\cos i - r_y\dot{i}\sin i)\cdot\cos\Omega \\ \dot{r}_y\sin i + r_y\dot{i}\cos i \end{bmatrix}, \end{aligned} \tag{F.3}$$

with

$$\dot{r}_x = \dot{r}\cos u - r\dot{u}\sin u, \tag{F.4}$$
$$\dot{r}_y = \dot{r}\sin u + r\dot{u}\cos u, \tag{F.5}$$
$$\dot{\Omega} = \dot{\Omega} - \dot{\Omega}_e, \tag{F.6}$$
$$\dot{u} = \dot{\nu} + 2\dot{\nu}(C_{\mathrm{us}}\cos(2u) - C_{\mathrm{uc}}\sin(2u)), \tag{F.7}$$
$$\dot{r} = Ae\dot{E}\sin E + 2\dot{\nu}(C_{\mathrm{rs}}\cos(2u) - C_{\mathrm{rc}}\sin(2u)), \tag{F.8}$$
$$\dot{i} = \dot{i} + 2\dot{\nu}(C_{\mathrm{is}}\cos(2u) - C_{\mathrm{ic}}\sin(2u)), \tag{F.9}$$
$$\dot{\nu} = \frac{\sqrt{1-e^2}\cdot\dot{E}}{1 - e\cos E}, \tag{F.10}$$

$$\dot{E} = \frac{\dot{M}}{1 - e\cos E}, \tag{F.11}$$

$$\dot{M} = n. \tag{F.12}$$

Fig. F.1 depicts the accuracy of the satellite velocity from a randomly chosen PRN 9 in GPS week 1761, where the reference is obtained from the IGS precise sp3 final orbit, i.e.

$$\dot{\vec{\boldsymbol{r}}}^{\,k}_{\mathrm{sp3}}(t) = \frac{\vec{\boldsymbol{r}}^{\,k}_{\mathrm{sp3}}(t + \Delta t) - \vec{\boldsymbol{r}}^{\,k}_{\mathrm{sp3}}(t - \Delta t)}{2\Delta t}, \tag{F.13}$$

with Δt chosen sufficiently small, such as 0.1 seconds. Although the error of the broadcast orbits are in the meter level, the velocity matches with the reference on the level of sub-millimeter per second. Similar accuracies also apply for the other satellites.

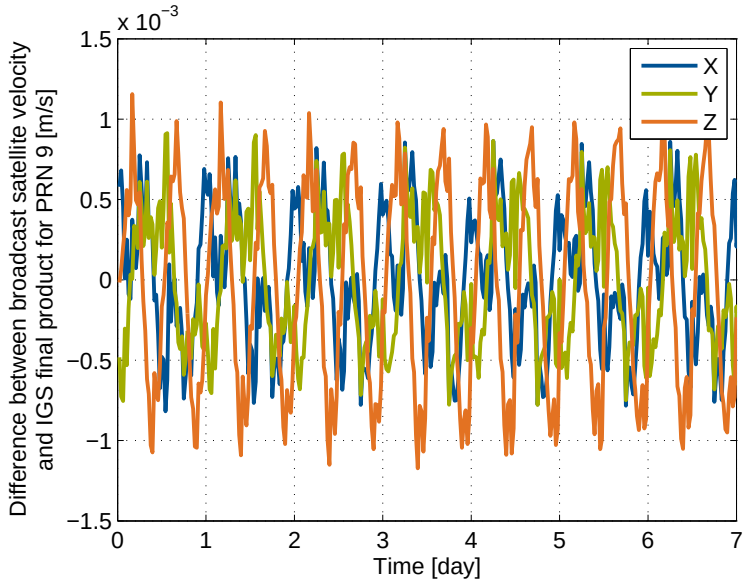

Figure F.1: Comparison of satellite velocities from broadcast ephemerides and IGS final product for a randomly chosen PRN 9.

Bibliography

[1] C. Günther, *Lecture Notes on Satellite Navigation*. Technische Universität München, 2013.

[2] B. Hofmann-Wellenhof, H. Lichtenegger, and J. Collins, *Global Positioning System: Theory and Practice*. Springer-Verlag, 1997.

[3] P. Misra and P. Enge, *Global Positioning System: Signals, Measurements and Performance Second Edition*. Lincoln, MA: Ganga-Jamuna Press, 2006.

[4] R. M. Alkan, "GPS-Single point positioning without selective availability," in *The 2001 US Hydrographic Conference, Norfold, Virginia*, 2001.

[5] S. Bisnath and Y. Gao, "Current state of precise point positioning and future prospects and limitations," in *Observing our changing earth*. Springer, 2009, pp. 615–623.

[6] H. Landau, X. Chen, S. Klose, R. Leandro, and U. Vollath, "Trimbles RTK and DGPS solutions in comparison with precise point positioning," in *Observing our Changing Earth*. Springer, 2009, pp. 709–718.

[7] J. Zumberge, M. Heflin, D. Jefferson, M. Watkins, and F. Webb, "Precise point positioning for the efficient and robust analysis of GPS data from large networks," *Journal of Geophysical Research: Solid Earth (1978–2012)*, vol. 102, no. B3, pp. 5005–5017, 1997.

[8] D. Laurichesse, F. Mercier, J.-P. Berthias, P. Broca, and L. Cerri, "Integer ambiguity resolution on undifferenced GPS phase measurements and its application to PPP and satellite precise orbit determination," *Navigation*, vol. 56, no. 2, pp. 135–149, 2009.

[9] D. Laurichesse, F. Mercier, and J. Berthias, "Real-time PPP with undifferenced integer ambiguity resolution, experimental results," in *Proceedings of the ION GNSS*, 2010, pp. 2534–2544.

[10] M. Ge, G. Gendt, M. Rothacher, C. Shi, and J. Liu, "Resolution of GPS carrier-phase ambiguities in precise point positioning (PPP) with daily observations," *Journal of Geodesy*, vol. 82, no. 7, pp. 389–399, 2008.

[11] J. Geng, C. Shi, M. Ge, A. H. Dodson, Y. Lou, Q. Zhao, and J. Liu, "Improving the estimation of fractional-cycle biases for ambiguity resolution in precise point positioning," *Journal of Geodesy*, vol. 86, no. 8, pp. 579–589, 2012.

[12] P. Henkel, Z. Wen, and C. Günther, "Estimation of satellite and receiver biases on multiple galileo frequencies with a kalman filter," in *Proceedings of the ION ITM*, 2010, pp. 1067–1074.

[13] Z. Wen, "Estimation of code and phase biases in satellite navigation," 2010, Master Thesis, Technische Universität München.

[14] Z. Wen, P. Henkel, and C. Günther, "Reliable estimation of phase biases of GPS satellites with a local reference network," in *Proceedings of 53rd International Symposium ELMAR*. IEEE, 2011, pp. 321–324.

[15] M. Vergara, M. Sgammini, Y. Zhu, S. Thoelert, and F. Antreich, "Tracking Error Modeling in Presence of Satellite Imperfections," in *Proceedings of the ION ITM*, 2014, pp. 246–253.

[16] A. van Dierendonck, P. Fenton, and T. Ford, "Theory and Performance of Narrow Correlator Spacing in a GPS Receiver," *Navigation*, vol. 39, no. 3, pp. 265–283, 1992.

[17] A. Komjathy, L. Sparks, A. J. Mannucci, and X. P. Nasa, "An assessment of the current WAAS ionospheric correction algorithm in the south American region," *Navigation*, vol. 50, no. 3, pp. 193–204, 2003.

[18] N. Jakowski, M. M. Hoque, and C. Mayer, "A new global TEC model for estimating transionospheric radio wave propagation errors," *Journal of Geodesy*, vol. 85, no. 12, pp. 965–974, 2011.

[19] A. J. Mannucci, B. Iijima, L. Sparks, X. Pi, B. Wilson, and U. Lindqwister, "Assessment of global TEC mapping using a three-dimensional electron density model," *Journal of Atmospheric and Solar-Terrestrial Physics*, vol. 61, no. 16, pp. 1227–1236, 1999.

[20] A. Komjathy, B. Wilson, T. Runge, B. Boulat, A. Mannucci, L. Sparks, and M. Reyes, "A new ionospheric model for wide area differential GPS: the multiple shell approach," in *Proceedings of ION NTM*, 2002, pp. 460–466.

[21] E. Kaplan and C. Hegarty, *Understanding GPS: principles and applications*. Artech house, 2005.

[22] J. Kouba, "A guide to using International GNSS Service (IGS) products," *International GNSS*, 2009.

[23] "IGS Products," http://igs.org/products, accessed on Jan. 7th, 2015.

[24] M. Schenewerk, "A brief review of basic gps orbit interpolation strategies," *GPS solutions*, vol. 6, no. 4, pp. 265–267, 2002.

[25] M. Horemuž and J. V. Andersson, "Polynomial interpolation of GPS satellite coordinates," *GPS solutions*, vol. 10, no. 1, pp. 67–72, 2006.

[26] Navstar, "Navstar GPS Space Segment/Navigation User Interfaces," *Arinc research corporation*, 2000.

[27] "NGA GPS Division Documentation Page," http://earth-info.nga.mil/GandG/sathtml/documentation.html, accessed on December 29th, 2013.

[28] D. L. Warren and J. F. Raquet, "Broadcast vs. precise GPS ephemerides: A historical perspective," *GPS Solutions*, vol. 7, no. 3, pp. 151–156, 2003.

[29] R. Schmid and M. Rothacher, "Estimation of elevation-dependent satellite antenna phase center variations of GPS satellites," *Journal of Geodesy*, vol. 77, no. 7-8, pp. 440–446, 2003.

[30] R. Schmid, M. Rothacher, D. Thaller, and P. Steigenberger, "Absolute phase center corrections of satellite and receiver antennas," *GPS solutions*, vol. 9, no. 4, pp. 283–293, 2005.

[31] R. Schmid, "Zur Kombination von VLBI und GNSS," Ph.D. dissertation, Technische Universität München, 2009.

[32] R. Schmid, P. Steigenberger, G. Gendt, M. Ge, and M. Rothacher, "Generation of a consistent absolute phase-center correction model for GPS receiver and satellite antennas," *Journal of Geodesy*, vol. 81, no. 12, pp. 781–798, 2007.

[33] R. Dach, U. Hugentobler, P. Fridez, M. Meindl *et al.*, "Bernese GPS software version 5.0," *Astronomical Institute, University of Bern*, vol. 640, 2007.

[34] S. Schaer and P. Steigenberger, "Determination and use of GPS differential code bias values," in *IGS Workshop*, 2006, pp. 8–11.

[35] J. Ray, "New pseudorange bias convention," IGS Mail No. 2744, IGS Central Bureau Information System, 2000.

[36] G. Petit and B. Luzum, "IERS technical note 36," *IERS Conventions*, 2010.

[37] D. C. Agnew, "Earth tides," in *Treatise on Geophysics: Geodesy*, T. A. Herring, Ed. New York: Elsevier, 2007.

[38] M. S. Bos and T. F. Baker, "An estimate of the errors in gravity ocean tide loading computations," *Journal of Geodesy*, vol. 79, no. 1-3, pp. 50–63, 2005.

[39] D. Zhao, X. Xu, J. Li, J. Duan, and L. Yu, "Ocean Tidal Loading Effects to Displacements at GNSS Sites," in *China Satellite Navigation Conference (CSNC) 2013 Proceedings*. Springer, 2013, pp. 21–29.

[40] J. A. Klobuchar, "Ionospheric time-delay algorithm for single-frequency GPS users," *IEEE Transactions on Aerospace and Electronic Systems*, no. 3, pp. 325–331, 1987.

[41] European Commission, "European GNSS(Galileo) Open Service - Ionospheric Correction Algorithm For Galileo Single Frequency Users," *Issue 1.2*, 2016.

[42] J. Saastamoinen, "Atmospheric correction for the troposphere and stratosphere in radio ranging satellites," *The use of artificial satellites for geodesy*, pp. 247–251, 1972.

[43] J. Davis, T. Herring, I. Shapiro, A. Rogers, and G. Elgered, "Geodesy by radio interferometry: Effects of atmospheric modeling errors on estimates of baseline length," *Radio science*, vol. 20, no. 6, pp. 1593–1607, 1985.

[44] G. Elgered, J. Davis, T. Herring, and I. Shapiro, "Geodesy by radio interferometry: Water vapor radiometry for estimation of the wet delay," *Journal of Geophysical Research: Solid Earth (1978–2012)*, vol. 96, no. B4, pp. 6541–6555, 1991.

[45] J. W. Marini, "Correction of satellite tracking data for an arbitrary tropospheric profile," *Radio Science*, vol. 7, no. 2, pp. 223–231, 1972.

[46] A. E. Niell, "Global mapping functions for the atmosphere delay at radio wavelengths," *Journal of Geophysical Research: Solid Earth (1978–2012)*, vol. 101, no. B1, pp. 3227–3246, 1996.

[47] J. Böhm, R. Heinkelmann, and H. Schuh, "Short note: a global model of pressure and temperature for geodetic applications," *Journal of Geodesy*, vol. 81, no. 10, pp. 679–683, 2007.

[48] M. Rothacher and G. Beutler, "The role of GPS in the study of global change," *Physics and Chemistry of the Earth*, vol. 23, no. 9, pp. 1029–1040, 1998.

[49] J. T. Wu, S. C. Wu, G. A. Hajj, W. I. Bertiger, and S. M. Lichten, "Effects of antenna orientation on GPS carrier phase," *Manuscripta Geodaetica*, vol. 18, no. 2, pp. 91–98, 1993.

[50] P. Teunissen, "The least-squares ambiguity decorrelation adjustment: a method for fast GPS integer ambiguity estimation," *Journal of Geodesy*, vol. 70, no. 1-2, pp. 65–82, 1995.

[51] ——, "GNSS ambiguity bootstrapping: theory and application," in *Proceedings of international symposium on kinematic systems in Geodesy, geomatics and navigation*, 2001, pp. 246–254.

[52] ——, "GNSS Best Integer Equivariant Estimation," in *A Window on the Future of Geodesy*. Springer, 2005, pp. 422–427.

[53] P. De Jonge and C. Tiberius, "The LAMBDA method for integer ambiguity estimation: implementation aspects," *Publications of the Delft Computing Centre, LGR-Series*, vol. 12, no. 12, pp. 1–47, 1996.

[54] C. Günther and P. Henkel, "Integer Ambiguity Estimation for Satellite Navigation," *IEEE Transactions on Signal Processing*, vol. 60, no. 7, pp. 3387–3393, 2012.

[55] F. Dilssner, "GPS IIF-1 Satellite Antenna Phase Center and Attitude Modeling," *Inside GNSS*, vol. 5, no. 6, pp. 59–64, 2010.

[56] M. Ge, G. Gendt, G. Dick, F. Zhang, and C. Reigber, "Impact of GPS satellite antenna offsets on scale changes in global network solutions," *Geophysical Research Letters*, vol. 32, no. 6, 2005.

[57] S. Zhu, F.-H. Massmann, Y. Yu, and C. Reigber, "Satellite antenna phase center offsets and scale errors in GPS solutions," *Journal of Geodesy*, vol. 76, no. 11-12, pp. 668–672, 2003.

[58] N. T. Penna, M. S. Bos, T. F. Baker, and H.-G. Scherneck, "Assessing the accuracy of predicted ocean tide loading displacement values," *Journal of Geodesy*, vol. 82, no. 12, pp. 893–907, 2008.

[59] M. M. Hoque and N. Jakowski, "Higher order ionospheric effects in precise GNSS positioning," *Journal of Geodesy*, vol. 81, no. 4, pp. 259–268, 2007.

[60] W. G. Melbourne, "The case for ranging in GPS-based geodetic systems," in *Proceedings of the First International Symposium on Precise Positioning with GPS, Rockville, Maryland*, 1985, pp. 373–386.

[61] G. Wübbena, "Software developments for geodetic positioning with GPS using TI-4100 code and carrier measurements," in *Proceedings of the First International Symposium on Precise Positioning with the Global Positioning System, Rockville, Maryland*, 1985, pp. 403–409.

[62] S. Loyer, F. Perosanz, F. Mercier, H. Capdeville, and J.-C. Marty, "Zero-difference GPS ambiguity resolution at CNES–CLS IGS Analysis Center," *Journal of Geodesy*, vol. 86, no. 11, pp. 991–1003, 2012.

[63] G. Blewitt, "Carrier phase ambiguity resolution for the global positioning system applied to geodetic baselines up to 2000 km," *Journal of Geophysical Research: Solid Earth (1978–2012)*, vol. 94, no. B8, pp. 10 187–10 203, 1989.

[64] "NOAA/NGS Analysis Strategy Summary," http://igscb.jpl.nasa.gov/igscb/center/analysis/noaa.acn, accessed on Jan. 7, 2015.

[65] M. Ge, G. Gendt, G. Dick, and F. Zhang, "Improving carrier-phase ambiguity resolution in global GPS network solutions," *Journal of Geodesy*, vol. 79, no. 1-3, pp. 103–110, 2005.

[66] "GFZ Analysis Strategy Summary," http://igscb.jpl.nasa.gov/igscb/center/analysis/gfz.acn, accessed on Jan. 7, 2015.

[67] "ESOC IGS Analysis Strategy Summary," http://igscb.jpl.nasa.gov/igscb/center/analysis/esa.acn, accessed on Jan. 7, 2015.

[68] S. A. Brown and P. Y. C. Hwang, *Introduction to Random Signals and Applied Kalman Filtering*, 3rd ed. John Wiley & Sons, New York, 1997.

[69] Z. Wen, P. Henkel, and C. Günther, "Precise Point Positioning with Estimation of Code Multipath Subset," in *Proceedings of 55th International Symposium ELMAR*. IEEE, 2013, pp. 345–348.

[70] Galileo Joint Undertaking, "Galileo open service, signal in space interface control document (OS SIS ICD)," *Draft 0*, May, 2006.

[71] G. W. Hein, J. Godet, J.-L. Issler, J.-C. Martin, R. Lucas-RodrigueZ, and T. Pratt, "Status of Galileo frequency and signal design," in *Proceedings of ION GPS*. Citeseer, 2002.

[72] P. Steigenberger, S. Hackel, U. Hugentobler, and O. Montenbruck, "One year of galileo iov orbit and clock determination," in *EGU General Assembly*, vol. 15, 2013, p. 2616.

[73] N. Mishukova, "RTK and PPP with Galileo and GPS," 2013, Master Thesis, Technische Universität München.

[74] P. Henkel, "Reliable carrier phase positioning," Ph.D. dissertation, Technische Universität München, 2010.

[75] M. J. Gabor and R. S. Nerem, "Satellite–Satellite Single-Difference Phase Bias Calibration As Applied to Ambiguity Resolution," *Navigation*, vol. 49, no. 4, pp. 223–242, 2002.

[76] Z. Wen, P. Henkel, M. Davaine, and C. Günther, "Satellite Phase and Code Bias Estimation with Cascaded Kalman Filter," in *Proceedings of European Navigation Conference*, 2011.

[77] "SAPOS Referenzstationen in Bayern," https://sapos.bayern.de/refmap.php, accessed on Jun. 7, 2011.

[78] Z. Wen, P. Henkel, A. Brack, and C. Günther, "Satellite bias determination with global station network and best integer equivariant estimation," in *Proceedings of the 25th ION GNSS*, Nashville, Sep. 2012, pp. 3675–3682.

[79] BKG/AdV, "Internal communication extracted from Abschlussbericht SAPOS - Koordinatenmonitoring," Bundesamt für Kartographie und Geodäsie, December 2008.

[80] D. Kim and R. B. Langley, "Instantaneous real time cycle-slip correction of dual-frequency GPS data," in *Proceedings of the International Symposium on Kinematic Systems in Geodesy, Geomatics and Navigation*, 2001, pp. 5–8.

[81] J. A. Bryson and L. Henrikson, "Estimation using sampled data containing sequentially correlated noise," *Journal of Spacecraft and Rockets*, vol. 5, no. 6, pp. 662–665, 1968.

[82] K. Wang, Y. Li, and C. Rizos, "Practical approaches to Kalman filtering with time-correlated measurement errors," *IEEE Transactions on Aerospace and Electronic Systems*, vol. 48, no. 2, pp. 1669–1681, 2012.

[83] D. S. Coco, C. Coker, S. R. Dahlke, and J. R. Clynch, "Variability of GPS satellite differential group delay biases," *IEEE Transactions on Aerospace and Electronic Systems*, vol. 27, no. 6, pp. 931–938, 1991.

[84] Z. Li, Y. Yuan, H. Li, J. Ou, and X. Huo, "Two-step method for the determination of the differential code biases of COMPASS satellites," *Journal of Geodesy*, vol. 86, no. 11, pp. 1059–1076, 2012.

[85] A. Mannucci, B. Wilson, D. Yuan, C. Ho, U. Lindqwister, and T. Runge, "A global mapping technique for GPS-derived ionospheric total electron content measurements," *Radio science*, vol. 33, no. 3, pp. 565–582, 1998.

[86] S. Schaer, "Mapping and Predicting the Earth's Ionosphere Using the Global Positioning System," Ph.D. dissertation, Astronomical Institutes, University of Berne, 1999.

[87] "Global Ionosphere Maps Produced by CODE," http://aiuws.unibe.ch/ionosphere/, accessed on Mar. 19th, 2015.

[88] "WM7D's Solar Resource Page," http://www.wm7d.net/hamradio/solar/index.shtml, accessed on July 3rd, 2014.

[89] J. Blanch, "An ionosphere estimation algorithm for WAAS based on Kriging," in *Proceedings of ION GPS*, 2002, pp. 24–27.

[90] J. Blanch, T. Walter, and P. Enge, "Application of spatial statistics to ionosphere estimation for WAAS," in *Proceedings of ION NTM*, vol. 10, 2002, pp. 24–40.

[91] ——, "Adapting Kriging to the WAAS MOPS ionospheric grid," in *Proceedings of ION NTM*, 2003.

[92] J. Blanch, "Using Kriging to bound satellite ranging errors due to the ionosphere," Ph.D. dissertation, Stanford University, 2003.

[93] R. Webster and M. A. Oliver, *Geostatistics for environmental scientists*. John Wiley & Sons, 2007.

[94] Z. Wen, Y. Zhu, P. Henkel, and C. Günther, "Estimation of code ionospheric biases using Kriging method," in *Proceedings of IEEE Aerospace Conference*, 2015.

[95] E. Sardon, A. Rius, and N. Zarraoa, "Estimation of the transmitter and receiver differential biases and the ionospheric total electron content from Global Positioning System observations," *Radio Science*, vol. 29, no. 3, pp. 577–586, 1994.

[96] J. Feltens, "IGS ionosphere models comparison," in *IGS Presentation, JPL Ionosphere Workshop*, 1998.

[97] F. S. T. Van Diggelen, *A-GPS: Assisted GPS, GNSS, and SBAS*. Artech House, 2009.

[98] H. Kosola, S. Ali-Loytty, and R. Piche, "Converting GNSS satellite orbit segments to GPS-compatible format," in *Ubiquitous Positioning, Indoor Navigation, and Location Based Service (UPINLBS)*. IEEE, 2012, pp. 1–5.

[99] G. González Peytaví, "Generation of Broadcast Ephemeris Information for GIOVE-A/B Satellites," 2010, Master Thesis, Technische Universität München.

[100] T. Reid, T. Walter, and P. Enge, "L1/L5 SBAS MOPS Ephemeris Message to Support Multiple Orbit Classes," in *Proceedings of the ION ITM*, 2013.

[101] O. Montenbruck and E. Gill, *Satellite Orbits: Models, Methods, Applications*, 3rd ed. Springer, 2005.

[102] Y. Wu, G. Liu, and Z. Zhang, "Research on the Fitting Algorithm of Broadcast Ephemeris Parameters Based on Non-Singular Transformation," *Journal of Astronautics*, vol. 32, no. 12, pp. 2478–2483, 2011.

[103] "IGS Antenna Files," ftp://igscb.jpl.nasa.gov/igscb/station/general/pcv_archive/, accessed on Dec. 29th, 2013.

[104] D. C. Agnew, "NLOADF: A program for computing ocean-tide loading," *Journal of Geophysical Research: Solid Earth (1978–2012)*, vol. 102, no. B3, pp. 5109–5110, 1997.

[105] W. E. Farrell, "Deformation of the Earth by surface loads," *Reviews of Geophysics*, vol. 10, no. 3, pp. 761–797, 1972.

[106] D. A. Vallado, *Fundamentals of astrodynamics and applications*. Springer Science & Business Media, 2001, vol. 12.

[107] J. M. Wahr, "Deformation induced by polar motion," *Journal of Geophysical Research: Solid Earth (1978–2012)*, vol. 90, no. B11, pp. 9363–9368, 1985.

[108] W. H. Munk and G. J. Macdonald, *The rotation of the earth: a geophysical discussion*. Cambridge University Press, 1975.